

UNIVERSITÄT ZU LÜBECK

From the Institute for Biochemistry
of the University of Lübeck
Director: Prof. Dr. Thomas Krey

A human cerebral organoid model to investigate the role of the host-pathogen interface in Ebola virus persistence in the central nervous system

Dissertation
for the fulfillment of the requirements
for the doctoral degree of the University of Lübeck

from the Department of Natural Sciences

submitted by

Lina Widerspick
from Aschaffenburg, Germany

Lübeck, 2024

First referee: Prof. Dr. Lars Redecke
Second referee: Prof. Dr. Norbert Tautz
Date of oral examination: 14.10.2024
Approved for printing: 25.10.2024

Acknowledgements

Firstly, I would like to thank Prof. Lars Redecke who so kindly supervised this dissertation at the University of Lübeck. A special thank you to Prof. César Muñoz-Fontela for all of the opportunities, scientific freedom, and support I have received during the last years at his lab at the Bernhard-Nocht-Institute for Tropical Medicine in Hamburg (BNITM). Thank you for enabling my scientific growth. Here, I also extend my warmest thank you to all Virus Immunology^{+} members throughout the years who supported me wherever they could.

I would like to further acknowledge all other collaborators who have helped me with this project. Firstly, thank you Dr. Leonore Mensching and Dr. Angelique Hoelzemer at Leibniz Institute of Virology (LIV, Hamburg) for introducing me to the iPSC and organoid culture. Thank you to Prof. Dennis Tappe and Petra Allartz at BNITM for the supervision and for letting me use their resources and magical powers, respectively. Here, I would love to extend my highest gratitude towards Dr. Johanna Steffen, who excitedly shared this adventure with me from the beginning. A special thank you to Dr. Lisa Oestereich at BNITM for always having a solution to my problems. I would also like to thank Prof. Esther Schnettler for her supervision as well as all unofficial supervisors and technical supporters I have acquired at BNITM over the past years. Thank you, to my BSL-4 suit for being a trusty companion and all BSL-4 staff and technicians for making the project possible.

Finally, I am grateful to Dr. Jens H. Kuhn, Dr. Gabriella Worwa, and Dr. Ian Crozier for welcoming me to their laboratory at the Integrated Research Facility (IRF) at NIH/NIAID (Frederick, MD, USA). A special thanks to Dr. Santiago Vidal Freire at Icahn School of Medicine at Mt. Sinai (MSSM, New York, NY, USA) who shared this experience with me and supported the project together with Prof. Gustavo Palacios and Shruti Shirsate at MSSM.

For the funding of this work, I am thankful to the Federal Institute for Risk Assessment (Bundesministerium für Risikobewertung, BfR) for awarding me with the Bf3R grant as well as DZIF for sponsoring my travels to the US. Moreover, I am most thankful to my highest contributing funders – my parents – who have been supportive throughout my adventure in the world of science and beyond. Thank you (and sorry) to my siblings, family, and friends, who now know more about Ebola virus persistence in the brain than they ever wanted to but will hopefully never forget.

Lastly, I'd like to acknowledge the tick that tried to kill me in 2005 but failed and taught me my first lesson on brain infections. You wish!

Contents

Contents IV

List of Figures XI

List of Tables XIII

List of Abbreviations XIV

1 Abstract 1

2 Zusammenfassung 2

3 Introduction 3

3.1 Ebola virus and Ebola virus disease 3

3.1.1 Ebola virus phylogeny and transmission 3

3.1.2 Ebola virus genome organization 5

3.1.3 Ebola virus lifecycle and suppression of the antiviral response 6

3.1.4 Ebola virus disease, treatment, and correlates of protection 9

3.1.5 Neurological manifestations of Ebola virus disease 11

3.1.6 Post-acute sequelae of Ebola virus disease 12

3.2 Ebola virus persistence 13

3.2.1 Definition of Ebola virus persistence 13

3.2.2 Historical evidence and implications of Ebola virus persistence in humans 13

3.2.3 Determinants of Ebola virus persistence in humans 16

3.3 Modeling Ebola virus CNS persistence 17

3.3.1 Animal models of Ebola virus CNS persistence 17

3.3.2 In vitro models of Ebola virus persistence 19

3.4 Lassa virus in the context of CNS persistence 20

3.5 Human cerebral and choroid plexus organoids 22

3.5.1 Human embryonic cerebral cortex 23

3.5.2 Human cerebral and choroid plexus organoids 25

3.6 Microglia and astrocytes in neuroinflammation 27

4 Objectives 28

5 Materials and Methods 29

5.1 Cell culture models 29

5.1.1 2D cell culture 29

5.1.2 3D cell culture . . . 32
5.1.3 2D and 3D cell culture quality control . . . 35
5.2 Viruses . . . 35
5.2.1 Virus amplification . . . 35
5.3 Experimental methodology . . . 36
5.3.1 Virus-immunological methodology . . . 36
5.3.2 Virus-immunological read-outs . . . 45
5.3.3 Molecular biology methodology . . . 53
5.4 General software . . . 55
5.5 Statistics . . . 56
5.6 Bulk RNA sequencing . . . 56
5.6.1 RNAseq data acquisition microglia and astrocytes 3, 6, 12 dpi . . . 56
5.6.2 RNAseq data acquisition microglia and astrocytes 20dpi . . . 58
5.6.3 RNAseq data acquisition of persistently infected microglia passage 10+3 58
5.6.4 RNAseq data analysis, *H. sapiens* . . . 59
5.7 Viral RNA sequencing . . . 60
5.7.1 EBOV gene expression analysis . . . 60
5.7.2 Viral RNA sequencing of RNA isolated from the supernatant . . . 61

6 Results 62
6.1 Establishment of partially immunocompetent human cerebral and choroid plexus organoids for viral persistence studies. . . . 62
6.1.1 Explorative Nipah virus and RESTV-GFP infection in human cerebral organoids to establish infection conditions. . . . 64
6.2 EBOV establishes a persistent infection of at least 120 days in human cerebral organoids. . . . 65
6.2.1 Persistent EBOV infection is associated with an increase in detected viral RNA versus infectious viral particles. . . . 68
6.2.2 EBOV defective viral genome species diversity increases in the supernatant of persistently infected cerebral organoids. . . . 69
6.2.3 Acute and persistent viral infection in human cerebral organoids translate to different neuroinflammatory cytokine profiles. . . . 70
6.2.4 EBOV infects diverse CNS cell subsets at different stages in human cerebral organoids. . . . 74
6.2.5 Establishment of cerebral organoid persistence is conserved across orthoebolaviruses. . . . 80

6.3 Exploration of 2D cell culture models to achieve long-term infection with Ebola virus. 84
6.3.1 EBOV replicates in primary monocyte-derived microglia 84
6.3.2 EBOV and LASV productively infect immortalized microglia, astrocytes, and neuroblastoma cells. 85
6.3.3 EBOV establishes a long-term infection in immortalized microglia and astrocytes. 86
6.3.4 Long-term infection of more than 91 days of human microglia cultures can be achieved via passaging. 94
6.4 The role of chemokine receptor CX3CR1 in EBOV CNS persistence. 96
6.4.1 EBOV infection enriches CX3CR1 surface expression in microglial ramifications. 99
6.4.2 Inhibition of CX3CR1 does not decrease EBOV replication or interfere with viral persistence in a 2D culture context. 99
6.4.3 Inhibition of CX3CR1 does not prevent EBOV persistence in choroid plexus organoids. 101
6.5 Host response to EBOV persistence in the CNS 104
6.5.1 Transcriptome analysis of human immortalized microglia and astrocytes infected with EBOV reveals differential response at 12dpi. 104
6.5.2 The transcriptome of microglia and astrocytes persistently infected with EBOV for 20 days. 112
6.5.3 The transcriptome of microglia passaged with EBOV for 10+3 passages. 121
6.5.4 Transcriptomic trends in Ebola virus CNS persistence. 128
6.6 EBOV variants in persistent CNS infections. 131
6.6.1 EBOV gene expression during persistent microglia and astrocyte infection. 131
6.6.2 Accumulation of SNP in EBOV serially passaged in microglia. 133
6.6.3 Isolation of naturally occurring EBOV$_{n120}$ variants grown for 120 days in human cerebral organoids via limited dilution assay. 133
6.6.4 Replication of EBOV$_{n120}$ variants in immortalized microglia and astrocytes reveals distinct replication profiles. 134
6.6.5 Viral RNA sequencing reveals accumulations of coding SNPs across EBOV genome upon CNS selection. 140
6.6.6 Naturally occurring EBOV$_{n120}$ variants display the same persistence profile in human cerebral organoids. 142
6.6.7 Staining for NP and GP in EBOV$_{n120}$ variants reveals distinct antigenic distribution and infection phenotype. 144

7 Summary of results 156

8 Discussion 158

8.1 Studies on Ebola virus CNS persistence in a tissue context using human cerebral and choroid plexus organoids 158

8.1.1 Partially immunocompetent human cerebral and choroid plexus organoids 158

8.1.2 Ebola virus persistence in human cerebral and choroid plexus organoids 159

8.1.3 Cellular reservoirs of Ebola virus in the CNS 161

8.1.4 Limitations of human cerebral and choroid plexus organoids: barrier function and adaptive immune compartment in Ebola virus persistence 162

8.1.5 Neuroinflammation in persistently infected human cerebral organoids 163

8.2 Studies on Ebola virus persistence on the cellular level 164

8.2.1 Ebola virus infection in microglia 164

8.2.2 Ebola virus infection in astrocytes and neuroblastoma cells 166

8.2.3 Persistent replication of Ebola virus in microglia and astrocytes 167

8.3 Molecular mechanisms of Ebola virus CNS persistence 169

8.3.1 The role of the antiviral response in Ebola virus persistence 169

8.3.2 Ebola virus gene expression in persistence 172

8.3.3 Altered infection dynamics during persistence: from entry to exit . . . 172

8.4 Naturally occurring Ebola virus variants in CNS persistence 175

8.4.1 Defective viral genomes and defective interfering particles in Ebola virus persistence 175

8.4.2 Low-level viral replication and evolutionary dynamics in Ebola virus persistence 176

9 Outlook 182

References XI

10 Appendix XL

List of Figures

1 Taxonomy of orthoebolaviruses and EVD outbreak variants. 3
2 EBOV transmission cycle. 4
3 EBOV, genome organization and gene expression. 6
4 Ebola virus lifecycle. 8
5 Ebola virus pathogenesis and Ebola virus disease. 10
6 Post-acute sequelae of Ebola virus disease. 12
7 Evidence and implications of EBOV persistence. 14
8 Host-pathogen-determinants of EBOV persistence. 17
9 Lassa virus overview. 21
10 Embryonic cortex and cerebral organoid architecture. 24

11 MDMi generation. 32
12 Cerebral organoid generation. 33
13 Choroid plexus organoid generation. 34
14 Multicycle-replication assay timelines. 38
15 MRA of EBOV in CX3CR1 inhibitor treated cells. 40
16 Passaging of EBOV in microglia timeline. 40
17 Cerebral organoid experiment timeline. 42
18 Choroid plexus organoid experiment timeline. 44
19 Workflow for the generation of naturally occurring variants 45
20 Workflow of RNAseq data acquisition, processing and analysis. 60

21 Light microscopy images of human cerebral and choroid plexus organoids. . 62
22 Immunohistochemistry staining of cerebral organoid cell types 63
23 Immunofluorescence microscopy of Nipah virus-infected cerebral organoids. 64
24 Immunofluorescence microscopy of RESTV-GFP-infected cerebral organoids. 65
25 Distribution and productivity of infection in cerebral organoids. 66
26 EBOV and LASV kinetics in infected human cerebral organoids. 67
27 Normalization of viral titers and RNA in infected cerebral organoids. 69
28 Semiquantification of 5’cbDVGs in EBOV persistence 70
29 Cytokine/chemokine kinetics in the supernatant of infected human cerebral organoids. 73
30 AUC for cytokines/chemokines in the supernatant of infected human cerebral organoids. 74
31 Immunohistochemistry staining of EBOV in cerebral organoids 76
32 Immunohistochemistry staining of EBOV-infected cerebral organoids 120dpi 77

33 Immunohistochemistry staining of LASV in cerebral organoids 78
34 Immunohistochemistry staining of LASV-infected cerebral organoids 120dpi . 79
35 EBOV-GFP and RESTV-GFP kinetics in infected human cerebral organoids. 81
36 Immunofluorescence microscopy of EBOV-GFP and RESTV-GFP-infected human cerebral organoids: GFAP staining. 82
37 Immunofluorescence microscopy of EBOV-GFP and RESTV-GFP-infected human cerebral organoids: CX3CR1 staining. 83
38 Multicycle-replication assay of EBOV in MDMi. 84
39 Infection of immortalized human cells with EBOV, LASV, EBOV-GFP, and RESTV-GFP. 85
40 Multicycle-replication assay at different MOI of EBOV and LASV in VeroE6 cells, Huh7 cells, microglia and astrocytes. 87
41 Monolayers of immortalized cells 25dpi with EBOV or LASV. 89
42 Immunofluorescence microscopy of EBOV and LASV-infected VeroE6 cells 25dpi. 90
43 Immunofluorescence microscopy of EBOV and LASV-infected Huh7 cells 25dpi. 91
44 Immunofluorescence microscopy of EBOV and LASV-infected microglia 25dpi. 92
45 Immunofluorescence microscopy of EBOV and LASV-infected astrocytes 25dpi. 93
46 EBOV passaging in microglia. 95
47 Flow cytometry of microglia infected with EBOV-GFP or RESTV-GFP. 97
48 Flow cytometry of MDMi infected with EBOV-GFP or RESTV-GFP. 98
49 Immunofluorescence microscopy staining of EBOV and CX3CR1 in microglia. 99
50 Serial dilution of AZD8797 CX3CR1 inhibitor and treatment of microglia. . . . 100
51 EBOV replication in human immortalized microglia, astrocytes or VeroE6 cells under the influence of 1 µM CX3CR1 inhibition. 101
52 EBOV replication in human choroid plexus organoids treated with 1 µM CX3CR1 inhibitor. 103
53 Replication, PCA, and DEGs in microglia and astrocytes infected with EBOV 3, 6, 12 dpi. 104
54 GO-Term and KEGG enrichment in microglia and astrocytes 12dpi with EBOV 106
55 Replication of EBOV and LASV in microglia and astrocytes before sequencing 20dpi 112
56 PCA and DEGs in microglia and astrocytes 20 dpi with EBOV or LASV 114
57 GO-Term and KEGG enrichment in microglia and astrocytes 20dpi with EBOV 115
58 PCA and DEGs in microglia after passaging with EBOV 121
59 GO-Term and KEGG enrichment in microglia passaged with EBOV 123
60 Heatmap of Log2FC in the expression of selected host factors in EBOV infections 129

61 Heatmap of Log2FC in the expression of selected host factors in antiinflammatory pathways . . . 130
62 Heatmap of Log2FC in the expression of selected host factors in RNA editing 130
63 EBOV gene expression in microglia and astrocytes. . . . 132
64 Limited dilution assay. . . . 134
65 Replication of EBOV$_{n120}$ variants in VeroE6 cells and microglia . . . 135
66 Multicycle-replication of EBOV$_{n120}$ in VeroE6 cells, Huh7 cells, microglia and astrocytes . . . 136
67 AUC for EBOV$_{n120}$ variants in central nervous system (CNS) cells. . . . 137
68 Monolayers of immortalized cells 25dpi with EBOV$_{n120}$ variants. . . . 138
69 Plaque size in EBOV$_{n120}$. . . . 140
70 Coding SNPs in EBOV$_{n120}$. . . . 142
71 Replication of EBOV$_{n120}$ in human cerebral organoids . . . 143
72 Expression of EBOV NP and GP in EBOV alpha. . . . 145
73 Expression of EBOV NP and GP in EBOV beta. . . . 146
74 Expression of EBOV NP and GP in EBOV gamma. . . . 148
75 Expression of EBOV NP and GP in EBOV delta. . . . 149
76 Expression of EBOV NP and GP in EBOV epsilon. . . . 150
77 Expression of EBOV NP and GP in EBOV omega. . . . 152
78 Expression of EBOV NP and GP in EBOV kappa. . . . 153
79 Expression of EBOV NP and GP in EBOV lambda. . . . 154
80 Expression of EBOV NP and GP in EBOV sigma. . . . 155

81 HE staining of 220 days old cerebral organoids . . . XL
82 Transcriptome analysis microglia 3, 6, 12dpi: supplementary data limma-voom. XLI
83 Transcriptome analysis astrocytes 3, 6, 12dpi: supplementary data limma-voom. XLII
84 Transcriptome analysis 20dpi: supplementary data limma-voom. . . . XLIII
85 Transcriptome analysis after passaging: supplementary data limma-voom. . XLIV
86 Heatmap of Log2FC in the expression of selected cytokine/chemokine signaling XLV
87 Heatmap of Log2FC in the expression of selected host factors in apoptotic signaling . . . XLVI
88 Heatmap of Log2FC in the expression of selected host factors in MAPK/PI3K/mTOR/AMPK signaling . . . XLVII
89 Heatmap of Log2FC in the expression of selected host factors in PRR signaling XLVIII
90 Heatmap of Log2FC in the expression of selected host factors in cellular adhesion and motility signaling . . . XLIX

91 Heatmap of Log2FC in the expression of selected host factors in endocytosis pathway signaling L
92 Cytokine/chemokine concentration in the supernatant of human choroid organoids treated with CX3CR1 Inhibitor. LI
93 Replication of LASV$_{n120}$ in VeroE6 cells, Huh7 cells, microglia, and astrocytes LII
94 AUC of LASV$_{n120}$ in VeroE6 cells, Huh7 cells, microglia, and astrocytes . . . LIII
95 Ethics approval PBMC. LIV

List of Tables

1 Viruses 35
2 Microglia flow cytometry panel. 48
3 Immunofluorescence microscopy antibodies 49
4 Immunohistochemistry antibodies 53
5 Software 55
5 Software 56
6 RNAseq sample inclusion days 3, 6, 12 57
7 RNAseq sample inclusion day 20 58
8 RNAseq sample inclusion passage 10+3 59

9 All differentially expressed genes in microglia 6 dpi with EBOV: upregulation . 107
10 Top 50 differentially expressed genes in microglia 12 dpi with EBOV: upregulation 107
10 Top 50 differentially expressed genes in microglia 12 dpi with EBOV: upregulation 108
11 Top 50 differentially expressed genes in microglia 12 dpi with EBOV: downregulation 108
11 Top 50 differentially expressed genes in microglia 12 dpi with EBOV: downregulation 109
12 Top 50 differentially expressed genes in astrocytes 12 dpi with EBOV: upregulation 109
12 Top 50 differentially expressed genes in astrocytes 12 dpi with EBOV: upregulation 110
13 Top 50 differentially expressed genes in astrocytes 12 dpi with EBOV: downregulation 111
14 Top 50 differentially expressed genes in microglia 20 dpi with EBOV: upregulation 116
14 Top 50 differentially expressed genes in microglia 20 dpi with EBOV: upregulation 117
15 Top 50 differentially expressed genes in microglia 20 dpi with EBOV: downreguation 117
15 Top 50 differentially expressed genes in microglia 20 dpi with EBOV: downreguation 118
16 All differentially expressed genes in microglia 20 dpi with LASV: upregulated 118
17 All differentially expressed genes in microglia 20 dpi with LASV: downregulation 118
18 Top 50 differentially expressed genes in astrocytes 20 dpi with EBOV: upregulation 119
19 Top 50 differentially expressed genes in astrocytes 20 dpi with EBOV: downregulation 120

20 All differentially expressed genes in astrocytes 20 dpi with LASV: upregulation 121
21 Top 50 differentially expressed genes in microglia after passaging with EBOV (A): upregulation 124
22 Top 50 differentially expressed genes in microglia after passaging with EBOV (A): downregulation 125
23 Top 50 differentially expressed genes in microglia after passaging with EBOV (B): upregulation 126
24 Top 50 differentially expressed genes in microglia after passaging with EBOV (B): downregulation 127
25 SNP in EBOV passaging. 133
26 EBOV$_{n120}$ SNP and replication summary 141

List of Abbreviations

ADAR	adenosine deaminase acting on RNA
ASC	adult stem cells
AUC	area under the curve
BBB	blood-brain-barrier
BDBV	Bundibugyo virus (species *Orthoebolavirus bundibugyoense*)
BDNF	brain-derived neurotropic factor
BoDV-1	Borna disease virus 1
BOMV	Bombali virus (species *Orthoebolavirus bombaliense*)
bNGF	β nerve growth factor
BSA	bovine serum albumin
BSL-4	biosafety level 4
CatB	cathepsin B
CatL	cathepsin L
CCL-2	chemokine (C-C motif) ligand 2
CD68	Cluster of Differentiation 68
CFR	case fatality ratio
CLIC6	chloride intracellular channel 6
CNS	central nervous system
CP	cortical plate
CPE	cytophatic effect
CSF	cerebrospinal fluid
CT	cycle threshold
CTL	C-type lectin
CX3CL1	C-X3-C motif ligand 1
CX3CR1	C-X3-C motif ligand receptor 1
CXCL10	C-X-C motif chemokine 10
DAPI	4′,6-diamidino-2-phenylindole
DC	dendritic cells
DC-SIGN	dendritic cell-specific ICAM-3-grabbing nonintegrin, CD209
dd	double distilled
DEGs	differentially expressed genes
DIP	defective interfering particles
DMEM	Dulbecco's Modified Eagle Medium
DMSO	dimethyl sulfoxide
DNA	deoxyribonucleic acid
DRC	Democratic Republic Congo
DVG	defective interfering genomes
EBOV	Ebola virus (species *Orthoebolavirus zairense*)
EBV	Epstein-Barr virus
EDTA	ethylenediamine tetraacetic acid
EGF	endothelial growth factor
EOMES	eomesodermin
ER	endoplasmic reticulum
EVD	Ebola virus disease
ESC	embryonic stem cells
ESCRT	endosomal sorting complexes required for transport
FasL	Fas ligand
FCS	fetal calf serum
FDR	false discovery rate
FFU	focus forming units
GFAP	glial fibrillary acidic protein
GFP	green fluorescent protein
GM-CSF	granulocyte-macrophage colony-stimulating factor
GOIs	genes of interest
GP	glycoprotein
GPC	glycoprotein
HBV	Hepatitis B virus
HEPES	(4-(2-hydroxyethyl)-1-piperazineethanesulfonic acid)
HIV	Human Immunodeficiency virus
HLA	human leukocyte antigen
HPV	Human Papilloma virus
HSV-1	Herpes Simplex virus 1
IBA1	ionized calcium-binding adaptor molecule 1
IBs	inclusion bodies
IF	immunofluorescence
IFN	interferon
IFNAR	Interferon-α/β receptor
IL	interleukin
IL-6	interleukin 6

IL-10	interleukin 10
IL-18	interleukin 18
IMHu	immortalized human microglia
iPSC	induced pluripotent stem cells
IRF-3	interferon regulatory factor 3
IRF-7	interferon regulatory factor 7
ISG	interferon stimulated genes
iSVZ	inner subventricular zone
IZ	intermediate zone
JEV	Japanese Encephalitis virus
L	L protein
LASV	Lassa virus
LDA	limited dilution assay
LF	Lassa fever
LOD	limit of detection
LPS	lipopolysaccharide
M-CSF	macrophage colony-stimulating factor
mAB	monoclonal antibody
MAP2	microtubule-associated protein 2
MAPK	mitogen-activated protein kinases
MARV	Marburg virus (species *Orthomarburgvirus marburgense*)
MCM	medical countermeasures
MCP-1	monocyte chemoattractive protein 1
MDM	monocyte-derived macrophages
MDMi	monocyte-derived microglia
MeV	Measles virus
MIP	macrophage inflammatory protein
moDC	monocyte-derived dendritic cells
MOI	multiplicity of infection
MLD	mucin-like domain
MLV	Murine Leukemia virus
MRA	multicycle-replication assay
MTA	material transfer agreement
mTOR	mammalian target of rapamycin
MZ	marginal zone
NeuN	neuronal nuclear protein
NFW	nuclease-free water
NHP	non-human primate
NIRV	non-retroviral integrated virus
NP	nucleoprotein
NPC1	Niemann Pick 1
OCT	optimal cooling temperature
OLIG1	oligodendrocyte lineage gene 1
oSVZ	outer subventricular zone
pVim	p-Vimentin
P2RY12	purinergic receptor P2Y, G-protein coupled 12
P/S	penicillin / streptomycin
PACT	protein activator of the dsRNA-activated protein kinase
PASE	post-acute sequelae of EVD
PAX6	paired box 6
PBMC	peripheral blood mononuclear cells
PCA	principal component analysis
PCR	polymerase chain reaction
PBS	phosphate buffered saline
PD-L1	programmed cell death ligand-1
PD-L2	programmed cell death ligand-1
PFA	paraformaldehyde
PI3K	phosphatidylinositol-3-kinase
PKC	protein kinase C
PKR	protein kinase R
PMA	phorbol-12-myristate-13-acetate
PP1	protein phosphatase 1
PRR	pattern recognition receptors
PS	phosphatidylserine
PSC	pluripotent stem cells
PU.1	transcription factor PU.1
RANTES	regulated and normal T cell expressed and secreted (CCL5)
RAVV	Ravn virus
RdRp	RNA-dependent RNA polymerase
RESTV	Reston virus (species *Orthoebolavirus restonense*)
RNA	ribonucleic acid
RNAi	RNA interference
RNP	ribonucleoprotein
RIG-I	retinoic acid inducible gene I
RISC	RNA-inducing silencing complex
ROCK	rho-associated protein kinase
ROS	reactive oxygen species

RSV	Respiratory Syncytial virus
SCID	severe combined immunodeficiency
SeV	Sendai virus
sGP	soluble glycoprotein
SMAD	Suppressor of mothers against decapentaplegic
SMYD3	SET and MYND domain containing 3
SNP	single nucleotide polymorphism
shedGP	shed gylcoprotein
STAT-1	signal transducer and activator of transcription 1
sTREM-1	soluble triggering receptor expressed on myeloid cells 1
SOX2	sex determining region Y-box 2
SUDV	Sudan virus (species *Orthoebolavirus sudanense*)
SVZ	subventricular zone
TAFV	Taï Forest virus (species *Orthoebolavirus taiense*)
TBR1	T-box brain transcription factor 1
TBR2	T-box brain transcription factor 2
TGF	tumor growth factor
TIM-1	T cell immunoglobulin and mucin domain 1
TLR-3	Toll-like receptor 3
TLR-4	Toll-like receptor 4
TMEM119	transmembrane protein 119
TNF	tumor necrosis factor
TNT	tunneling nanotubules
TRBP	TAR RNA-binding protein
TTR	transthyretin
TUJ1	beta-III-tubulin
VEEV	Venezuelan equine encephalitis virus
VILIP-1	visinin-like protein 1
VLP	virus-like particle
VP	viral protein
VSV	Vesicular Stomatitis virus
VSV-G	recombinant Vesicular Stomatitis virus expressing EBOV GP
VZ	ventricular zone
Z	Zink-binding

1 Abstract

Ebola virus (EBOV) is a member of the *Filoviridae* family, which is endemic in Equatorial Africa. In humans, EBOV causes Ebola virus disease (EVD), a severe, systemic illness with an average case-fatality ratio (CFR) of 45 %. The recent finding that EBOV not only causes severe acute disease but can also persist in certain body sites in humans for years, changed our understanding of how EVD epidemics start and develop. Not only does EBOV persistence have consequences at the population level, whereby outbreak resurgences and flare-ups are particularly noteworthy. Instances of severe recrudescent inflammatory disease in EVD survivors have populated the notion that EBOV persistence in humans is a threat to individual health as well. Here, EBOV CNS persistence remained particularly unexplored, despite cases of severe meningoencephalitis in EVD survivors. Although these do not come with the immediate risk of transmission to naïve individuals, as perceived for the persistence in semen, the overall high prevalence of neurological post-acute sequelae of Ebola virus disease (PASE) in survivors and inaccessibility of the central nervous system (CNS) in the context of large-scale follow-up studies as seen for testicular persistence, emphasize the need for further studies on EBOV CNS persistence in humans.

EBOV persistence entails the presence of viable, replicating virus in any site of the human body after the acute phase of EVD has been resolved. To understand EBOV persistence in the human CNS, the phenomenon must be studied on the level of the host, its tissues, at the level of the individual cells as well as on the molecular level, including the viral genome. All of this constitutes the host-pathogen interface in EBOV CNS persistence. Congruently, this thesis presents the first human cerebral and choroid plexus organoid models for EBOV persistence as well as persistently infected 2D tissue cultures of microglia and astrocytes. Thereby, this study provides the first evidence for the persistent replication of EBOV in human CNS tissue for at least 120 days and reports a broad target range of EBOV in humans, encompassing neurons, astrocytes, and microglia. Furthermore, putative mechanisms for the establishment and maintenance of EBOV persistence on the tissue and cellular as well on the viral level are proposed. These include a differential antiviral response in microglia and astrocytes, evidence of cell-cell EBOV transmission in microglia and astrocytes, possibly aided by host CX3CR1, as well as the role of defective viral genomes (DVG) and naturally occurring EBOV variants in the CNS.

2 Zusammenfassung

Ebola Virus (EBOV) ist ein in Äquatorialafrika endemisches Virus der *Filoviridae* Familie. In Menschen verursacht die Infektion mit EBOV das Ebolafieber, eine schwere sytemische Erkrankung mit einer außerordentlich hohen Sterblichkeitsrate von 45 %. Über die akute Erkrankung hinaus, hat sich im Rahmen der letzten Ebolafieberausbrüche ergeben, dass das Virus zusätzlich in bestimmten Nischen des menschlichen Körpers über Jahre hinweg persistieren kann. Auf diese Weise können EBOV Ausbrüche verlängert werden oder neu ausbrechen. Bei Überlebenden des Ebolafiebers, in denen EBOV persistiert, treten zusätzlich Rekrudeszenzen mit schweren entzündlichen Erkrankungen auf, sodass das Risiko einer persistenten Infektion nicht zu unterschätzen ist. Die EBOV Persistenz im menschlichen Gehirn blieb bisher unerforscht, obwohl es bereits Fälle von Meningoenzephalitis bei Ebolafieberüberlebenden gab. Während die Persistenz von EBOV im menschlichen Hoden ein bedeutendes Risiko für die weitere Transmission darstellt und daher intensiv erforscht wird, bleibt das Ausmaß der Persistenz im zentralen Nervensystem (ZNS) weiterhin unklar. Die hohe Anzahl an neurologischer post-akuter Folgeerkrankungen des Ebolafiebers legt jedoch nahe, dass eine beträchtliche Dunkelziffer der ZNS Persistenz existieren könnte, was eine vertiefte wissenschaftliche Erfoschung notwendig macht.

Die Persistenz von EBOV setzt voraus, dass replikationsfähiges Virus in einer Nische des Körpers nach überstandener Ebolafiebererkrankung erhalten bleibt. Für das Verständnis des Phänomens der EBOV Persistenz im ZNS, sollte dieses auf Wirts-, Gewebe-, Zell- und Molekularebene sowie anhand des Virus untersucht werden. Zusammen ergibt sich daraus die Wirt-Pathogen-Schnittstelle. In diesem Rahmen präsentiert diese Abschlussarbeit das erste Gehirn-, sowie Plexus Choroideus Organoid Modell der EBOV Persistenz, sowie weitere, persistent infizierte 2D Zellkulturmodelle. Basierend auf den Ergebnissen der vorliegenden Arbeit wird erstmals die anhaltende Replikation von EBOV in ZNS Gewebe über einen Zeitraum von 120 Tagen bestätigt, wobei diverse Zielzellen aufgezeigt werden. Dieser beinhalten Neuronen, Astrozyten und Mikroglia. Des Weiteren werden potenzielle Mechanismen für die Entstehung und Aufrechterhaltung der EBOV Persistenz auf dem Gewebs- und Zelllevel, sowie auf der Seite des Virus vorgestellt. Hier sind vor allem die differenziellen antiviralen Antworten von Mikroglia und Astrozyten, sowie die Bestätigung der Zell-Zell-Transmission von EBOV in Astrozyten und Mikroglia, die potenziell durch den Wirtsfaktor CX3CR1 unterstützt wird, hervorzuheben. Darüber hinaus werden die Konsequenzen der Anhäufung von defekten viralen Genomen (DVG) und natürlich auftretenden Anpassungen des EBOV Genoms an das ZNS aufgezeigt.

3 Introduction

3.1 Ebola virus and Ebola virus disease

3.1.1 Ebola virus phylogeny and transmission

Although considered endemic in Equatorial Africa [1], Ebola virus (species *Orthoebolavirus zairense*) (EBOV) is recognized for its alarmingly high pandemic potential [2]. The virus causes Ebola virus disease (EVD) in humans, a mild to severe systemic illness with an exceptionally high case fatality ratio (CFR) of approximately 45 % averaged across all outbreaks (rev. in [3]).

EBOV is a member of the *Filoviridae* virus family which comprises a growing group of single-stranded, negative sense (-) ribonucleic acid (RNA) viruses within the *Mononegavirales* order [4–6]. Amongst the *Filoviridae*, viruses originating from two genera pose the most relevant threat to individual and public health: orthoebolaviruses and orthomarburgviruses. Among the orthoebolaviruses EBOV, Sudan virus (species *Orthoebolavirus sudanense*) (SUDV), Bundibugyo virus (species *Orthoebolavirus bundibugyoense*) (BDBV), and Taï Forest virus (species *Orthoebolavirus taiense*) (TAFV) can cause disease in humans [4–6]. Meanwhile, Reston virus (species *Orthoebolavirus restonense*) (RESTV) is considered apathogenic in humans [7], while no human infections with Bombali virus (species *Orthoebolavirus bombaliense*) (BOMV) have been reported (rev. in [3]) (Figure 1).

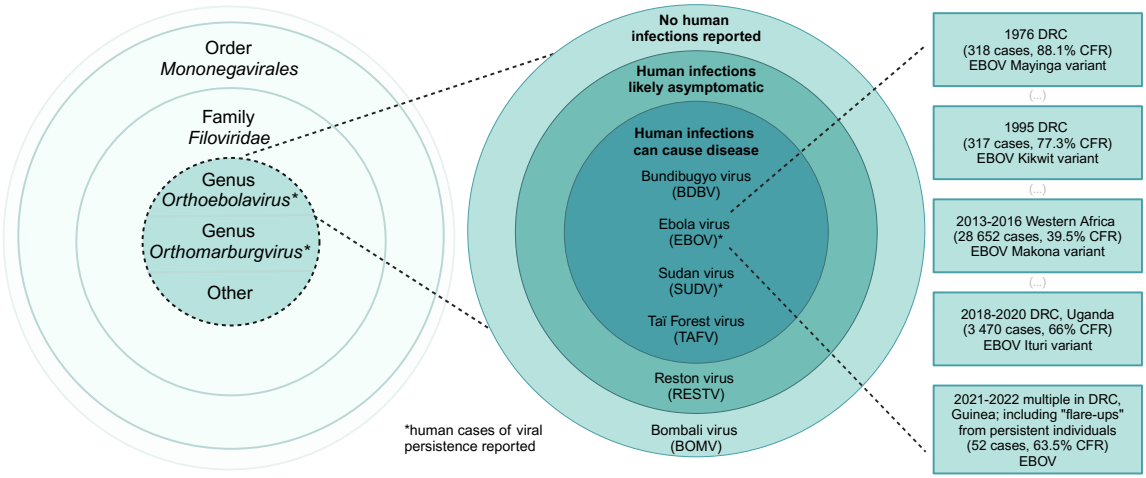


Figure 1: Taxonomy of orthoebolaviruses and EVD outbreak variants. Summary of *Orthoebolaviridae* taxonomy adapted from Jacob *et al*. with changes [3]. Updated nomenclature from Biedenkopf *et al*. [6] and case numbers from the CDC register [8]. Reported cases of human viral persistence (*). Major and most recent EVD outbreaks and reported cases and Case Fatality Ratio (CFR). Democratic Republic Congo (DRC). Created with BioRender.com.

Although infectious EBOV has never been detected in the wild, certain bat species are suspected to serve as a wild-life reservoir for this (re-)emerging virus (rev. in [9]). Nevertheless, evidence of other filoviruses replicating within wild bats [10–20] together with the discovery of paleoviral EBOV non-retroviral integrated virus (NIRV) sequences in bats suggest a close

relationship between EBOV and its suspected reservoir [21–23]. Importantly, Angolan free-tailed bats have been shown to actively replicate and shed EBOV, possibly also vertically transmitting the virus to their offspring [9]. Bats tolerate the infection with EBOV and do not develop morbidity [9]. In contrast, hosts that are part of the enzootic cycle of EBOV, chimpanzees, duikers, and gorillas among others, have been found to suffer severe disease caused by EBOV [13, 24–26] (Figure 2).

Historically, EVD outbreaks in humans started with a single spillover event from a wild-life reservoir or animal host to the human (rev. in [3]). Thereafter, EBOV subsequently establishes robust human-to-human transmission via fomite and direct contact with contaminated bodily fluids, spreading via complex transmission chains, often diversified by superspreaders [13, 27]. Especially at early stages of outbreaks, EBOV disseminates in vulnerable settings involving close bodily contact. This leaves treatment unit personnel and caring family members or participants of traditional burial practices at risk (rev. in [3]).

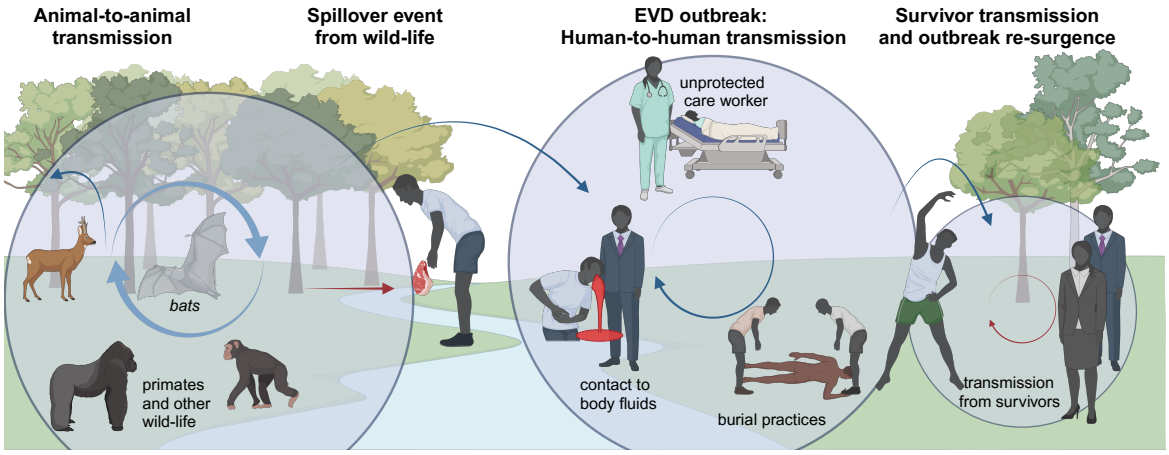


Figure 2: EBOV transmission cycle. Schematic of EBOV enzootic cycle, spillover from wild-life, human-to-human transmission during EVD outbreaks, and survivor transmission during outbreak re-surgence. Created with BioRender.com.

Between 1976 and 2013, EBOV has caused multiple, sporadic EVD outbreaks in Equatorial Africa, particularly DRC and Gabon (rev. in [3]). Notably, these remained geographically limited but nevertheless culminated in 1 403 reported cases and a CFR of 46.9 % to 90.9 % (rev. in [3]). Strikingly, between 2013 and 2016 the largest ever recorded EVD epidemic occurred in Western African countries, initiated in Guinea and subsequently spreading through Liberia, Mali, Senegal, and Sierra Leone, whereby cases were further exported internationally (rev. in [3, 13]). Here, 28 652 cases of EVD were confirmed and throughout the outbreak a CFR of 39.5 % established (rev. in [3]). Thereafter, multiple smaller outbreaks in DRC and Guinea and particularly the 2018 to 2020 DRC outbreak with 3 324 cases and a CFR of 66.4 % further highlighted the ongoing public health threat associated with EBOV (rev. in [3]). The most recent EVD outbreak in DRC was declared over in July 2022, resulting in 5 cases

all of which were fatal [8].

Importantly, during the large 2013 to 2016 EVD outbreak, novel, atypical transmission chains of EBOV variants, previously thought to be contained, re-emerged in geographically distinct locations. This was later attributed to the persistence of EBOV in survivors and subsequent transmission to naïve individuals [28–32]. Indeed, evidence for sexual transmission of EBOV up to 500 days after disease was confirmed by viral sequencing, strongly suggesting EVD outbreak dynamics to be affected by flare-ups from convalescent survivors [28–32]. Moreover, in 2021, a transmission chain from the 2013-2016 EVD outbreak resurged, indicating five years of persistence of EBOV in an unknown site in an EVD survivor [33]. Taken together, a novel mode for the start of EVD outbreaks has been established, whereby humans may serve as reservoirs for subsequent virus transmission [33].

3.1.2 Ebola virus genome organization

The EBOV genome comprises 18.96 kb and encodes seven genes for the expression of ten proteins/peptides (rev. in [34, 35]) (Figure 3). These proteins/peptides include the nucleoprotein (NP), viral protein (VP) 24, 30, 35, and 40, the RNA-dependent RNA polymerase (RdRp) encoded in the L protein (L) as well as multiple transcriptionally and post-transcriptionally edited forms of the viral glycoprotein (GP, soluble glycoprotein (sGP), ssGP, Δ-peptide) (rev. in [35–37]). The (-)-genome is synthesized as a continuous RNA molecule from an (+)-antigenome template, while the sequential mRNA transcription and gene expression nearly linearly decrease across the genome (NP>VP35>VP40>GP>VP30>VP24>L) (rev. in [34, 35]). The ends of the EBOV genome comprise a 3' leader and 5' trailer sequence, while the open reading frames of the single genes are separated by non-coding, untranslated regions which regulate initiation and stop of the transcriptional units (rev. in [34]). Notably, these regions are of variable size and overlap between the adjacent genes [34, 35]. Viral mRNA is further 5'-capped and poly-adenylated for downstream translation in the cytoplasm or rough endoplasmic reticulum (ER) (rev. in [34, 35]).

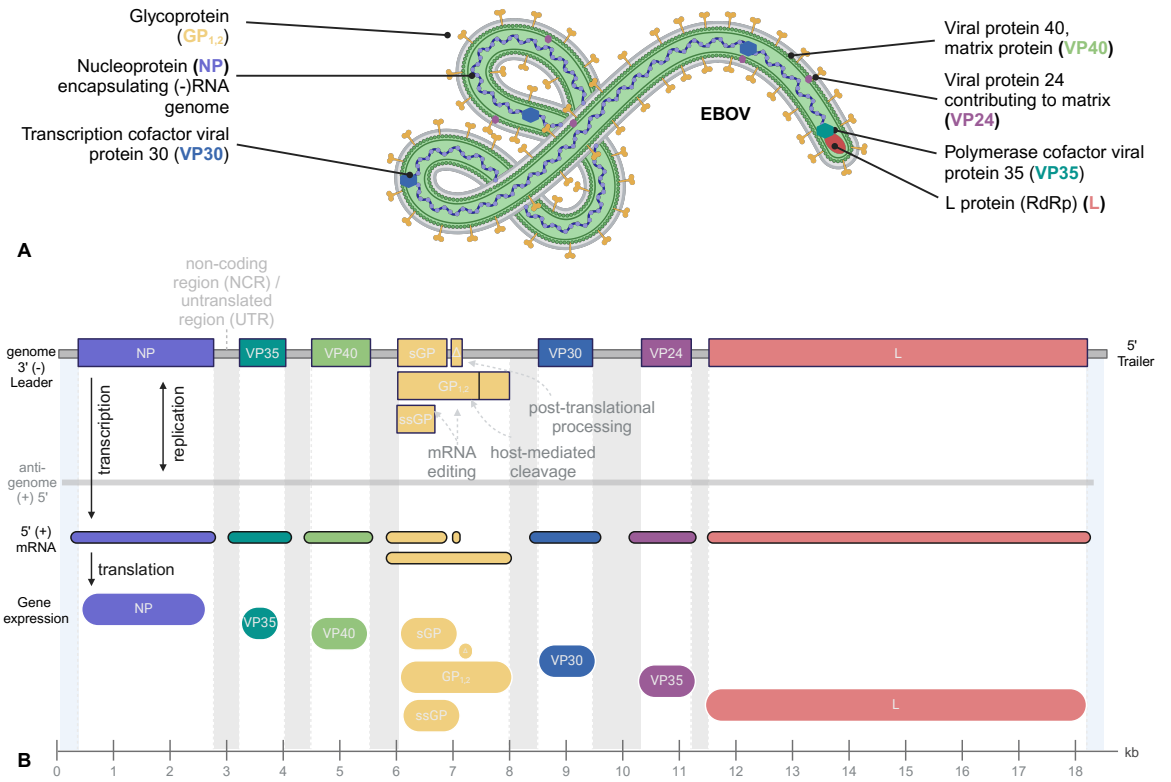


Figure 3: EBOV, genome organization and gene expression. (A) Schematic overview of EBOV filamentous particles containing glycoprotein $GP_{1,2}$ in the envelope, viral proteins VP40 and VP24 as matrix proteins and a genome encapsulated in nucleoprotein (NP). L-protein and co-factors VP30 and VP35 are contained in the particle. **(B)** EBOV genome organization and gene expression. Negative sense (-, 3'5') RNA genome organization: Nucleoprotein (NP), viral protein (VP)35, VP40, sGP, Δ-peptide, full-length glycoprotein ($GP_{1,2}$), short secreted glycoprotein (ssGP), VP30, VP40 and L protein encoding an RNA-dependent RNA polymerase. Transcription to (+, 5'3') mRNAs in order and therefore decreasing gene expression across the genome length. Genome position is indicated in grey in kilobases (kb). Non-coding regions (NCR)/untranslated regions (UTR) between the open-reading frames. sGP expression directly from the genome, $GP_{1,2}$ expression via mRNA editing, cleavage into GP_1 or GP_2 via host proteases. Δ-peptide expression via post-translational processing of sGP and expression of ssGP via mRNA editing. Created with BioRender.com.

3.1.3 Ebola virus lifecycle and suppression of the antiviral response

In its primary target cells, EBOV establishes a productive infection which culminates in the release of infectious viral progeny (Figure 4). The infection of a cell with EBOV is initiated by the attachment of the virion to a multitude of host factors, including C-type lectin (CTL) receptors and phosphatidylserine (PS) receptors such as dendritic cell-specific ICAM-3-grabbing nonintegrin, CD209 (DC-SIGN) and T cell immunoglobulin and mucin domain 1 (TIM-1), among many others [38–44]. Here, the trimeric EBOV glycoprotein $(GP)_{1,2}$, which is embedded in the viral envelope, engages with the respective attachment receptors, mediating internalization via the macropinocytotic pathway [42, 45–49]. Upon arrival in late endolysosomes, the local acidification facilitates the precursor $GP_{1,2}$ being cleaved by the host proteases cathepsin B (CatB) and cathepsin L (CatL) into GP_{CL}, whereby the mucin-like domain (MLD) and glycan cap of GP_1 are removed [50–53]. Conclusively, GP_{CL} can

subsequently bind to the endosomal cholesterol transporter Niemann Pick 1 (NPC1), inducing a conformational change enabling the GP_2-mediated fusion of the virion with the endosomal membrane [50–53]. The following formation of a pore, possibly triggered by TIM-1-assisted linkage of GP_2 to envelope PS, finally leads to the liberation of the viral ribonucleoprotein (RNP) into the host cytoplasm [50–54]. Further determinants of a successful fusion seemingly comprise an adequately low pH, enhanced Ca^{2+} concentration as well as disassembly of the VP40 viral matrix [51, 53, 55]. Importantly, NPC1 is essential and thereby tropism-restricting in EBOV infection, whereby its expression levels, together with the expression of CatB and CatL, are rate-limiting for EBOV endosomal escape [53, 56–59]. As the cellular EBOV tropism is thereby determined by these factors, most host cells can be productively infected by the virus (rev. in [3]). However, it must be noted that some host cells that express both attachment receptors and NPC1, such as T cells, are non-permissive to EBOV infection and the cells ultimately undergo apoptosis upon EBOV infection without producing infectious particles [60, 61].

In the host cytoplasm, the EBOV genome transcription takes place, whereby a complex formed by the L polymerase, NP, VP30 and VP35 is established (rev. in [47, 62]). Here, the phosphorylation status of VP30 has been identified as a determinant for the switch between viral genome replication versus transcription [63–66]. In case VP30 is phosphorylated, replication occurs, while transcription is blocked [64, 65]. Accordingly, dephosphorylation by host phosphatases, such as protein phosphatase 1 (PP1), must take place to initiate viral transcription [63–66]. Transcription of the EBOV genome further requires a multitude of host factors and finally enables translation and expression of viral proteins (rev. in [47, 67–72]). Viral protein translation, either in the cytoplasm or the rough ER ($GP_{1,2}$), is mainly driven by the host machinery, although suppression of host restriction factors like protein kinase R (PKR) by VP35 further enables the process (rev. in [47, 72]).

Viral genome replication, upon phosphorylation of VP30 by host kinases [63–66], takes place in perinuclear inclusion bodies (IBs), where the genome is amplified and packed in progeny RNP [73–75]. EBOV IBs comprise liquid organelles consisting of oligomerized NP, further enriched with viral RNP proteins and host factors relevant to replication and assembly [73, 74, 76, 77]. Concluding progeny formation, viral proteins and RNP are trafficked to the host membrane for their egress, whereby the host cytoskeletal transport network including the endosomal sorting complexes required for transport (ESCRT) machinery and host exocytosis recycling machinery are exploited (rev. in [70, 78–83]). Viral budding takes place at designated PS-enriched areas at the host membrane (lipid rafts), where VP40 oligomerization and RNP protrusion into the host membrane occurs [78, 84–88]. During the budding, the EBOV GP is incorporated into the viral envelope, while host scramblases interact further with VP40 to flip PS in the particle, which is subsequently beneficial for re-infection [78, 84–88]. The

final release of the virion from the membrane requires interference with host restriction factor activity such as Tetherin (Bst-2), which traps egressing particles to the cell surface [89–91].

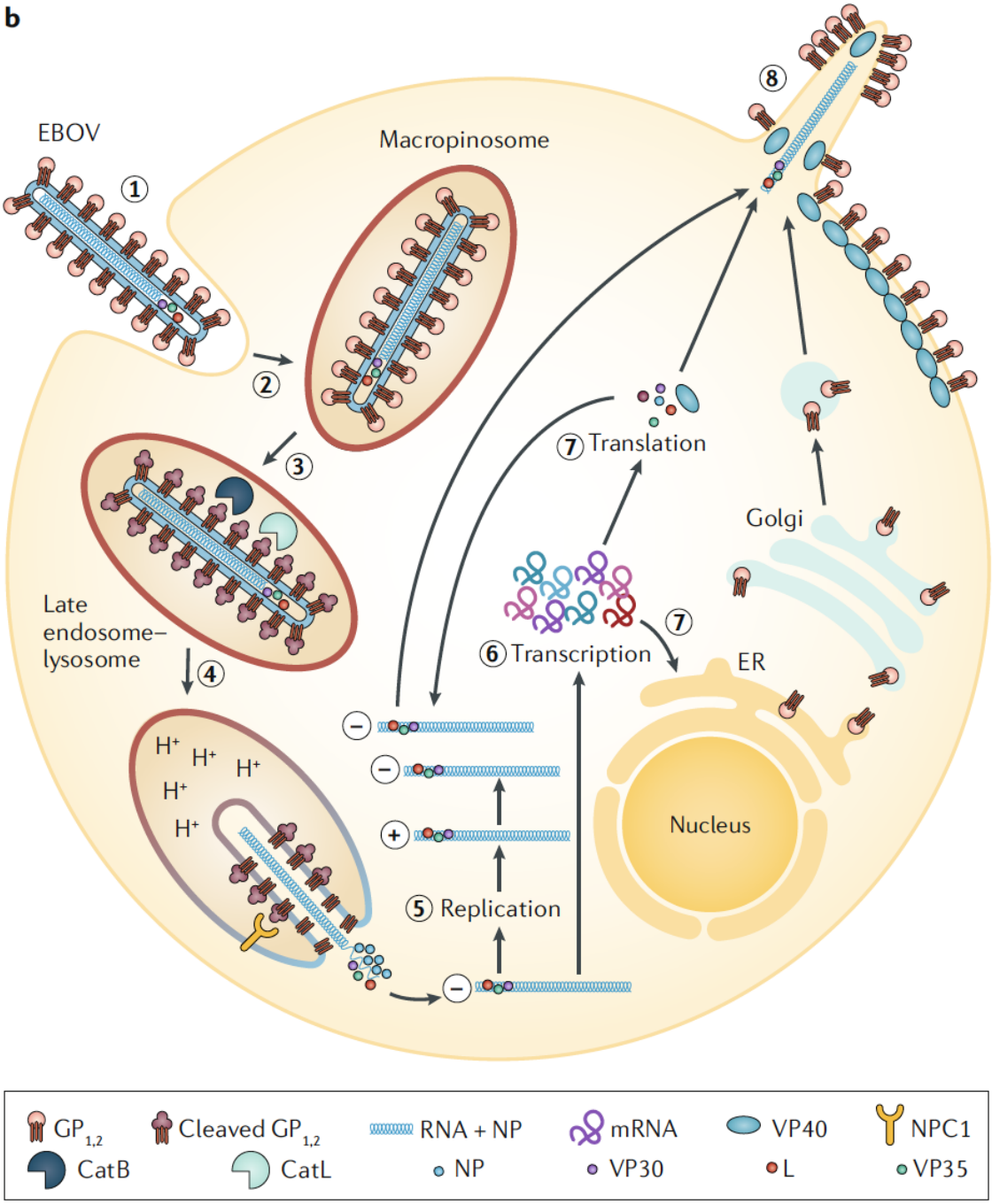


Figure 4: Ebola virus lifecycle. Schematic of the Ebola virus (EBOV) lifecycle. (1) EBOV attaches to the target cell and is (2) taken up via macropinocytosis. Subsequently, (3) $GP_{1,2}$ cleavage by host Catepsins B and L (CatB, CatL) and subsequent engagement with Niemann Pick 1 (NPC1) enables (4) fusion with the late endolysosomal membrane. (5) Replication of the (-)sense viral genome in inclusion bodies as well as (6) transcription in the host cytoplasm are followed by (7) translation of viral proteins in the cytoplasm or rough endoplasmic reticulum (ER) ($GP_{1,2}$). (8) Viral egress is driven by the penetration of the membrane via matrix protein VP40 and nucleoprotein (NP) oligomerization. Insertion of $GP_{1,2}$ into the viral particle surface during final budding. Figure taken from Jacob *et al.* [3] with the permission of the authors.

As an alternative route to budding, EBOV employs multiple cell-to-cell transmission pathways, whereby intercellular connections allow the transfer of RNP and virions [91–94]. Here, GP enables transmission via cellular fusion in an actin- and TIM-1-dependent manner [91, 92]. Syncytia formation has also been observed [92, 93, 95]. Furthermore, EBOV seemingly exploits the tunneling nanotubules (TNT) network for intercellular spread and translocation of RNP between cells [94]. Here, long-range actin-formed cell connectors, which form a continuous membrane between neighboring cells, seemingly allow for a novel mechanism of EBOV dissemination within a tissue [94].

Besides virions, EBOV-infected cells release sub-viral particles such as extracellular vesicles containing VP40 or GP, as well as sGP by itself, all of which have been implicated in modulating the host cellular environment and immune response [37, 96, 97]. In addition, EBOV interference with host pattern recognition receptors (PRR), which induce the production of interferons and downstream the expression of interferon stimulated genes (ISG), is one major virulence factor of the virus (rev. in [98–103]). In brief, EBOV abrogates retinoic acid inducible gene I (RIG-I) signaling by ultimately preventing interferon regulatory factor 3 (IRF-3) and interferon regulatory factor 7 (IRF-7) translocation to the nucleus [100–105]. In addition, VP24 prevents interferon expression [106] and signal transducer and activator of transcription 1 (STAT-1) translocation to the nucleus, further interfering with the expression of ISG (rev. in [99]).

In acute RNA virus infections, foreign dsRNA species accumulate. The sensing of such viral dsRNA by host PRR not only leads to the downstream expression of interferons and ISG, moreover, RNA interference (RNAi) is further triggered via the engagement of the RNA-inducing silencing complex (RISC) complex (Dicer/TAR RNA-binding protein (TRBP)/protein activator of the dsRNA-activated protein kinase (PACT)/Argo) (rev. in [107]). However, EBOV prevents RNAi and thereby clearance of viral RNA from the cell, via mechanisms orchestrated by VP30, 40 and 35 (rev. in [104, 107]). In addition, downstream signaling, including PKR activation and thus inhibition of viral and host gene expression, are antagonized by EBOV during acute infection (rev. in [107]). In fact, by blocking PKR, VP35 facilitates gene expression and thereby enables EBOV progeny production [76, 102].

3.1.4 Ebola virus disease, treatment, and correlates of protection

After surpassing initial physical barriers (skin and mucosal membranes), EBOV primarily infects immune cells such as macrophages and dendritic cells (DC), before disseminating to its target organs via the lymphatic system for amplification and final spread through the circulatory system [3, 13]. At sites of amplification (liver, spleen, and kidney), inflammation, damage, and necrosis occur (rev. in [13]). Clinically, acute EVD initially manifests as systemic febrile illness with subsequent severe gastrointestinal signs. These may progress towards multi-organ

failure with hematological abnormalities and overt inflammation (cytokine storm), ultimately leading to the death of the individual if not contained by the host response or treatment (rev. in [3]) (EVD pathogenesis summary in Figure 5). Only in rare cases, do hemorrhagic events occur, although EBOV has classically been grouped as a viral hemorrhagic fever virus. More recently, serological studies and case reports have implicated that while EVD is highly fatal in some cases, asymptomatic infection is also possible (rev. in [3, 108]). Factors influencing human survival have been suggested but are mostly based on low-resolution clinical data and animal models. Nevertheless, putative influencers of survival include viral determinants like exposure route, virus variant, and viral load (viremia) [109, 110] but also host-related factors such as age, sex, genetics, nutrition, and co-infections [111] as well as immune status and recognition or treatment of EVD (rev. in [3]). Importantly, individual survival can be boosted since 2019, when a Vesicular Stomatitis virus (VSV)-vector based EBOV vaccine (Ervebo) has been approved as a consequence of the *Ça-Suffit!* trial [112]. Moreover, in 2020, *PALM*-trial efforts culminated in the approval of monoclonal antibody therapies REGN-EB3 (Inmazeb) and mAB114 (Ebanga) [113, 114]. Despite targeted efforts, robust symptomatic treatment and aggressive supportive care are needed [114].

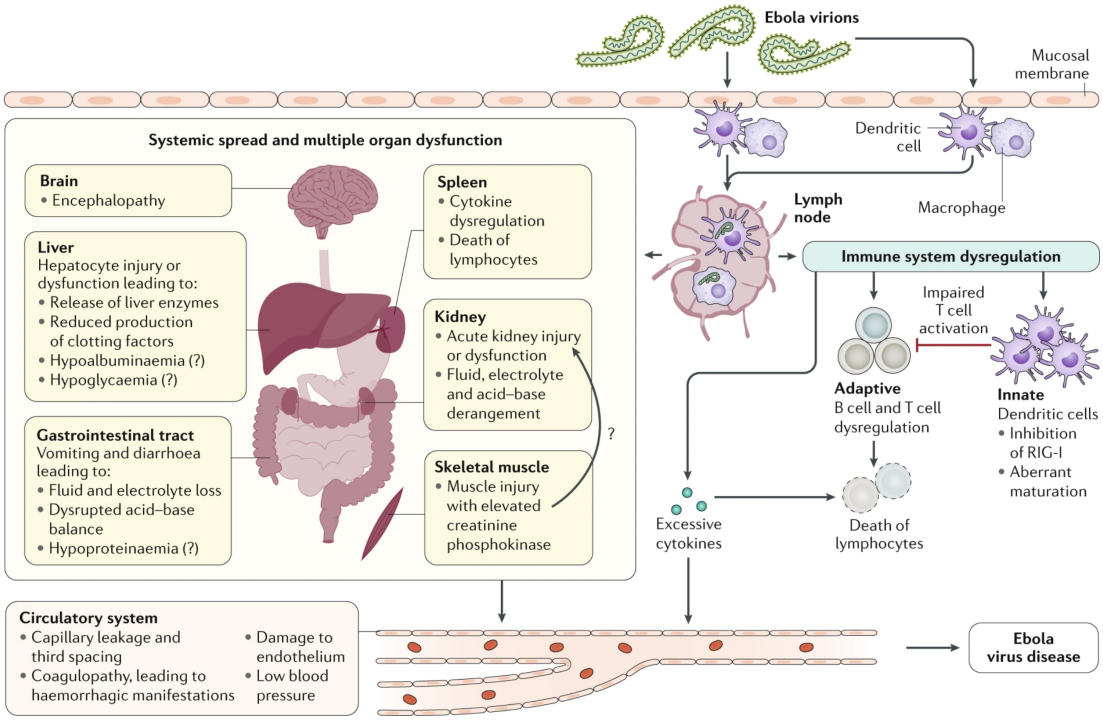


Figure 5: Ebola virus pathogenesis and Ebola virus disease. Schematic of EBOV pathogenesis and EVD in humans. EBOV crosses mucosal barriers, after which primary target cells such as dendritic cells and macrophages are infected. These spread the virus through the lymphatics and subsequently to other target organs. Amplification of the virus leads to the establishment of viremia, while infection of immune cells and bystander effects cause immune system dysregulation. Consequences of infection and immunopathology/dysregulation lead to organ dysfunction and listed pathology associated with EVD. Figure taken from Jacob *et al.* with the permission of the authors [3].

The immune correlates of protection to natural infection remain to be determined [108]. It has been shown that EBOV disrupts the innate immune response by infecting major players such as macrophages and DC (rev. in [3, 108, 115]). Coherently, monocyte-derived dendritic cells (moDC) are unable to bridge the innate and adaptive immune response upon EBOV infection, indicating that EBOV might prevent the initiation of virus-specific immunity [116]. Nevertheless, in acute EVD patients, both the humoral and cellular adaptive immune response are strongly activated, and survivors of EVD develop robust T cell memory and antibody titers [117–120]. Only in fatal cases of EVD, the T cell response fails to control viral replication [118]. Here, effector T cells increase early but are seemingly dysregulated, lacking the necessary receptor diversity for viral clearance and regressing towards an exhaustion phenotype (PD-L1, CTLA-4) [109, 118, 119]. In addition, fatal EVD has been associated with lymphocyte apoptosis, dysregulated proinflammatory cytokine profiles (classically: cytokine storm), and an inadequate humoral immune response, lacking appropriate IgG and IgM antibody titers necessary for viral control [119, 121].

3.1.5 Neurological manifestations of Ebola virus disease

In recent EVD outbreaks, neurological manifestations have been observed in some patients during the acute phase of EVD [122, 123]. Here, non-specific headaches are the most common acute neurological symptom in up to 53 % of patients [122–125]. Moreover, acute EVD patients have shown altered consciousness ranging from delirious to comatose [126–128], possibly induced by electrolyte loss due to diarrhea and vomiting, sepsis-shock-like cerebral hypoperfusion, or in rare cases, virus-related encephalitis [124]. Severe meningo-encephalitic symptoms are very rare and poorly reported [123, 128–130], however singular published cases of patients give some insights into the course of such neurological manifestations [128, 131]. To that end, Sagui *et al*. reported upon a young, male EVD patient who developed seizures and subsequently tested positive for EBOV RNA in the cerebrospinal fluid (CSF), although RNA copies/ml were 10.000-fold lower than in the blood [128]. The patient died of multi-organ failure during acute EVD [128]. Another case report by Chertow *et al*. further details a case of severe EVD, where a male patient upon multi-organ failure additionally presented with signs of meningoencephalitis [131]. The patient survived and 33 days after disease onset, lesions in the cerebral white matter, the left lateral wall of the fourth ventricle, and the spinal cord were detected, which were resolved 7 months after disease [131]. EBOV RNA was not detected in the CSF during acute disease or convalescence [131]. Therefore, the direct involvement of EBOV in these lesions was not conclusively shown.

3.1.6 Post-acute sequelae of Ebola virus disease

With large EVD survivor cohorts being established during and following the 2013–2016 West African EVD epidemic, it has become increasingly clear that many survivors are affected by post-acute sequelae of EVD (PASE). These, as extensively reviewed elsewhere [3, 123, 132–134], comprise any morbidity associated with a former but resolved infection with EBOV. PASE may range from general symptoms like fatigue but also psychological disorders, respiratory, gastrointestinal, or musculoskeletal abnormalities as well as skin changes, involvement of the urinary and reproductive tracts, sensory issues including eyesight and hearing as well as a large group of neurological symptoms [132] (rev. in [3]) (Figure 6). Except for uveitis, all PASE seemingly decrease over time post-acute disease [132].

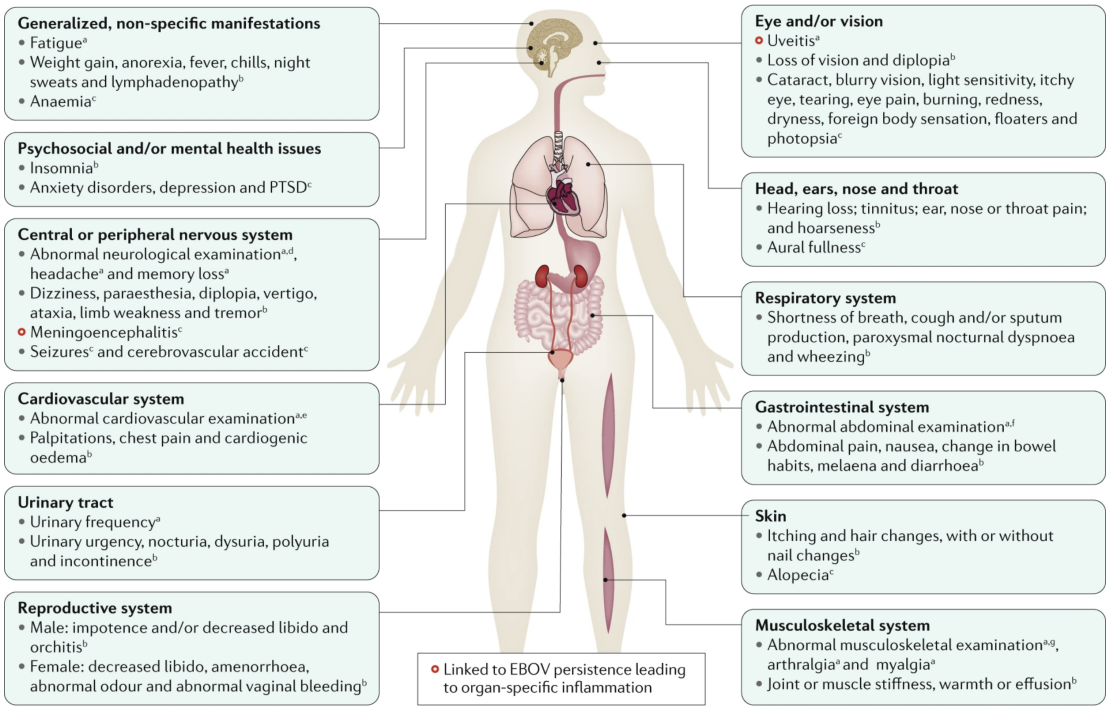


Figure 6: Post-acute sequelae of Ebola virus disease. Schematic summarizing post-acute sequelae of Ebola virus disease (PASE) in humans. PASE linked to EBOV persistence and organ-specific inflammation are highlighted in red. Figure taken from Jacob *et al.* with the permission of the authors [3].

Neurological PASE in survivors include but are not limited to abnormal reflexes, tremors, balance abnormalities, speech, and cranial nerve abnormalities, or cognitive symptoms such as memory loss and insomnia [122, 127, 132, 135]. Moreover, difficulties concentrating, changed moods, peripheral paresthesia or dysesthesia, dizziness, migraines, and tiredness as well as seizures and strokes have been reported [122, 123, 127, 129, 132, 136, 137]. Computer tomography scans of the neurological symptomatic individuals can show signs of cerebral or cerebellar atrophy and stroke [127]. Notably, the prevalence of neurological PASE differs in diverse follow-up studies, nevertheless up to a third of individuals may be affected [127, 132]. The reason why PASE occur remains unknown. However, they are hypothesized

to either be an indirect consequence of severe disease due to excessive inflammation, shock, and hypoperfusion of the CNS or caused by the undetected presence and damage caused by EBOV in the CNS during acute disease [134]. Importantly, the occurrence of neurological PASE during convalescence is to be differentiated from ongoing replication of EBOV as seen in EBOV persistence.

3.2 Ebola virus persistence

3.2.1 Definition of Ebola virus persistence

Classically, EVD was understood as a severe, acute disease that the individual either survives by clearing the viral infection or succumbs to. However, in the wake of the largest ever recorded EVD epidemic from 2013 to 2016 in Western Africa, evidence accumulated which suggested a third possible outcome of EVD: survival with EBOV persistence [130, 132, 138–140]. A virus that sustains the clearance of the innate and adaptive immune response without killing the host (cells) may be considered persistent upon ongoing replication [141]. This ongoing replication demarcates viral persistence from latency, where no replication is necessary for the maintenance of the infection [141]. Enabling viral replication beyond acute time frames requires essential viral and host factors to be continuously produced in the site of persistence of the virus as well as the maintenance of a viable viral genome [141]. Conclusively, EBOV persistence may be defined as a state in which an EVD survivor has viable, replicating EBOV genome in any site of their body.

3.2.2 Historical evidence and implications of Ebola virus persistence in humans

Singular case reports outlining that filoviruses may harbor the potential to persist in certain sites of the human body have already been populated starting in 1968 amongst the first cases of Marburg virus (species *Orthomarburgvirus marburgense*) (MARV) disease [142–146]. To that end, Martini *et al*. detail a case in which MARV persisted in the semen of a survivor and was possibly sexually transmitted three months after the initial onset of symptoms [142]. Meanwhile, an early case of EBOV persistence in the semen of a survivor of EVD was confirmed after a laboratory-related accident with the first identified EBOV Mayinga outbreak variant in 1977 [147]. Here, infectious virus was recovered from the semen 61 days after disease onset [147]. To this date, this remains the only known case of EBOV Mayinga variant persistence in humans. Persistence of EBOV RNA in the semen of EVD survivors was subsequently confirmed in the 1995 EVD outbreak in Kikwit, DRC [148, 149], and during the Western African outbreak 2013 to 2016 (EBOV Makona variant) [28, 30–32, 132, 133, 138, 150–163]. Importantly, EBOV RNA was found to persist intermittently for more than 800 days after disease onset [132, 163], while infectious virus was recovered from semen

more than 200 days after disease onset [155]. The consequences of testicular persistence of EBOV in humans subsequently became increasingly clear, whereby multiple cases of sexual transmission were suggested or evidenced (rev. in [164]). Moreover, transmissions seemingly flared up at later stages, whereby a case of confirmed sexual transmission 500 days after disease [31] as well as an outbreak resurgence 5 years after its suspected containment are particularly noteworthy [33]. Here, the former led to 13 confirmed cases including 8 deaths in Liberia in 2015 [31], whereas the latter culminated in 16 confirmed cases including 12 deaths in Guinea in 2021 [33]. Notably, in the latter case, the site of persistence was not identified [33]. Besides posing a risk for outbreak flare-ups, cautious evidence further suggests testicular EBOV persistence might affect male reproductive health, where some survivors are not able to produce semen samples due to erectile dysfunction and testicular pain [159]. Whether testicular EBOV persistence might reduce fertility remains to be shown (Figure 7).

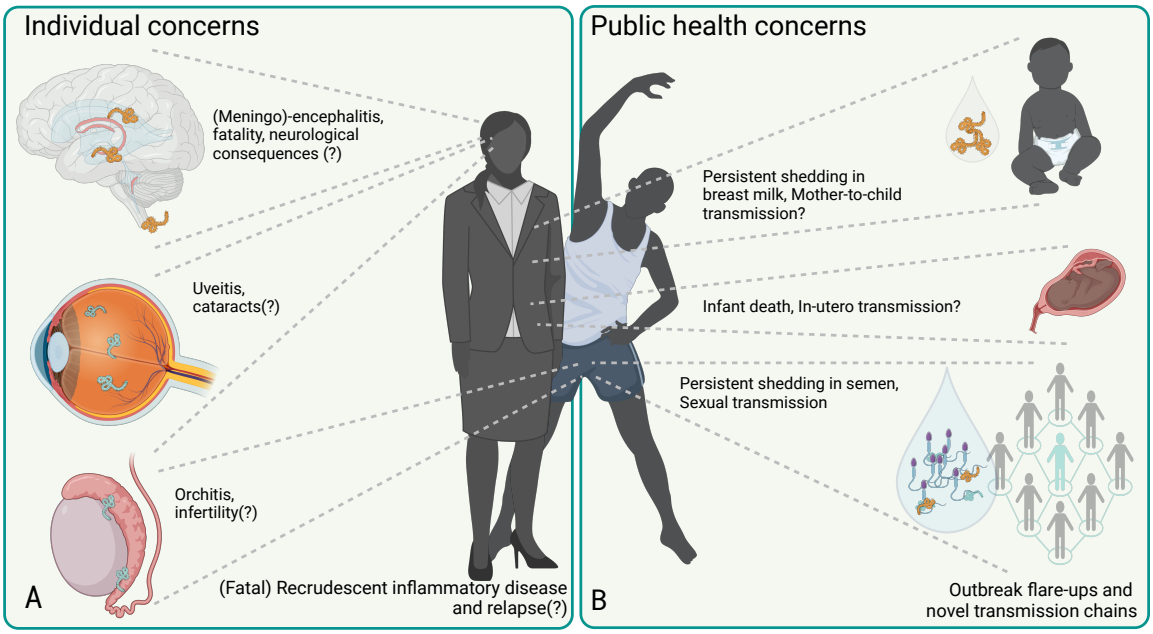


Figure 7: Evidence and implications of EBOV persistence. (A) Individual concerns and consequences of EBOV persistence in the central nervous system (CNS), eyes and testes. **(B)** Public health concerns and consequences of EBOV persistence in breast milk, the uterus, and semen. Created with BioRender.com.

Where testicular persistence was associated with atypical transmission chains, rare cases of viral persistence further implied mother-to-child transmission via breast milk [155, 165]. Here, lactating mothers seemingly transmitted EBOV to their children, resulting in their developing of EVD [155, 165]. Furthermore, a case of potential in-utero transmission from a mother to a subsequently stillborn infant [166] further highlights potential consequences of EBOV persistence in females for EVD outbreak dynamics. Notably, recovery of EBOV RNA from vaginal fluid was also successful more than 30 days after disease [148, 167].

Besides cases of novel transmission chains associated with persistence, the ongoing

replication of EBOV in a certain site might further cause recrudescent inflammatory disease. Here, morbidity arises due to local proliferation or the immune response to EBOV replication [130, 138, 139], although a true ”relapse” of acute, systemic EVD did not occur in these cases. In agreement with this, Varkey *et al*. describe a case of severe EVD in which a survivor developed ocular EBOV persistence [138]. The patient was initially treated with small interfering RNAs, convalescent plasma as well as aggressive supportive care and survived despite having a complicated and severe case of EVD [138]. Upon release, the patient had mild speech difficulties and fatigue, although the only body fluid tested positive for EBOV RNA and viral activity was semen [138]. Ten weeks after discharge, the convalescent individual reported symptoms of uveitis which worsened over a four-week time course [138]. As a consequence, the patient's aqueous humor tested positive for EBOV RNA and infectious virus evidencing that EBOV had persisted in the eye for at least 10 weeks, as confirmed via sequencing [138, 162]. Due to the high prevalence of uveitis as PASE [132], Shantha *et al*. further sampled the aqueous humor and conjunctivae of EVD survivors in the scope of the *EVICT* study [168]. However, no evidence of EBOV RNA was detected in EVD survivors 19 to 34 months after disease [168].

Severe recrudescent inflammatory disease in EVD survivors may further affect the CNS. Accordingly, in a case report by Jacobs *et al*., a female EVD patient presented with meningoencephalitis caused by EBOV persistence nine months after her discharge [139]. In brief, the patient was initially treated with aggressive supportive care, the antiviral brincidofovir, monoclonal antibodies, and convalescent plasma due to her severe primary illness [139]. Here, it was determined that the individual had an extremely high viral load and biomarkers which would have been indicators of a fatal outcome in comparable cases [139, 169]. Nevertheless, convalescence was achieved, although PASE remained [139]. Nine months after the initial discharge, the patient returned due to neck pain, photophobia, and febrile illness [139]. Here, EBOV RNA and infectious virus were detected at high levels in the CSF and low levels in the plasma of the patient, providing sequence-confirmed evidence for EBOV CNS persistence causing meningoencephalitis in humans [139]. The patient was treated with supportive care, corticosteroids, and nucleoside analog GS-5734 (remdesivir) for final convalescence [139]. Importantly, EBOV CNS persistence was further observed by Howlett *et al*. whose patient became confused and lost consciousness two weeks after primary convalescence [130]. In the following weeks, the individual continuously tested negative for EBOV in blood and synovial fluid, however, at day 40 after disease onset, the CSF tested positive via RT-PCR [130]. The authors attributed the neurological symptoms to encephalitis possibly caused by the persistently replicating virus.

Notably, only one case of a true relapse of EVD has been confirmed so far [140]. Mbala-Kingebeni *et al*. to that end report the case of a young man who survived EVD with classical

symptoms of illness and gastrointestinal manifestation [140]. At 171 days after the initial disease, the patient relapsed with symptoms of acute EVD including headache, anorexia, diarrhea, and transient loss of consciousness [140]. Clinical testing revealed markers of multi-organ failure and organ dysfunction, which culminated in the patient's death shortly after [140]. Importantly, EBOV was detected in the serum and via oral swab using RT-PCR during the relapse, confirming a true relapse [140]. Reinfection was excluded via sequencing, which revealed evolutionary conservation of the viral variant [140]. The consequence of the relapse was 91 subsequent transmissions, of which 26 were directly linked. The site of persistence remained undetected [140]. Based on this case, detrimental individual and public health concerns caused by EBOV persistence were indubitably validated (Figure 7). Warranted by the potentially fatal consequence of EBOV persistence, further research is crucial to determine how EBOV establishes and maintains persistence in certain sites. Here, the CNS is of particular interest since the current understanding is limited to rare but highly severe case reports as large-scale follow-up studies on survivors, as seen for persistence in the semen and eye, are highly complicated.

3.2.3 Determinants of Ebola virus persistence in humans

No causative determinants of Ebola virus persistence have been uncovered so far (Figure 8). Nevertheless, case reports and observational cohorts have provided evidence for factors that might influence the development of EBOV persistence within a host or population [132]. Generally, EBOV persistence may only be achieved upon the survival of the individual. Therefore, factors influencing survival might influence persistence. Notably, disease severity and biomarkers of outcome (viral load) were noted as possible determinants in case reports of recrudescent inflammatory disease upon EBOV persistence [138, 139, 169]. Moreover, questions regarding the role of treatment with monoclonal antibodies, convalescent serum, or other therapies [138, 139] in EBOV persistence were further populated, although this remains highly speculative. Notably, disease severity signified by high viral load has been identified as a contributing factor in an observational cohort study in survivors with EBOV persistence in the semen [161], although contradictory reports exist [152]. Across two cohorts, age ($\geq$35 years) has been identified as a significant risk factor for EBOV persistence in the semen of male survivors [161, 163]. Additionally, PASE-associated morbidities seemingly occurred more frequently in patients with persistent EBOV RNA in the semen [157]. Coinfections, such as Human Immunodeficiency virus (HIV), were hypothesized based on singular reports [151], however, have not been confirmed on a population/cohort level. Finally, certain HLA-types (HLA-C*03:04), as well as serum IgG3 titers, have been linked to late clearance of EBOV from the semen in one cohort [152], although, no causative conclusions could be drawn from this study. At the population level, knowledge and abstinence from (unprotected) sexual

intercourse determine the persistence and flare-up potential of EBOV and EVD outbreaks, respectively [30, 152]. Conclusively, male survivor cohorts with the rationale of informative and educational purpose, such as the Liberian *Men's Health Screening Program (MHSP)* were established [152]. Intervention with persistence via targeted treatment with antivirals, such as remdesivir, has been attempted in the *PREVAIL IV* study, however, only marginal changes in EBOV clearance from survivor semen have been achieved [133]. Further determinants for the establishment and maintenance of EBOV persistence on an individual and population level might be hypothesized based on accumulative evidence from human studies (summarized in Figure 8) but require future investigation to be conclusively associated.

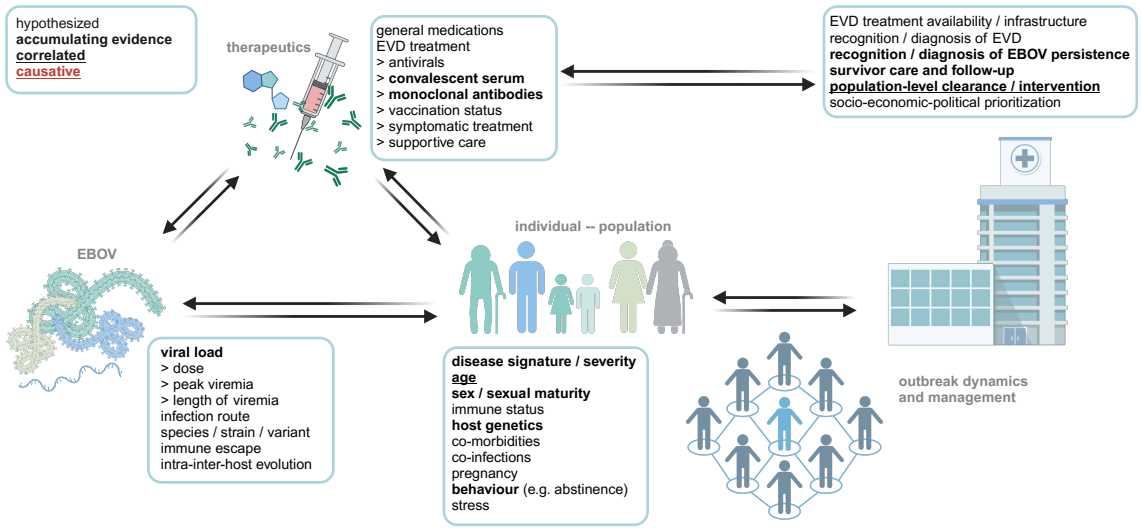


Figure 8: Host-pathogen-determinants of EBOV persistence. Hypothesized, evidenced, correlated, or causative host-pathogen-determinants of EBOV persistence on the level of the virus, host, treatment, public, and environment. Created with BioRender.com.

3.3 Modeling Ebola virus CNS persistence

3.3.1 Animal models of Ebola virus CNS persistence

Historically, non-human primate (NHP) models – cynomolgus macaques (*Macaca fascicularis*) and rhesus macaques (*Macaca mulatta*) – are considered the gold-standard for filoviral research and preclinical development, given their natural susceptibility to disease (rev. in [170, 171]). NHP models of EVD are considered uniformly lethal within two weeks of infection and are known to display human-like symptoms. Besides this, hemorrhagic events are more common than in humans and human apathogenic RESTV causes fatal disease in NHPs [7, 171]. Ferrets (*Mustela putorius furo*) also develop disease upon infection with EBOV, whereby the hallmarks of disease and tissue tropism are similar to those in humans [172, 173]. In contrast, guinea pigs, hamsters, and wild-type inbred mice do not develop fatal disease upon challenge with filoviruses, necessitating either adaptation of the viruses to the host or genetic modification of the model organism (rev. in [170]). Genetic modifications that render

mice susceptible to EBOV-induced disease include Interferon-α/β receptor (IFNAR)^{ko} and STAT-1^{ko} (rev. in [170]). More recently, humanization or generation of chimeras of these immunosuppressed mice has led to the development of more sophisticated models that capture differences amongst filovirus pathogenicity and human donors [174–177].

Animal models of EVD usually reach humane endpoint criteria during the acute phase of disease within two weeks, complicating studies on PASE and EBOV persistence [171]. Nevertheless, multiple studies and retrospective analyses of study materials have shown that EBOV penetrates and replicates in sites associated with human persistence (eyes, testes, and CNS) in mice, hamsters, ferrets, and guinea pigs during acute disease [173, 176, 178–180]. Small animal models, in which EBOV persistence was achieved, included CD4 T cell- or B cell-deficient mice [181] as well as collaborative-cross mice challenged with mouse-adapted EBOV [178]. Moreover, sexual transmission via vaginal inoculation of IFNAR^{ko} mice has been modeled [178].

NHP usually do not survive EBOV infection and die within 5 to 11 days after challenge [182–184]. Therefore, natural survivors of EVD are rare, necessitating medical countermeasures (MCM) or atypical cases with delayed death to study EBOV persistence. Acute EVD in NHP, as in humans, is a systemic febrile illness that progresses towards multi-organ failure and death, whereby EBOV may be detected in the lymphoid organs, spleen, thymus, and liver, as well as lymph nodes and kidney (rev. in [182, 185]). NHP which succumb to acute EVD classically do not have histopathological lesions or evidence of viral replication in the parenchyma of the brain or the eyes (rev. in [182]). Nevertheless, acute neurological signs in NHP have been observed [186]. In contrast, CNS involvement in NHP has been uncovered in several instances of delayed death upon EBOV challenge [182–184, 187, 188]. In these, mostly NHP that previously received MCM (e.g. monoclonal antibody therapy) displayed a delayed time of death (18–26 dpi), accompanied by rapid deterioration and signs of meningoencephalitis [182, 184, 187, 188]. Retrospective analyses by Liu *et al*. and Zeng *et al*. to that end revealed that EBOV still replicated in choroid plexus and perivascular regions in the CNS in delayed death animals, whereby monocyte and macrophage infiltration into the site of infection was observed [183, 189].

Among the very rare cases of NHP which ultimately survive EBOV challenge, most have received MCM. In NHP that have received monoclonal antibody treatment, persistent EBOV infection was retrospectively uncovered, whereby EBOV seemingly persists in the ventricular system and choroid plexus of the brain in approximately 20 % of survivors [183]. Coherently, signs of choroid plexitis and ventriculitis were detected, while CD68+ macrophages/microglia presented as EBOV reservoir during persistence [183]. Notably, survivors who displayed signs of EBOV CNS persistence after treatment had significantly higher plasma RNA loads during the acute phase of the disease than survivors where no antigen was detected [183].

EBOV CNS persistence has not been observed in any NHP naturally surviving the acute phase of EVD. These natural NHP survivors had notably less viremia during acute disease than NHP that succumbed to the viral challenge [183]. Notably, in one NHP that died later than usual (36 days after infection), EBOV protein expression was detected in the brain within glial nodules formed by $CD68^+$ microglia [189]. In the case of persistent EBOV in the CNS of MCM receiving NHP, cases of recrudescent inflammatory disease were further reported, whereby signs of severe meningoencephalitis and local inflammation warranted euthanasia [183]. In these cases, no peripheral EBOV pathology was associated with the recrudescent disease [183].

In summary, the achievement of EBOV persistence in animal models either necessitates modification of the virus or the host in small animal models or is mostly limited to retrospective studies on rare survivor NHP. Conclusively, alternative models are necessary to study filovirus persistence.

3.3.2 In vitro models of Ebola virus persistence

In general, cellular persistence, when established by lytic viruses, requires the abrogration of viral clearance and maintenance of cellular viability [141]. Furthermore, persistence necessitates ongoing viral replication and progeny production [141]. Thus, viable long-term in vitro cultures are necessary to study EBOV persistence.

In vitro, EBOV infection causes cytophatic effect (CPE) in human and NHP cells, limiting studies on persistent infections. Therefore, the molecular mechanism behind EBOV persistence in certain human tissues such as the eye, testes, and CNS, is mostly unknown. However, multiple hypotheses have been put forward. These include but are not limited to the suppression of the antiviral host response, the role of defective interfering genomes (DVG) and defective interfering particles (DIP) [190], reduced viral replication and gene expression, cell-cell transmission [91, 94] as well as viral genomic adaptation (rev. in [13]).

In the context of EBOV persistence, only one of the aforementioned hypotheses has been studied in vitro. Accordingly, the generation of DVG and DIP has been identified as a potential mechanism for viral persistence in VeroE6 cells by Calain *et al*. [190, 191]. DVG are replication defective viral genomes, which accumulate during infection due to detrimental mutations, truncations as well as copy-back/snap-back mechanisms (rev. in [190, 192, 193]). In the case of EBOV, DVG have been shown to reduce the replication of viable viral RNA, thereby reducing progeny production and tissue culture CPE [190, 194]. This way, EBOV may replicate for multiple cellular passages in vitro, whereby DVG are stochastically formed and seemingly increase the viability of the cells [190]. Notably, replication of DVG requires the presence of viable virus in the same cell, as crucial genes must be expressed from viable genomes. At the same time, although released DIP may infect novel target cells by

themselves, replication and therefore productive infection also necessitates the presence of viable virus [190, 194]. In vivo, DVG have been observed in both acute infections of NHP [192] as well as cases of human EBOV persistence [162], although their role outside the VeroE6 cell culture context remains elusive.

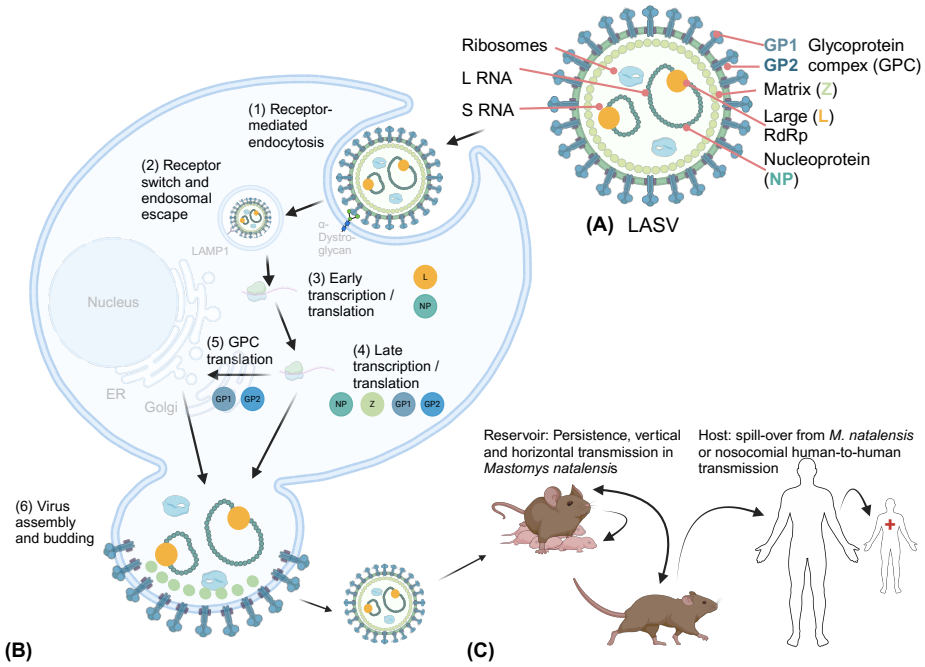
Overall, besides some hypotheses for general EBOV persistence mechanisms, further studies are needed to conclusively determine the niche-specific mechanisms that govern the establishment and maintenance of EBOV persistence in a cell or tissue context in the human host. Importantly, although descriptive in vitro studies in testicular and retinal pigment cells have been recently attempted [195, 196], no studies investigating the establishment of EBOV persistence in the CNS have been published yet. Therefore, a knowledge gap regarding how EBOV CNS persistence occurs and is maintained remains.

3.4 Lassa virus in the context of CNS persistence

In this thesis, the establishment of EBOV persistence in certain CNS in vitro models will be compared to Lassa virus (LASV) to determine virus-specific mechanisms. Therefore, this section provides a brief overview of LASV in the context of CNS persistence.

LASV is a member of the *Arenaviridae* virus family, which comprises a group of viruses with segmented, ambisense single-stranded RNA genomes (rev. in [197, 198]). Each of the two LASV genome segments encodes two proteins separated by intergenic non-coding regions (rev. in [197, 198]). The small segment (S, 3.4 kb) encodes the viral NP (-) as well as glycoprotein (GPC) precursor (+) and the large segment (L, 7 kb) encodes the viral RdRp L (-) as well as matrix protein Zink-binding (Z) protein (+) (rev. in [197, 198]). Notably, NP and L are both transcribed early from the genome, while GPC and Z protein are transcribed late from the antigenome (rev. in [197, 198]). While GPC mediates LASV attachment and internalization, NP encapsulates the viral genome, mediates viral transcription and replication, and plays an important role in immune evasion (rev. in [197, 198]). L is crucial for viral replication and mechanisms necessary for downstream protein translation such as cap-snatching, while the Z protein makes up the viral matrix and thereby enables viral assembly and budding (rev. in [197, 198]) (Figure 9).

LASV is the causative agent of Lassa fever (LF) in humans, a viral hemorrhagic fever that is fatal in 30 % of hospitalized cases (rev. in [197, 199]). The main reservoir of LASV is *Mastomys natalensis* [200, 201], a rodent species living close to humans across Western Africa (rev. in [197, 201]). In the endemically infected reservoir population [201], LASV is vertically transmitted to the offspring and horizontally to humans and other rodents (rev. in [197, 201–203]). Human-to-human spread is rare and mostly limited to healthcare settings (rev. in [197, 204]). For LF, there are no specific MCM available, and a vaccine has not been approved as of yet (rev. in [197]).



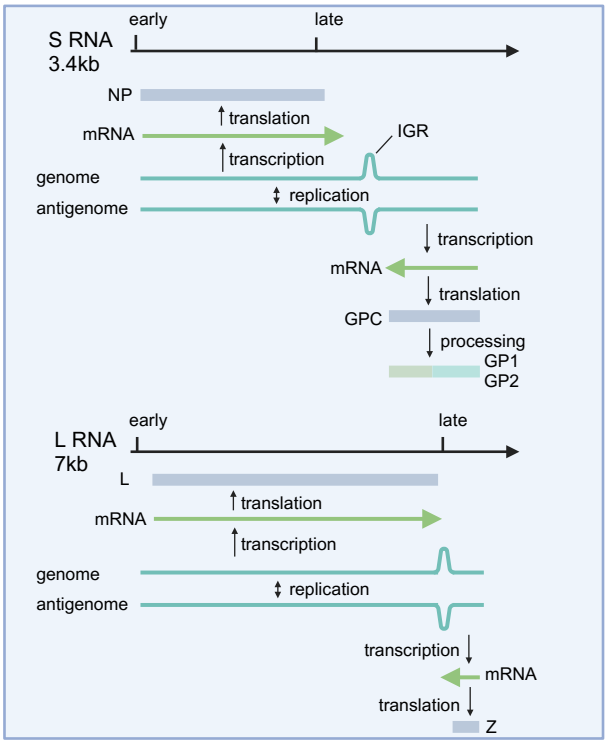


Figure 9: Lassa virus overview. (A) LASV structure with two ambisense RNA genome segments (Large (L), Small (S)), encapsulated in the nucleoprotein (NP). L protein (L) serves as RNA-dependent RNA polymerase (RdRp) and additional host ribosomes contained in an enveloped particle. Glycoprotein complex (GPC, GP1, GP2) contained in the envelope and exposed to the virion surface. Viral matrix is formed by the Zinc-binding (Z) protein. **(B)** LASV lifecycle starting from (1) receptor-mediated endocytosis by binding to α-Dystroglyan and subsequent (2) receptor switch to LAMP1 for internalization via endosomal escape. (3) Early transcription and translation of LASV L and NP in the cytoplasm, followed by (4) late transcription and translation of NP, Z, and GPC, whereby (5) GPC translation occurs in the rough ER and Golgi. (6) Virus assembly and budding from the host membrane via LASV Z. **(C)** LASV enzootic vertical and horizontal transmission within its natural reservoir species *Mastomys natalensis* as well as spill-over to the human host. Rare nosocomial human-to-human transmission. **(D)** Schematic of LASV transcription and replication of the small (S) and large (L) RNA genome segments. Transcription of NP from the viral genome (early) and GPC from the antigenome (late) of the S segment. Downstream processing of GPC to GP1 and GP2. Transcription of L from the L segment genome (early) and Z from the antigenome (late). Figure adjusted from Garry *et al*. [197] and created with BioRender.com.

The infection with LASV is in most cases asymptomatic or mild with unspecific symptoms of febrile illness (rev. in [197, 199]). Nevertheless, in severe cases of LF, the acute disease leads to kidney failure and in rare cases manifests as viral hemorrhagic fever with bleeding from orifices and mucosal surfaces. Ultimately, severe LF ends in multi-organ failure and the death of the individual (rev. in [197]). It is modeled that there are approximately 500.000 LASV infections occurring annually, while 5 000 of those may lead to the death of the individual (approx. overall CFR=1 %) (rev. in [197]). Notably, CNS manifestations, which occur in approximately 40 % of severe LF cases, have been associated with poor outcome [199, 205, 206]. Here, signs of viral (meningo-)encephalitis and encephalopathy were reported [199, 207, 208], whereby LASV RNA can in some - but not all [208] - cases be detected in the CSF [205, 209], even upon clearance form the serum [207]. Similar to EVD, LF survivors often experience post-acute sequelae such as deafness as well as visual and neurological defects [210].

In *Mastomys natalensis*, LASV causes persistent infections in neonates and younger juveniles of up to 16 months [203]. Here, LASV may be detected systemically in the reservoir host, although no signs of morbidity and tissue histopathology were observed [203]. In these rodents, besides classical target sites, LASV antigen can be detected in ganglion cells of the retina, various tissues of the reproductive tract, including Sertoli cells in the testes, and the epithelium of the epididymis as well as in neurons, brain endothelial cells, oligodendrocytes, and choroid plexus epithelial cells [203]. No other LASV persistence studies in animal models are available as of now. In a retrospective cohort study in LF survivors, infectious LASV and LASV RNA were recovered from the semen of survivors up to 9 or 12 months after disease, respectively [204]. Here, longer persistence was associated with higher viremia and disease severity and longer hospitalization [204]. Notably, in the same study LASV RNA was not detected in plasma, urine, saliva, lacrimal fluid, or vaginal fluid at later time points [204].

Moreover, Günther *et al*. report a singular case in which their patient initially presented with severe LF, whereby only neurological signs indicative of encephalopathy, not fever, were present at the final stages of the disease approximately 3 weeks after symptom onset [207]. At this stage, LASV RNA was only present in the CSF not the serum, which the authors cautiously suggest might hint towards the capacity of LASV to persist in the CNS [207]. Notably, the patient succumbed to the disease due to respiratory failure [207]. Unlike for EBOV, no other reports of LASV persistence in humans, LASV recrudescent inflammatory disease, or relapse exist in the literature (rev. in [197, 207, 211, 212]).

3.5 Human cerebral and choroid plexus organoids

As EBOV persistence is insufficiently studied in animal models and no model for long-term in vitro infection of human CNS cells exists, human cerebral and choroid plexus organoids

were used in this study. To understand the models and their relevance to viral persistence studies, the following chapter explains the development of the human embryonic cerebral cortex, which is ultimately most similar to the architecture of the organoid models, as well as the generation and characteristics of human cerebral and choroid plexus organoids.

3.5.1 Human embryonic cerebral cortex

The mammalian cortex develops via the expansion of the neuronal epithelial stem cells within the neural tube during early embryonic development (rev. in [213]). All neural and glia cell populations of the neuroectodermal lineage derive from these neural stem cells, leading to the establishment of the embryonic cortex and its regions as depicted in Figure 10 (rev. in [213]).

Early on, ventricular (apical) radial glia cells are created and subsequently divide at the apical surface of the ventricular zone (VZ) (rev. in [213, 214]). Thereby, intermediate progenitors which populate the adjacent subventricular zone (SVZ) and immature neurons are generated (rev. in [213, 214]). These neurons migrate outwards through the intermediate zone (IZ), populating their designated layer within the cortical plate (CP). The CP, together with the marginal zone (MZ), later develops into the adult cortical layers (rev. in [213, 214]). Intermediate progenitors mostly locate in the inner subventricular zone (iSVZ) while in the outer subventricular zone (oSVZ) the human-specific stem cell population of outer (basal) radial glia establishes (rev. in [213, 214]). These stem cells derive from ventricular radial glia and contribute to the extreme cortical expansion in humans (rev. in [213]). Astrocyte progenitors ($GFAP^+$) are produced from multiple progenitor cells, including radial glia which underwent a gliogenic switch from neuronal to glia cell production (rev. in [215]). From the SVZ, cortical astrocyte progenitors migrate to the cortex after birth, where they further expand locally, increasing their processes during their final maturation (rev. in [215]). Notably, astrocytes comprise multiple subpopulations that have diverse functions crucial to brain homeostasis, including neuron and oligodendrocyte protection, synapse formation and modulation as well as maintenance of the blood-brain-barrier (BBB) and blood-CSF barriers for instance at the CSF-producing choroid plexus (rev. in [215, 216]). Within the BBB, which further comprises microvascular endothelial cells and pericytes, astrocytes further ensure CNS protection and nutrient supply (rev. in [216]).

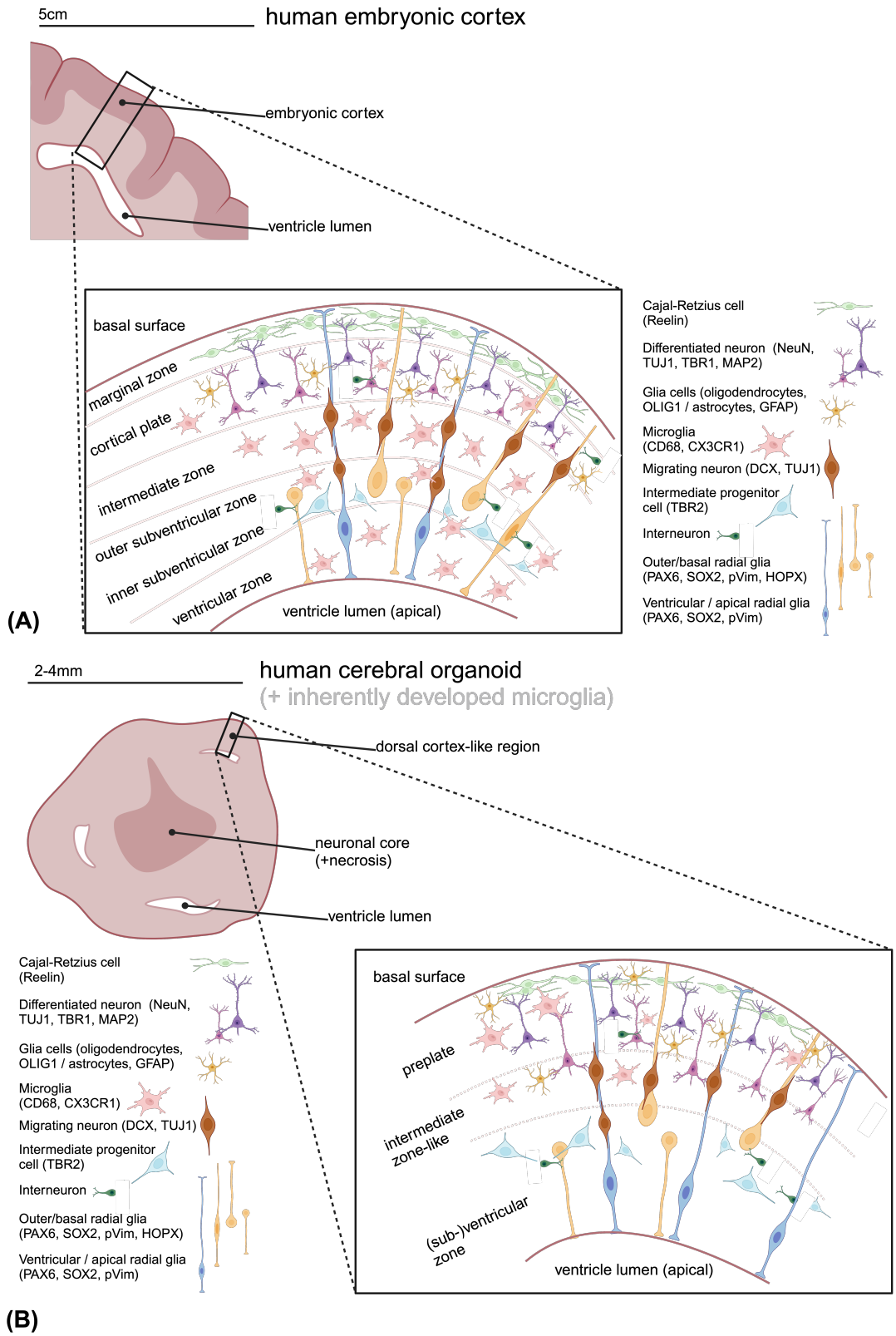


Figure 10: Embryonic cortex and cerebral organoid architecture. Schematic of the **(A)** human embryonic cortex and **(B)** cerebral organoid architecture including indicated cell types and associated marker expression. Microglia in cerebral organoids according to Ormel *et al*. [217]. Cerebral organoid layering according to Lancaster *et al*. [214]. Layering of embryonic cortex according to Penisson *et al*. and Qian *et al*. [213, 218]. Microglia population in the embryonic cortex according to Hattori *et al*. [219]. Schematic adjusted from Qian *et al*. [218]. Markers: beta-III Tubulin (TUJ1), T-box brain transcription factor 1 (TBR1), microtubule-associated protein 2 (MAP2), oligodendrocyte lineage gene 1 (OLIG1), glial fibrillary acidic protein (GFAP), CX3C motif chemokine receptor 1 (CX3CR1), cluster of differentiation 68 (CD68), doublecortin (DCX), T-box brain transcription factor 2 / eomesodermin (TBR2/EOMES), paired box 6 (PAX6), sex-determining region Y-box 2 (SOX2), p-Vimentin (pVim), homeodomain-only protein homeobox (HOPX). Created with BioRender.com.

Microglia are the resident immune cells of the CNS. They scan the brain parenchyma for invading agents or debris of dying cells and thereby upkeep homeostasis (rev. in [217, 219]). Importantly, they are not generated from neuronal stem cells of the neuroectodermal lineage but derive from the mesoderm (rev. in [217, 219]). During early embryonic development, primitive macrophages leave the yolk sac to enter the brain before the formation of the BBB, colonize the parenchyma, and proliferate during subsequent stages, whereby their distribution is stage-dependent (rev. in [219]). This leads to microglia being transiently absent from the CP during some stages (rev. in [219]). During neurogenesis, microglia inhabit important functions for cellular survival, circuit formation, synaptogenesis, and glia cell development, thereby contributing to region-specific functions (rev. in [217, 219]). Early microglia display an amoeboid shape indicative of immature microglia, which are highly migratory and necessary for the population of the brain (rev. in [219]). With ongoing maturation, microglia will display a more ramified phenotype, increasing their processes (rev. in [219]). While microglia are rather scarce in the embryonic brain (0.5-1 %), the cells increase their population size substantially to 5-15 % in adults (rev. in [219]).

3.5.2 Human cerebral and choroid plexus organoids

Principally, organoids may be defined as three-dimensional tissues that are generated from stem cells that differentiate and undergo organogenesis as seen during fetal development (rev. in [170, 217]). Thereby, they represent models that resemble the native tissue architecture and physiology, comprising multiple cell types [217]. Depending on the type of organoid, they are generated from either embryonic stem cells (ESC), pluripotent stem cells (PSC)/induced pluripotent stem cells (iPSC) or adult stem cells (ASC). Notably, ESC and iPSC are totipotent and pluripotent, respectively, hence they have tri-lineage potential and can in principle differentiate into any cell type of the human body (endoderm, ectoderm, and mesoderm) (rev. in [220]). ASC are resident, lineage-restricted stem cells which locally replace lost tissue via division and differentiation (rev. in [221]). As multipotent stem cells, they are limited in their differentiation capacity (rev. in [221]).

Human cerebral organoids are neural 3D cultures, which are generated from human ESC or iPSC lines that undergo embryoid body formation and subsequent neural organogenesis, guided by tissue intrinsic cues and supply of external patterning factors [214, 217]. They are of various regional identities discretely localized within the organoid, whereby cortical organization in line with early brain development in humans is achieved [214] (Figure 10). In the case of human cerebral organoids, upon formation of embryoid bodies, the neuroectodermal lineage is defined and subsequently expanded upon using a Matrigel matrix [214]. This way, within 8 – 10 days, neuroectoderm is formed, and within 15 – 40 days, different neural identities of defined brain regions are established at the surface of the organoid while

a large neuronal mass forms in the center [214]. Overall, heterogeneous tissues of about 2 – 4 mm are generated, comprising regions of the cerebral cortex (mostly dorsal cortex), choroid plexus, immature retina, and meninges at the surface, if left freely to differentiate [214]. The original cerebral organoid published by Lancaster *et al*. showed typical layering of the dorsal cortex regions, whereby deeper regions contain radial glia (paired box 6 $(PAX6)^+$, mitotic: p-Vimentin$^+$) which develop into glia and neurons (microtubule-associated protein 2 $(MAP2)^+$, T-box brain transcription factor 1 $(TBR1)^+$, neuronal nuclear protein $(NeuN)^+$) populating the organoid surface [214]. Moreover, intermediate neuronal progenitor cells (T-box brain transcription factor 2 (TBR2)/eomesodermin $(EOMES)^+$) were found in adjacent regions [214]. This indicates that cerebral organoids undergo either the classical development steps (PAX6 > TBR2 > TBR1) or a direct development (PAX6 > TBR1) from radial glia towards post-mitotic projecting neurons ($TBR1^+$, $NeuN^+$) [222]. Moreover, in cerebral organoids, a rudimentary inside-out orientation, with progenitors in the core of the organoid (apical) and more mature neurons at the surface (basal) of the organoid, establishes [214]. Importantly, cerebral organoids lack tissue vascularization. Therefore, due to lack of oxygen and nutrients in deeper layers, cell death may occur, establishing necrotic cores and neuroinflammatory signatures which must be taken into account [214].

Principally, cerebral organoids can be generated via stringent lineage restriction to the neuroectoderm, as achieved by dual Suppressor of mothers against decapentaplegic (SMAD) inhibition [217]. These, however, do not contain mesoderm-derived microglia [217]. Therefore, less restricting protocols have been established, which allow the formation of mesoderm-derived progenitors [214, 217]. Ormel *et al*. showed that these progenitors, within the CNS-environment of cerebral organoids, innately differentiate into microglia which are seeded throughout the organoid and display both immature and adult phenotypes (ionized calcium-binding adaptor molecule 1 $(IBA1)^+$, Cluster of Differentiation 68 $(CD68)^+$, C-X3-C motif ligand receptor 1 $(CX3CR1)^+$, human leukocyte antigen (HLA)-DR^+, $CD45^+$, $CD11c^+$, $CD14^+$) [217]. Regarding their functionality, organoid-derived microglia further surround neurons and synapses [217]. Moreover, such partially immunocompetent cerebral organoids containing microglia have been found to respond to proinflammatory stimuli such as lipopolysaccharide (LPS) via the release of cytokines such as interleukin (IL)-6 and tumor necrosis factor (TNF)-α [217].

In unguided cerebral organoid protocols where no further differentiation factors are supplied, as published by Lancaster *et al*., choroid plexus structures may innately develop [214]. Moreover, a more directed approach for the generation of choroid plexus organoids, which model the CSF-producing structure of the brain ventricles, has been established by Pellegrini *et al*. [214, 223]. The choroid plexus is a selective, polarized epithelial layer that makes up a barrier between the blood and CSF (rev. in [223, 224]). Therefore, the choroid plexus

is crucial to brain nutrient supply and prevention of neurotoxic agents reaching the brain parenchyma as well as a primary barrier and entry site to peripheral immune cells (rev. in [223, 224]). Choroid plexus organoids, as published by Pellegrini *et al*., consist of a cerebral body of intermediate progenitors and neurons as well as stroma and elongated neuroepithelial (transthyretin (TTR)$^+$, chloride intracellular channel 6 (CLIC6)$^+$) structures which produce a CSF-like fluid and form a selective barrier [223]. Therefore, choroid plexus organoids contain cells of both neuroectodermal and mesenchymal lineages [223, 224]. At later stages, choroid plexus organoids form large, CSF-like fluid-filled vacuolar compartments that can reach multiple centimeters in diameter [223]. In choroid plexus organoids, the surrounding media represents the basal (blood) compartment, whereby the fluid-filled vacuole represents the apical, ventricular compartment [223].

3.6 Microglia and astrocytes in neuroinflammation

CD68$^+$ microglia have been suggested as EBOV reservoir in persistent EBOV infection in NHP survivors [183, 189]. Microglia and astrocytes tightly collaborate to maintain brain homeostasis. Based on the local environment, microglia polarize into a diverse spectrum of activation states, which manifest in a range of proinflammatory *"A1-like"* or antiinflammatory *"A2-like"* phenotypes (rev. in [216]). Particularly danger- or pathogen-associated signal sensing with Toll-like receptor 4 (TLR-4) and other PRR drives microglia polarization, where autocrine positive feedback loops further exacerbate the polarization (rev. in [216]). Upon neuroinflammation, activated microglia switch towards an amoeboid phenotype which allows phagocytosis, production of reactive oxygen species (ROS) as well as release of proinflammatory mediators (rev. in [216]). These mediators, including TNF-α, IL-1α, complement factor C1q, further orchestrate a neurotoxic-polarized phenotype in astrocytes (rev. in [216]). *"A1-like"* astrocytes reduce their supportive function and facilitate immune cell recruitment across the BBB to the CNS via the release of neurotoxic factors such as complement factor C3 and C-X-C motif chemokine 10 (CXCL10) (rev. in [216]). Meanwhile, during tissue damage and ischemia, astrocytes adopt an *"A2-like"* state, which drives neuroprotection and proliferation, causing glial scar formation, BBB repair as well as clearance of debris (rev. in [216]). Notably, dichotomous *A1* and *A2* classification does not capture the full spectrum of either microglia or astrocyte activity, which are a spectrum covering inflammatory and repair-associated phenotypes [216].

4 Objectives

This thesis aims to investigate the host and viral factors driving the establishment and maintenance of EBOV persistence in the human CNS by addressing the tissue, cellular, and molecular mechanisms involved at the CNS host-pathogen interface.

The first goal of this thesis therefore is the development of novel in vitro models that would be able to capture EBOV persistence and thereby overcome limitations inhabited by classical animal models and in vitro systems. This comprises the establishment of partially immunocompetent human cerebral and choroid plexus organoid models and long-term 2D in vitro cultures.

As the second objective, cerebral organoids are used to address whether EBOV establishes and maintains a persistent infection in human CNS tissue, including the determination of long-term targets of infection and possible phenotypes of EBOV persistence. Here, the robustness of the model is evaluated by comparison to LASV and human apathogenic RESTV. As read-outs, viral titers, and RNA are measured throughout time frames that have been observed in human case reports of persistence (>1 month), while the presence of viral protein is evaluated using immunohistochemistry and immunofluorescence stainings. Moreover, to determine possible inflammatory signatures, multiplex cytokine assays are employed.

The third objective of this thesis aims to characterize the state of persistent EBOV replication in different CNS cell models. Thereby, a hypothesis for the role of host factors in CNS persistence is developed using cell-culture-based multicycle-replication assays, immunofluorescence microscopy as well as bulk RNA sequencing. Here, the focus is on microglia and astrocytes as major players of the CNS innate immune response and homeostasis.

The fourth aim subsequently anticipates identifying viral factors mediating persistence. Here, naturally occurring CNS variants are studied in the context of CNS infections in 2D and 3D.

Finally, a synthesis is attempted, whereby mechanisms governing the establishment and maintenance of EBOV persistence in the human CNS at the host-pathogen interface are proposed.

5 Materials and Methods

5.1 Cell culture models

5.1.1 2D cell culture

VeroE6, HEK 293T and Huh7 immortalized cell lines

VeroE6 (American Type Culture Collection (ATCC), Manassas, MA, VA) passages 20 to 40 were used for virus amplification and titration. They were cultured in Dulbecco's Modified Eagle Medium (DMEM) (PAN™Biotech GmbH, Aidenbach, Germany) containing 5 % fetal calf serum (FCS) (Thermo Fisher Scientific Inc., Waltham, MA, USA) and 1 % penicillin / streptomycin (P/S) (Thermo Fisher Scientific Inc., Waltham, MA, USA) at 37 °C, 5 % CO_2. VeroE6 were split twice per week at 80 % confluency and diluted 1:5 to 1:10 after detachment with Trypsin ethylenediamine tetraacetic acid (EDTA) (Thermo Fisher Scientific Inc., Waltham, MA, USA) for 5 min at 37 °C.

HEK 293T (American Type Culture Collection (ATCC), Manassas, MA, VA) passages 15 to 30 were cultured in DMEM with 10 % FCS and 1 % P/S as described for VeroE6 cells. They were mechanically disrupted for splitting.

Huh7 cells (American Type Culture Collection (ATCC), Manassas, MA, VA) passages 40 to 50 were cultured in DMEM with 10 % FCS and 1 % P/S as described for VeroE6 and HEK 293T cells. They were split twice per week at 80 % confluency 1:5 using Trypsin EDTA for 5 min at 37 °C

THP-1 - immortalized monocyte cell line

THP-1 (American Type Culture Collection (ATCC), Manassas, MA, VA, TIB-202) cells were cultured in suspension culture in RPMI 1640 (Thermo Fisher Scientific Inc., Waltham, MA, USA) medium containing 10 % FCS and 1 % P/S at 37 °C, 5 % CO_2. They were split twice a week 1:5 to 1:10.

IMHu - immortalized Human Microglia SV40

Immortalized human microglia (Applied Biological Materials Inc., Vancouver, Canada (ABM, T0251)), as characterized by Chiavari *et al*. [225], were kindly provided by J. Steffen (Bernhard-Nocht-Institute for Tropical Medicine, Hamburg) and maintained in RPMI 1640 (Thermo Fisher Scientific Inc., Waltham, MA, USA) medium containing 10 % FCS (Thermo Fisher Scientific Inc., Waltham, MA, USA), 1 % P/S (Thermo Fisher Scientific Inc., Waltham, MA, USA), and 2 % (4-(2-hydroxyethyl)-1-piperazineethanesulfonic acid) (HEPES) (PAN™Biotech GmbH, Aidenbach, Germany). Tissue-culture ware was pre-coated with 0.1 mg/ml collagen-1 (Life Technologies Corporation, Carlsbad, CA, USA) in phosphate buffered saline (PBS)

(PAN™Biotech GmbH, Aidenbach, Germany) at 37 °C for 1 h as described by Chiavari *et al*. [225]. Pre-coated plates were stored at 4 °C for up to two weeks.

The cells were split 1:5 to 1:10 at 80 % confluency twice per week using trypsin EDTA (Thermo Fisher Scientific Inc., Waltham, MA, USA) for 2 min at room temperature. Maintenance conditions were 37 °C, 5 % CO_2, and the cells were kept up until passage 10.

Immortalized human astrocytes, fetal

Immortalized fetal human astrocytes (Applied Biological Materials Inc., Vancouver, Canada (ABM, T0280), supplied by J. Steffen, Bernhard-Nocht-Insitute for Tropical Medicine, Hamburg) were maintained in RPMI 1640 medium containing 10 % FCS, 1 % P/S, 2 % HEPES and 10 ng/ml human endothelial growth factor (EGF) (Applied Biological Materials Inc., Vancouver, Canada (ABM)) on tissue-culture ware pre-coated with 0.1 mg/ml collagen-1 in PBS.

The cells were split 1:5 at 80 % confluency twice per week using trypsin EDTA for 2 min at room temperature. Maintenance conditions were 37 °C, 5 % CO_2, and the cells were kept up until passage 10.

Immortalized human neuroblastoma cells - SH5-SY5

SH5-SY5 neuroblastoma cells (provided by Johanna Steffen, BNITM) were maintained in RPMI 1640 medium containing 10 % FCS, 1 % P/S and 2 % HEPES. The cells were split 1:5 at 80 % confluency twice per week using trypsin EDTA for 2 min at room temperature. Maintenance conditions were 37 °C, 5 % CO_2, and the cells were kept up until passage 10.

Coating of microscopy coverslips with poly-D-Lysine and collagen-1

To guarantee attachment of immortalized microglia, astrocytes, and neuroblastoma cells to coverslips, they were pre-coated with poly-D-lysine (Sigma Aldrich, Merck KGaA, St. Louis, MO, USA) and collagen-1. To this end, glass coverslips were disinfected with 100 % ethanol by dipping and air drying before being placed in a 24-well plate. Within the plate, they were firstly coated with 0.1 mg/ml poly-D-lysine in PBS (250µl/well) which was incubated for 2 h at room temperature. Due to its cytotoxicity, poly-D-lysine was subsequently washed off three times with 500 µl endotoxin-free water, and dried off for 2 h. Next, 0.1 mg/ml collagen-1 in PBS was added for 2 h at 37 °C and subsequently washed off two times with 500 µl PBS. After drying the coverslips, they were used for culturing.

Monocyte isolation from PBMC

Pseudonymized whole blood of healthy volunteer blood donors with informed consent for the use of blood for research use was attained from the Institute of Transfusion Medicine of the

University Hospital Eppendorf, Hamburg, under the approval for peripheral blood mononuclear cells (PBMC) isolation where no data is collected concerning age and ethnicity and donors were chosen at random (Figure 95).

In brief, whole blood was kept a maximum of 24 h at room temperature before being processed to PBMC using the following protocol. Firstly, the whole blood was diluted to a total volume of 500 ml in pre-heated (37 °C) MACS Buffer containing autoMACS®Rinsing Solution (Miltenyi Biotec, Bergisch Gladbach, Germany, PBS and EDTA) enriched with 10 % FCS (in the following: wash buffer). Subsequently, 35 ml of the mixture was layered on top of 14 ml pre-heated human Pancoll (PAN™Biotech GmbH, Aidenbach, Germany) and centrifuged for 45 min at 37 °C and 500 *x g* (acceleration = 1, brake = 0) to attain a PBMC layer. The ”buffy coat” (PBMC layer) was harvested and subsequently washed three times by diluting in 40 ml wash buffer and centrifuging at 500 *x g* for 10 min at 37 °C. After the last washing step, the PBMC were diluted in ice-cold R10 medium containing 10 % FCS, 1 % P/S in RPMI 1640 prior to being counted and spun at 500 *x g* for 10 min at 4 °C.

At this point, isolated PBMC were either resuspended in freezing medium containing 90 % FCS and 10 % dimethyl sulfoxide (DMSO) (Santa Cruz Biotechnology, Inc., Dallas, TX, USA,) at -80 °C and subsequently stored in the gas phase of the liquid nitrogen tank. Alternatively, the PBMC were immediately used for $CD14^+$ monocyte isolation.

To isolate the $CD14^+$ monocytic fraction of the PBMC, CD14 microbreads (Miltenyi Biotec, Bergisch Gladbach, Germany, 130-050-201) were utilized as suggested by the manufacturer. In brief, up to $1x10^9$ PBMC from one donor were diluted in ice-cold autoMACS®Rinsing Solution containing 0.5 % bovine serum albumin (BSA) (Sigma Aldrich, Merck KGaA, St. Louis, MO, USA) and washed at 300 *x g* at 4 °C for 10 min. Hereafter, the cells were re-suspended in the appropriate amount of $CD14^+$ microbeads and incubated for 15 min in the fridge. Lastly, the left-over PBMC from one buffy coat were separated from the retained $CD14^+$ fraction by running the mixture through an LS column (Miltenyi Biotec, Bergisch Gladbach, Germany, 130-042-401) placed within a magnetic stand. After two rounds of washing, up to $2x10^7$ monocytes per donor were isolated and collected for freezing as described above.

MDMi - monocyte-derived microglia

The monocyte-derived microglia (MDMi) were generated as described by Ryan *et al*. [226]. In short, monocytes were thawed and washed in pure RPMI 1640, prior to beeing seeded in RPMI GlutaMAX™medium (Thermo Fisher Scientific Inc., Waltham, MA, USA) containing 1 % P/S, 2.5 µg/ml Amphotericin B, 10 ng/ml macrophage colony-stimulating factor (M-CSF) (BioLegend, San Diego, CA, USA, 574804), 10 ng/ml granulocyte-macrophage colony-stimulating factor (GM-CSF) (R&D Systems, Minneapolis, MN, USA, 215-GM-010/CF), 10 ng/ml β nerve growth factor (bNGF) (R&D Systems, Minneapolis, MN, USA, 256-GF-100/CF), 100 ng/ml

chemokine (C-C motif) ligand 2 (CCL-2) (BioLegend, San Diego, CA, USA, 571404), and 100 ng/ml IL-34 (R&D Systems, Minneapolis, MN, USA, 5265-IL-010/CF). The medium of the $1x10^6$ cells per well in a six-well plate was exchanged every three to four days for two weeks before achieving final differentiation to MDMi (adherent). The phenotype was confirmed via flow cytometry as described later (subsubsection 5.3.2).

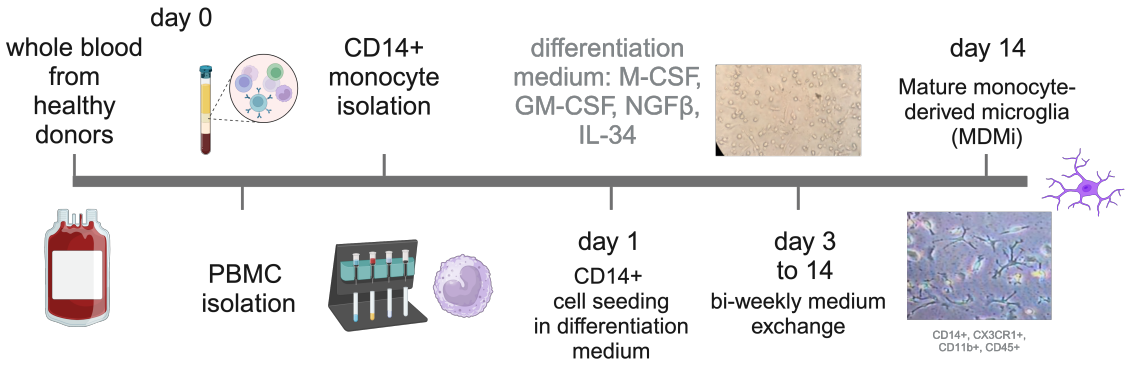


Figure 11: MDMi generation. Timeline for the generation of human monocyte-derived microglia (MDMi) from whole blood. Created with BioRender.com.

HMGU1 - human induced pluripotent stem cells

The human foreskin fibroblast-derived iPSC cell line HMGU1 was generated and provided by the iPSC Core Facility of the Helmholtz Centre in Munich via a material transfer agreement (MTA) at passage 10.

The cells were maintained on Nunc™cell culture treated six-well plates (Thermo Fisher Scientific Inc., Waltham, MA, USA) pre-coated for 1 h at 37 °C with 1 % Matrigel®(Corning, Corning, NY, USA, 354277) in pure RPMI 1640 medium. HMGU1 were kept in StemMACS™iPSC-Brew XF (Miltenyi Biotec, Bergisch Gladbach, Germany, 130-104-368) which contained 10 µM Y-27632 rho-associated protein kinase (ROCK) inhibitor (Selleck Chemicals GmbH, Cologne, Germany S1049) for the first 24 h after splitting. In general, iPSC cultures were split using a gentle cell dissociation solution (STEMCELL Technologies, Vancouver, Canada, 100-0485) at 70 % confluency according to the manufacturer's protocol without dissociating the colonies. Culturing conditions were 37 °C, 5 % CO_2. HMGU1 iPSC were used 2 to 3 passages after thawing for the generation of human cerebral and choroid plexus organoids.

5.1.2 3D cell culture

Cerebral organoids

Cerebral organoids were generated based on the works of Lancaster *et al.* [214] with the STEMdiff™Cerebral Organoid Differentiation (STEMCELL Technologies, Vancouver, Canada, 08570) and STEMdiff™Cerebral Organoid Maturation (STEMCELL Technologies, Vancouver,

Canada, 08571) kits. In brief, following the manufacturer's protocol, the above-mentioned HMGU1 iPSC were seeded to a confluency of 70 % forming large, flat-edged iPSC colonies before being harvested and reduced to a single cell suspension. Following, 9000 cells per well of a 96-well round-bottom ultra-low adhesion plate (Corning, Corning, NY, USA, 7007) were seeded in seeding medium containing 4:1 basal medium 1 and supplement A, together with 10 µM ROCK inhibitor. As a consequence, embryoid bodies formed at the bottom of the wells, which were fed 48 h, and 96 h after seeding with the same medium but without ROCK inhibitor. Five days after embryoid body formation, neuronal induction was induced by transferring the embryoid bodies into 24-well ultra-low adhesion plates (Corning, Corning, NY, USA, 3473) containing the respective medium with 99:1 parts of basal medium 1 and supplement B. Two days after neuronal induction, after which the embryoid bodies should have round, optically translucent edges, organoid expansion was induced via Matrigel® (Corning, Corning, NY, USA, 354277) embedding. Here, single embryoid bodies were covered in 15 µl of ice-cold Matrigel® and set out to polymerize for 30 min at 37 °C. Thereafter, the embedded embryoid bodies were washed into six-well ultra-low adhesion plates (Corning, Corning, NY, USA, 3471) containing organoid expansion medium consisting of 97:1:2 parts of basal medium 2, supplement C, and supplement D. After 72 h, small organoids with budding neuroepithelia on their surface should have formed. Their medium was exchanged every three to four days with organoid maturation medium made up of 98 % basal medium 2 and 2 % supplement E. After adding the first maturation medium, organoids were maintained on an orbital shaker (VEVOR GmbH, Cologne, Germany) at 60 rpm, 37 °C, and 5 % CO_2.

Following day 40, the organoids were considered mature [214], however, they were used at 100 d old to guarantee glia cell formation within the organoids. Importantly, organoids were cultured without shaking following infection.

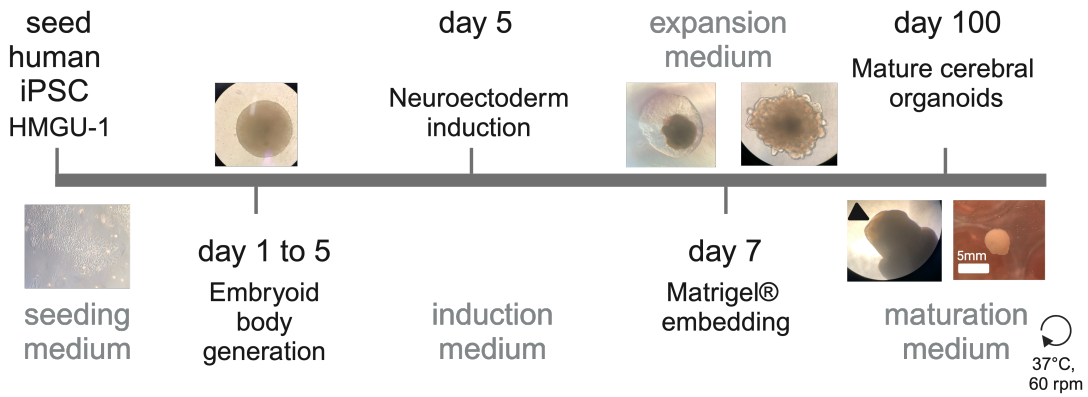


Figure 12: Cerebral organoid generation. Timeline for the generation of human cerebral organoids from HMGU-1 induced pluripotent stem cells (iPSC) cells. Created with BioRender.com.

Choroid plexus organoids

Choroid plexus organoids, as described by Pellegrini *et al*. [223], were generated following the manufacturer's instruction of the STEMdiff™Choroid Plexus Organoid (STEMCELL Technologies, Vancouver, Canada, 100-0824) kit, where on day 10 post embryoid body induction during the organoid maturation step, 3 µM CHIR and 20 ng/ml BMP-4 are supplemented in the maturation medium for 5 d to direct regional differentiation. In brief, HMGU-1 iPSC cells were harvested and seeded in 4:1 STEMdiff™Neural Organoid Basal Medium 3 with STEMdiff™Neural Organoid Supplement E, adding 10 µM ROCK inhibitor on the day of seeding but not during the subsequent feeding on day two and four after embryoid body formation. The day after the last feeding, neuroectodermal induction was initiated via medium replacement to 99:1 STEMdiff™Neural Organoid Basal Medium 3 with STEMdiff™Neural Organoid Supplement F for 48 h. Two days later, the embryoid bodies were embedded in Matrigel® as described above and expanded in 97:1:2 STEMdiff™Neural Organoid Basal Medium 4, STEMdiff™Neural Organoid Supplement G, and STEMdiff™Neural Organoid Supplement using 15 µl of Matrigel® per organoid. In contrast to cerebral organoids, three days after expansion, the choroid plexus organoids were differentiated via the addition of 97:2:1 STEMdiff™Neural Organoid Basal Medium 4 with Neural Organoid Supplement I, and Neural Organoid Supplement J. After three days of differentiation, the organoids were maintained on an orbital shaker (VEVOR) at 60 rpm, 37 °C, and 5 % CO_2 until usage in the experiment. Notably, the budding of the embryoid body surface expanded during that time of choroid plexus formation. Finally, after three days of differentiation, factor J was removed and the organoids were maintained in 98:2 STEMdiff™Neural Organoid Basal Medium 4 with Neural Organoid Supplement I for the remainder of the culture. Medium exchange was performed every three to four days. Organoids were used from 100 d after the start of generation. Notably, organoids were cultured without shaking following infection.

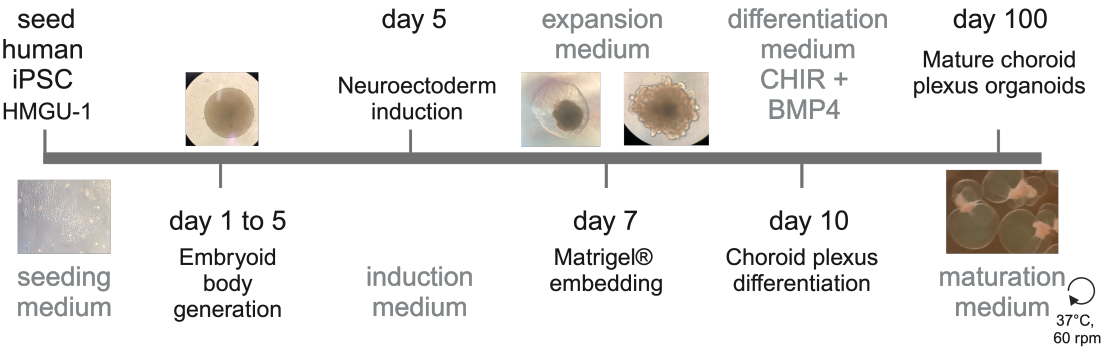


Figure 13: Choroid plexus organoid generation. Timeline for the generation of human choroid plexus organoids from HMGU-1 induced pluripotent stem cells (iPSC) cells. Created with BioRender.com.

5.1.3 2D and 3D cell culture quality control

All cell-based systems were regularly monitored for mycoplasma contamination using a polymerase chain reaction (PCR) kit (PromoCell, PK-CA91-1048).

HMGU1 iPSC were additionally monitored for their pluripotency via the StemLight™ Pluripotency Antibody Kit (Cell Signaling Technologies, Danvers, MA, USA, 9656) and through capacity of embryoid body formation (lineage-undefined). Mature cerebral organoids and choroid plexus organoids were monitored for their integrity via visual observation (e.g. vacuolar formation) as well as histology analyses of cell compositions.

5.2 Viruses

The following viruses were used in the scope of this project: Table 1.

Table 1: Viruses

Viruses	Source, NCBI Accession/Assembly
Ebola virus (species: *Orthoebolavirus zairense*, Mayinga variant)	1976 Zaire outbreak variant, AF086833.2, GCA_000848505.1
EBOV-GFP	T. Hoenen, Friedrich-Loeffler-Institut (FLI, Greifswald, Germany) KF990213.1 [227], GMO: IB17-42/13
RESTV-GFP	T.Hoenen (FLI, Greifswald, Germany), GMO: IB17-42/13
Lassa virus (recombinant Bantou 366 (BA366) variant)	European Virus Archive Global partner site BNITM, isolated from *Mastomys natalensis* clustering with lineage IV variants, GU830839.1 [228]
Nipah virus (species: *Henipavirus nipahense*, Malaysia variant)	Markus Eickmann, Institute for Virology at the Philipps University Marburg (Marburg, Germany), AF212302.2/MK673562.1

5.2.1 Virus amplification

Nipah virus, LASV, EBOV and recombinant EBOV-green fluorescent protein (GFP) as well as recombinant RESTV-GFP were amplified on 60 % confluent VeroE6 cells as follows.

The day after seeding of VeroE6 cells (5 % FCS in DMEM with 1 % P/S), the cells were infected for 1 h at 37 °C with multiplicity of infection (MOI)=0.1 of the respective virus. Following, the virus was taken off and replaced with DMEM containing 2.5 % FCS and 1 % of P/S. After incubation of four to eight days, depending on the virus, at 37 °C, 5 % CO_2, the supernatant containing the virus was harvested via centrifugation at 2000 *x g* for 10 min at 4 °C and frozen at -80 °C.

Viruses were maximally passaged two to three times on VeroE6 before usage in experiments.

5.3 Experimental methodology

5.3.1 Virus-immunological methodology

Infection of 2D cell culture models

Unless otherwise indicated, all infections were principally carried out with the respective virus for 1 h at 37 °C at the indicated MOI. Before infection, maintenance media was removed and the cells were washed with PBS. After infection, the respective media containing a reduced concentration of FCS (2.5 %) and in the case of astrocytes no EGF was applied and samples were cultured at 37 °C for the indicated time frames and sampled as indicated. Supernatant was cleared at 2000 *x g* for 10 min at 4 °C and frozen at -80 °C until titration.

Multicycle-replication assays and long-term infections of 2D cultures

To measure the replication kinetics of EBOV versus LASV within a certain cell type, multicycle-replication assay (MRA) were performed in microglia, VeroE6 cells, Huh7 cells, and astrocytes (Figure 14 (A)). Here, 50 % confluent cells of the respective type were seeded and infected the following day with three different MOI, namely 0.1, 0.01, or 0.001 for 1 h at 37 °C. Per group, n=4 wells were infected. Thereafter, an FCS-reduced (2.5 %) medium of the respective kind was supplied. Sampling of the supernatant occurred every 4 days until 12 dpi and weekly thereafter until the conclusion of the experiment. In these cases, half of the medium was taken off, cleared (2000 *x g* for 10 min at 4 °C), and frozen. For weekly time points, the whole medium was exchanged. Finally, cells were harvested for immunofluorescence staining in-well at 25 dpi (subsubsection 5.3.2). In the same experiment, an MRA was performed for the later-described (subsubsection 5.3.1), naturally occurring EBOV$_{n120}$ variants. Here, the infection was carried out at MOI=0.01. As initial (d0i) titers were more in line with MOI=0.1 samples of the original stock controls, comparisons took higher MOI original stocks into account to align the back-titered infection doses. Statistics were performed by generating the area under the curve (AUC) and subsequent one-way ANOVA with post-hoc Dunnet's multiple hypotheses correction as indicated (n=4, infected at the same time) (Figure 14 (B)). Immunofluorescence microscopy was performed 25 dpi.

An MRA was furthermore performed in VeroE6 cells and microglia (n=2) at MOI=0.01 (Figure 14 (C)). Per group, two wells were seeded with the respective cell type at 50 % confluency the previous day and thereafter infected at MOI=0.01 (1 h at 37 °C) with the indicated EBOV$_{n120}$ variants or the EBOV stock virus. Sampling was performed every three days until 13 dpi by collecting half of the supernatant, clearing, and subsequent titration (subsubsection 5.3.2).

An MRA was furthermore performed for naturally occurring LASV$_{n120}$ variants originating from the L9 persistently infected human cerebral organoids (subsubsection 5.3.1). As depicted

in Figure 14 D, astrocytes, microglia, VeroE6 cells, and Huh7 cells were infected for 1 h at 37 °C with an MOI=0.01, followed by maintenance in FCS-reduced media. Sampling of the supernatant occurred every three days until 12 dpi as described above. Statistics were performed by generating the AUC and subsequent one-way ANOVA with post-hoc multiple hypotheses correction as indicated (n=4, infected at the same time).

An MRA of EBOV was furthermore employed to determine the EBOV replication in primary MDMi. In this case, MDMi were generated (Figure 11) and infected after two weeks of differentiation upon morphological phenotype confirmation, at a MOI=10 for 1 h at 37°C. Thereafter, cells were washed and the medium was replaced with fresh MDMi medium. Samples were collected daily by replacing half of the supernatant. A day 0 sample after the fresh addition of media after infection was collected (n=4, infected at different time points) (Figure 14 (E)).

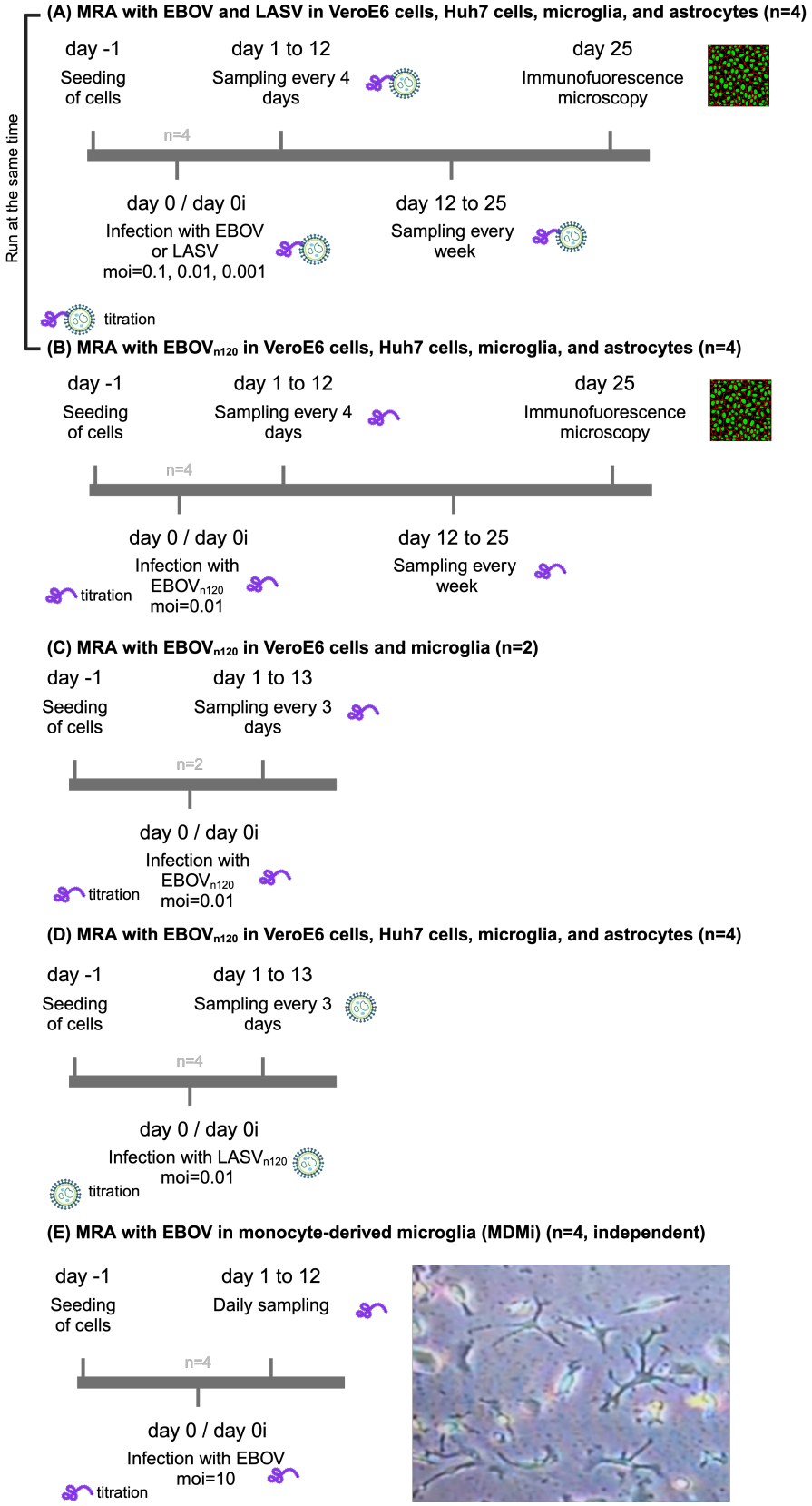


Figure 14: Multicycle-replication assay timelines. Timeline for the multicycle-replication assays performed with **(A)** EBOV and LASV in VeroE6 cells, Huh7 cells, microglia, and astrocytes (n=4, MOI=0.1, 0.001, 0.001) as well as **(B)** naturally occurring EBOV$_{n120}$ variants in VeroE6 cells, Huh7 cells, microglia, and astroytes (n=4, MOI=0.01). **(C)** MRA with naturally occurring EBOV$_{n120}$ variants in VeroE6 cells and microglia (n=2, MOI=0.01). **(D)** MRA in VeroE6 cells, Huh7 cells, microglia, and astrocytes using naturally occurring LASV$_{n120}$ variants. **(E)** MRA in MDMi with EBOV at MOI=10. Figure created with BioRender.com.

Treatment of microglia, astrocytes, and VeroE6 cells with CX3CR1 inhibitor and infection with EBOV

CX3CR1 inhibitor experiments were performed to elucidate the role of this receptor in EBOV persistence. To inhibit CX3CR1 activity, the allosteric non-competitive CX3CR1 inhibitor AZD8797 (MedChemExpress LLC, Monmouth Junction, NJ, USA) was added to the respective media in the indicated concentration.

An initial screening for AZD8797 cytotoxicity in immortalized human microglia was performed with serial dilutions from 10 µM to 10 nM in DMSO. Here, microglia were seeded at 50 % confluency the day before the treatment. Next, the respective concentration of inhibitor was applied to the normal microglia medium via medium exchange. As a control, media supplied with the highest volume of DMSO corresponding to the highest inhibitor application (1:1000) was applied. The tissue culture morphology was observed 24 h treatment.

For the MRA with EBOV upon CX3CR1 inhibitor treatment, 1 µM of AZD8797 was employed. As the inhibitor was reconstituted in DMSO, an equal volume of DMSO was applied serving as the untreated controls. Briefly, a 2D cell culture MRA with inhibitor was performed by seeding VeroE6 cells, microglia, or astrocytes (n=4 wells each) to 50 % confluency in a six-well plate two days before infection in standard media specified above (d-2). The following day (d-1), the media was exchanged to standard media containing 1 µM AZD8797 (in DMSO) in the treated group and 1:10.000 DMSO in normal media in the untreated controls. On the following day of infection (d0), infection with EBOV was carried out as previously described at MOI=0.0025 for 1 h at 37 °C. Thereafter, the media was exchanged to the respective infection medium containing only 2.5 % FCS and either 1 µM AZD8797 or 1:10.000 DMSO, respectively. A negative control was treated with 1 µM AZD8797 as cytotoxicity control. Thereafter, media was exchanged to inhibitor or control media every three days until 12 dpi and once at day 18. At the day of media exchange, samples were collected, cleared, and subsequently titrated via immunofocus assay (subsubsection 5.3.2), whereby 24 dpi was the last sampled time point. Statistics were performed by generating the AUC and subsequent unpaired, two-tailed Student's T-test as indicated (n=4, infected at the same time).

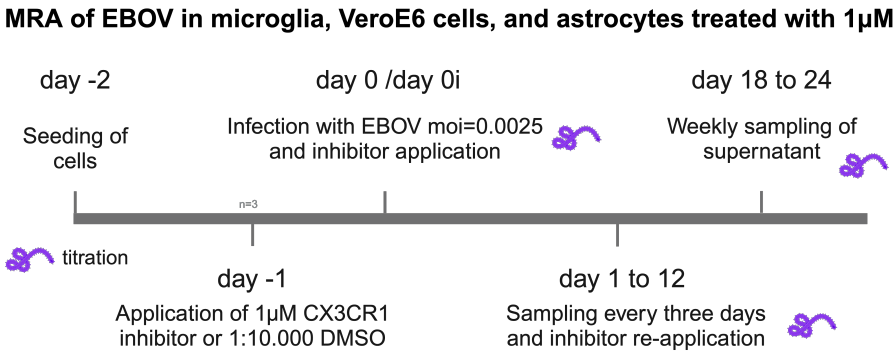


Figure 15: MRA of EBOV in CX3CR1 inhibitor treated cells. Procedure for the treatment of VeroE6 cells, microglia, and astrocytes with CX3CR1 inhibitor AZD8797 and subsequent multicycle-replication assay (MRA). Figure created with BioRender.com.

Passaging of EBOV in microglia

Passaging of EBOV, following protocols published by Calain *et al*. [190], was performed in microglia which were maintained at reduced FCS (2.5 %) conditions. The timeline for the experiment is depicted in Figure 16. Briefly, cells were infected with EBOV (MOI=10 (1x), MOI=1 (2x, flask A and B)) for 1 h at 37 °C and subsequently grown for one week. A day 0 sample was collected after the addition of fresh medium after viral inoculation. The cells were split weekly 1:5 using Trypsin EDTA, whereby samples for total RNA extraction as well as viral titration were collected. From passage 3 onwards, $1x10^6$ fresh microglia were supplied to the infected groups to maintain the culture. At passage 10 after infection, cells were frozen in 10 % DMSO in FCS. After thawing, cells were passaged without the addition of uninfected microglia in persistently infected groups in n=4 flasks/group (EBOV MOI=1 flask A and B, negative control passage). Passage 10+3 was harvested for RNA sequencing as described in a later section (subsection 5.6.3). CPE was observed at all passages via microscopy and images were taken via light microscopy at passage 10 before freezing and passage 10+3 (i.e. three passages after thawing).

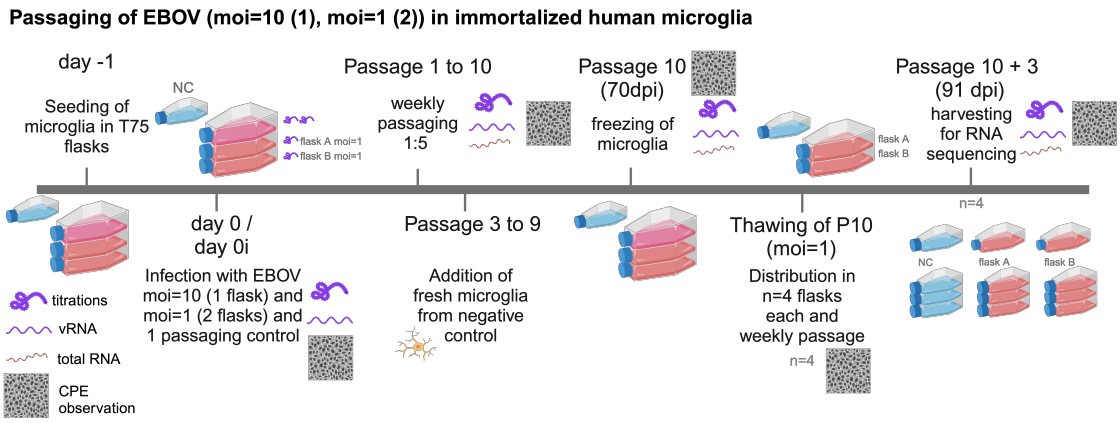


Figure 16: Passaging of EBOV in microglia timeline. Timeline for the passaging of EBOV-infected microglia following protocols by Calain *et al*. [190]. Figure created with BioRender.com.

Infection of human cerebral organoids

Four different infection experiments were performed using human cerebral organoids, depicted in Figure 17. In general, human cerebral organoids were generated for 100 days and thereafter selected based on quality criteria visible, including the lack of choroid-plexus-like formations and the absence of obvious lesions. The timeline of the pre-experiment phase and an example of a selected organoid can be seen in Figure 12.

An explorative infection with Nipah virus and RESTV-GFP was performed to determine whether the infectious dose for subsequent experiments was sufficient. Infection was performed for 1 h at 37 °C with 10^4 focus forming units (FFU)/organoid and organoids were harvested after 10 d.p.i. without further sampling. Immunofluorescence staining (subsubsection 5.3.2) was done to determine the productivity of infection (Figure 17 (A)).

For all further viral kinetics in human cerebral organoids, infections were coherently carried out for 1 h at 37 °C with 10^4 FFU/organoid, whereby organoids were washed in PBS before and the infection volume was 500 µl. As negative control, pure DMEM was used. A day 0 sample was taken before infection as a cytokine assay baseline, and a sample following the infection and the addition of fresh cerebral organoid media following the infection was taken as a baseline sample for the titration on day 0 (d0i).

For experiments with EBOV and LASV (two batches), two independent experiments depicted in Figure 17 (B) were performed. In this case, for the first two weeks, samples were taken daily, where half of the supernatant was replaced. Thereafter, samples were taken weekly with replacement of supernatant. Samples were cleared and frozen for titrations. Furthermore, on 3, 6, 15, 48, 85, and 120 dpi samples were also collected for cytokine assays (subsubsection 5.3.2). Immunohistochemistry staining was performed on the organoids harvested for FFPE embedding and sectioning (subsubsection 5.3.2).

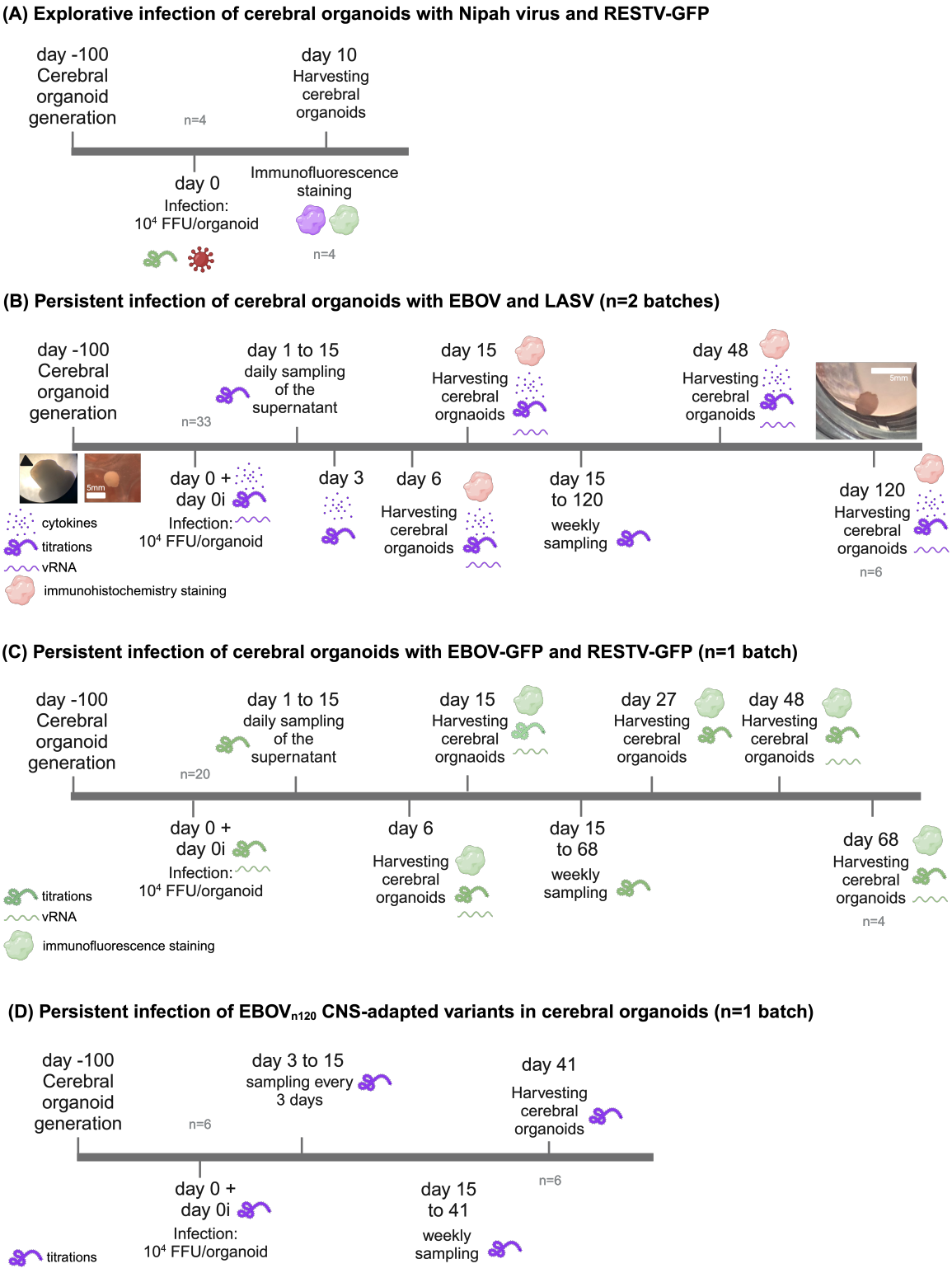


Figure 17: Cerebral organoid experiment timeline. Timeline for organoid generation, infection, and sampling for the cerebral organoid infection experiments. Initial and longitudinal group sizes as indicated. **(A)** Explorative infection of cerebral organoids with Nipah virus and RESTV-GFP. **(B)** Persistent infection of cerebral organoids with EBOV and LASV. **(C)** Persistent infection of cerebral organoids with EBOV-GFP and RESTV-GFP. **(D)** Persistent infection of EBOV$_{n120}$ variants in cerebral organoids. Figure created with BioRender.com.

For EBOV-GFP and RESTV-GFP (1 batch, 1 independent experiment in Figure 17 (C)) infections, in the first two weeks, samples were taken daily, whereby half of the supernatant

was replaced. Thereafter, samples were taken weekly, whereby all supernatant was replaced. Samples were cleared and frozen for titrations. Immunofluorescence images were taken of cryosectioned organoids, as described in the following sections (subsubsection 5.3.2).

Lastly, in the fourth cerebral organoid experiment the naturally occurring $EBOV_{n120}$ variants were employed for the infection (subsubsection 5.3.1). Here, sampling of the supernatant for titrations was performed every three days for the first two weeks and weekly thereafter (Figure 17 (D)). At 41 dpi, organoids were harvested.

In general, in all experiments, for immunohistochemistry/immunofluorescence staining, cerebral organoids were serially harvested, thereby group sizes decreased over the experimental time frames as indicated. Statistical analysis to evaluate differences in viral replication (and cytokine assays if applicable) was performed by generating the AUC of the infected groups and subsequent unpaired, two-tailed Student's T-test/one-way ANOVA and post-hoc multiple hypothesis correction as indicated.

Treatment of choroid plexus organoids with CX3CR1 inhibitor and infection with EBOV

CX3CR1 inhibitor experiments in choroid plexus organoids were carried out in 100 d old choroid plexus organoids generated as described above in two independent experiments using two different organoid batches (Figure 18). The organoids were distributed in single wells a week before the start of the experiment. The day before infection (d-1), the supernatant was collected as a cytokine baseline sample before treatment. Thereafter, media was exchanged for choroid plexus organoid medium (above) containing either 1 µM AZD8797 or 1:10.000 DMSO in both EBOV infection group and negative control group. On the day of infection (d0), a d0 sample before infection was collected as a cytokine sample for the baseline following inhibitor treatment for 24 h. Next, the choroid plexus organoids were infected for 1 h at 37 °C with 10^4 FFU/ml EBOV or treated with pure DMEM. Thereafter, the virus was taken off and replaced with fresh choroid plexus medium infused with either inhibitor or DMSO for both groups. A sample was collected as a baseline control for the viral infection (d0i). For the following 15 days, half of the media was exchanged daily for titration and replaced with fresh media containing the inhibitor/DMSO. On day 3, 6, 15 samples for cytokine assays (subsubsection 5.3.2) were further collected. After two weeks, media exchange including inhibitor/DMSO application, and the sampling switched to once weekly until the end of the experiment 48 dpi (batch 1) or 41 dpi (batch 2). This longitudinal time point was further collected for cytokine assays. CSF-like fluid was sampled 3, 6, and 15 dpi to determine EBOV penetration into the ventricular compartment. To that end, organoids were washed twice with 2 ml PBS for 5 min before the clean organoid vacuoles were punctured with a 10 µl tip. Thereafter, CSF-like fluid was collected and cleared at 2000 xg for 10 min. CSF sampling was only performed with batch 1 organoids.

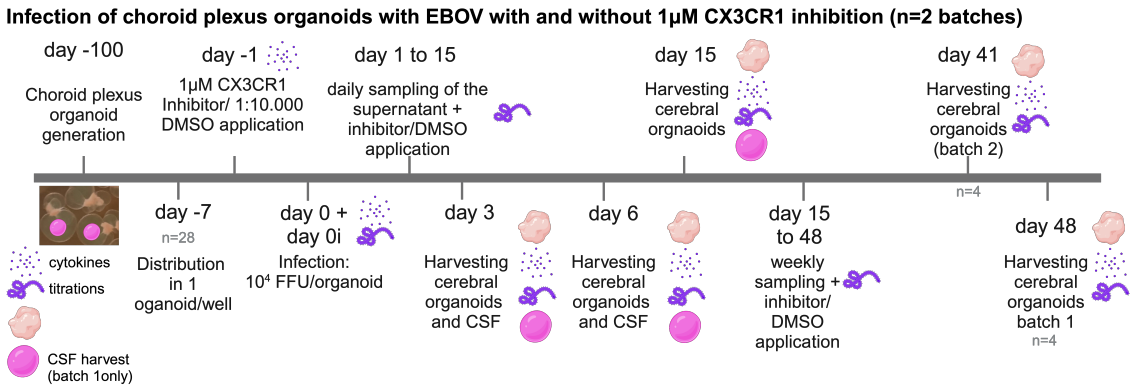


Figure 18: Choroid plexus organoid experiment timeline. Timeline for organoid generation, infection, and sampling for the choroid organoid infection experiment and CX3CR1 inhibitor (AZD8797, 1µm) treatment. Initial and longitudinal group sizes as indicated. Figure created with BioRender.com.

Limited dilution assay (LDA)

With the rationale of isolating naturally occurring viral sub-populations, a limited dilution assay (LDA) was performed using the supernatant from 120 dpi human cerebral organoids (EBOV or LASV L9, Figure 19). A dilution was calculated for each sample which would return 8-20 infectious particles per 96-well plate, thereby ensuring positive wells to contain a single viral variant. Accordingly, VeroE6 cells seeded at 40 % confluency the previous day were washed with PBS before being infected with the respective diluted virus (in DMEM containing 1 % P/S) for 1 h at 37 °C. Thereafter, DMEM with 2.5 % FCS and 1 % P/S was supplied for viral amplification for 7 d (250 µl/well). On the day of harvest, 200 µl were collected per well and transferred into a 96 well plate for storage at -80 °C (Passage 1 virus). Inactivation of cells was performed by incubating the plates for 1 h in 10 % Formalin containing 4 % paraformaldehyde (PFA). Subsequent staining was performed in the same way as for the titrations and the plates were read via the AID multiSpot Reader 08. Supernatants of positive wells were retained as isolates, sequenced, and subsequently propagated as previously described (Passage 2 virus). Naturally occurring variants were used in viral kinetics studies in immortalized human cell lines (microglia, astrocytes, VeroE6 cells, Huh7 cells) as well as human cerebral organoids to observe replicative behavior and capacity of EBOV to infect the cells.

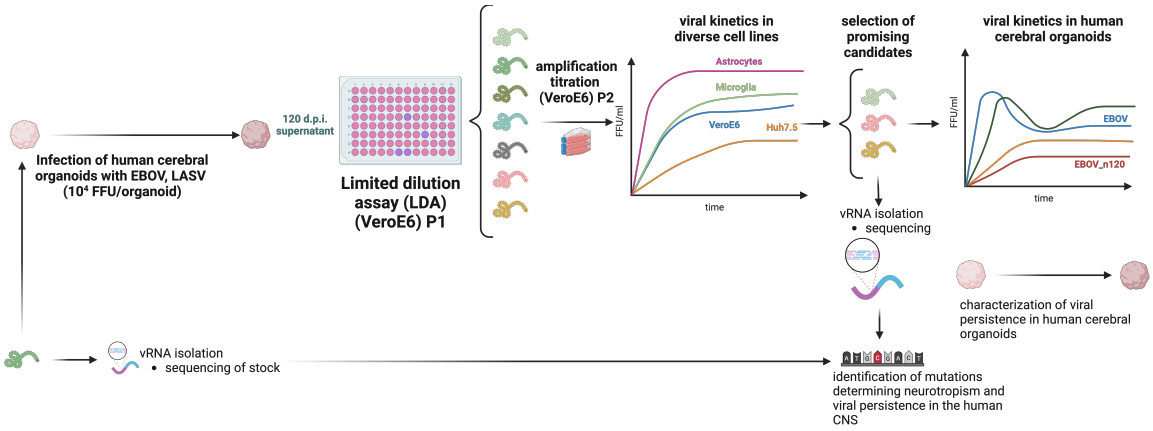


Figure 19: Workflow for the generation of naturally occurring variants. Schemata for the isolation of naturally occuring, CNS-grown EBOV, and LASV variants. Day 120 supernatant of virus grown in human cerebral organoids was diluted in an LDA (VeroE6 cells) to generate individual viral variants (P1) which were subsequently amplified in VeroE6 cells (P2) and screened in diverse human immortalized cell lines. Variants were used in human cerebral organoids to determine the phenotype of naturally occurring CNS variants in human CNS infection kinetics.

5.3.2 Virus-immunological read-outs

EBOV and LASV titration via immunofocus assay

EBOV and LASV were titrated on >90 % confluent VeroE6 cells in 96-well plates (96 F Nunclon Delta White Microwell, Thermo Fisher Scientific Inc., Waltham, MA, USA). Here, 3.6x10^6 cells/plate were seeded in the whole plate in DMEM with 5 % FCS and 1 % P/S the day prior to infection.

On the day of titration, freshly thawed samples were prepared in 10-fold dilutions ranging from undiluted to a 10^{-5} dilution. As a next step, 50 µl of every well were transferred onto the VeroE6 cells in the 96 well plates previously washed with 50 µl PBS.

The cells were infected for 1 h at 37 °C before the virus was removed and replaced with 100 µl of overlay solution consisting of 40 % (v/v) autoclaved methylcellulose solution (Carl Roth GmbH, Karlsruhe, Germany) and 60 % (v/v) DMEM with 1 % P/S and 2.5 % FCS. After six days of incubation, the samples were harvested as described in the following.

Six days after infection, the samples were harvested by decanting the overlay and submerging the plates in 10 % Formalin containing 4 % PFA solution (ProTaqs, 400600305) for 1 h at room temperature to inactivate the virus for safe removal from the biocontainment facility. Afterward, the plates were washed three times in water and permeabilized with 1 % Triton-X 100 (Carl Roth GmbH, Karlsruhe, Germany) in PBS for 30 min at room temperature on a shaker. Upon permeabilization, the washing step was repeated before a blocking solution consisting of 5 to 10 % FCS in PBS was incubated for 1 h at room temperature while shaking. Following another washing step, a primary antibody against EBOV NP (polyclonal mouse anti PanEbola virus, in-house) or LASV NP (2B5 clone, [229]) in PBS was incubated for 1 h at room temperature and overnight at 4 °C in a 1:2000 (EBOV NP) or 1:100 (LASV NP)

dilution. After being removed and washed off, the secondary antibody (Sheep anti-Mouse (IgG H+L) HRP-conjugated, Jackson ImmunoResearch Laboratories, Inc., West Grove, PA, USA, NC1512695) was incubated for 2 h at 1:2000 in the dark. Lastly, the secondary antibody was removed as described above and TMB substrate (Mikrogen GmbH, Neuried, Germany) freshly prepared 1:1 in double distilled (dd)H_2O was used to generate a signal for focus forming units after >20 min of incubation at room temperature in the dark. Finally, FFU were counted from at least two dilutions per sample via an AID multiSpot Reader 08 to determine the viral titer. Day 0 samples in viral titrations correspond to samples collected from fresh media added after viral inoculation.

Images for plaque size comparison were retrieved from immunofocus assays.

EBOV-GFP and RESTV-GFP titration via immunofluorescent plaque formation

In the case of recombinant EBOV-GFP and RESTV-GFP, the titration was performed as already described up until after the inactivation. Here, the plates were simply washed and counted using the AID multiSpot Reader 08 visualizing GFP positive spots.

Cytokine assays using the Legendplex™Neuroinflammation kit

To determine the response of human cerebral organoids to infection, cytokine assays were performed on the supernatant of EBOV and LASV-infected cerebral organoids using the Legendplex™Human Neuroinflammation kit (BioLegend, San Diego, CA, USA, 740795, Lot: B334152). An adapted protocol with 25 % of the original volumes based on the centrifugation protocol was employed, kindly established by AG Zoonosen at BNITM. Here, 50 µl of freshly thawed samples (maximum second thawing) were inactivated via mixing with 50 µl assay buffer containing 2 % Triton-X-100 (equal volumes) to reach a final concentration of 1 % Triton-X-100 which inactivates filoviruses and LASV within 20 min of incubation at room temperature. The standards (performed in triplicates) were subsequently serially diluted 1:4 (C0, negative control to C7, undiluted) in assay buffer and mixed to equal parts with the Triton-enriched buffer to correspond to the inactivated samples. As a next step, either 12 µl standard-assay buffer or sample-assay buffer was transferred into a V-bottom plate (polypropylene low-binding, Greiner Bio-One GmbH, Frickenhausen, Germany) before adding 6 µl of beads (well vortexed) and subsequently detection antibody into each well. Hereafter, the plates were incubated overnight at 4 °C at 650 rpm on a shaker.

The following day, 6 µl of SA-PE were added per well and incubated for 30 min at 650 rpm on a shaker. After two subsequent washing steps which included adding 200 µl of 1:20 washing buffer in ddH_2O before centrifugation steps at 1000 *x* g for 5 min at room temperature, the samples were re-suspended in 150 µl washing buffer and analyzed using the BD LSRII-

Fortessa autosampler (HTS). Data analysis was performed using the Legendplex™ analysis Qognit software provided by BioLegend. Day 0 samples in cytokine assays resemble samples taken before infection. Statistical analysis of different time points was performed via Mixed Effects Modeling and subsequent Tukey's Multiple comparison test. Furthermore, AUC analysis was performed of the total AUC (d0–d120), acute AUC (d0–d15), or persistent AUC (d22–d120) by one-way ANOVA and subsequent multiple hypothesis correction as indicated.

Microglia flow cytometry

The phenotype of all microglia, i.e. immortalized microglia and MDMi primary microglia, was analyzed using a novel microglia flow cytometry panel (Table 2). Following infections at MOI=0.0025 using EBOV-GFP or RESTV-GFP (or uninfected) for 3 or 6 days, the cells were harvested via Trypsin EDTA. Thereafter, cells were washed twice with PBS by centrifuging at 500 *x g* for 5 min at room temperature and subsequently stained using 1:500 Zombie UV™ (BioLegend, San Diego, CA, USA, 423107) live/dead staining for 10 min at room temperature in the dark. Hereafter, the cells were washed as described and blocked in 1:100 FcX block (BioLegend, San Diego, CA, USA) in PBS for 10 min at room temperature, before the 1:25 diluted surface antibodies (Table 2) were incubated in the same mix at an equal volume, diluting the antibodies to a final concentration of 1:50. After 30 min of incubation at room temperature in the dark, the cells were washed twice as already described and inactivated as well as permeabilized for 1 h at room temperature using Cytofix/Cytoperm (Becton Dickinson Biosciences, Franklin Lakes, NJ, USA, 15817868) solution supplemented with 37 % PFA to achieve a final concentration of 4 % PFA.

Consecutively, the cells were removed from the biocontainment facility and washed twice using 1X Perm/Wash Buffer (Becton Dickinson Biosciences, Franklin Lakes, NJ, USA) at 500 *x g* for 5 min at room temperature. Next, the intracellular anti-CD68 (Table 2) was incubated 1:50 in Perm/Wash for 30 min at room temperature in the dark, before being washed off. Finally, the cells were re-suspended in 300 µl of PBS and separated using a cell strainer into the flow cytometry tubes for processing in the Cytek Aurora. Analysis was done using FloJo.

Compensation was performed using anti-mouse (Becton Dickinson Biosciences, Franklin Lakes, NJ, USA, 552843) and anti-rat (Becton Dickinson Biosciences, Franklin Lakes, NJ, USA, 552845) compensation beads, depending on the antibody species (Table 2) as instructed by the manufacturer. Zombie-UV controls, GFP-only controls, and unstained controls were generated using cells. Gating was performed via a respective unstained control as well as fluorescence minus one controls (FMOs) and single stain controls (data not shown). Statistical analysis was performed using a Kruskal Wallis non-parametric test and subsequent Dunn's Multiple comparisons for multiple hypothesis correction.

Table 2: Microglia flow cytometry panel. List of antibodies and their specifications for microglia flow cytometry analysis.

Antibody	Fluoro-chrome	Source, Ref.	Species, Clone, Isotype	Phenotype
HLA-DR	PerCP-Cy5.5	BioLegend, San Diego, CA, USA, 307629	Mouse, L243, IgG2a, K	Microglia activation
Infection	GFP	Inherent	N/A	Infection
CX3CR1	PE-Cy7	BioLegend, San Diego, CA, USA, 341612	Rat, 2A9-1, IGg2b, κ	Microglia
CD68 (i.c.)	PE	BioLegend, San Diego, CA, USA, 333808	Mouse, IgG2b, κ	Microglia
CD11c	AF750	Biolegend, San Diego, CA, USA, 337218	Mouse, Bu15 10E2, IgG1, κ	Microglia
CD45	AF700	BioLegend, San Diego, CA, USA, 304023	Mouse, HI30, IgG1, κ	Microglia activation
CD14	APC	BioLegend, San Diego, CA, USA, 325608	Mouse, HCD14, IgG1, κ	Microglia lineage
CD11b	BV711	BioLegend, San Diego, CA, USA, 101242	Rat, M1/70, IgG2a, K	Microglia
CD40	BV650	BioLegend, San Diego, CA, USA, 353729	Mouse, 5C3, IgG1 κ	Maturation
CD86	BV605	BioLegend, San Diego, CA, USA, 305430	Mouse, IT2.2, IgG2b, K	Activation
CD1a	BV421	BioLegend, San Diego, CA, USA, 300127	Mouse, HI149 IgG1, κ	Maturation
Zombie UV	BUV395	BioLegend, San Diego, CA, USA, 423107	N/A	Live/Dead
Siglec-1 (CD169)	BUV737	Becton Dickinson Bio-sciences, Franklin Lakes, NJ, USA, 748925	Mouse, 7-239, IgG1, κ	Expression

Immunofluorescence microscopy staining of 2D cultures

Immunofluorescence microscopy staining was performed in collagen-1-precoated 96-well plates (Greiner Bio-One, Kremsmünster, Austria) or with cells grown on coverslips pre-coated with collagen/Poly-D-Lysine in 24-well plates as previously described. Cells grown in 96-well plates were harvested by inactivating in 10 % formalin for 1 h at room temperature. Cells grown on coverslips in 24-well plates were inactivated by incubation for 1 h in methanol after the indicated time of infection, whereby the coverslips were lifted after 30 min to ensure inactivation.

Thereafter, washing with PBS was performed three times. In the case of formalin inactivation, cells were subsequently permeabilized in 1 % (v/v) Triton-X-100 in PBS for 10 min at room temperature and washed three times. Then, cells from either inactivation protocol were blocked in 5 % FCS in PBS for 30 min at room temperature. Next, washing was repeated and followed by primary antibody staining (Table 3) for two hours at room temperature in a wet chamber. After washing three times, secondary antibodies were applied (Table 3) for 2 h at room temperature in a wet chamber in the dark. Following another washing step, in

the case of 96-well plates, F-actin staining using Phalloidin-AlexaFluor-488 (Thermo Fisher Scientific Inc., Waltham, MA, USA) was performed at 1X concentration in PBS for 1 h at room temperature together with DAPI counterstaining (Thermo Fisher Scientific Inc., Waltham, MA, USA). Coverslips were alternatively retrieved from their well, washed once with ddH_2O, and mounted on microscopy slides using an anti-fade mounting medium containing DAPI (Carl Roth GmbH, Karlsruhe, Germany). The coverslips were fixed with nail polish. Images were taken using the Axio Imager M1 (Zeiss, Aalen, Germany) or Evos™FL Auto imager system (Invitrogen, Thermo Fisher Scientific Inc., Waltham, MA, USA). Image analysis/processing was performed using FIJI.

Table 3: Immunofluorescence microscopy antibodies

Antibody	Company/Source	Usage	Phenotype
CX3CR1 (Rabbit, IgG, polyclonal)	Biozol Diagnostica Vertrieb GmbH., Eching, Germany, PRS-2093	1:100 overnight	microglia
GFAP (Chicken, IgY, polyclonal)	LifeSpan Biosciences Inc., Seattle, WA, USA, LS-C204526)	1:100 overnight	astrocytes
panEBOV NP (Mouse, polyclonal)	In-house	1:100 in PBS 2h or overnight	EBOV NP
EBOV GP 5E6 (Mouse, IgG2a, monoclonal)	Sigma Aldrich, Merck KGaA, St. Louis, MO, USA, MABF1982	1:100 in PBS 2h	EBOV GP
LASV NP 2B5 (Mouse, monoclonal)	In-house, Lisa Oestereich, BNITM	1:100 in PBS 2h	LASV NP
LASV GPC 2A1 (Mouse, monoclonal, IgG2a)	[230]	1:100 in PBS 2h	LASV GPC (GP2 subunit)
Nipah virus N (Mouse, polyclonal)	Indre Kucinskaite-Kodze from the Life Science Center at Vilnius University, Vilnius, Lithuania	1:700 in PBS overnight	Nipah virus nucleoprotein
Goat anti-Rabbit IgG (H+L) Cross- Adsorbed Secondary Antibody Alexa Fluor®568	Thermo Fisher Scientific, A-11011	1:1000 in PBS 2h	secondary antibody
Goat anti-Mouse IgG (H+L) Cross- Adsorbed Secondary Antibody Alexa Fluor®488	Thermo Fisher Scientific, A-11001	1:1000 in PBS 2h	secondary antibody
Goat anti-Mouse IgG1 Cross-Adsorbed Secondary Antibody Alexa Fluor®568	Thermo Fisher Scientific, A-21124	1:1000 in PBS 2h	secondary antibody
Goat anti-Mouse IgG (H+L) Cross- Adsorbed Secondary Antibody Alexa Fluor®647	Thermo Fisher Scientific, A-21235	1:1000 in PBS 2h	secondary antibody
Goat anti-Chicken IgY (H+L) Secondary Antibody Alexa Fluor®647	Thermo Fisher Scientific, A-21449	1:1000 in PBS 2h	secondary antibody

Cerebral organoid staining for Nipah virus and F-actin

For imaging of Nipah virus-infected cerebral organoids and the respective controls, they were first washed twice for 15 min in PBS and subsequently fixed in 10 % Formalin with 4 % PFA. To guarantee the safe removal of biosafety level 4 (BSL-4) specimen, they were first

inactivated for 24 h at room temperature on a shaker before exchanging the formalin solution with fresh reagent (still within the high containment facility). Next, the organoids were again incubated for 24 h with the inactivating reagent before washing them three times for 15 min in PBS. At this point, the organoids were stored at 4 °C until further processing.

For cryosectioning, the organoids were subsequently embedded in 15 % sucrose (Sigma Aldrich, Merck KGaA, St. Louis, MO, USA) in PBS overnight at 4 °C until the specimen sunk to the bottom. The following day, the solution was exchanged for a 30 % sucrose solution and again incubated as described. Cryo-protected organoids were finally washed in PBS like mentioned above and placed onto a Cryomold® (A. Hartenstein, GmbH, Würzburg, Germany, CMB/CMM) of the appropriate size. Next, the specimen was covered in Tissue-Tek™optimal cooling temperature (OCT) Compound (Thermo Fisher Scientific Inc., Waltham, MA, USA) and shock frozen on top of a metal tray within liquid nitrogen. The specimen blocks were thereafter sent for cryosectioning at the Centre for Structural Systems Biology (CSSB), Hamburg at a width of 16 µm. These were layered onto SuperFrost/Plus microscopy slides (Glaswarenfabrik Karl Hecht GmbH & Co. KG, 42409110) and stored at -20 °C until further processing.

For staining, as a first step, an ImmEDGE™Hydrophobic Barrier Pen (Thermo Fisher Scientific Inc., Waltham, MA, USA) was used to determine the area for staining to commence with two washes of PBS for 5 min for temperature equilibration. Hereafter, the specimen was permeabilized in 1 % Triton-X-100 in PBS for 30 min at room temperature. Next, the slides were washed as before and blocked with 5 % FCS in PBS for 30 min at room temperature and subsequently counter-stained with 0.1 % Sudan Black (Carl Roth GmbH, Karlsruhe, Germany) in 70 % ethanol for 10 min to reduce autofluorescence. After another round of washing, the organoids were stained with the primary anti-Nipah virus nucleoprotein (N) antibody (1:700 in PBS, Indre Kucinskaite-Kodze from the Life Science Center at Vilnius University, Vilnius, Lithuania) for 24 h at room temperature. In three rounds of washing, the primary antibody was removed, before the secondary antibody (Goat anti-Mouse IgG (H+L) Cross-Adsorbed Secondary Antibody Alexa Fluor®647, Thermo Fisher Scientific Inc., Waltham, MA, USA) was added for 2 h at room temperature in the dark, together with F-actin staining using Phalloidin-Alexa Fluor-488 (Thermo Fisher Scientific Inc., Waltham, MA, USA). Finally, the samples were washed three times, dipped in ddH_2O and mounted with 4′,6-diamidino-2-phenylindole (DAPI)-containing mounting medium and 1 mm coverslips (Carl Roth GmbH, Karlsruhe, Germany). Lastly, coverslips were fixated with nail polish.

CX3CR1 and GFAP staining in EBOV-GFP and RESTV-GFP-infected organoids.

Cerebral organoids infected with EBOV-GFP and RESTV-GFP were harvested as described for Nipah virus-infected organoids. Staining was performed as previously described, whereby

microglia ($CX3CR1^+$, Rabbit, IgG, polyclonal, Biozol Diagnostica Vertrieb GmbH., Eching, Germany, PRS-2093) and astrocytes ($GFAP^+$, Chicken IgY, LifeSpan Biosciences Inc., Seattle, WA, USA, LS-C204526) were detected with the respective primary antibody 1:100 in PBS overnight and secondary antibodies 1:1000 in PBS for 2h at room temperature (Goat anti-Rabbit IgG (H+L) Cross- Adsorbed Secondary Antibody Alexa Fluor®568, Thermo Fisher Scientific; Goat anti-Chicken IgY (H+L) Antibody Alexa Fluor®647, Thermo Fisher Scientific).

Organoid embedding and deparaffinization

All histology processing and staining were performed by Petra Allartz (AG Zoonosen, BNITM). For histology processing, the organoids were inactivated in 10 % formalin containing 4 % PFA (BIOCYC Ges. f. Biotechnologie & Recyclingverfahren mbH, Potsdam, Germany, 400600305) for a total of 48 h, where the formalin was exchanged after 24 h. Subsequently, they were embedded in 2 % agarose (w/v, in ddH_2O) drops to increase their size for downstream processing as follows. The organoids were placed in a small mould within parafilm and all excess formalin was taken off. Thereafter, 30 µl of 2 % agarose were pipetted onto the organoids, making sure the organoids were retained within the middle of the drop during polymerization. Once the drop hardened, it was placed within a filter-paper-covered cassette and washed for 10 min in tap water, before soaking it under the sink. As a next step, the cassettes were run through the histokinette to dehydrate overnight, followed by paraffin embedding the next day. Slices were cut with a microtome at a width of 3 µm. To deparaffinize the slides, they were placed in a glass slide holder and run through i) Xylene 2 x 5 min, ii) 100 % ethanol 2 x 5 min, iii) 96 % ethanol 2 x 5 min, iv) 80 % ethanol 1 x 5 min, v) 70 % ethanol 1 x 5 min, vi) dH_2O 1 x 5 min before downstream staining.

Haematoxylin-eosin (HE) staining

When performing HE-staining, the cells were deparaffinized as described above and subsequently stained in hematoxylin for 10 min before being developed for 10 min under running tap water. Next, the slides were counterstained with 0.1 % eosin for 5 min and as a next step dehydrated again. To this end, the slides were dipped two to three times in i) 70 % ethanol, ii) 80 % ethanol, iii) 96 % ethanol, iv) 100 % ethanol and v) 3 x 5 min xylene. Thereafter, a drop of Eukitt® mounting medium (VWR International GmbH, Darmstadt, Germany) was placed on a coverslip with a glass rod and the coverslip was mounted onto the slide to dry overnight in a fume hood.

Periodic-acid Schiff (PAS)-staining

PAS staining was performed after deparaffinization and rehydration by starting with 10 min periodic acid incubation which was washed with distilled water. Next, Schiff's reagent was incubated for 10 min and washed for 5 min in water, before hematoxylin was incubated for 3 min and developed for 10 min under running tap water. Last, the slides were quickly dehydrated and mounted with Eukitt as described for the HE-staining.

Immunhistochemistry

Immunohistochemistry staining, HE staining, and PAS staining was performed by Petra Allartz (AG Zoonoses, BNITM). After the deparaffinization an epitope retrieval either via 2 min cooking in citrate buffer (pH6.0, 2 l dH_2O, 4.2 g citric acid (Merck KGaA, Darmstadt, Germany) or Tris buffer (pH9.0, 2 l dH_2O, 6.06 g Tris (Merck KGaA, Darmstadt, Germany), 1.48 g EDTA) in a pressure cooker or 5 min proteinase K treatment followed. Thereafter, the slides were washed in wash buffer (pH7.4, 2.5 l dH_2O, 20.5 g sodium chloride (Merck KGaA, Darmstadt, Germany), 3 g Tris (hydroymethyl) aminomethane (Merck KGaA, Darmstadt, Germany)) for 5 min on a shaker before being blocked in self-made peroxidase blocking reagent with 3 % hydrogen peroxide (10 ml 30 % H_2O_2 (Merck KGaA, Darmstadt, Germany) + 90 ml H_2O) or Dako peroxidase blocking reagent (Agilent, Santa Clara, CA, USA, S2001) for 30 min at room temperature. After another washing step with washing buffer, primary antibodies, diluted in Dako Antibody Diluent (Agilent, Santa Clara, CA, USA, S0809) to 100 µl total volume, were incubated overnight at room temperature in a humidity chamber (Table 4). Following this, a washing step of 5 min was performed, followed by a polylink secondary antibody staining for 30 min in the dark before immunophosphatase (AP) or immunoperoxidase (HRP) staining with the DC AP Detection Kit (DCS-diagnostics, Hamburg, Germany) or DCS AEC-2-Komponenten kit (DCS-diagnostics, Hamburg, Germany, AC131C100). After, another washing step and labelling via AP (DCS Polymerreagenz) or peroxidase (HRP) (DCS AEC-2-Komponentenkit PD330R050), respectively, for 30 min in the dark was concluded. Once washed, either APAAP development (substrate pH8.7, filtered:(A) 87.7 ml dH_2O, 31.25 ml propandiole (Carl Roth GmbH, Karlsruhe, Germany), 0.05 g levamisole (Merck KGaA, Darmstadt, Germany) + (C) 625 µl 4 % sodium nitrate solution (Merck KGaA, Darmstadt, Germany), 250 µl 5 Neufuchsin (basic violet 2) solution (Carl Roth GmbH, Karlsruhe, Germany) + (B) 750 µl dimethyleformamide (Carl Roth GmbH, Karlsruhe, Germany), 0.0625 g naphthole-AS-bi-phosphate (Merck KGaA, Darmstadt, Germany)) for approximately 5 min or AEC-development (1 ml AEC substrate buffer with 20 µl AEC substrate, AEC-2-Komponenten Kit, AC131C100) for approximately 4 min was undertaken until sufficient, then the reaction was stopped by immersing in water. The slides were then transferred into a washing buffer and stained for 1 min with hematoxylin, developed

for 10 min in running tap water. The slides were lastly mounted with Kaiser's glycerol gelatin (pre-warmed, Carl Roth GmbH, Karlsruhe, Germany) and a cover slip.

Table 4: Immunohistochemistry antibodies

Antibody	Company/Source	Usage	Phenotype
Rabbit anti-GFAP	Zytomed Systems GmbH, Bargteheide, Germany (RBK037)	1:200 overnight, AP	astrocytes
Rabbit anti-CD68	Cell Signaling Technologies, Danvers, MA, USA (76437)	1:200 overnight, AP or HRP	microglia/-macrophages
Rabbit anti-NeuN	Cell Signaling Technologies, Danvers, MA, USA (24307)	1:100 overnight, AP or HRP	mature neurons
Mouse anti-panEBOV NP	In-house	1:100 overnight, AP	EBOV NP
Human anti-Lassa virus glycoprotein subunit 2 Clone 22.5D	Zalgen Labs, USAMRIID, Frederick, MD, USA (Ab00225D-0.2)	1:200 overnight, AP or HRP	LASV GP2

5.3.3 Molecular biology methodology

Filoscreen and LASV RT-PCR

Viral RNA was isolated for sequencing and RT-PCR using the QIAamp viral RNA Mini Kit (Qiagen, Hilden, Germany, 52904) without carrier RNA. Briefly, 140 µl of thawed cell culture supernatant (previously cleared) was mixed with 560 µl of AVL buffer via vortexing and subsequently incubated for 10 min at room temperature. As a next step, the mixture was inactivated by supplementing 560 µl 100 % Ethanol which was vortexed and incubated for at least 10 min. Subsequent steps were performed according to the manufacturer's protocol using spin columns. RNA was finally eluted in 60 µl AVE buffer.

The RealStar®Filovirus Screen RT-PCR Kit 1.0 (Altona Diagnostics, Hamburg, Germany, 441003) for EBOV detection or RealStar®Lassa Virus RT-PCR Kit 2.0 RUO (Altona Diagnostics, Hamburg, Germany, 642003, performed by J. Mueller), were run according to the manufacturers protocol with the internal control added to the master mix. The samples were run on the Rotor-Gene®6000 (Corbett Research) with the following dye settings for the Filovirus kit: Ebolavirus specific RNA FAM™ (no quencher), Marburgvirus specific RNA Cy®5 (no quencher), Internal Control IC JOE™ (no quencher). Reverse transcription was performed for 20 min at 55 °C prior to 2 min denaturation at 95 °C prior to 45 cycles of i) denaturation (95 °C, 15 s), ii) annealing (58 °C, 45 s), and iii) polymerization (72 °C, 15 s). The internal positive control was used to generate a relative cycle threshold (CT) value to normalize among RT-PCR runs.

5'copy-back defective viral genomes (DVG) RT-PCR

5'copy-back DVG RT-PCR, adapted from Johnson *et al.* [192], was performed on viral RNA from the supernatant, total RNA samples extracted from cells via the RNeasy Mini Kits (Qiagen, Hilden, Germany, 74104-9) or total RNA extracted from organoids via a Trizol (Ambion, Kaufungen, Germany)-RNeasy combined protocol or Qiagen RNeasy FFPE RNA isolation kit (Qiagen, Hilden, Germany, 73504).

For RNA from the supernatant, an equal volume (1.75 µl) of the sample was used for the one-step RT-PCR reaction, while for total RNA an equal amount of RNA (100 ng) was used for the reaction. To this end, Superscript™IV RT-PCR one-step (Thermo Fisher Scientific Inc., Waltham, MA, USA) was used for reverse transcription and RT-PCR with both published primers, EBOV-1 (5'-CGTGGTCAATGTCTTAATTATCATTA-3', 51.5°C) and EBOV-2 primer (5'-GGGACTCCTTTC-GTTATTTAAATAGTTGTT-3', 55.6°C) by Johnson *et al.* [192]. Each reaction included 2X Platinum™SuperFi™RT-PCR Master Mix (final: 1X), Forward and Reverse primers (0.5 µM), SuperScript™IV RT Mix (0.25 µl) and template RNA (filled up to a total volume of 25 µl with nuclease-free water). The reaction ran as follows: i) reverse transcription (45–60 °C, 10 min), ii) denaturation (98 °C, 2 min), iii) 40 cycles of amplification with a) denaturation (98 °C, 10 s), b) annealing (55 °C, 10 s), c) elongation (72 °C, 1 min 30 s) and iv) final extension (72 °C, 5 min). Lastly, samples (10 µl, 1X (1:10.000) GelRed®Merck KGaA, Darmstadt, Germany) were run on a 1.5 % agarose gel in 1X TAE buffer (50X 50X: 2 M Trisbase, 1 M acetic acid, 0.05 M EDTA in 1 l ddH_2O) for 40 min at 100 V with a GeneRuler 1 kb ladder mix (Thermo Fisher Scientific Inc., Waltham, MA, USA). Bands were counted to determine DVG species diversity.

RNA extraction from Trizol-homogenized tissue

To extract via Trizol reagent, organoids were washed twice in PBS before being placed in a homogenizer tube (Sarstedt, Nümbrecht, Germany) containing ceramic beads (Lysing Matrix D, MP Biomedicals, Irvine, CA, USA) and 750 µl Trizol reagent for inactivation and homogenization for 5x30 s (MP Biomedicals™FastPrep™-24 5G).

For RNA extraction, the samples were subsequently intensely pulse-vortexed for 30 s each before the tubes were set to let the large clumps set to the bottom. 700 µl of Trizol homogenate were then transferred to a new 1.5 ml reaction tube under a fume hood, and 140 µl chloroform was supplemented before the samples were pulse-vortexed for 15 s. After 3 min of incubation at room temperature, the mixture was centrifuged at 12 000 *x* g for 15 min at 4 °C. After, the upper clear, aqueous phase was carefully transferred to a new reaction tube and the 1.5x volume of 100 % ethanol was added on top. This mixture was then loaded onto the RNeasy column for isolation with on-column DNase digest. This, in brief, includes spinning at 8000 *x* g

for 15 s, discarding the flow through and adding 350 µl RW1, spinning at 8000 *x* g for 15 s, and a subsequent DNase I digest (10 µl DNase + 70 µl RDD buffer, RNase-Free DNase Set, Qiagen, Hilden, Germany, 79254) for 15 min at room temperature. After, the RNeasy manufacturer's protocol was followed, and the samples were washed in 350 µl RW1, spinning at 8000 *x* g for 15 s, 500 µl RPE, spinning at 8000 *x* g for 15 s, and dried at full speed for 2 min to be finally eluted in 60 µl RNase-free water (1 min incubation, 8000 *x* g for 15 s).

RNA extraction from FFPE tissue

For each sample, 5 sections with a width of 3 µm each were used for RNA extraction. In brief, they were deparaffinized by incubating in 1 ml Xylol for 20 min at 37 °C. Subsequently, the samples were spun at 20.000 *x* g for 2 min, after which the supernatant was discarded. After two following washing steps with 1 ml of 100 % ethanol centrifuged at 20.000 *x* g for 2 min, the pellets were dried at 37 °C. In the next step, the samples were lysed in 240 µl PKD buffer including 20 µl (5 mg/ml) Proteinase K and incubated overnight at 56 °C on a shaker at 600 rpm. RNA extraction was then performed according to the manufacturer's protocol. In brief, the lysate was incubated for 15 min at 80 °C on a shaker, placed on ice for 3 min and then centrifuged for 15 min at 20.000 *x* g. The thus generated supernatant was transferred and a DNAse I digest performed (25 µl DNase Booster buffer, 10 µl DNAse I stock) for 15 min at room temperature. Thereafter, 500 µl RBC buffer was added, mixed and supplemented with 1.200 µl 100 % ethanol. 700 µl of this mixture was transferred onto the RNeasy column, centrifuged (8 000 *x* g, 15 s) and the flow-through discarded. This was repeated until the whole sample was loaded. 400 µl RPE were subsequently added twice as washing steps (8 000 *x* g, 15 s), where the flow-through was discarded and a final drying step for 5 min at 20.000 *x* g was performed. Finally, the RNA was eluted in 30 µl RNase-free water (1 min) and centrifuged at 20.000 *x* g for 1 min.

5.4 General software

Table 5: Software

Software	Application
FIJI / Image J2 V2.3.0/1.53q (open source, [231])	Image processing and analysis
Adobe Photoshop 2023 (Adobe, San José, CA, USA)	Figures
BioRender.com (BioRender, Toronto, ON, CA)	Figures
FlowJo v10 (Becton Dickinson Biosciences, Franklin Lakes, NJ, USA)	Flow Cytometry data analysis
Prism 10 (GraphPad, Boston, MA, USA)	Statistics
RStudio 2023.12.1 (Posit PBC, Boston, MA, USA)	Statistics
AID multiSpot (AID Autoimmun Diagnostika GmbH, Straßberg, Germany)	AID plate reader software for IFAs

Table 5: Software

Software	Application
Legendplex / Qognit (Biolegend, San Diego, CA, USA / Qognit, San Carlos, CA, USA)	Cytokine assay processing and analysis
MS Office 2021 (Microsoft Corporation, Seattle, WA, USA)	Data analysis
Overleaf.com (Digital Science UK Limited, London, UK)	Thesis writing

5.5 Statistics

Most data described herein is descriptive, in which case no statistical analysis was performed. For kinetics of cytokines and viral titers, AUC was initially calculated and subsequently used for pair-wise comparisons using the respective statistical test as indicated (unpaired, two-tailed Student's T-test/ one-way ANOVA). Post-hoc multiple-hypothesis testing was additionally carried out as indicated for the respective experiment if warranted. Longitudinally cytokine release was analyzed using a Mixed Effects Model with post-hoc Tukey's multiple hypothesis correction. Flow cytometry statistics were performed using the Kruskal Wallis non-parametric test with post-hoc Dunn's Multiple Comparisons for correction. Statistical significance was reported upon $p/pAdj \leq 0.05$.

5.6 Bulk RNA sequencing

5.6.1 RNAseq data acquisition microglia and astrocytes 3, 6, 12 dpi

Bulk RNAseq analysis was performed for immortalized human microglia or astrocytes infected with EBOV at MOI=0.0025 for 3 d (early stage), 6 d (exponential replication), or 12 d (saturated stage) (n=2 to 4, independent biological replicates Table 6). To this end, cells were seeded in 12 well-plates pre-coated with collagen-1 as previously described (medium: RPMI, 10 % FCS, 1 % P/S, 2 % HEPES), providing 50 % confluency at the day of infection. As baseline sample (d0), supernatant samples were collected after adding fresh medium following infection (medium: RPMI, 2.5 % FCS, 1 % P/S, 2 % HEPES). All supernatant samples of this experiment were cleared at 2 000 x g for 10 min before freezing at -80 °C.

The infection was subsequently carried out at MOI=0.0025 at 37 °C for 1 h; as a negative control, cells were mock infected with FCS-free DMEM medium. Following, fresh RPMI medium containing reduced FCS (2.5 %) was supplied, and an infection baseline (d0i) was sampled.

Every three days, the supernatant was collected from all samples, while on days 3, 6, or 12 the respective cells were harvested using the RNeasy®Plus Mini Kit (Qiagen, Hilden, Germany, 74136) according to the manufacturer's protocol (including DNA removal). Finally, total RNA was eluted in 60 µl nuclease-free water (NFW) and stored at -80 °C until further processing.

The viral titer of the supernatants was measured as described above (subsubsection 5.3.2). Importantly, uninfected outliers - based on the viral RNA STAR gene counts (i.e. uninfected and titration) - were excluded from the differential gene expression analysis in the EBOV group (Table 6).

RNA quality control was performed using a Nanodrop and Bioanalyzer (Agilent, Santa Clara, CA, USA) with the Agilent RNA 6000 Nano Kit (Agilent, Santa Clara, CA, USA, 5067-1511) to obtain the respective RIN values. All samples had RIN$\geq$8.9 and 28S/18S RNA values of 1.6-2.0 and were thus of good quality and sent for DNBSEQ Eukaryotic Strand-specific Transcriptome Resequencing (DNB, DNA nanoball sequencing) by BGI Genomics (Shenzhen, China). At BGI, polyA-enrichment, mRNA fragmentation, first (dTTP) and second strand (dUTP) synthesis were performed before sequencing on a DNBseq™ platform using a DNBSEQ Eukaryotic Strand-specific mRNA library with a PE100 read-length (100 bp) and clean fastq phred quality score of 33. The sequencing depth was at least 24 million reads per sample. BGI service included quality-scoring the raw data (reporting overall good quality scores), adapter-trimming the reads, and removing low-quality reads using SOAPnuke [232]. Adaptors were filtered if the sequence matches at least 25 % with a maximum of two mismatches allowed. Reads were discarded when the minimum length of 100 bp was not achieved or N content accounted for above 1 % of the read. PolyX (with X being A, T, G, or C) were removed when exceeding 50 bp as well as reads with at least 30 % of bases having a low-quality score (<20). The output value of read quality was set to Phred+33.

Table 6: RNAseq sample inclusion in days 3, 6, 12. RNAseq sample inclusion in days 3, 6, 12.

Cell type	Infection	Included groups	Independent biological replicates
Microglia	Negative (3)	A, B, C	3
Microglia	Negative (6)	A, B, C, D	4
Microglia	Negative (12)	A, B, C	3
Microglia	EBOV (3)	A, B, C, D	4
Microglia	EBOV (6)	A, C	2
Microglia	EBOV (12)	A, C, D	3
Astrocytes	Negative (3)	A, B, C, D	4
Astrocytes	Negative (6)	A, C, D	3
Astrocytes	Negative (12)	A, B, C, D	4
Astrocytes	EBOV (3)	B, C, D	3
Astrocytes	EBOV (6)	A, C	2
Astrocytes	EBOV (12)	A, B	2

5.6.2 RNAseq data acquisition microglia and astrocytes 20dpi

Bulk RNAseq analysis was performed for immortalized human microglia and astrocytes infected with EBOV or LASV at MOI=0.0025 20 dpi (n=3, independent biological replicates pooled from 2 wells each). To this end, cells were seeded in 12 well-plates pre-coated with collagen-1 as previously described (medium: RPMI, 10 % FCS, 1 % P/S, 2 % HEPES), providing 50 % confluency at the day of infection. As baseline sample (d0), supernatant samples were collected after adding fresh medium following infection (medium: RPMI, 2.5 % FCS, 1 % P/S, 2 % HEPES). All supernatant samples of this experiment were cleared at 2 000 x g for 10 min before freezing at -80 °C.

Table 7: RNAseq sample inclusion day 20. RNAseq sample inclusion day 20.

Cell type	Infection	Included groups	Independent biological replicates
Microglia	Negative (20)	1, 2, 3	3
Microglia	EBOV (20)	1, 2, 3	3
Microglia	LASV (20)	1, 2, 3	3
Astrocytes	Negative (20)	4, 5, 6	3
Astrocytes	EBOV (20)	4, 5, 6	3
Astrocytes	LASV (20)	4, 5, 6	3

The supernatant was collected from all samples 6, 13, and 20 dpi when the respective cells were harvested using the RNeasy®Plus Mini Kit (Qiagen, Hilden, Germany, 74136) according to the manufacturer's protocol, whereby cells from two wells within a group were pooled to increase the yield (e.g.microglia N1+N2 = N1, N3+N4 = N2, N5 + N6 = N3; astrocytes N1+N2 = N4, N3+N4 = N5, N5 + N6 = N6 see: Table 7). Finally, total RNA was eluted in 60 µl NFW and stored at -80 °C until further processing. Viral titer of the supernatants was measured as described above for each initial well (n=6). RNA quality control and sequencing were performed as described above.

5.6.3 RNAseq data acquisition of persistently infected microglia passage 10+3

Bulk RNAseq analysis was performed for immortalized human microglia passaged upon or without persistent EBOV (MOI=1, flask A or B) infection. Note these are the same cells as described above in the passaging experiment. In brief, one flask of microglia each was infected with EBOV (MOI=1, flask A and flask B) at baseline, whereby one flask was treated with DMEM as control. After 1 h infection at 37 °C, the cells were grown for 1 week (medium: RPMI, 2.5 % FCS, 1 % P/S, 2 % HEPES) before being split 1:5, whereby samples were taken. This was continued for 10 passages, although from passage 3 onwards uninfected microglia were supplied to the infected groups to keep the culture viable. At passage 10, cells were harvested and frozen (10 % DMSO in FCS). These were subsequently thawed and distributed

in n=4 wells per group (negative control, EBOV passaged flask A, EBOV passaged flask B) and set to recover in RPMI, 10 % FCS, 1 % P/S, 2 % HEPES. After three subsequent passages (P10+3), cells were harvested (n=4, Table 8) for bulk RNA sequencing using the RNeasy®Plus Mini Kit (Qiagen, Hilden, Germany, 74136) according to the manufacturer's protocol. Finally, total RNA was eluted in 60 µl NFW and stored at -80 °C until further processing. The viral titer of the supernatants was measured as described above for each passage before freezing as well as at passage 10+3 before harvesting. RNA quality control and sequencing were performed as described above.

Table 8: RNAseq sample inclusion passage 10+3. RNAseq sample inclusion passage 10+3.

Cell type	Infection (passage)	Included groups	Independent biological replicates
Microglia	Negative (P10+3)	1, 2, 3, 4	4
Microglia	EBOV flask A (P10+3)	1, 2, 3, 4	4
Microglia	EBOV flask B (P10+3)	1, 2, 3, 4	4

5.6.4 RNAseq data analysis, *H. sapiens*

RNAseq data processing and analysis were performed using the Galaxy EU server [233, 234]. Here, the reads attained from BGI (paired-end, stranded, R1, R2, .fastq) were uploaded and again adaptor trimmed using Trimmomatic [235]. In detail, read pairs were trimmed using SLIDINGWINDOW with 4 bases averaged across and an average quality of 20 required. Subsequently, quality control using Fast QC [236] was performed.

Alignment to the human genome[1] was undertaken using the RNA STAR algorithm [237] (generates .sam file) and the incorporated SAMtools [238] with Galaxy default options (generating .bam files). Specifically, a temporary index using the human genome was generated with an SA pre-indexing string of 14, while splice-junctions were annotated with a length of 100bp around annotated junctions. 2-pass mapping was performed in groups separated by cell type and chimeric alignments were reported as junctions. Further output filters were set as default (–outFilterMultimapScoreRange 1, –outFilterMultimapNmax 10, put (–outFilterMismatchNmax 10, –outFilterMismatchNoverLmax 3, –outFilterMismatchNoverReadLmax 1, –outFilterScoreMin 0, –outFilterScoreMinOverLread 0.66, –outFilterMatchNmin 0, –outFilterMatchNminOverLread 0.66, –outSAMmultNmax -1). Finally, per gene read counts were retrieved with stranded information, where the second strand corresponds to the (+) strand, i.e. the transcripts (mRNA) as the library is reverse-stranded. An annotation file was generated using annotateMyIDs [239]. The gene counts file was cleaned up to retrieve unique entries and finally, differential gene expression analysis was performed using the Galaxy internal limma-voom [240–243]

[1] GRCh38, GCA_000001405.15, https://ftp.ncbi.nlm.nih.gov/genomes/all/GCF/000/001/405/GCF_000001405.26_GRCh38

with implemented edgeR [244–247], where normalization was performed to total depth (TMM) and genes were excluded if 5.0/million maps on n=2 samples were not achieved. A correction for mean expression was performed and the false discovery rate (FDR) was set to FDR$\leq$0.05 via Benjamini and Hochberg (1995) algorithm (limma-voom details in the appendix).

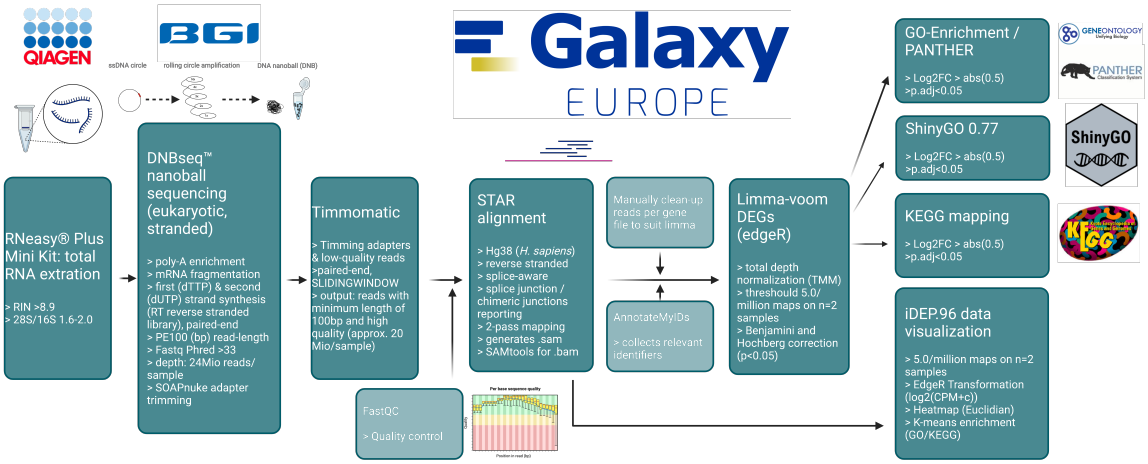


Figure 20: Workflow of RNAseq data acquisition, processing and analysis. Total RNA isolation via the RNeasy Plus Mini Kit (Qiagen) was followed by polyA-enrichment and DNBseq™nanoball sequencing using a eukaryotic, stranded library by BGI. Quality-controlled and trimmed reads were subsequently re-trimmed using Trimmomatic on the Galaxy.eu server, followed by STAR indexing and alignment against the human genome. Thereafter, differential gene expression analysis was carried out using the limma-voom algorithm with total depth normalization. Data interpretation and visualization were performed with the aid of iDEP.96 suite, GO-enrichment, and KEGG pathways mapping via ShinyGO.

The iDEP [248] suite was additionally explored for heatmap generation and k-means enrichment analysis. GO-Enrichment was run using the Gene Ontology Resource with all significantly expressed genes (Log2FC$\geq$abs(0.5), adjusted p-value $\leq$0.05) [249] and via ShinyGo 0.77 using the same constraints [250].

5.7 Viral RNA sequencing

5.7.1 EBOV gene expression analysis

Pre-processed and trimmed total RNA files for EBOV gene expression analysis were the same previously used for the human gene expression analysis as described above (Table 6, Table 7, Table 8). Viral genome sequences and gtf files were retrieved for EBOV (Mayinga strain) from the NCBI database [2]. The Galaxy EU server [233, 234] was used to run the RNA STAR alignment [237] against the EBOV genome for which temporary indexes were created. Exon junction information for mapping splices (–sjdbGTFfile) was set to 100 and two-pass mapping was performed on all samples. Chimeric alignments were reported in a Junction file (–chimOutType) and HITag values were one-based (–outSAMattrIHstart). MAPQ value for unique mappers was set to 60 (–outSAMmapqUnique). Read counts for the respective

[2]ViralProj14703, GCF_000848505.1,https://ftp.ncbi.nlm.nih.gov/genomes/all/GCF/000/848/505/GCF_000848505.1_ViralProj14703

EBOV genes were obtained from STAR for both strands, the first strand (genome, (-)), and the second stand (mRNA, (+)). Counts per gene were normalized to the gene length for either the first or second strand. Gene expression (mRNA, second strand) counts were further normalized to genome maps (first strand) to determine expression per genome presence.

5.7.2 Viral RNA sequencing of RNA isolated from the supernatant

Viral RNA was isolated from the supernatant of human cerebral organoids using the QIAmp viral RNA Mini Kit without carrier RNA as described above. In case of the isolated variants, RNA was subjected to reverse transcription (SuperScript IV Reverse transcriptase) using random primers and the library was prepped using the QIAseq FX DNA Library kit (UDI, Qiagen, Hilden, Germany, 180477) before being sequenced on the NextSeq2000 using the P1 flow cell (P1 300) (strand-specific, paired-end, Illumina, 20050264). All data acquisition downstream of the RNA isolation was performed by the NGS Core Facility of the BNITM and the help of Daniel Cadar and his colleagues.

Data analysis was performed by Shruti Shirsathe at Icahn School of Medicine at Mt. Sinai (MSSM, New York, NY, USA) under the supervision of Prof. Gustavo Palacios (MSSM). Adapter sequences were removed with cutadapt (-j 10 –cut 8 -U 8), filtered by quality with Prinseq (min_qual_mean 20, trim_qual_right 20, and min_len 50), and aligned to the EBOV (Mayinga) reference[3] with bowtie2 [251] and BWA [238]. Duplicate reads were removed with PICARD[4], and variant calling was performed with IVAR (-q 20 -t 0.03 -m 10) [252]. Major single nucleotide polymorphism (SNP) were identified by filtering IVAR output to only include mutations that passed IVAR internal checks, had an alternate frequency greater than 0.6, and were non-synonymous. SNP were reported if they were not present in the stock sequence used for infection.

[3] AF086833; Ebola virus - Mayinga, Zaire, 1976, complete genome.
[4] MarkDuplicates (Picard), GATK, Broad Institute

6 Results

6.1 Establishment of partially immunocompetent human cerebral and choroid plexus organoids for viral persistence studies.

EBOV can persist up to months in the human CNS, causing recrudescent inflammatory disease either via replication or immunopathologic effects [130, 139]. In NHP, the persistence of EBOV in the CNS has been pinpointed to the $CD68^{+}$ microglia population as well as structures adjacent to the vasculature and the choroid plexus [183, 189]. For humans, neither the acute nor persistent CNS targets of EBOV infection have been elucidated at the time of writing. Coherently, the first objective of this work entails the establishment of partially immunocompetent human cerebral and choroid plexus organoid models [214, 217, 223] which may be used to address the EBOV CNS targets, whether EBOV persists in human brain tissue in vitro and how such a persistence manifests itself.

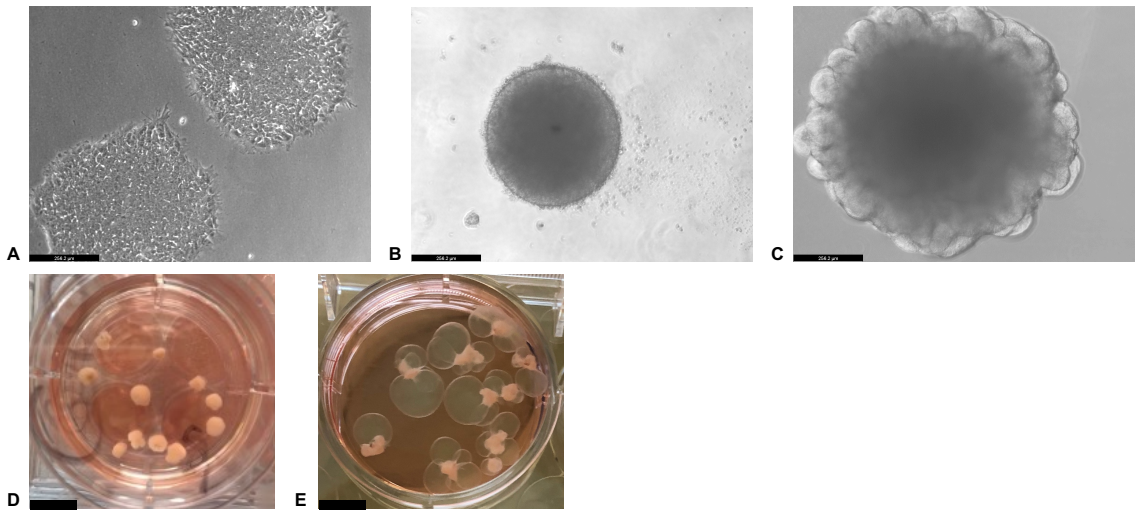


Figure 21: Light microscopy images of human cerebral and choroid plexus organoids. Representative light microscopy images of **(A)** human iPSC HMGU-1 cell line cultures, **(B)** embryoid bodies 5 days after seeding, **(C)** human cerebral organoids 3 d after embedding in Matrigel, **(D)** 100 d old human cerebral organoids, and **(E)** 100 d old human choroid plexus organoids. The scale bar indicates 256 µm (A, B, C) or 5 mm (D, E). Images A, B, and C, taken in collaboration with Shuiqing Yu at Integrated Research Facility (IRF)-Frederick at Fort Detrick, Frederick, MD, USA (NIH/NIAID).

To this end, the HMGU-1 iPSC line was used to generate human cerebral organoids as well as choroid plexus organoids, which were both characterized after 100 days of growth. As is shown in Figure 21 A-E, both types of organoids were generated by undergoing the required steps of organogenesis from lineage unspecified embryoid bodies towards neuroepithelial tissues. Finally, heterogeneous 3D cultures of 2 –4 mm of size were obtained in the case of the cerebral organoids (Figure 21, D), partially displaying vacuolar structures. Meanwhile, choroid plexus organoids herein generated presented with large fluid-filled vacuoles throughout, reaching up to several centimeters in diameter (Figure 21, E).

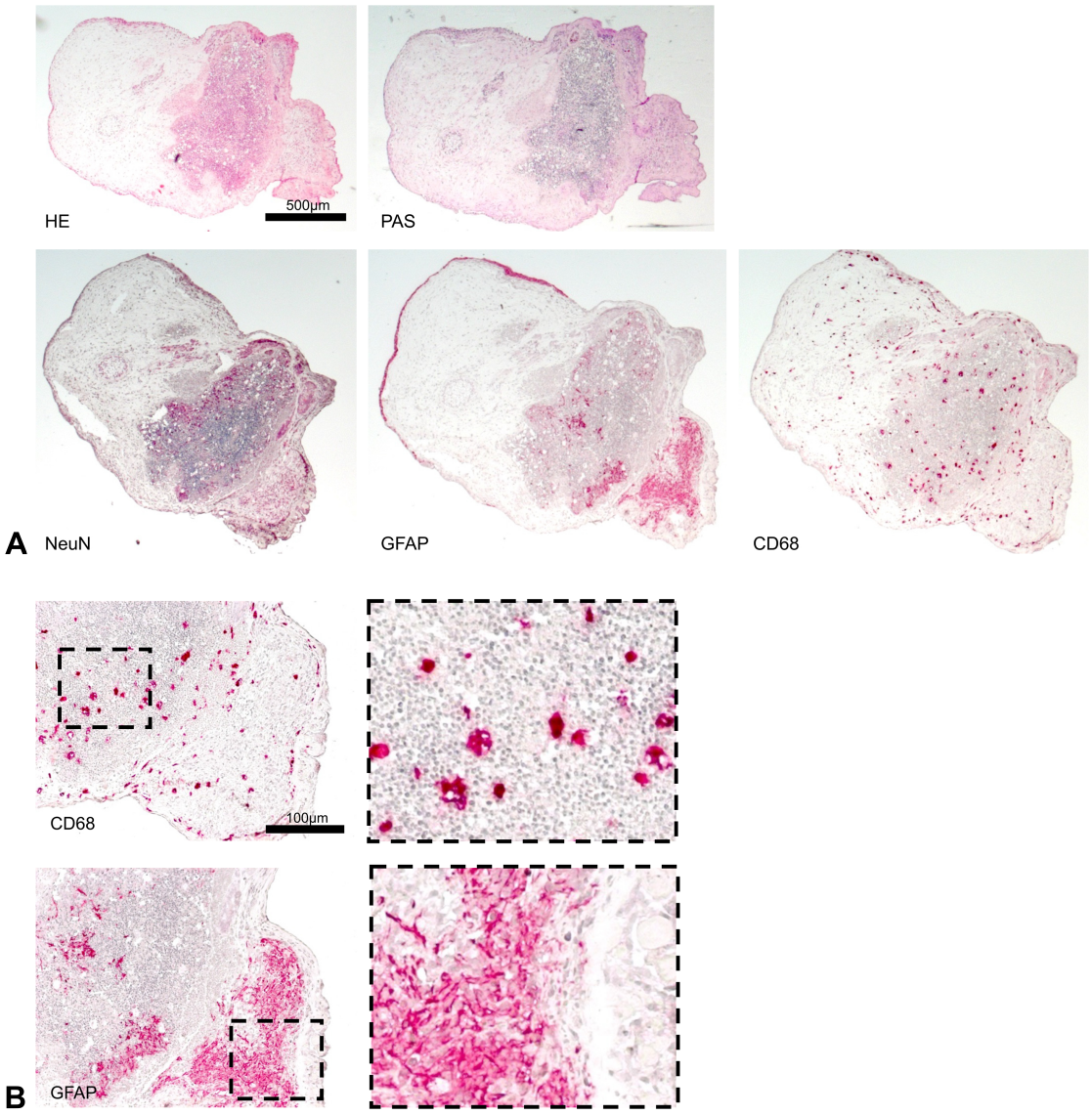


Figure 22: Immunohistochemistry staining of cerebral organoid cell types. (A) Representative human cerebral organoid stained for HE, PAS, mature neurons (NeuN), astrocytes (GFAP), and microglia (CD68). The scale bar indicates 500µm. **(B)** Human cerebral organoid stained for CD68 and GFAP with the respective area zoomed in. The scale bar indicates 100µm.

Immunohistochemistry staining was further obtained to confirm the presence of mature neurons ($NeuN^+$), astrocytes ($GFAP^+$) as well as mesoderm-derived microglia-like cells ($CD68^+$) in human cerebral organoids (Figure 22 (A)). Overall, as depicted in the representative images shown in Figure 22, cortical layering was less pronounced 100 days after induction in the organoids. As such, they mostly contained mature projecting neurons ($NeuN^+$) at the surface as well as throughout the 3D tissue, whereby patches of astrocytes ($GFAP^+$) were seeded in between. Notably, astrocytes displayed a ramified phenotype (Figure 22 (B)) and quantity varied amongst organoids. Organoids of 100 days and older contained dense regions with $NeuN^+$ neurons and some necrotic areas, which presented as dense, dark tissue (Figure 22 (A)). The $CD68^+$ microglia population was dispersed evenly throughout the organoid in a

steady state, with the microglia mostly displaying an amoeboid shape indicative of either immaturity or activity/motility (Figure 22 (B)).

6.1.1 Explorative Nipah virus and RESTV-GFP infection in human cerebral organoids to establish infection conditions.

Nipah virus is known to harbor an extensive neurotropism and cause severe encephalitis in humans [253]. Therefore, it was initially anticipated that infection of human cerebral organoids would be successful and therefore can be used to establish infection conditions and serve as an acute/positive control for subsequent infections with EBOV. Accordingly, 100 days old human cerebral organoids were initially infected with a low Nipah virus dose of 10^4 FFU/organoid for 1 h at 37 °C and subsequently set to incubate for 10 days. On the final day, cerebral organoids were harvested and used for immunofluorescence microscopy.

As shown in Figure 23, after 10 days of infection NiV had penetrated deeply into the cerebral organoid, establishing infection throughout. Moreover, rupture of the outer layer (Figure 23) was observed. As the viral dose was already low, it was therefore concluded that Nipah virus infection of human cerebral organoids was too severe to allow for long periods of infection, as anticipated for persistence studies. Therefore, future experiments were performed using LASV as a control.

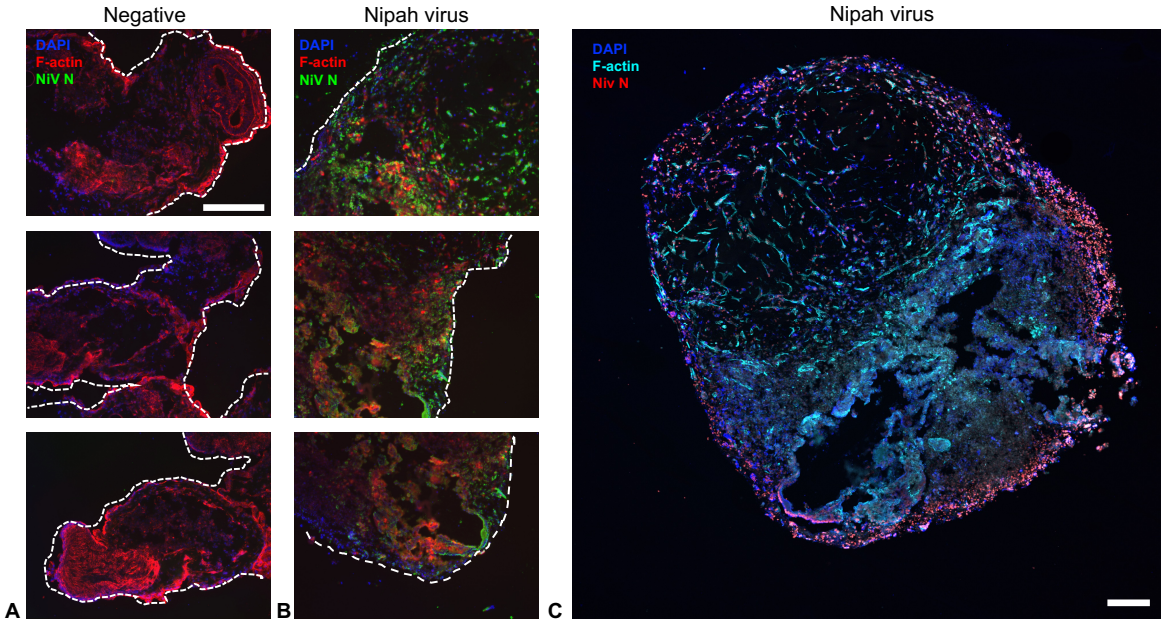


Figure 23: Immunofluorescence microscopy of Nipah virus-infected cerebral organoids. (A) Negative control organoids stained for F-actin (red) and NiV nucleoprotein (N) (green), counterstained for DAPI in 10x Magnification. **(B)** Nipah virus infected organoid stained for F-actin (red) and NiV nucleoprotein (N) (green), counterstained for DAPI in 10x magnification. **(C)** Same Nipah virus infected organoid stained for F-actin (cyan) and Nipah virus N (red), counter-stained with DAPI in 10X Magnification imaged via the Olympus FV3000 confocal microscope. Scale bar indicative of 100µm.

Next to Nipah virus infection, it was sought out to determine whether the infectious dose

(10^4 FFU/organoid) applied for only one hour was sufficient to cause a productive infection with EBOV and RESTV, the seemingly human apathogenic orthoebolavirus [7]. Therefore, a RESTV-GFP infection was performed similarly. As shown in Figure 24, RESTV-GFP infection at 10 dpi in human cerebral organoids was detectable in outer layers of the organoids. Consequently, it was established that 10^4 FFU/organoid can be used in future virus inoculations in subsequent experiments querying longer time frames.

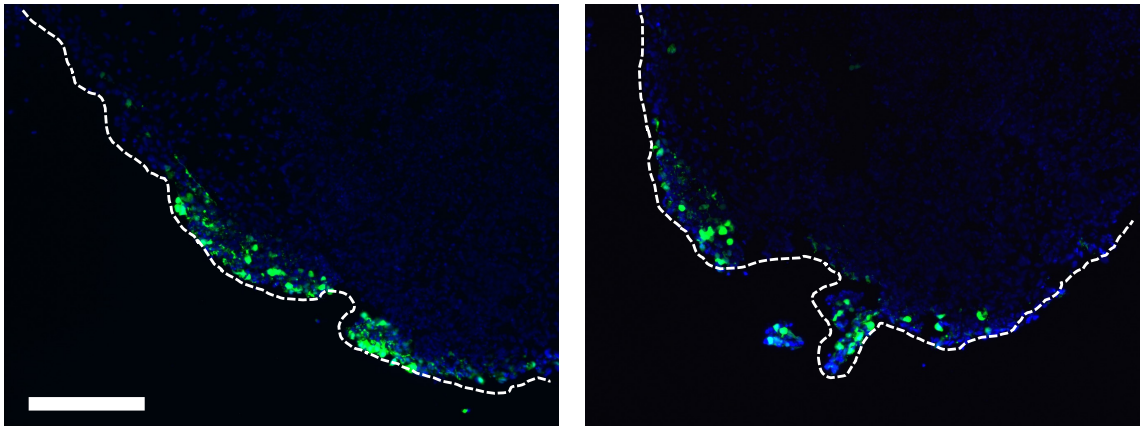


Figure 24: Immunofluorescence microscopy of RESTV-GFP-infected cerebral organoids. Immunofluorescence microscopy images (10X magnification) of RESTV-GFP (green)-infected human cerebral organoids 10 dpi at 10^4 FFU/organoid. Counter-staining using DAPI. Scale bar indicative of 100µm.

6.2 EBOV establishes a persistent infection of at least 120 days in human cerebral organoids.

As proposed within objective two, human cerebral organoids were used to explore whether EBOV infects and subsequently establishes a persistent infection in human CNS tissue. Furthermore, to demarcate the specificity of the EBOV persistence model, the replication of EBOV was compared to LASV, a phylogenetically more distant, human-pathogenic hemorrhagic fever virus that can colonize the CNS [254].

One hundred days old human cerebral organoids were infected with EBOV or LASV with 10^4 FFU per organoid, wherein two independent experiments were performed using different organoid batches. During the experiment, organoids were harvested for immunohistochemistry staining, reducing longitudinal group size to a minimum of n=6 organoids per group (Figure 25 (A)). Notably, as shown in Figure 25 B, not all organoids inoculated with the virus became productively infected, as defined by the detection of viral particles above the limit of detection (LOD) in an immunofocus assay at one point during the experiment. Nevertheless, both EBOV and LASV established a productive infection in >90 % of cerebral organoids. Next to the capacity of the different viruses to establish a productive infection throughout the experiment, the percentage of infected organoids actively releasing infectious particles at

any given time point was analyzed. Coherently, at 120 dpi, all organoids infected with EBOV had viral titers above the LOD (Figure 25 (C)), meeting the criteria of viral persistence. In contrast, within 48 days all but one LASV infected organoid remained at/below LOD without resurgence throughout the 120 days (Figure 25 (C)). Hence, LASV differs substantially from EBOV in its capacity to establish productive persistent infection in the CNS.

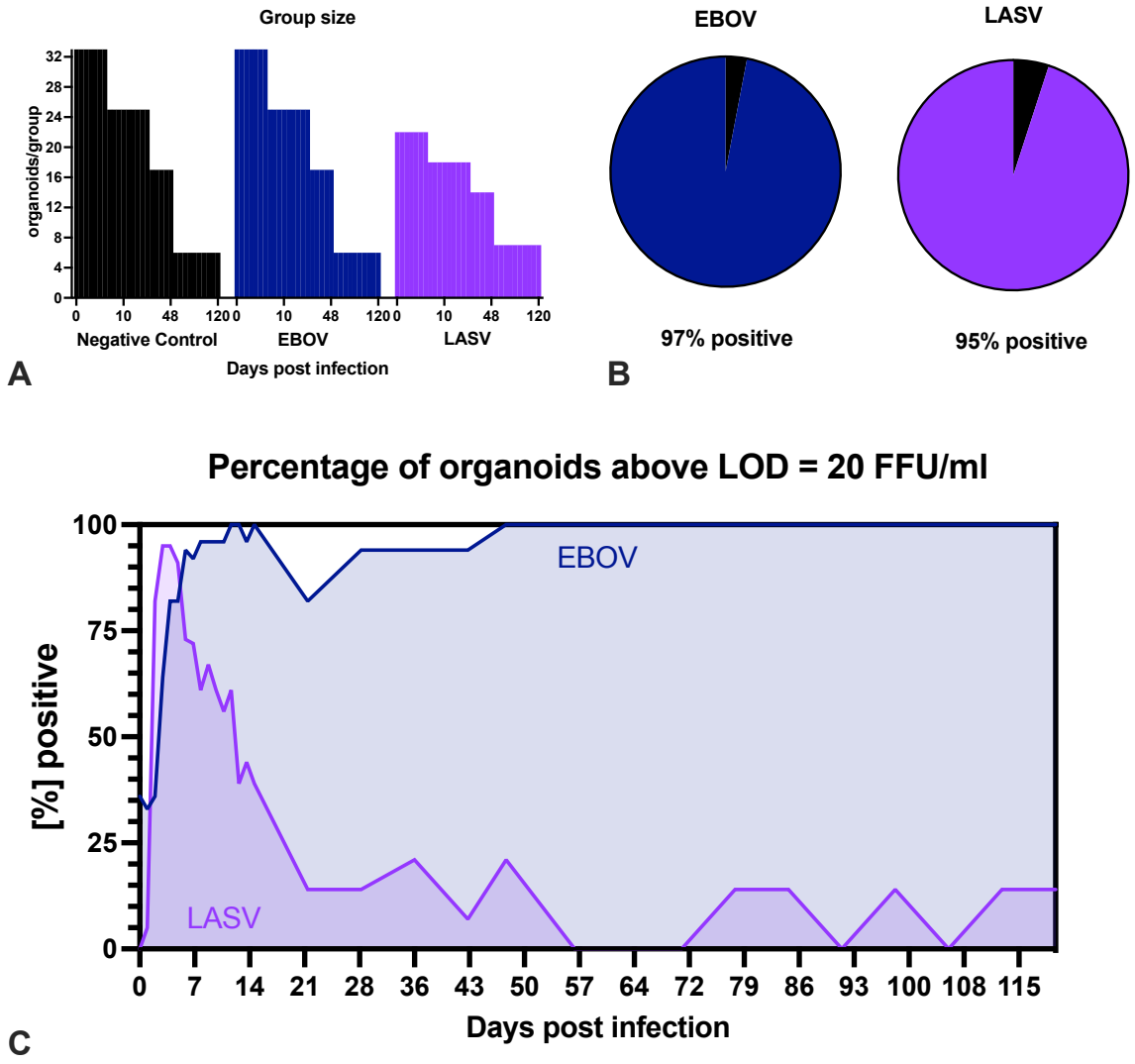


Figure 25: Distribution and productivity of infection in cerebral organoids. (A) Amount of organoids per group throughout the two independent experiments. **(B)** Pie charts of percentages of cerebral organoids developing a productive infection with EBOV (blue = positive) or LASV (purple = positive) as defined by having a viral titer above the LOD=20FFU/ml within the experimental time frame for individual organoids. **(C)** Percentage of organoids with a viral titer above the LOD (20 FFU/ml) at the indicated time point during the experiment with minimum n=6 longitudinal organoids per group at 120 dpi. Data was generated using two independent organoid batches.

Besides the overall productivity of infection, viral titers were used to determine the kinetics of the replication of both viruses in those organoids that were productively infected, displayed in Figure 26. Uninfected organoids were kept as negative controls. Here, a large range across the organoids within each group was observed. Nevertheless, overall trends were clear. In the human cerebral organoid model, EBOV infection reached its highest titer at 6–14 dpi

at approximately 10^5 FFU/ml before declining by 10 to 100-fold and replicating persistently at 10^3-10^4 FFU/ml for the remainder of the 120 days, producing infectious virus. Moreover, EBOV RNA released into the supernatant increased from 6 to 120 dpi.

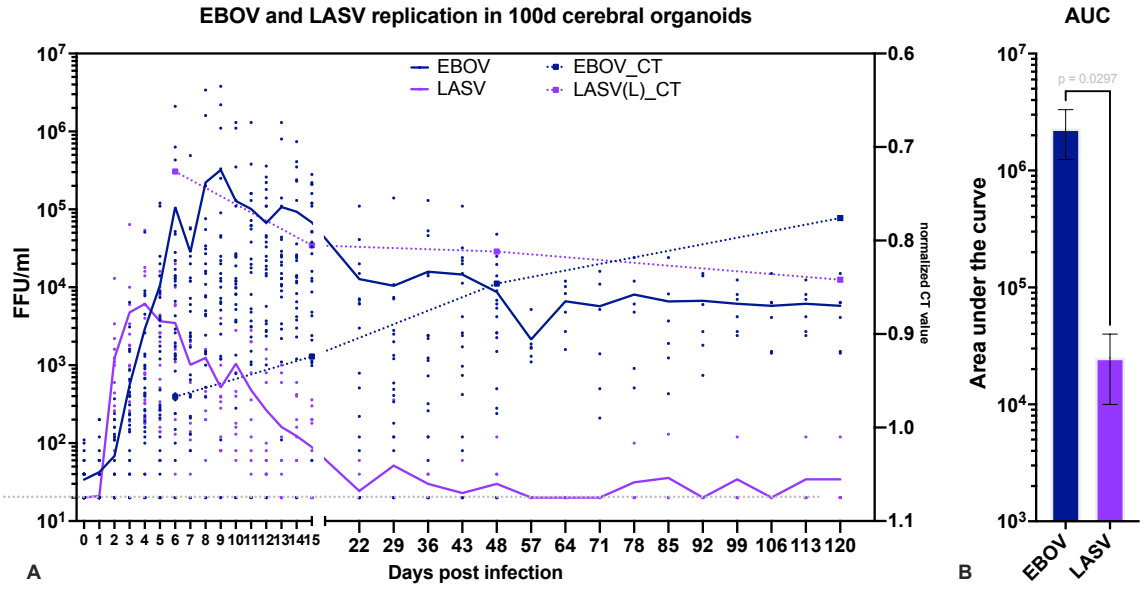


Figure 26: EBOV and LASV kinetics in infected human cerebral organoids. (A) Range of viral titers ([FFU/ml], line through the mean) measured in the supernatant of human cerebral organoids infected with 10^4 FFU of EBOV (blue) or LASV (purple). Group size is at least n=6 ($\geq$48 dpi) with serial sacrifices every other day amounting to a maximum group size of 34 for earlier time points. Organoids originated from two batches and were used in two independent experiments at 100 d post embryoid body generation. Uninfected organoids were removed from the infected group. LOD at 20 FFU/ml indicated as a grey dotted line. Right y-axis: CT values of RNA extracted from the supernatant normalized to the internal positive kit control for each run. Normalized CT-values on 6, 15, 48, and 120 dpi are indicated by large squares in the respective color. The line was plotted through the mean. **(B)** Area under the curve analysis and unpaired, two-tailed Student's T-test performed on EBOV- and LASV-infected cerebral organoid groups.

In contrast to the EBOV CNS persistence profile, LASV replication peaked 4 dpi at approximately 6x10^3 FFU/ml before a steady decline towards the LOD throughout the observed time frame (Figure 26). In general, the peak replication of LASV was approximately 30-fold lower in the supernatant of cerebral organoids when compared to EBOV. Additionally, only one out of seven longitudinal LASV-infected cerebral organoids released a low (120 FFU/ml) amount of infectious LASV particles after 48 dpi (organoid L9). In contrast, LASV RNA was detected in the supernatant of all cerebral organoids throughout the whole experiment, although overall normalized RNA titers decreased over time. Notably, relative amounts of LASV viral RNA in the supernatant were highest amongst both groups 6 dpi but lower than those upon EBOV infection 120 dpi (Figure 26). Taken together, the human cerebral organoid model thereby revealed that EBOV but not LASV can persist in human CNS tissue, releasing infectious particles for at least 120 days.

6.2.1 Persistent EBOV infection is associated with an increase in detected viral RNA versus infectious viral particles.

Mean viral titers in the supernatant of human cerebral organoids, represented as infectious viral particles released into the cerebral organoid supernatant, plateaued after 15 dpi in case of EBOV infection (Figure 26). Opposed to this, there was a steady increase in viral RNA detected in the supernatant towards the later stages of EBOV infection (Figure 26 and Figure 27 (B)). Indeed, when normalizing the viral titers throughout the whole range of 20 FFU/ml to $1x10^7$ FFU/ml (Figure 27 (A)), overall released infectious particles decreased after 6 dpi and remained approximately constant at 48 dpi after infection for EBOV. At the same time, normalized viral RNA (as normalized CT-values) in the cerebral organoid supernatant increased throughout the late stages of infection (Figure 27 (B)), thereby resulting in relatively more viral RNA released per infectious viral particle during persistent stages of cerebral organoid infection with EBOV (Figure 27 (C)). This indicates that viral RNA, which is not contained within an infectious viral particle, was increasingly shed from infected cerebral organoids during viral persistence. Meanwhile, for LASV, viral RNA was detected in the supernatant throughout the whole experimental period with decreasing tendency, although no infectious particles were released.

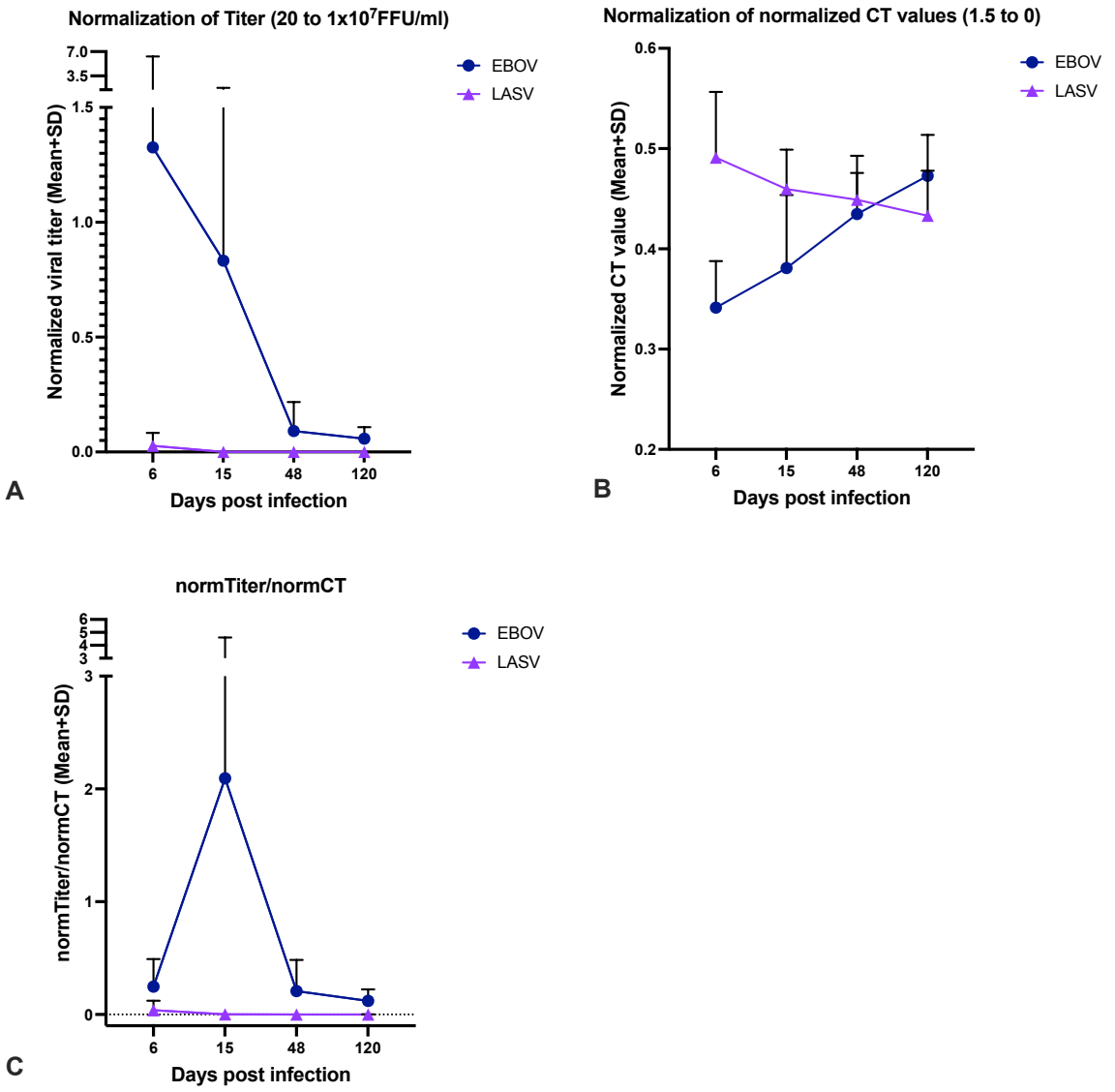


Figure 27: Normalization of viral titers and RNA in infected cerebral organoids. (A) Mean (+SD) viral titers normalized to the overall range of titers 20 FFU/ml to 1x10^7 FFU/ml, **(B)** Mean (+SD) of the reference gene normalized CT values of the viral RNA normalized to their total range of 1.5 to 0, **(C)** Mean (+SD) normalized titers normalized to the viral RNA. EBOV in blue dots and LASV in purple triangles. Group size n=6, respectively.

6.2.2 EBOV defective viral genome species diversity increases in the supernatant of persistently infected cerebral organoids.

The formation of DVG is a well-described persistence mechanism for many viruses. To determine whether the observed increase in non-infectious EBOV RNA species in the supernatant of persistently infected cerebral organoids originated from an accumulation of 5'copy-back DVG, RT-PCR screens [192] for EBOV DVG species diversity were performed on the viral RNA collected from the supernatant. Here, an increase of bands on a gel is indicative of increased species diversity, but not the total quantity of DVG. As shown in Figure 28, an increasingly diverse DVG repertoire was released over time from EBOV and recombinant EBOV-GFP infected human cerebral organoids (described in the following).

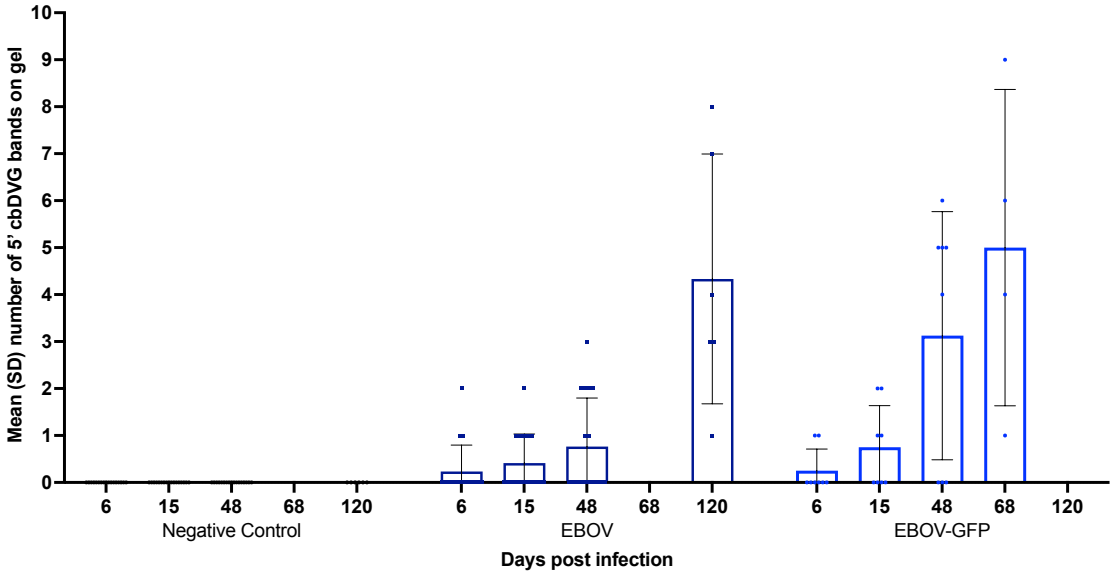


Figure 28: Semiquantification of 5'cbDVGs in EBOV persistence. Mean (SD) 5'cbDVG species detected by RT-PCR measured by the number of bands on a gel in the supernatant of human cerebral organoids infected with EBOV or EBOV-GFP. A minimum of 6 replicates per time point were collected from two organoid batches in the EBOV group and 4 replicates per time point from one batch in the EBOV-GFP group. Day 68 only measured for EBOV-GFP and day 120 only measured for EBOV.

6.2.3 Acute and persistent viral infection in human cerebral organoids translate to different neuroinflammatory cytokine profiles.

To unravel the mechanisms determining acute versus persistent infection in human cerebral organoids, a multiplex cytokine/chemokine assay was performed. Here, the levels of neuroinflammatory markers in the cell culture supernatant of the organoids were measured over a 120 d period, as depicted in Figure 29. Furthermore, AUC calculations were performed to compare total (d0-120), early (d0-15), and late (d15-d120) cytokine/chemokine release from infected and uninfected cerebral organoids.

Although many markers did not significantly change in their concentration upon infection of the organoids, some trends became apparent. Importantly, all organoids including the negative controls seemingly released more cytokines at later stages of the experimental period. Besides this, an increase in proinflammatory interleukin 6 (IL-6) release was uncovered upon EBOV infection 48 dpi during the persistent phase when compared to the negative control, while later time points appeared to follow a similar trend (not significant). Notably, AUC further confirmed overall increased levels of IL-6 (Figure 30 (A)). This trend, especially 85 dpi and 120 dpi, seemed different to the LASV infection where the development in IL-6 release rather resembled the one observed in the negative control following day 48 (Figure 29 (A)). Also significantly increased at 48 dpi was the immune-dysregulation marker soluble triggering receptor expressed on myeloid cells 1 (sTREM-1) upon EBOV infection, while no other conditions appeared distinct in their overall kinetics (Figure 29 (B)). AUC calculations further

followed this trend, whereby sTREM-1 was slightly elevated throughout. Meanwhile, the proinflammatory and chemotactic CCL-2 (Figure 29 (C)) was significantly elevated during acute (6 –15 dpi) infection with LASV as compared to all other conditions. More precisely, CCL-2 levels upon LASV infection in cerebral organoids were higher 6 dpi and 15 dpi in comparison to the negative control as well as 6 dpi in EBOV. At 15 dpi, there was no substantial difference between EBOV and LASV infection anymore, in fact, levels of CCL-2 were also elevated in EBOV compared to the negative control. Notably, AUC of total and early CCL-2 levels confirmed a trend towards elevated CCL-2 upon LASV infection, whereby this distinction appeared mostly in the early group (Figure 30 (C)). CCL-2 levels remained relatively high in all conditions at later stages of the experiment, including the negative control.

A minor trend in elevated inflammation upon persistence with EBOV was further noted with the C-X3-C motif ligand 1 (CX3CL1) release 48 –85 dpi (Figure 29 (E)). Total AUC calculations furthermore imply a slightly higher CX3CL1 release in EBOV-infected cerebral organoids in particular compared to the LASV group (Figure 30 (E)). This was however not significant.

Proinflammatory interleukin 18 (IL-18), a cytokine released upon neurodegeneration, was mostly released early upon LASV infection, as shown via the AUC calculation of the early timepoints (Figure 30 (F)). Indeed, levels of the cytokines were significantly elevated 6 –15 dpi in LASV infection compared to the negative control. Longitudinally, IL-18 was lowest upon LASV infection. Indeed, as per AUC calculation, overall IL-18 release in the LASV-infected group was comparable to the negative control. At the same time EBOV infected organoids seemingly released slightly elevated levels of IL-18 48 –85 dpi in comparison to LASV infected organoids. However, this was not statistically significant and only minorly observable in the late AUC stratification.

Neuroprotective brain-derived neurotropic factor (BDNF) largely accumulated over time in the negative control and in the supernatant of LASV infected organoids (Figure 29 (G)). In fact, BDNF was already substantially increased 15 dpi after LASV challenge in comparison to the negative control. The AUC calculating of early time points supports this finding, whereby BDNF released upon LASV infection d0-15 was accumulated highest (Figure 30 (G)). Meanwhile, persistent viral infection with EBOV led to a significant decrease of the neurogenesis marker 120 dpi, whereby the trend was already observable 85 dpi. In contrast, neurogenesis marker bNGF, depicted in Figure 29 H, did not confirm the trend. Indeed, bNGF was significantly elevated in the negative controls 85 dpi in comparison to both, EBOV and LASV infection, and seemed overall robustly increased between 15 dpi and 120 dpi. This trend was confirmed by AUC calculations, particularly in the late stratification d15–d120 (Figure 30 (H)).

In conclusion, the neuroinflammatory cytokine profiles of the long-term infected human cerebral organoids accumulated in distinct cumulative trends in the more acute infection with LASV, where viral release reduced from 4 dpi onwards (Figure 26). LASV infection manifested

itself with an earlier proinflammatory cytokine response in some markers, consisting of major players IL-18 and CCL-2. In contrast, persistent viral infection with EBOV was embodied by trends towards elevated levels of IL-6, IL-18, sTREM-1, or CX3CL1 during late stages of infection 48 dpi to 120 dpi.

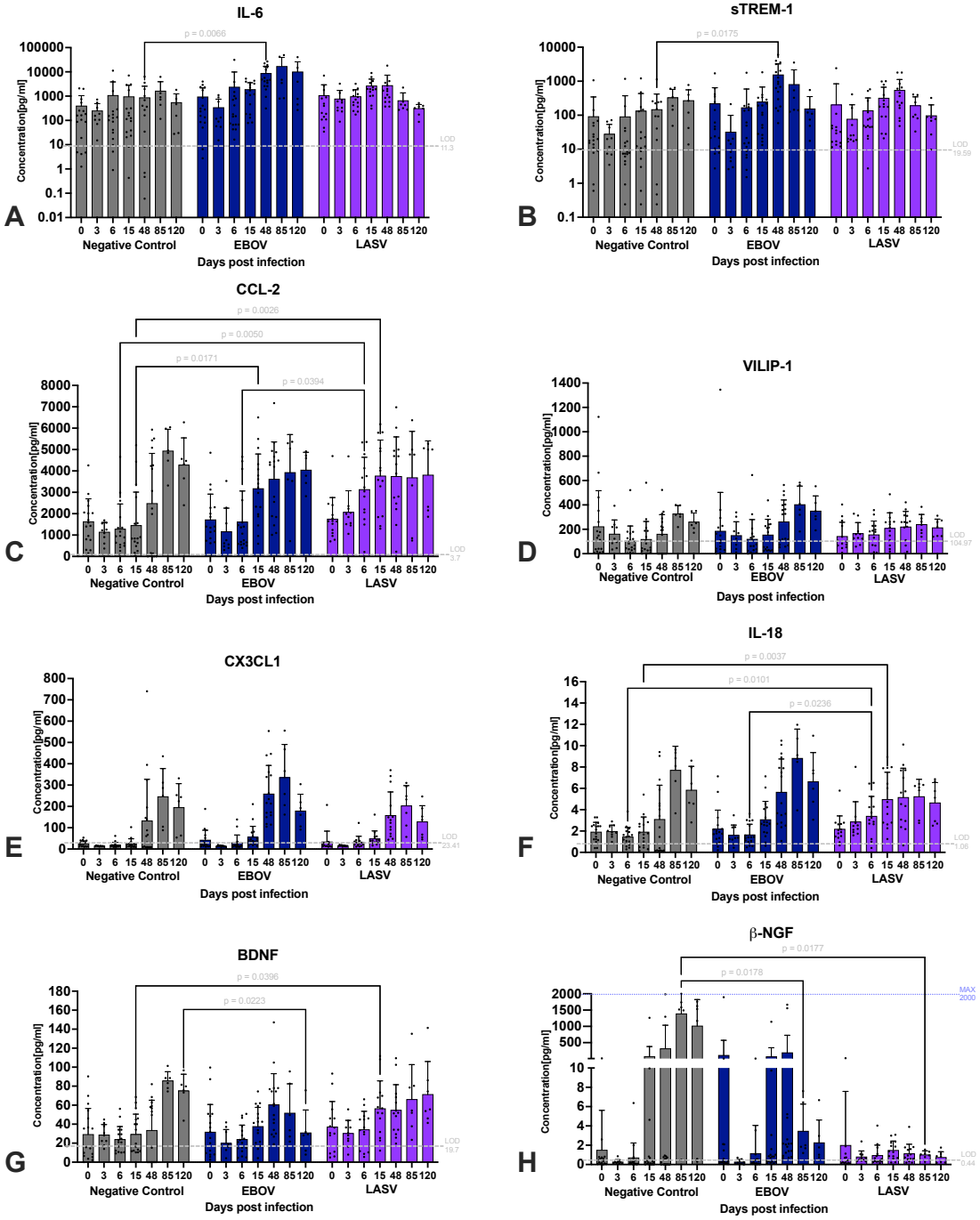


Figure 29: Cytokine/chemokine kinetics in the supernatant of infected human cerebral organoids. Mean (+SD) cytokine/chemokine levels [pg/ml] in the supernatant of EBOV (blue), or LASV (purple) infected human cerebral organoids before infection and at 3, 6, 15, 48, 85, or 120 days in comparison to the negative control (grey). At least n=6 organoids originating from two independent organoid batches and experiments per time point per group. Mixed-effects model with Tukey's multiple comparisons with significant differences ($p \leq 0.05$) indicated by brackets. Uninfected samples were removed from the group. LOD is indicated as a grey dotted line as marking the higher limit of either of the measurements. **(A)** Interleukin 6 (IL-6), **(B)** soluble triggering receptor expressed on myeloid cells 1 (sTREM-1), **(C)** monocyte chemoattractant protein 1 (MCP-1, CCL2), **(D)** visinin-like protein 1 (VILIP-1), **(E)** fractalkine, C-X3-C motif chemokine ligand 1 (CX3CL1), **(F)** interleukin 18 (IL-18), **(G)** brain-derived neurotropic factor (BDNF) and **(H)** β nerve growth factor (β-NGF).

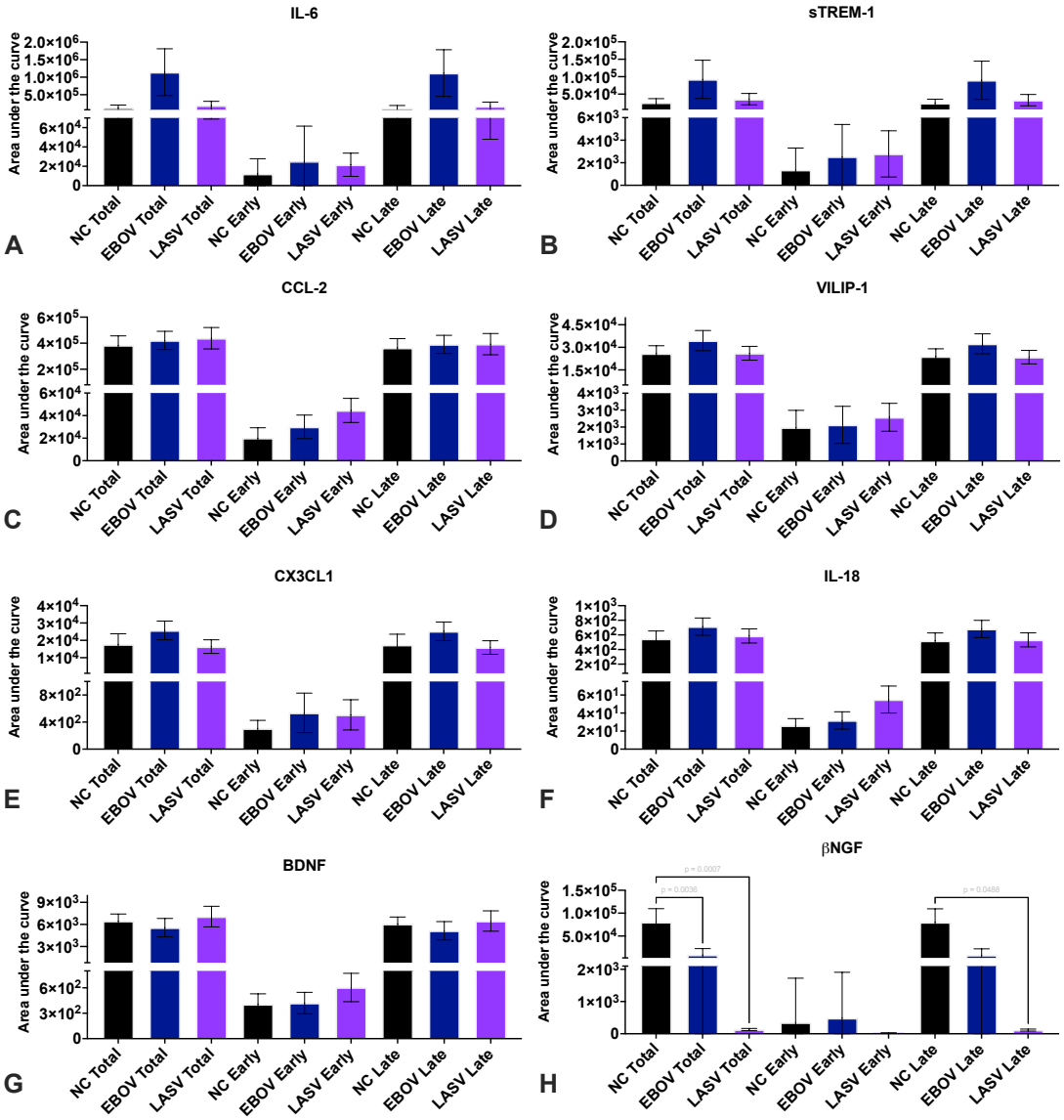


Figure 30: AUC for cytokines/chemokines in the supernatant of infected human cerebral organoids. Area under the curve (AUC) calculations for the total (d0-120), early (d0-15), and late (d15-120) cytokine/chemokine levels in the supernatant of EBOV (blue) or LASV (purple) infected human cerebral organoids in comparison to the negative control (black). At least n=6 organoids originating from two independent organoid batches and experiments per time point per group. Statistical analysis via AUC generation and subsequent one-way ANOVA with Sidak's Multiple Comparisons correction. Significant pairings are reported. **(A)** Interleukin 6 (IL-6), **(B)** soluble triggering receptor expressed on myeloid cells 1 (sTREM-1), **(C)** monocyte chemoattractant protein 1 (MCP-1, CCL2), **(D)** visinin-like protein 1 (VILIP-1), **(E)** fractalkine, C-X3-C motif chemokine ligand 1 (CX3CL1), **(F)** interleukin 18 (IL-18), **(G)** brain-derived neurotropic factor (BDNF) and **(H)** β nerve growth factor (β-NGF).

6.2.4 EBOV infects diverse CNS cell subsets at different stages in human cerebral organoids.

To determine the infection landscape of EBOV and LASV throughout the different stages of infection in CNS tissue, immunohistochemistry staining was performed using paraffin sections of human cerebral organoids after 6 d, 15 d, 48 d, or 120 d of infection (HE stainings of 120 dpi organoids of the uninfected control, EBOV 120 dpi and LASV 120 dpi organoids can be found in the appendix Figure 81).

For EBOV infected organoids, EBOV NP was detected throughout the observed period, where the virus was found in the outer layers of the organoid during the early acute phase until day 15. Here, mostly NeuN$^+$ mature neurons were located (Figure 31, A). From 15 d.p.i, CD68$^+$ microglia seemingly accumulated in the areas of infection (Figure 31, B). With time, the EBOV NP expression was detected in deeper layers of the cerebral organoid. As before, NeuN$^+$ mature neurons remained to be a target of infection. In addition, larger patches of glial fibrillary acidic protein (GFAP)$^+$ astrocytes were positive for EBOV NP at 48 dpi (Figure 31, C).

At 120 dpi, the latest time point acquired, EBOV NP was detected throughout all cerebral organoids, although some layers were seemingly preferably infected (Figure 32). Interestingly, the previously observed accumulation of CD68$^+$ microglia was not observed at this later time point. Evidence for infection of GFAP$^+$ astrocytes, as well as NeuN$^+$/Map2$^+$ neurons, was furthermore uncovered, confirming the overall broad spectrum of target cells of EBOV even at late stages of infection.

In pronounced contrast to EBOV infection at 6 dpi, LASV-infected human cerebral organoids displayed the highest levels of LASV NP-positive areas at this early time point (Figure 33 (A)). Here, particularly areas with many NeuN$^+$ mature neurons and GFAP$^+$ astrocytes were affected by the infection. As seen for EBOV infection, at 15 dpi in LASV-infected organoids, CD68$^+$ microglia increasingly accumulated in areas infected with LASV (Figure 33 (B)). In comparison to 6 dpi, no increase in LASV NP expression was detected at the later time point, in fact at 48 dpi only small areas were positive. Here, astrocytes were further observed in proximity to the infection (Figure 33 (C)).

Finally, in LASV-infected human cerebral organoids, 120 dpi, LASV NP was predominantly detectable in limited amounts at a distance to the surface of the respective organoid. As depicted in Figure 34, particularly NeuN$^+$ areas with many mature, projecting neurons appeared to be located in proximity to the areas positive for LASV antigen. Here, CPE was furthermore present. In the case of cerebral organoid L9, which still released infectious particles after 48 dpi (Figure 26), LASV NP was additionally detected at outer areas (Figure 34).

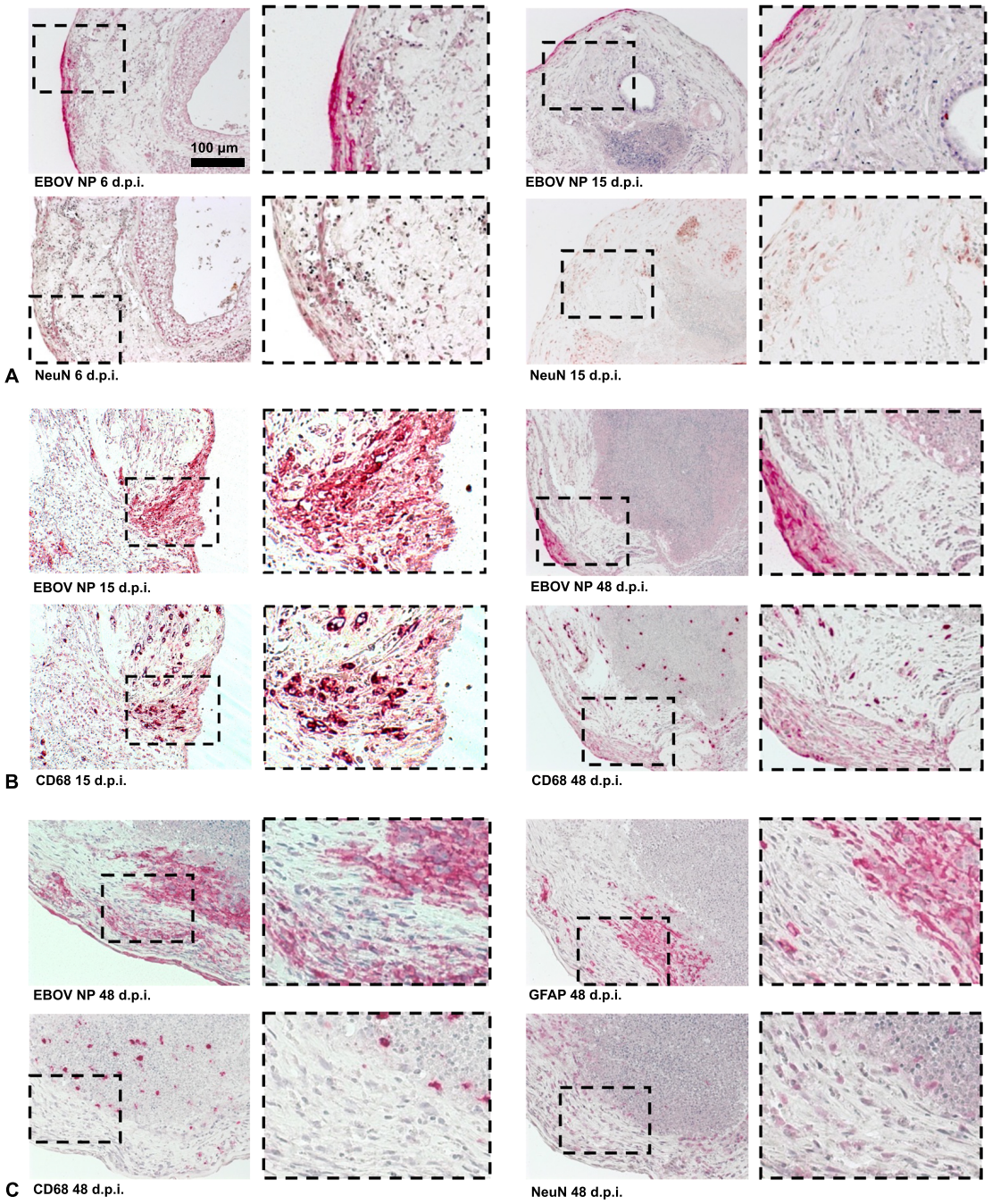


Figure 31: Immunohistochemistry staining of EBOV in cerebral organoids. (A) Cerebral organoids infected for 6 days (left) or 15 days (right) and the respective staining for EBOV NP and neurons (NeuN) in the consecutive section. **(B)** EBOV-infected cerebral organoids 15 days (left) or 48 days (right) after infection with the respective staining of EBOV NP and microglia (CD68) in the consecutive section. **(C)** EBOV-infected cerebral organoid 48 days after infection stained for EBOV NP (red), astrocytes (GFAP, red), microglia (CD68, red), and mature neurons (NeuN, red/brown) in serial sections. The scale bar indicates 100 µm, and the zoomed-in area is indicated by the black rectangle.

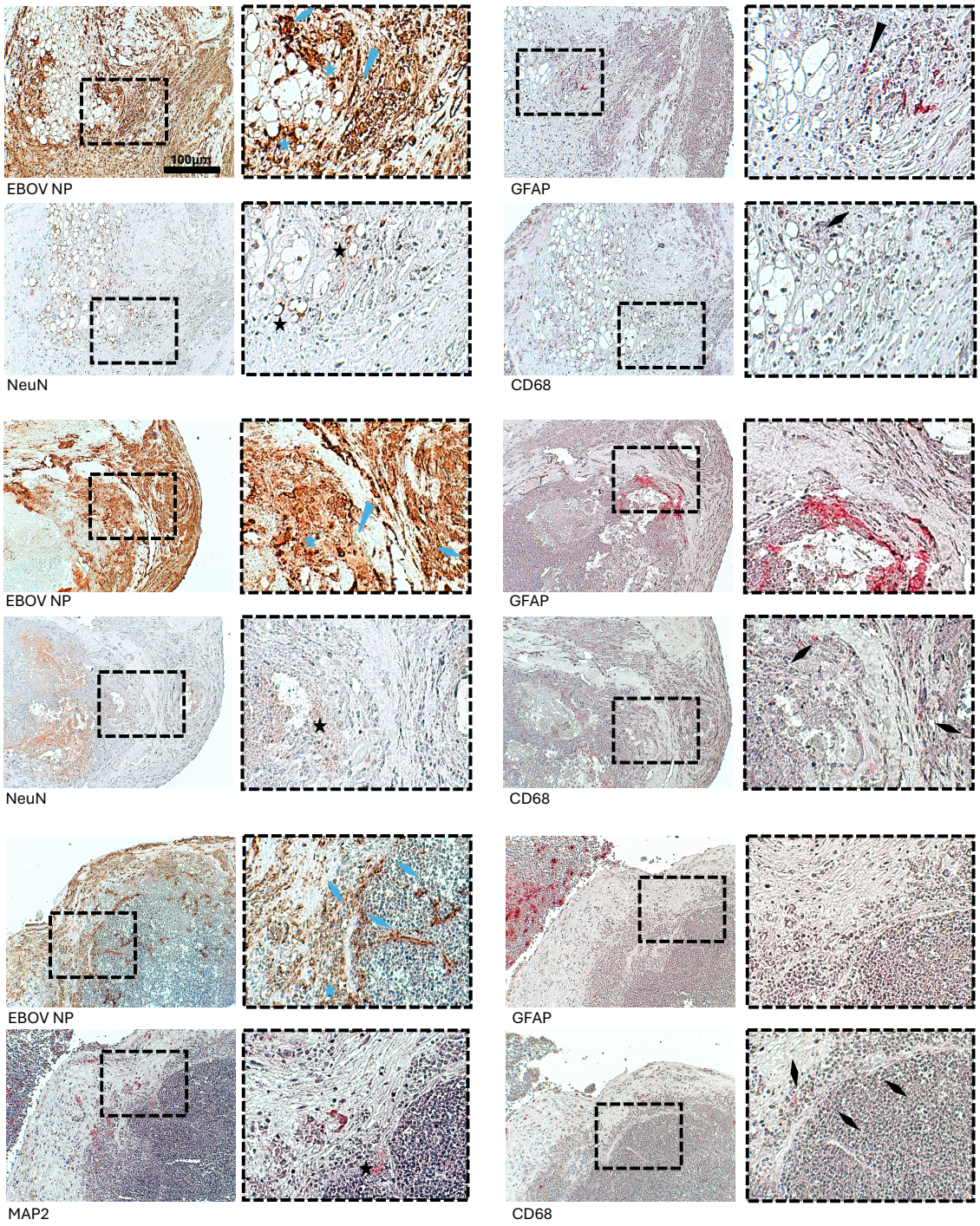


Figure 32: Immunohistochemistry staining of EBOV-infected cerebral organoids 120dpi. Immunohistochemistry staining of three representative human cerebral organoids that were infected for 120 days with EBOV. Staining for the EBOV nucleoprotein (NP, brown), astrocytes (GFAP, triangle, red), neurons (NeuN/Map2, star, red), or microglia (CD68, diamond, red) in the consecutive sections. The scale bar indicates 100 µm, and the zoomed-in area is indicated by the black rectangle.

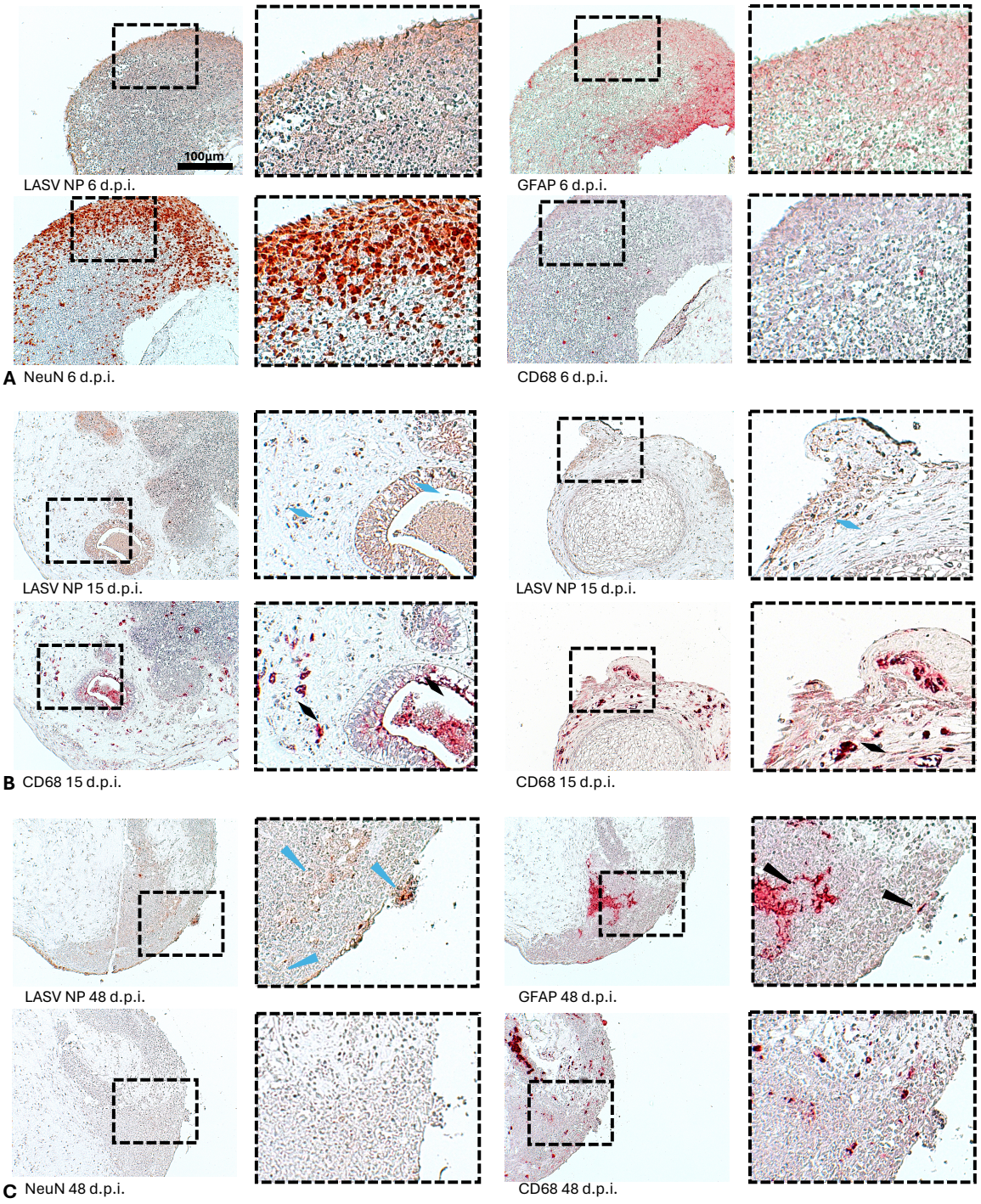


Figure 33: Immunohistochemistry staining of LASV in cerebral organoids. Cerebral organoids infected for **(A)** 6 days, **(B)** 15 days, or **(C)** 48 days with LASV. Staining for LASV NP as well as astrocytes (GFAP, red), mature neurons (NeuN, brown), and microglia (CD68, red) in consecutive sections. The scale bar indicates 100 µm, and the zoomed-in area is indicated by the black rectangle.

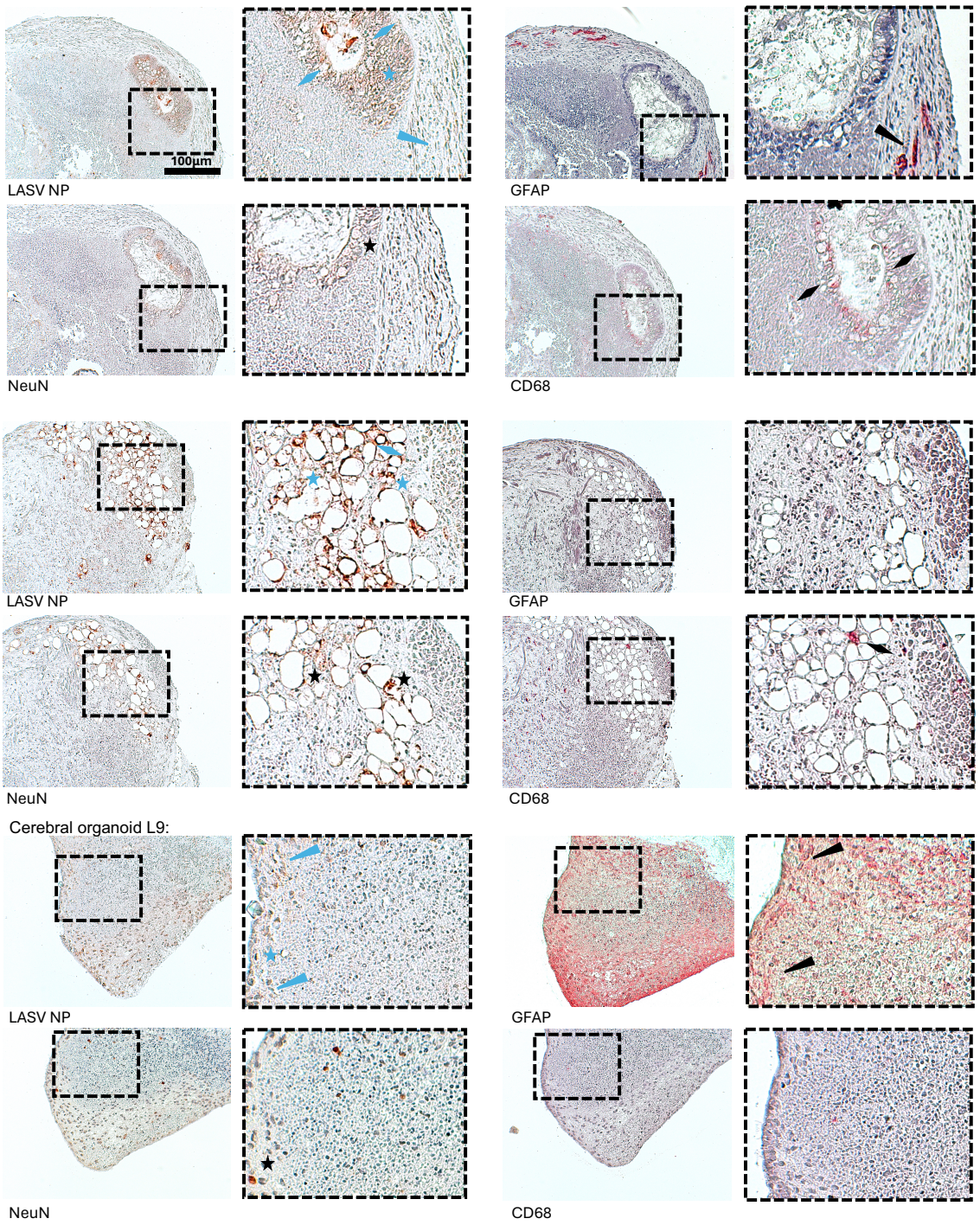


Figure 34: Immunohistochemistry staining of LASV-infected cerebral organoids 120dpi. Immunohistochemistry staining of three representative human cerebral organoids that were infected for 120 days with LASV. Staining for the LASV nucleoprotein (NP, brown), astrocytes (GFAP, triangle, red), neurons (NeuN/Map2, star, red), or microglia (CD68, diamond, red) in the consecutive sections. The scale bar indicates 100 µm, and the zoomed-in area is indicated by the black rectangle. Cerebral organoid L9 is highlighted as the one releasing infectious viral particles after 48 dpi.

6.2.5 Establishment of cerebral organoid persistence is conserved across orthoebolaviruses.

To determine whether EBOV persistence was a feature shared by other orthoebolaviruses, the infection profiles of EBOV and RESTV were compared in human cerebral organoids. To visualize and compare the courses of infection, we utilized recombinant versions of EBOV and RESTV expressing GFP. Again, persistence with the release of infectious particles occurred for both recombinant orthoebolaviruses in the majority of infected organoids (Figure 35). However, in both groups, some organoids were negative for infectious particles in the supernatant 68 dpi and possibly cleared the infection (Figure 35 (B)). Nevertheless, persistence was established in more than 50 % of either group.

When comparing the recombinant counterparts of EBOV and RESTV, RESTV-GFP displayed a reduced capacity for infection as well as a timely delay in comparison to EBOV-GFP (Figure 35 (A)). Strikingly, mean RESTV-GFP titers were approximately 10-100 fold lower than EBOV-GFP titers throughout (Figure 35 (B)), replicating lowly at <100 FFU/ml at 62 –68 dpi. Besides this, both recombinant viruses initially ceased to replicate 7-9 dpi, which was not observed in the wild-type EBOV infection (Figure 26).

It must be noted that to confirm these findings, a repetition in another batch is necessary. Nevertheless, it may overall be surmised that in the human cerebral organoid model, diverse (recombinant) orthoebolaviruses persistently replicate for several months. Additionally, it was found that although RESTV-GFP might inhabit reduced replicative capacity in CNS tissue, the recombinant virus is still capable of establishing persistence.

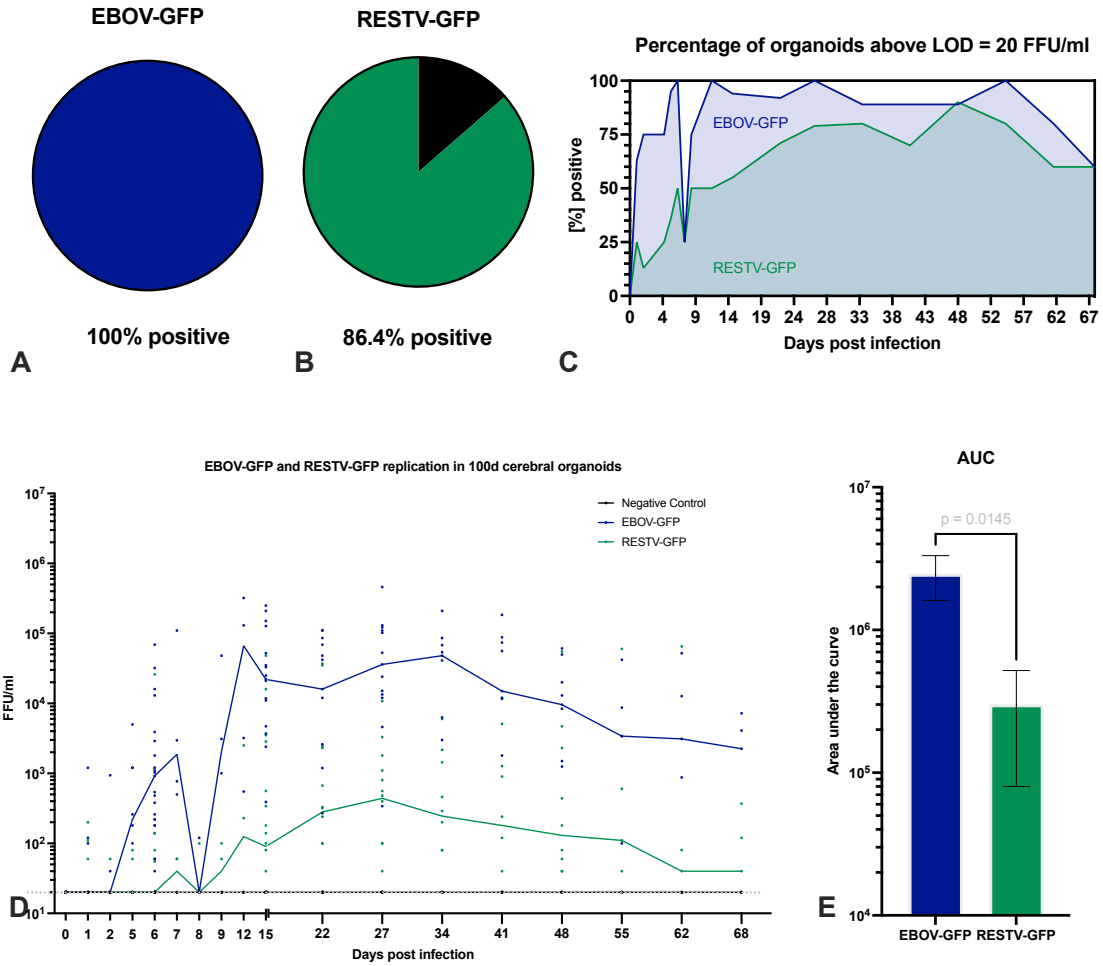


Figure 35: EBOV-GFP and RESTV-GFP kinetics in infected human cerebral organoids. Percentages of organoids per group that reach the LOD=20 FFU/ml at one point during the experimental time frame. EBOV-GFP (blue) **(A)** or RESTV-GFP (green) **(B)**. **(C)** Percentage of organoids with a viral titer above the LOD at the respective time point. **(D)** Range of viral titers ([FFU/ml], line through the mean) measured in the supernatant of human cerebral organoids infected with 10^4 FFU of recombinant EBOV-GFP (blue) or RESTV-GFP (green) for 68 days. Group size is at least n=5 ($\geq$48 dpi) with serial sacrifices every other day amounting to a maximum group size of 22 for earlier time points. Organoids originated from one batch and were used 100d post embryoid body generation. Uninfected organoids were removed from the infected group. LOD at 20 FFU/ml indicated as a grey dotted line. **(E)** Area under the curve calculation and unpaired, two-tailed Student's T-test comparing EBOV-GFP and RESTV-GFP.

Besides the observation of viral kinetics throughout the experimental time frame, immunofluorescence microscopy staining of human cerebral organoids infected with recombinant orthoebolaviruses was performed to elucidate the target cells of the infection. Here, infected organoids were harvested at different time points post-infection (6, 15, 27, 48, or 68 days). As shown in Figure 36 and Figure 37, EBOV-GFP and RESTV-GFP infection, as for wild-type EBOV, spread from the outer layers towards the inner layers over time. Here, early RESTV-GFP infection was only detected 15 dpi onwards, while first EBOV-GFP positive spots were detected as early as 6 dpi. Staining for astrocytes ($GFAP^+$) (Figure 36) further revealed the presence in proximity to and possibly infection of the cells 48 dpi with EBOV-GFP and 68 dpi with RESTV-GFP. Notably, immunofluorescence microscopy of EBOV-GFP-infected

human cerebral organoids 68 dpi revealed low GFP expression and overall smaller organoids which presented with a more pronounced CPE. This was not the case for the previously shown EBOV infection.

Besides staining astrocytes, microglia ($CX3CR1^{+}$) (Figure 37) were detected in proximity to a large infection herd with EBOV-GFP 15 dpi as well as 27 dpi in the case of RESTV-GFP infection. This confirms observations made with EBOV wild-type infection, where $CD68^{+}$ staining of microglia had revealed a migration of these innate immune cells towards areas of viral gene expression.

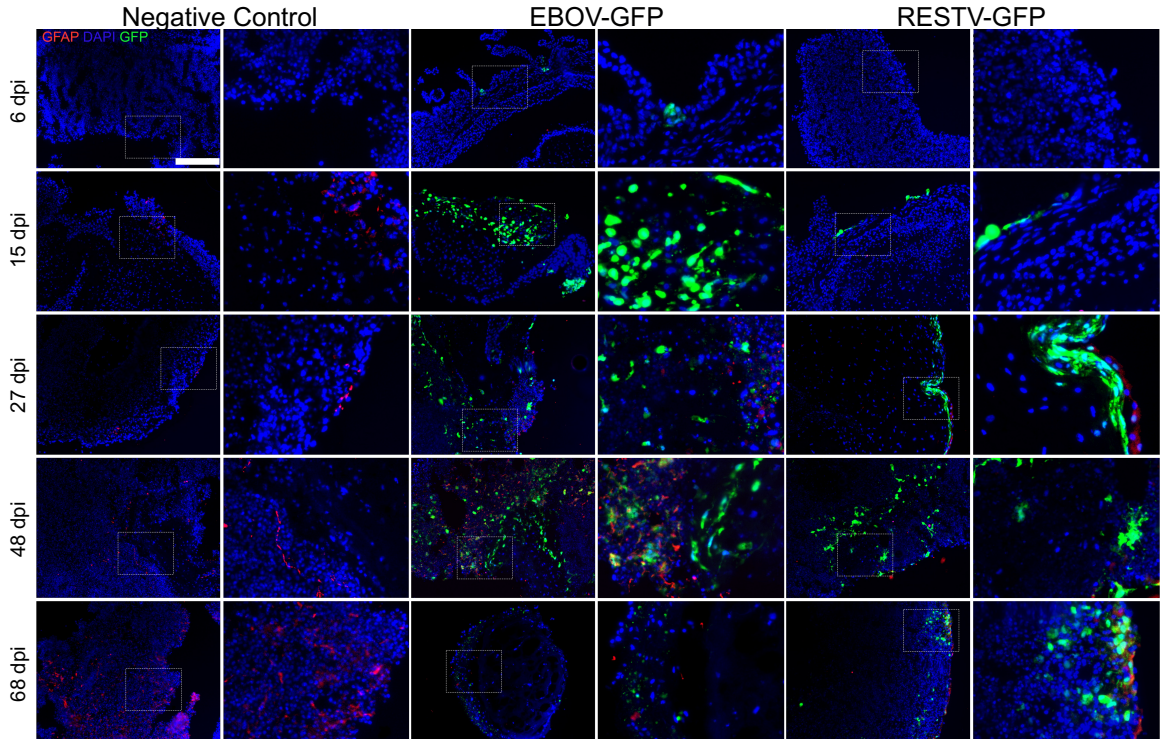


Figure 36: Immunofluorescence microscopy of EBOV-GFP and RESTV-GFP-infected human cerebral organoids: GFAP staining. Representative immunofluorescence microscopy images of human cerebral organoids infected with EBOV-GFP or RESTV-GFP for the indicated time frame (left). Staining for astrocyte marker GFAP (red) and counterstaining of nuclei using DAPI (blue). GFP (green) expression is indicative of viral gene expression. Images taken at 10X magnification. The scale bar indicates 100 µm.

To summarize the most important observations of the aforementioned results, the partially immunocompetent human cerebral organoid model was established and revealed that EBOV can persistently replicate in CNS tissue. This stands in contrast with LASV which ceased to be released from infected organoids at later stages, although RNA and viral protein remained detectable. For EBOV, late-stage infection was associated with an accumulation of viral RNA but not infectious particles. Generally, the long-term infection of the organoids with EBOV tended to translate to late neuroinflammation, while for LASV a neuroinflammatory response initiated earlier for some analytes. Finally, EBOV targeted astrocytes and neurons in the cerebral organoids. Meanwhile, $CD68^{+}$ microglia accumulated at the site of infection from

15 dpi onwards. The potential to establish persistence was overall conserved across different (recombinant) orthoebolaviruses.

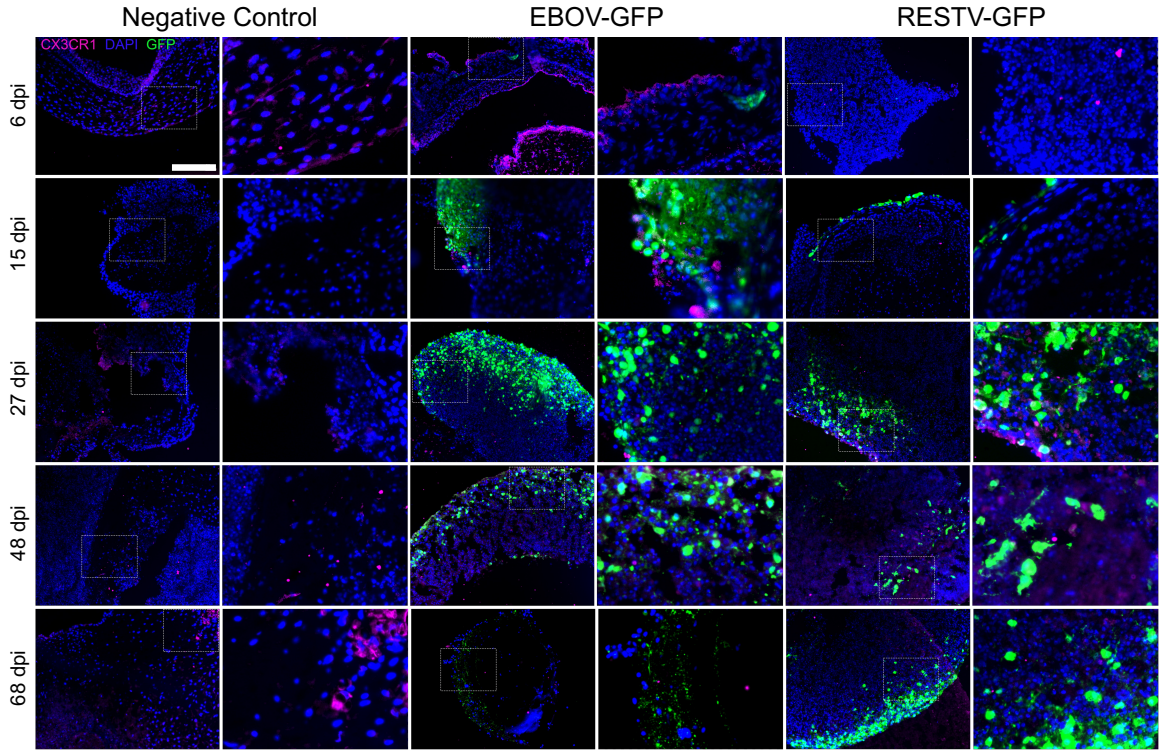


Figure 37: Immunofluorescence microscopy of EBOV-GFP and RESTV-GFP-infected human cerebral organoids: CX3CR1 staining. Representative immunofluorescence microscopy images of human cerebral organoids infected with EBOV-GFP or RESTV-GFP for the indicated time frame (left). Staining for microglia marker CX3CR1 (magenta) and counterstaining of nuclei via DAPI (blue). GFP (green) expression is indicative of viral gene expression. Images taken at 10X magnification. The scale bar indicates 100 µm.

6.3 Exploration of 2D cell culture models to achieve long-term infection with Ebola virus.

As a second objective, this study aims to characterize the state of persistent EBOV replication in CNS cells and thereby develop a hypothesis for the mechanism of EBOV persistence. To this end, 2D cell culture models, namely MDMi and immortalized human microglia and astrocytes were used in viral kinetics studies to determine their suitability as downstream models for EBOV persistence.

6.3.1 EBOV replicates in primary monocyte-derived microglia

Microglia are important players of innate immunity in the CNS and a suggested reservoir of EBOV during viral persistence [183, 189]. Hence, the capability of EBOV to infect human microglia was studied in primary MDMi.

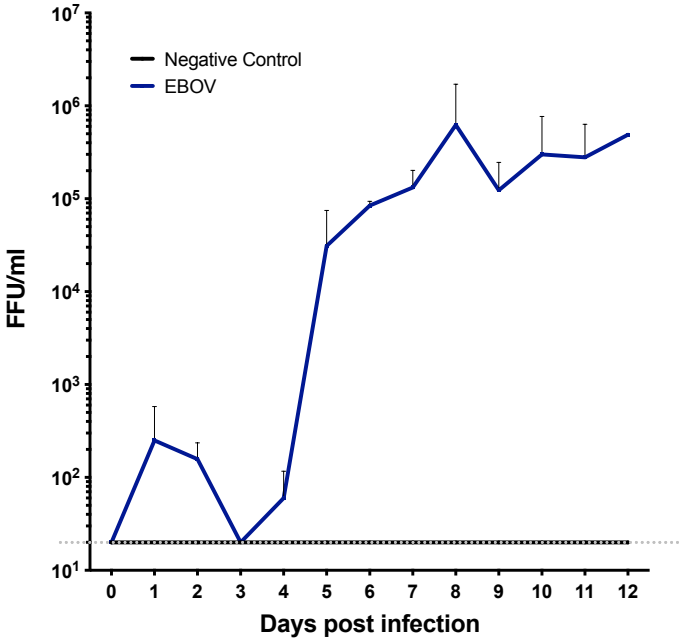


Figure 38: Multicycle-replication assay of EBOV in MDMi. Human primary monocyte-derived microglia infected with EBOV (blue) at MOI=10 and sampled daily. N=4 independent replicates over a 12 d period with mean + SD plotted. LOD at 20 FFU/ml indicated as a grey dotted line.

Two weeks after the generation of MDMi, the primary cells were infected with EBOV (MOI=10). Here, a high MOI was chosen given the fact that primary cells in general require a higher MOI for a productive infection [174, 255]. Figure 38 depicts how EBOV replicated in MDMi, peaking and subsequently plateauing at roughly 8–9 dpi at 10^5–10^6 FFU/ml without being cleared before the longitudinal time point 12 dpi. Notably, after 12 days, the quality of the culture in the negative control group decreased, thus limiting the queried time frame of the infection further. Therefore, immortalized cells were thereafter explored.

6.3.2 EBOV and LASV productively infect immortalized microglia, astrocytes, and neuroblastoma cells.

While the findings in the cerebral organoid model indicated a very broad range of targets of EBOV in the context of CNS infection and persistence, the potential of immortalized human cell lines to reproduce these findings was queried for future mechanistic studies. Thus, to gather whether EBOV, LASV, EBOV-GFP, and RESTV-GFP establish a productive infection in the hereafter used cells, they were used to infect immortalized human microglia, astrocytes, and neuroblastoma cells (MOI=0.1 for wild-type, MOI=1 for recombinant viruses, n=4) in an initial screening experiment. As depicted in Figure 39, all explored viruses replicated 5 dpi in either cell type.

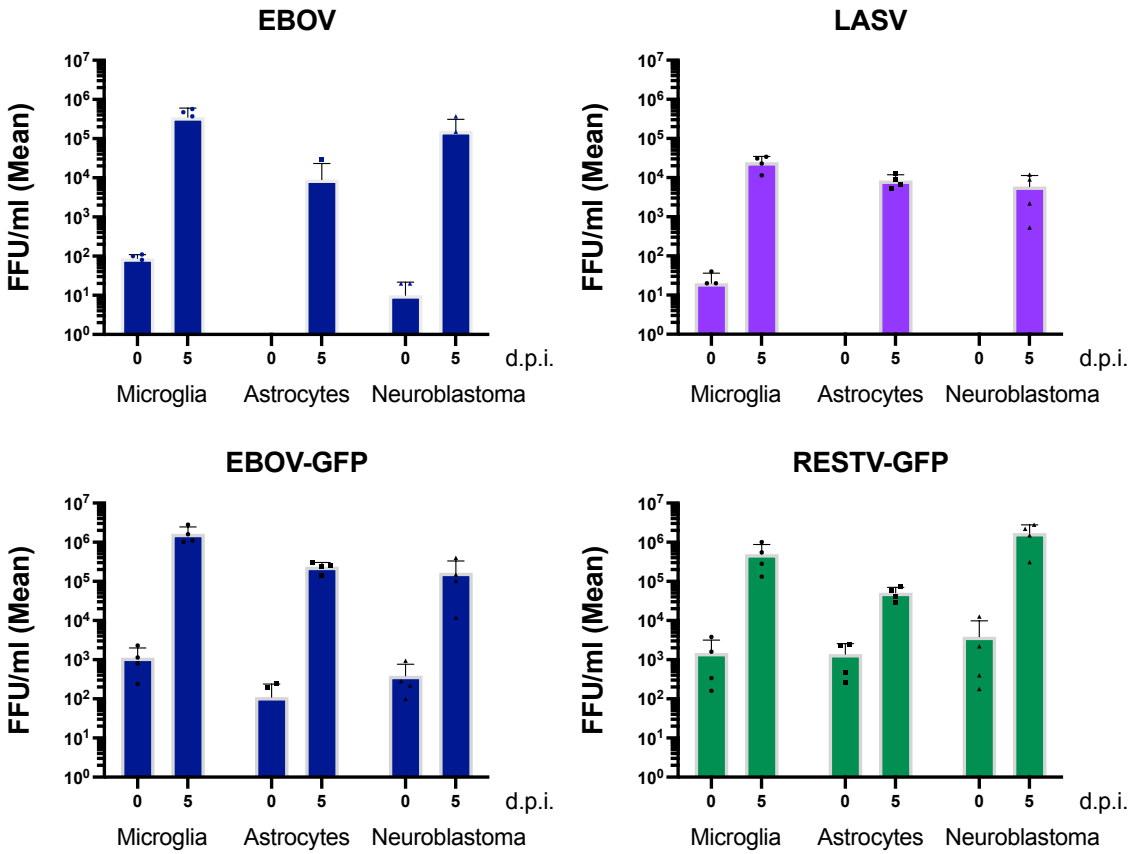


Figure 39: Infection of immortalized human cells with EBOV, LASV, EBOV-GFP, and RESTV-GFP. Explorative infection and results of an immunofocus assay for the titration of the viruses in microglia, astrocytes, and neuroblastoma cells after 5 days. Viruses used: EBOV (MOI=0.1), LASV (MOI=0.1), EBOV-GFP (MOI=1), or RESTV-GFP (MOI=1). LOD at 20 FFU/ml.

6.3.3 EBOV establishes a long-term infection in immortalized microglia and astrocytes.

Considering that microglia and astrocytes were involved in the late stages of cerebral organoid infection as well as possible reservoirs in previously published NHP studies [189], they were used in downstream long-term infection experiments. Consequently, an MRA of EBOV and LASV was carried out in immortalized human microglia, astrocytes, Huh7 or VeroE6 cells at three different MOI – 0.1, 0.01, 0.001 – to measure their replication over time and delineate putative viral load-dependent effects for future experiments. Of note, VeroE6 and Huh7 cells were used as control cell lines as VeroE6 are interferon-incompetent NHP cells that were used to amplify the viruses, and Huh7 cells, as human hepatoma cells with functional type I and II signaling [256], are commonly used to model EBOV infections.

As shown in Figure 40, both viruses established a productive infection in all cell types at least at one of the used MOI. Regarding EBOV, the lowest MOI=0.001 tested led to replication in all cell types except astrocytes, cautiously suggesting a lower susceptibility to EBOV infection of astrocytes (Figure 40, G) in comparison to VeroE6, Huh7 cells and microglia (Figure 40, A, C, E). Regarding the capacity for the establishment of persistence in the sense of maintaining replication for 25 days, no substantial viral load-dependent differences could be detected in microglia or VeroE6 cells. Both higher MOI (0.1, 0.01) showed a comparable profile. Notably, while EBOV replication plateaued in both lower MOI in microglia from 12 dpi onwards, an increase was observed 25 dpi in the highest MOI, hinting to a wave-like pattern. In Huh7 cells (Figure 40, C), the lower MOI resulted in a later peak. Overall, in all cell types at 25 dpi, there was a high EBOV titer detectable (mean $>10^4$ FFU/ml), highlighting the capacity of the virus to sustain for long times in diverse cell culture models.

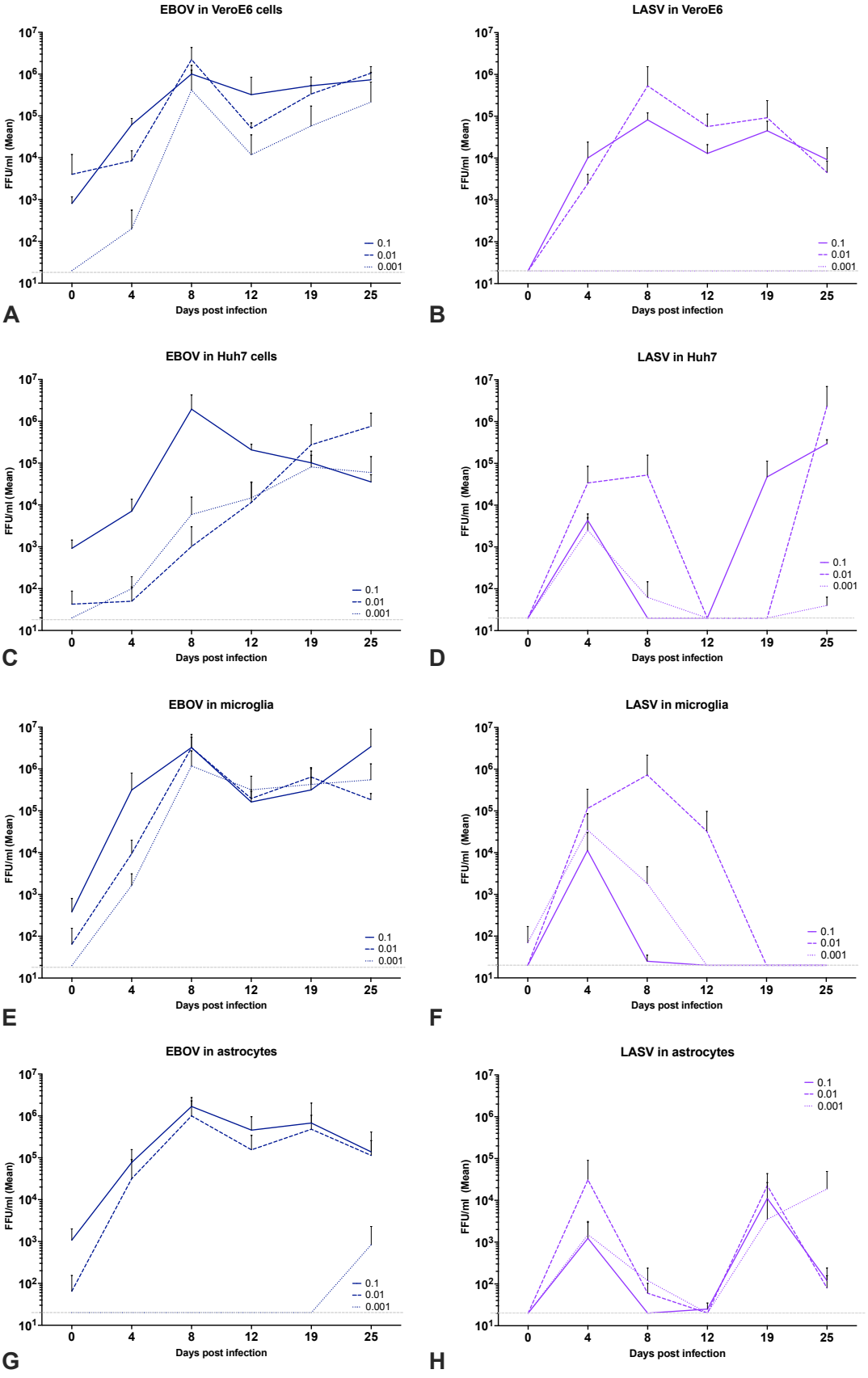


Figure 40: Multicycle-replication assay at different MOI of EBOV and LASV in VeroE6 cells, Huh7 cells, microglia and astrocytes. VeroE6, Huh7, microglia and astrocytes infected with EBOV (blue) or LASV (purple) at MOI=0.1 (line), MOI=0.01 (dashed line), or MOI=0.001 (dotted line) and sampled every 4 days until day 13 and weekly afterward at 19 dpi and 25 dpi (n=4 replicates). Mean virus titer (FFU/ml + SD). LOD at 20 FFU/ml indicated as a grey dotted line. **(A)** VeroE6 + EBOV, **(B)** VeroE6 + LASV, **(C)** Huh7 + EBOV, **(D)** Huh7 + LASV, **(E)** microglia + EBOV, **(F)** microglia + LASV, **(G)** astrocytes + EBOV, **(H)** astrocytes + LASV.

Upon infection with LASV, only the highest two MOI, namely MOI=0.1, MOI=0.01, consistently resulted in a productive infection, with MOI=0.001 not causing a productive infection in any of the replicates of VeroE6 infected cells (Figure 40 (B)). Otherwise, there was no viral load-dependent change in overall replicative behavior in LASV infected groups, whereby differences arose in the amplitude and timely delay of the curves. Notably, here the medium MOI=0.01 seemed to cause the highest maximum titers in all cell lines. In VeroE6 cells, LASV replication plateaued after the initial peak of infection and sustained high titers until 25 dpi as seen in the EBOV infected VeroE6 cells (Figure 40 A, B, C). In contrast to EBOV, LASV was cleared from the supernatant of microglia at all MOI, where it took longest for the medium MOI=0.01 which also established the highest titers (Figure 40 (F)). Moreover, in Huh7 cells and astrocytes (Figure 40 D, H), LASV replication viral load-independently led to a wave-like pattern. Here, after an early local maximum in the viral replication, LASV was nearly cleared from the supernatant but re-emerged again, resulting in high viral titers in Huh7 cells at 25 dpi, while astrocytes infected with LASV were in their second local minimum at 25 dpi having peaked at 19 dpi. This overall underlines the differential replication of EBOV in comparison to LASV in these 2D cell culture models.

Viral persistence observation in 2D cultures is limited by the survival of the culture.

To determine factors influencing the establishment and maintenance of viral persistence in 2D cell culture models, immunofluorescence stainings were performed. As depicted in Figure 41, counter-staining of the nuclei revealed that VeroE6 cells remained viable under all conditions irrespective of virus and MOI used during the initial infection. Indeed, this was confirmed by the finding that EBOV and LASV both persistently replicated in these cells for 25 days, given productive infection had initially established. At the same time, Huh7 cells, after 25 days of infection and culturing without passage, presented with similar monolayer confluency in all infected conditions in comparison to the negative control (Figure 41). Notably, both viruses replicated at 25 dpi in Huh7 cells, whereby LASV was at a local maximum of a second replication wave (Figure 40).

In the case of microglia and astrocytes, monolayers were damaged in the negative controls at 25 dpi, presenting with approximately 20 % and 60 % confluency, respectively. Monolayer damage was also observed upon EBOV infection. In LASV infected samples the monolayers of the two highest MOI were almost destroyed in both microglia and astrocytes, whereas the lowest MOI manifested with extensive CPE. No/minimal viral replication was observed in these cell types 25 dpi.

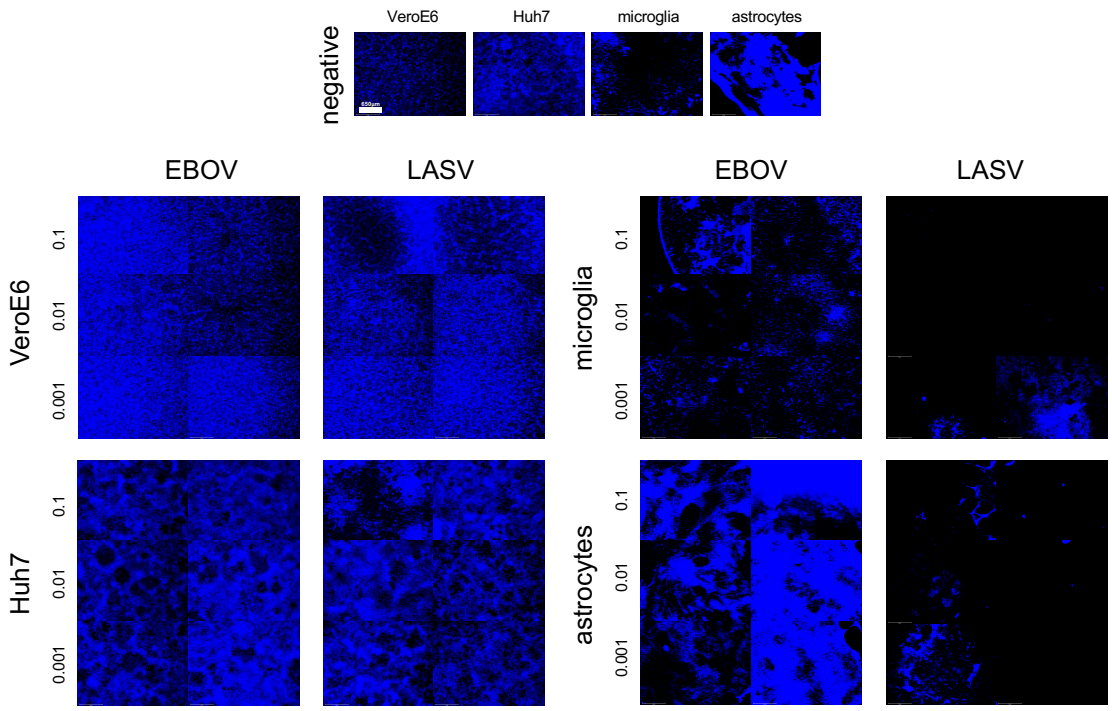


Figure 41: Monolayers of immortalized cells 25dpi with EBOV or LASV. Immunofluorescence microscopy images 25 dpi with EBOV or LASV of VeroE6, Huh7, microglia, and astrocytes stained with DAPI and imaged at 4x magnification. The scale bar indicates 650 µm, n=2 representative replicates each. MOI indicated on the side. Image contrast is maximized for purposes of visualization.

EBOV glycoprotein and nucleoprotein are consistently expressed in persistently infected microglia and astrocytes.

Besides the overall determination of tissue-culture CPE, immunofluorescence microscopy was used to determine the expression of viral proteins in persistently infected immortalized cells. Here, in the case of EBOV infected samples staining for ebolaviral NP and GP was performed, while LASV infected samples were stained for LASV NP or GPC, respectively. Due to extensive CPE in microglia and astrocytes upon LASV infection, no images were retrieved. Meanwhile, in VeroE6 and Huh7 cells, expression of both LASV proteins was confirmed in all three tested MOI 25 dpi (Figure 42, Figure 43).

In EBOV-infected cells, NP and GP expression was present in all MOI upon persistent infection 25 dpi. However, by observation via immunofluorescence microscopy, the levels of protein expression positivity varied amongst cell types and MOI. In VeroE6 cells, EBOV proteins were only sparsely expressed in some cells, as depicted in Figure 42. Meanwhile, in Huh7 cells, protein expression was overall more pronounced (Figure 43). Notably, for all MOI the viral kinetics revealed 25 dpi being a late-stage infection in VeroE6 cells. In contrast, in Huh7 cells in all but the highest MOI with EBOV infection, 25 dpi seemingly captured the peak of replication (Figure 40). This might result in overall increase of protein expression measured via immunofluorescence microscopy.

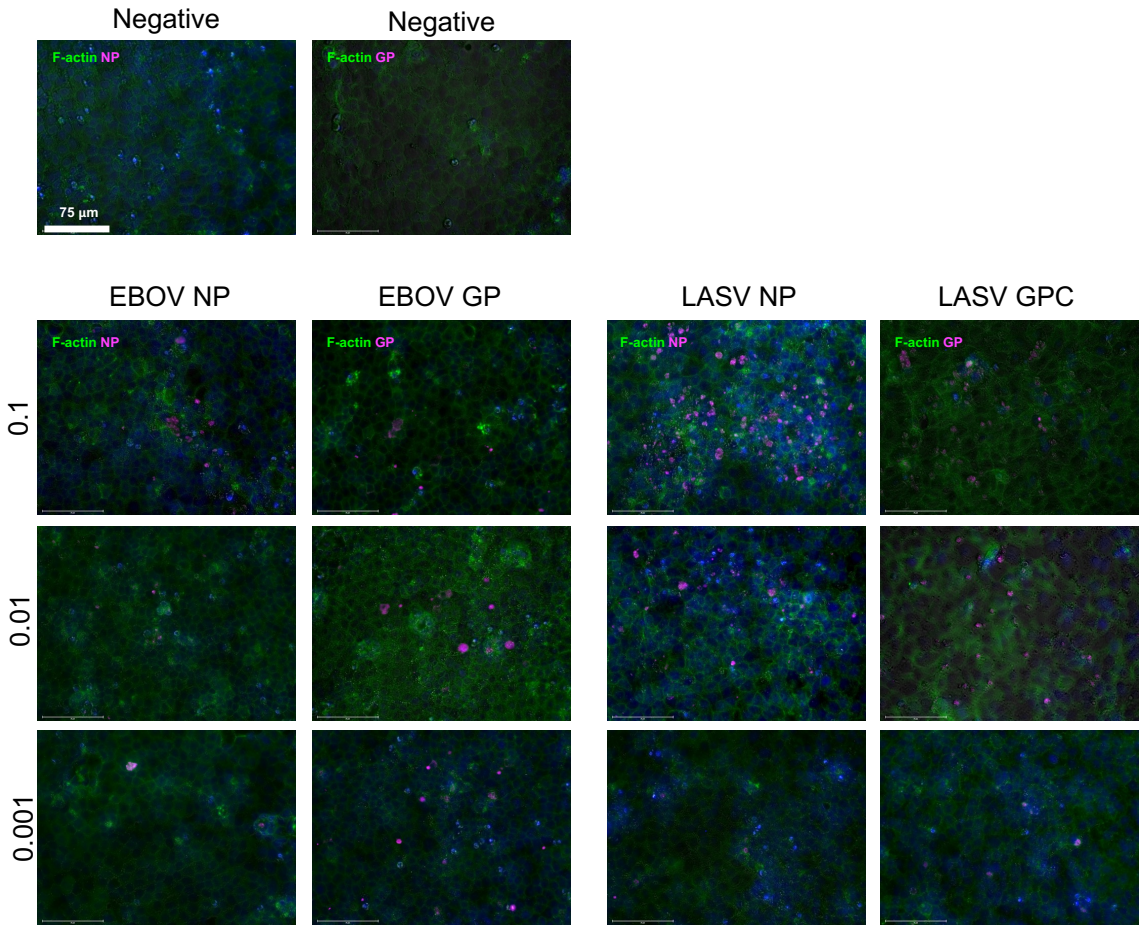


Figure 42: Immunofluorescence microscopy of EBOV and LASV-infected VeroE6 cells 25dpi. Immunofluorescence microscopy images 25 dpi with EBOV or LASV-infected VeroE6 cells counter-stained with DAPI and imaged at 40x magnification. Through-light (grey) merged into the images to reveal cellular phenotype. F-actin staining in green and viral nucleoprotein/glycoprotein of EBOV or LASV in magenta. The scale bar indicates 75 µm. Representative images each and MOI indicated on the side. Images were taken at equal brightness and modifications were done equally in all conditions. Negative controls represent uninfected cells stained with the same antibodies.

In contrast, microglia and astrocytes presented with a different phenotype, where more extensive CPE was observed 25 dpi in microglia than in either VeroE6 or Huh7 cells. Notably, staining of negative controls revealed that the overall confluency in microglia and astrocytes was lower at 25 dpi in general. Notwithstanding this, EBOV NP and GP were expressed in microglia under all conditions tested, shown in Figure 44. Moreover, as revealed by F-actin staining, long-range intercellular connections formed by the microglial dendrites appeared pronounced in conditions with lower cellular confluency. In astrocytes, EBOV NP and GP expression was similar to expression observed in microglia, although in some cases only individual cells seemed infected (Figure 45). Moreover, as revealed previously by imaging the monolayer, tissue culture CPE was low in astrocytes infected with EBOV.

Taken together, these findings indicate that EBOV persistently replicated in microglia and astrocytes across different MOI for up to 25 days. Culture viability impacted the experimental read-out due to the incubation lengths. The relevance of these results must be viewed in

connection with the reported EBOV GP and NP expression. Persistence necessitated culture viability and was therefore limited by the CPE. This was confirmed by LASV infection, where the replication ceased due to extensive CPE. Moreover, upon persistence, both EBOV NP and GP were expressed, which is in line with the retrieval of infectious viral particles from the supernatant, as measured via immunofocus assay.

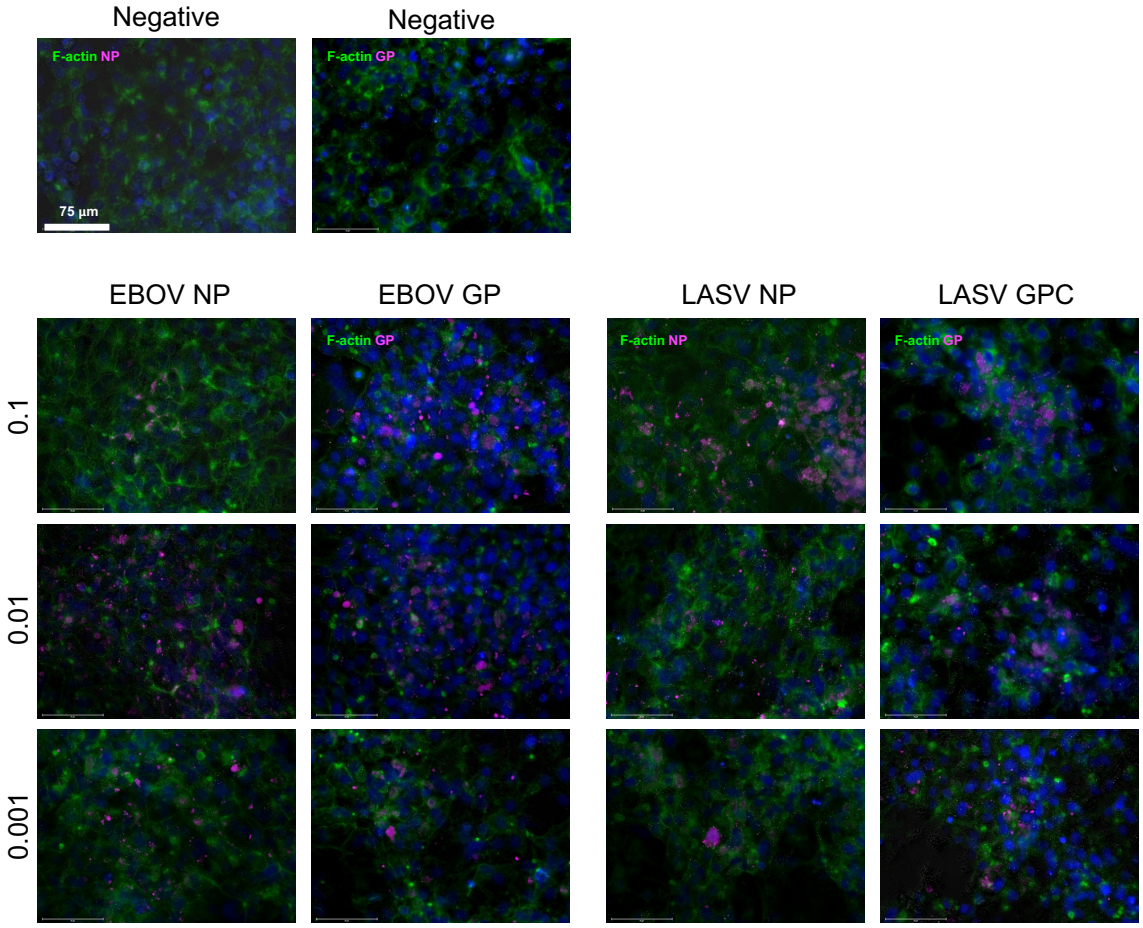


Figure 43: Immunofluorescence microscopy of EBOV and LASV-infected Huh7 cells 25dpi. Immunofluorescence microscopy images 25 dpi with EBOV or LASV-infected Huh7 cells counter-stained with DAPI and imaged at 40x magnification. Through-light (grey) merged into the images to reveal cellular phenotype. F-actin staining in green and viral nucleoprotein/glycoprotein of EBOV or LASV in magenta. Scale bar indicates 75 µm. Representative images each and MOI indicated on the side. Images were taken at equal brightness and modifications were done equally in all conditions. Negative controls represent uninfected cells stained with the same antibodies.

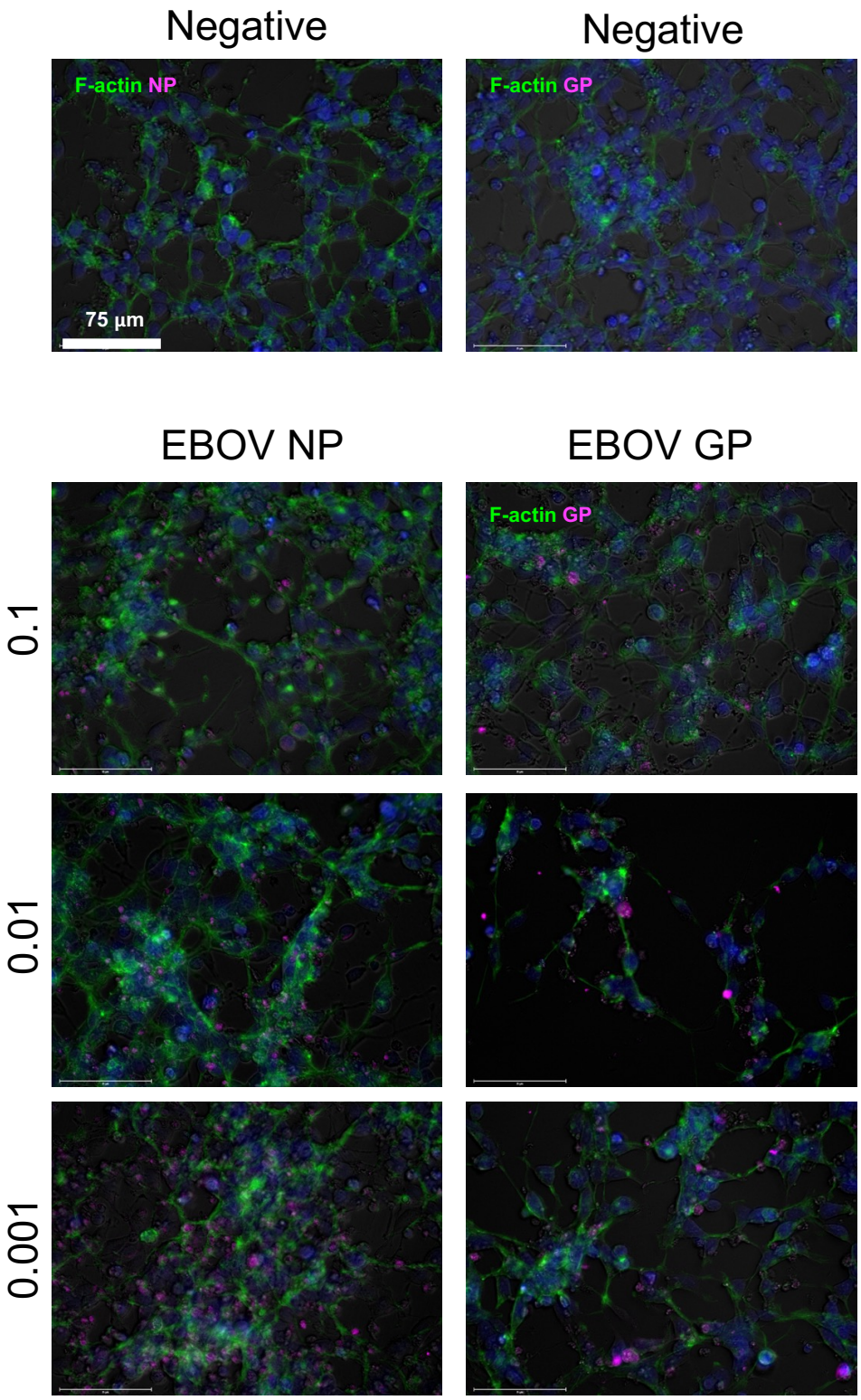


Figure 44: Immunofluorescence microscopy of EBOV and LASV-infected microglia 25dpi. Immunofluorescence microscopy images 25 dpi with EBOV or LASV-infected microglia counter-stained with DAPI and imaged at 40x magnification. Through-light (grey) merged into the images to reveal cellular phenotype. F-actin staining in green and viral nucleoprotein/glycoprotein of EBOV or LASV in magenta. Scale bar indicates 75 µm. Representative images each and MOI indicated on the side. Images were taken at equal brightness and modifications were done equally in all conditions. Negative controls represent uninfected cells stained with the same antibodies.

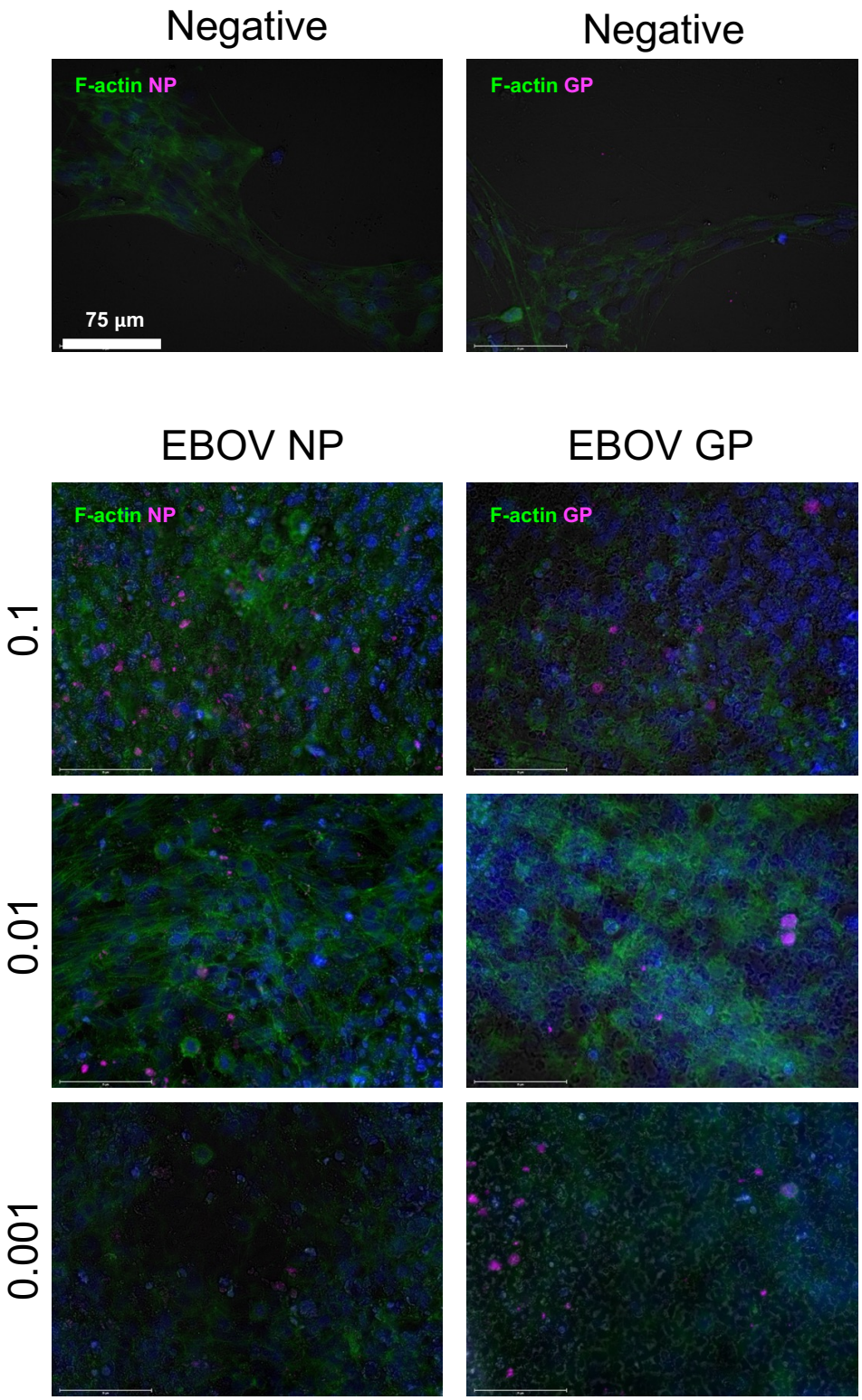


Figure 45: Immunofluorescence microscopy of EBOV and LASV-infected astrocytes 25dpi. Immunofluorescence microscopy images 25 dpi with EBOV or LASV-infected astrocytes counter-stained with DAPI and imaged at 40x magnification. Through-light (grey) merged into the images to reveal cellular phenotype. F-actin staining in green and viral nucleoprotein/glycoprotein of EBOV or LASV in magenta. The scale bar indicates 75 µm. Representative images each and MOI indicated on the side. Images were taken at equal brightness and modifications were done equally in all conditions. Negative controls represent uninfected cells stained with the same antibodies.

6.3.4 Long-term infection of more than 91 days of human microglia cultures can be achieved via passaging.

As an alternative approach to achieve a persistent infection in 2D cell culture, cells may be passaged as described in a model for persistent EBOV infection in VeroE6 cells by Calain *et al*. [190, 191]. Based on this model, the herein-described passaging included both microglia and supernatant being transferred to the following passage every seven days, which resulted in a selection of both cells and virus.

Viral replication during the passaging of microglia is displayed in Figure 46 A. Here, the viability of microglia upon EBOV (MOI=10 (1x), MOI=1 (2x)) infection was only sustained for three passages (21 days) before substantial CPE caused the collapse of the culture. This is shorter than the survival of cells without passage which were infected at a lower MOI (Figure 40). Notably, the CPE upon passaging occurred irrespective of the initial MOI of the infection for EBOV (MOI=10/MOI=1). To maintain the viability after passage 3, uninfected feeder microglia were supplied during subsequent passaging (Figure 46 (A)). During the 10 passages, 5'cbDVG were detected throughout, whereby DVG diversity was initially lower when RNA was isolated from the supernatant in direct comparison to DVG measured in the respective cells (Figure 46 (C)). Notably, unlike in cerebral organoids, DVG diversity did not continuously increase throughout the passaging.

The addition of feeder microglia resulted in the sustained replication of EBOV throughout 10 passages (70 days) in all three flasks (Figure 46 (A)). At passage 10, microglia were collected and frozen, depicted in Figure 46 (D). Finally, passage 10 MOI=1 EBOV (flask A, flask B) infected microglia were thawed and distributed into four flasks each to be individually recovered and passaged without the transfer of old supernatant. Here, at passage 3 after thawing (passage 10+3), infectious viral particles were still shed from the cells into the supernatant (Figure 46 (B)), indicating the establishment of a persistent infection that can be sustained even in frozen cells. Moreover, as shown in Figure 46 (E), the recovered cells did not present with as strong of a CPE as observed before freezing. However, persistently infected cells grew slower in comparison to the negative control passage.

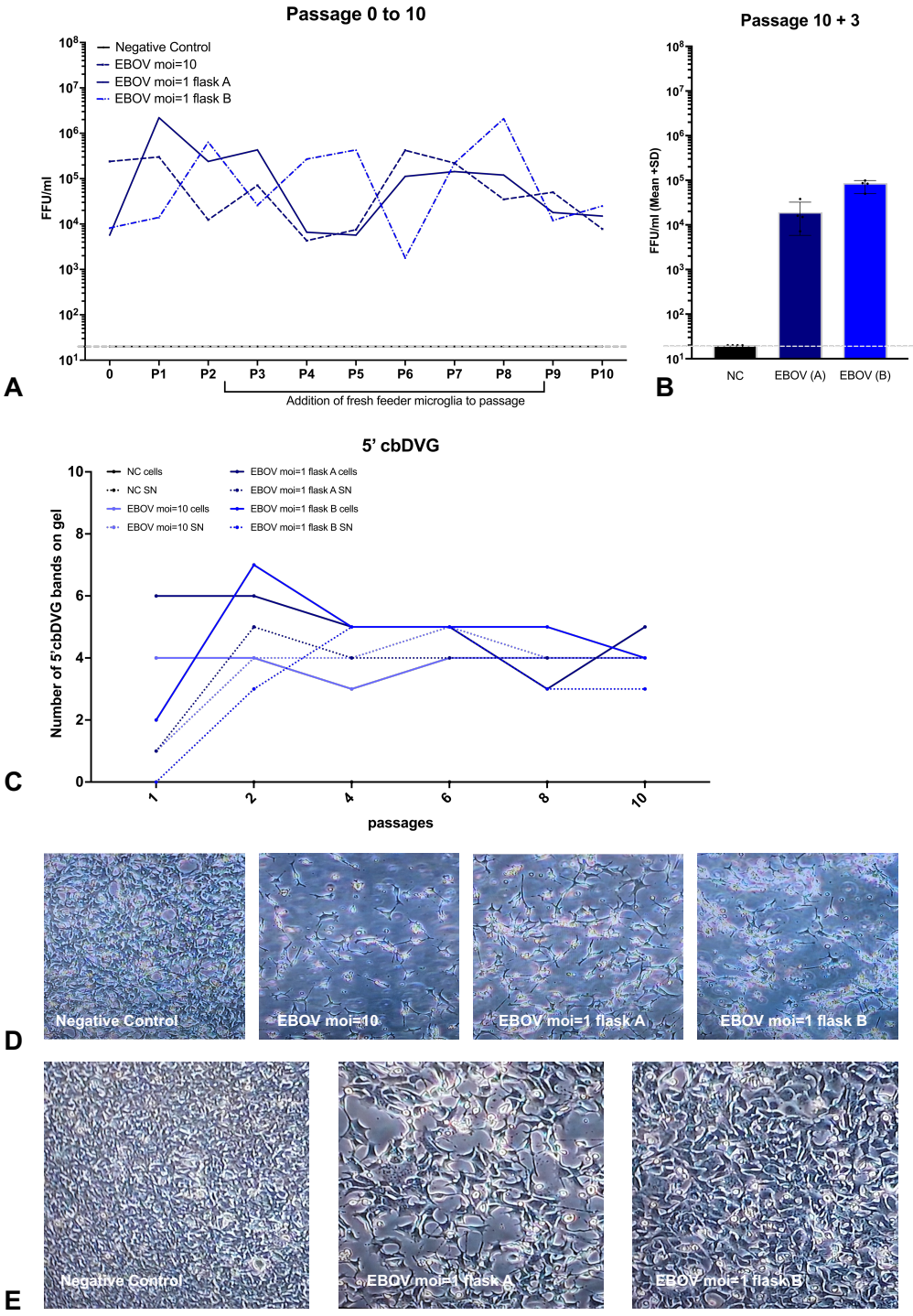


Figure 46: EBOV passaging in microglia. (A) Viral titers of individual passages of EBOV in human immortalized microglia split 1:5 weekly for ten weeks with the supply of uninfected human microglia from passage 3 onward. Initial infection at MOI=10 for 1 EBOV sample (dark blue, dashed) and MOI=1 for 2 EBOV (dark blue flask A, light blue + dash/dotted flask B) samples each. LOD at 20 FFU/ml indicated as a grey dotted line. **(B)** Mean (+SD) EBOV (flask A) or (flask B) titers of re-thawed and three-times passaged microglia. N=4 independent biological replicates per original flask. **(C)** Number of bands on a gel after 5'cbDVG RT-PCR in the cells (full line) or supernatant (SN, dotted line) of the indicated passages. NC = negative control (black), EBOV MOI=10 in light blue, EBOV MOI=1 flask A in dark blue, and EBOV MOI=1 flask B in blue. **(D)** Microscopy images of microglia passaged for 10 passages. **(E)** Microscopy images of re-thawed microglia after passage three. Representative images.

6.4 The role of chemokine receptor CX3CR1 in EBOV CNS persistence.

EBOV(-GFP) infection enriches CX3CR1 surface expression in microglia.

Within the scope of the third objective we sought to determine, host factors driving EBOV persistence in the human CNS. To determine the phenotype of EBOV-infected human microglia, flow cytometry assays were performed. Accordingly, immortalized human microglia (n=3) or MDMi (n=1) were infected with EBOV-GFP or RESTV-GFP at MOI=0.0025 or MOI=1, respectively. Thereafter, the cells were harvested 3 or 6 dpi. Notably, later time points were anticipated in immortalized microglia as well, however, at 9 dpi, all infected microglia were dead. Therefore, it was concluded that the recombinant GFP-expressing viruses do not establish persistence due to extensive CPE. In the case of immortalized human microglia, monocyte-like THP-1 cells were used as a control cell line.

As immortalized human microglia represented a homogenous population, infection rates and surface expression of CX3CR1 were determined by considering all live cells. Here, as is shown in Figure 47 (A), THP-1 were not infected with either EBOV-GFP or RESTV-GFP during the queried time frame. At the same time, the median EBOV-GFP infection rate increased from 3 dpi (2.11 %) to 6 dpi at 52.7 %. In contrast, RESTV-GFP infection carried out at the same MOI was only established at 6 dpi at 14.72 % median infection rate in microglia. Therefore, it can be concluded that RESTV-GFP infection in microglia is seemingly slower than EBOV-GFP (n=3).

Next to the infection rates, the increase in a subpopulation expressing high levels of CX3CR1 ($CX3CR1^{++}$) on their surface was analyzed (gating in Figure 47 (C)). Here, it was found that upon infection with EBOV-GFP, there was an increase in the $CX3CR1^{++}$ sub-population 3 dpi (0.26 %) to the median of 8.74 % of total live cells at 6 dpi (Figure 47 (B)). Notably, as shown in Figure 47 (C), the presence of $CX3CR1^{++}$ on the surface of the microglia also occurred in GFP^{-}, uninfected bystander microglia. Moreover, the increase in CX3CR1 expression on the surface upon infection was pronouncedly less in RESTV-GFP-infected samples (0.09 % $CX3CR1^{++}$ 6 dpi).

It was previously shown that MDMi may be infected by EBOV. Therefore, a follow-up experiment was performed at an MOI=1 to determine microglial marker expression in MDMi, particularly CX3CR1. To that end, MDMi differentiated for two weeks were infected with EBOV-GFP or RESTV-GFP (n=1, MOI=1) and subsequently harvested 6 dpi and analyzed using the same flow cytometry panel. Here, MDMi were defined as $CD14^{+}$, $CD11b^{+}$, $CD45^{+}$, $CX3CR1^{+}$ sub-population (Figure 48 (A)). Of those MDMi, CX3CR1 surface expression was differentiated in baseline ($CX3CR1^{+}$) and elevated ($CX3CR1^{++}$) regarding their geometric mean fluorescence (Figure 48 (C)). Indeed, as shown in Figure 48 (B), it was found that only upon EBOV-GFP stimulation, a small $CX3CR1^{++}$ population was detected (3 % of total

MDMi). This was not the case for the uninfected control and RESTV-GFP inoculated cells. Notably, as shown in Figure 48 (D), at 6 dpi at MOI=1, no cells in the infected groups were positive for the virus, as measured by expression of GFP.

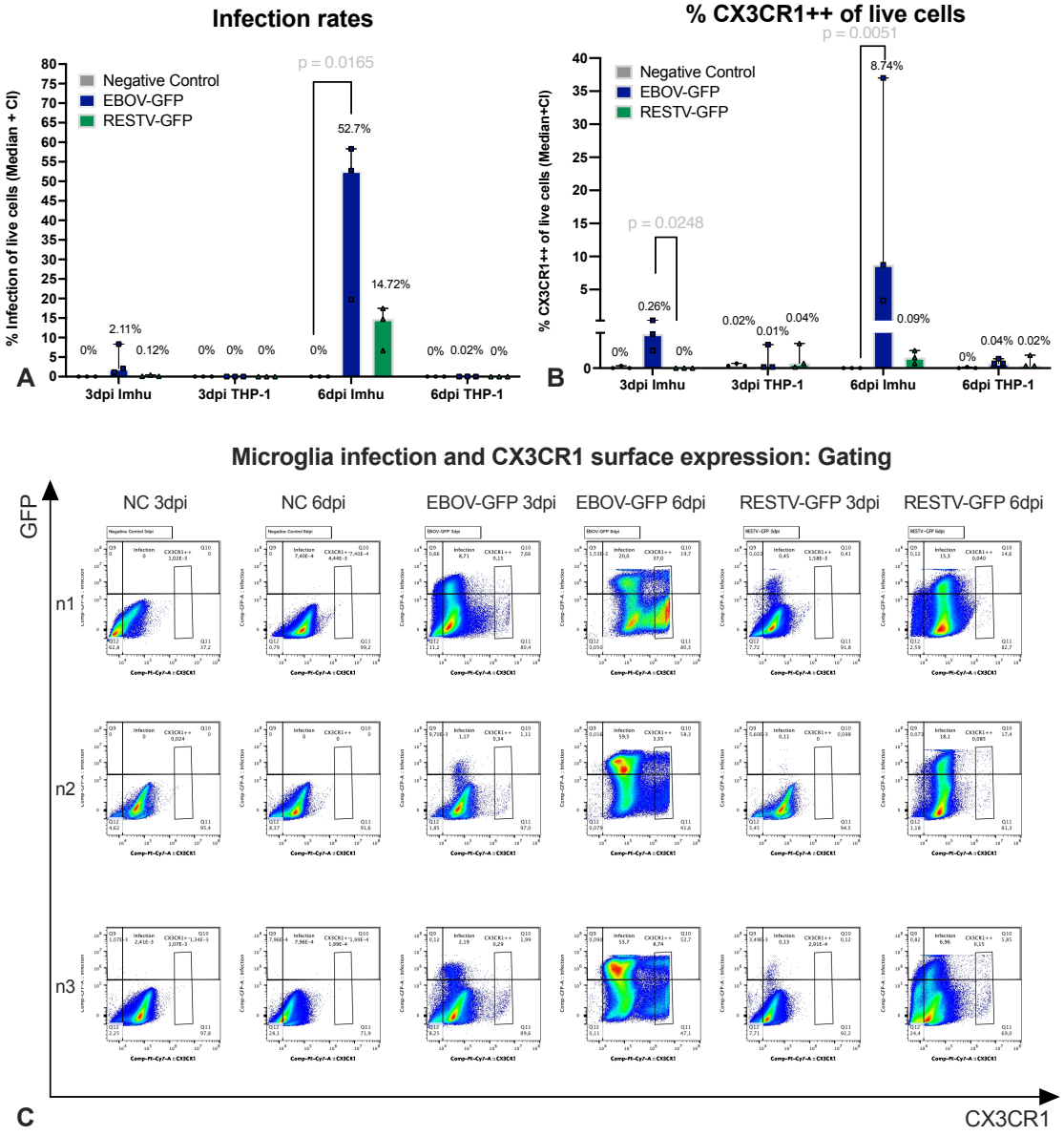


Figure 47: Flow cytometry of microglia infected with EBOV-GFP or RESTV-GFP. (A) Percent infection rates of microglia or THP-1 cells infected with EBOV-GFP (blue) or RESTV-GFP (green) for 3 or 6 days. Percentages are shown as median from three independent experiments of total live cells each. Kruskal Wallis non-parametric test + Dunn's Multiple Comparisons (pAdj reported). **(B)** Percent of microglia or THP-1 of total cells with high CX3CR1 surface expression. Plotted is the median (+CI) for EBOV-GFP (blue), RESTV-GFP (green), or uninfected (grey) samples. Kruskal Wallis non-parametric test + Dunn's Multiple Comparisons (pAdj reported). **(C)** Gating of $CX3CR1^{++}$ population and infection (GFP^{+}) exemplified in microglia (n=3) infected for 3 or 6 days with EBOV-GFP or RESTV-GFP. Gating was performed using unstained/uninfected samples and an FMO for CX3CR1.

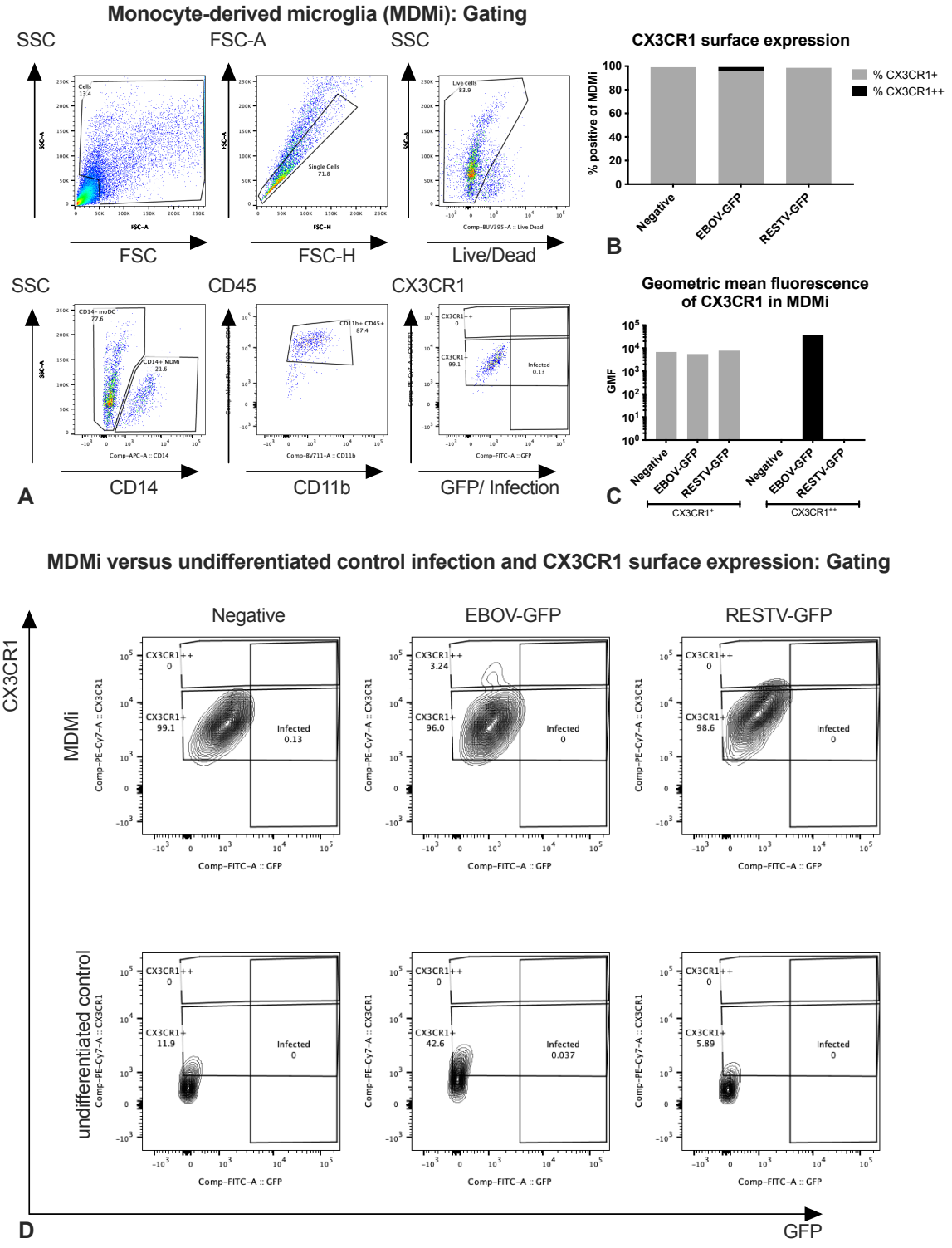


Figure 48: Flow cytometry of MDMi infected with EBOV-GFP or RESTV-GFP. (A) Gating strategy used to differentiate monocyte-derived microglia (MDMi, CD14^{+}, CD11b^{+}, CD45^{+}, CX3CR1^{+}) from undifferentiated cells. **(B)** Percent of MDMi expressing CX3CR1 on their surface at baseline CX3CR1^{+} or elevated levels CX3CR1^{++} in uninfected, EBOV-GFP, or RESTV-GFP-infected MDMi 6 dpi at MOI=1 (n=1). **(C)** Measured geometric mean fluorescence (GMF) of CX3CR1 in CX3CR1^{+} versus CX3CR1^{++} in uninfected, EBOV-GFP, or RESTV-GFP-infected MDMi (n=1). **(D)** Gating of MDMi versus undifferentiated control infection and CX3CR1 surface level expression. GFP represents infected cells 6 dpi at MOI=1.

6.4.1 EBOV infection enriches CX3CR1 surface expression in microglial ramifications.

Given that an increase in surface expression/presence of CX3CR1 in microglia was observed using flow cytometry, this finding was to be confirmed using immunofluorescence microscopy. Therefore, immortalized human microglia were infected with EBOV at MOI=0.1 for 5 days (n=4 wells). The higher MOI was chosen to increase infected cells/well. As shown in the representative images in Figure 49, total CX3CR1 baseline expression was not or only to a very limited extent detectable in the uninfected control. In contrast, upon EBOV infection, expression of CX3CR1 was increasingly detected, particularly in those cells also positive for the virus. Moreover, as pointed out in Figure 49, upon infection with EBOV, NP as well as CX3CR1 were found to be elevated in the ramifications of infected microglia. EBOV NP and CX3CR1 furthermore did not co-localize.

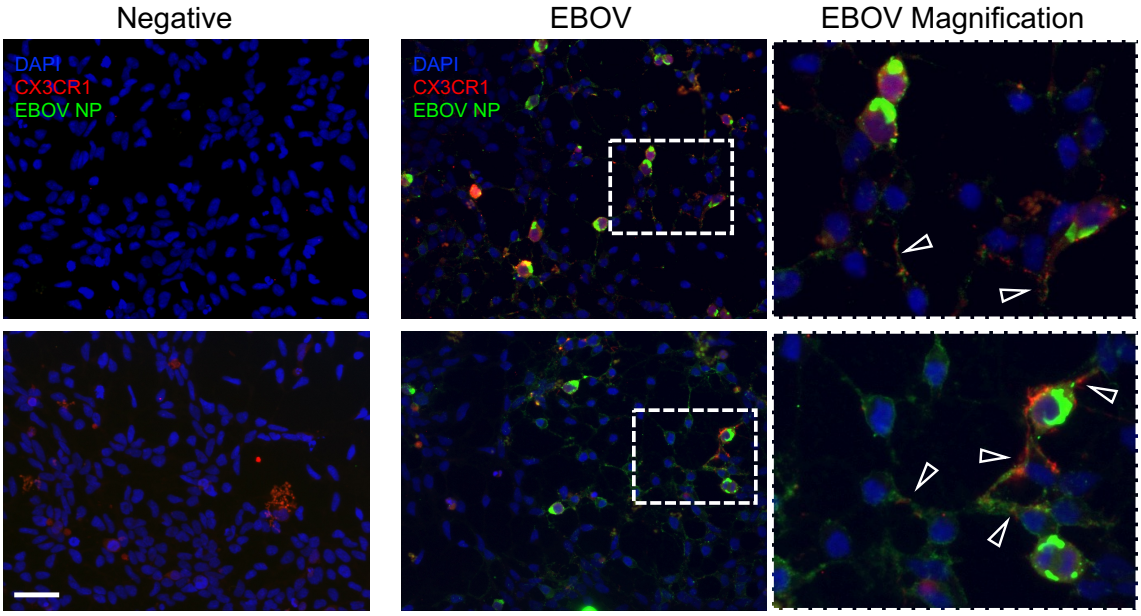


Figure 49: Immunofluorescence microscopy staining of EBOV and CX3CR1 in microglia. Immunofluorescence microscopy images of uninfected and EBOV-infected microglia (MOI=0.1) after 5 days. N=4, two representative images each are shown. Boxed sections are the areas magnified on the right. Staining for EBOV nucleoprotein (NP, green) and CX3CR1 (red). Counter-staining of nuclei using DAPI. Triangles point towards CX3CR1$^+$ EBOV NP$^+$ microglial dendrites. The scale bar indicates 100 µm (images taken at 20X magnification). Imaging was performed at the same exposure times for all conditions and image processing was done equally for all conditions.

6.4.2 Inhibition of CX3CR1 does not decrease EBOV replication or interfere with viral persistence in a 2D culture context.

As the infection with EBOV caused an increase in CX3CR1 surface expression in immortalized microglia and MDMi, the role of CX3CR1 in EBOV infection was questioned. Therefore, to determine whether the increase in CX3CR1 aids in EBOV replication or persistence, the consequences of CX3CR1 inhibition using the allosteric CX3CR1 inhibitor AZD8797 were explored in a 2D and 3D context. Here, to ascertain the concentration for the inhibitor in

downstream experiments and to exclude cytotoxicity in microglia, cells were treated for 24 h with the inhibitor (in DMSO) in 10-fold serial dilutions from 10 µM to 10 nM. As depicted in Figure 50, only the highest concentration of 10 µM led to visible cytotoxicity (cellular rounding), therefore, the second highest concentration of 1 µM was chosen for future studies.

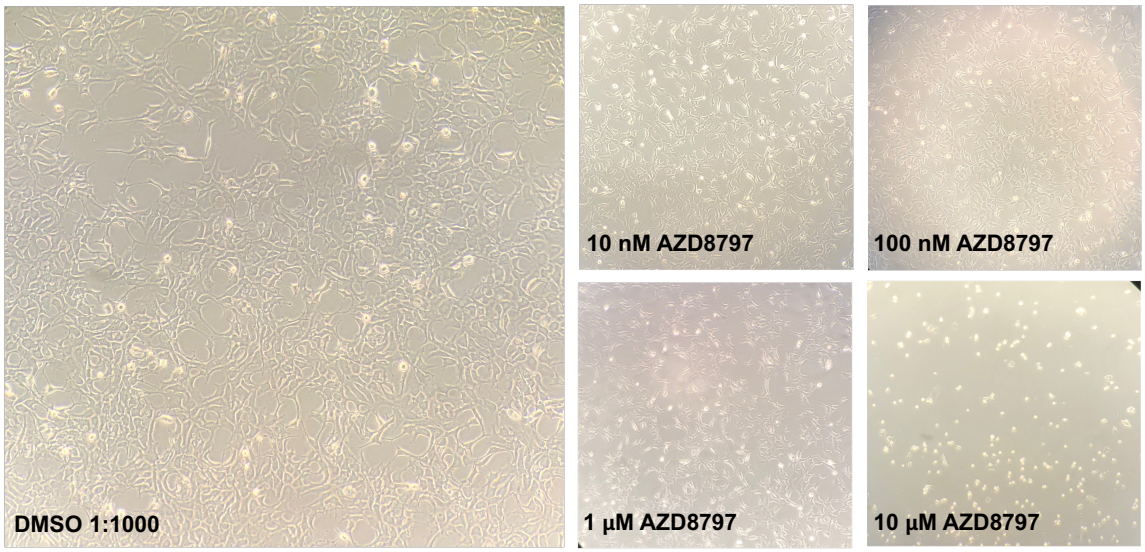


Figure 50: Serial dilution of AZD8797 CX3CR1 inhibitor and treatment of microglia. Light microscopy images of immortalized microglia treated with AZD8797 (in DMSO) at the indicated concentration ranging from 10 nM to 10 µM. DMSO control corresponds to a maximum concentration of DMSO in the media corresponding to 10 µM. Images taken 24 h after application at 10X magnification

An initial experiment was performed in which microglia, astrocytes, and VeroE6 cells were infected with EBOV at MOI=0.0025 and sampled for 24 days. Here, the cells were pre-treated (d-1) and subsequently treated every third day until day 12 and once more thereafter with 1 µM of the inhibitor or with DMSO. VeroE6 cells and astrocytes were employed as controls not expressing CX3CR1.

As shown in Figure 51, the application of the inhibitor did not negatively impact EBOV replication in immortalized microglia or influence the anticipated establishment of persistent replication for up to 24 days (n=3 in one experiment). In fact, in microglia, mean longitudinal titers 18 –24 dpi were higher in the treated group (not statistically significant). Meanwhile, in astrocytes and VeroE6 cells, both of which do not express CX3CR1, the treatment did not influence EBOV persistence either. Similar to the microglia, there was a slight trend towards elevated titers 18 –24 dpi in VeroE6 cells, which further confirms that the inhibition possibly did not specifically influence EBOV replication in microglia. Moreover, in astrocytes, replication was similar in both groups as well, although the plateau in the control group was reached earlier and the titers in the treated group were reduced 18 dpi. Overall, this leads to the conclusion that applying the CX3CR1 inhibition does not abrogate or decrease EBOV replication in immortalized microglia but may have unspecific effects. At the same time, the

inhibitor application does not prevent persistent replication of EBOV in 2D.

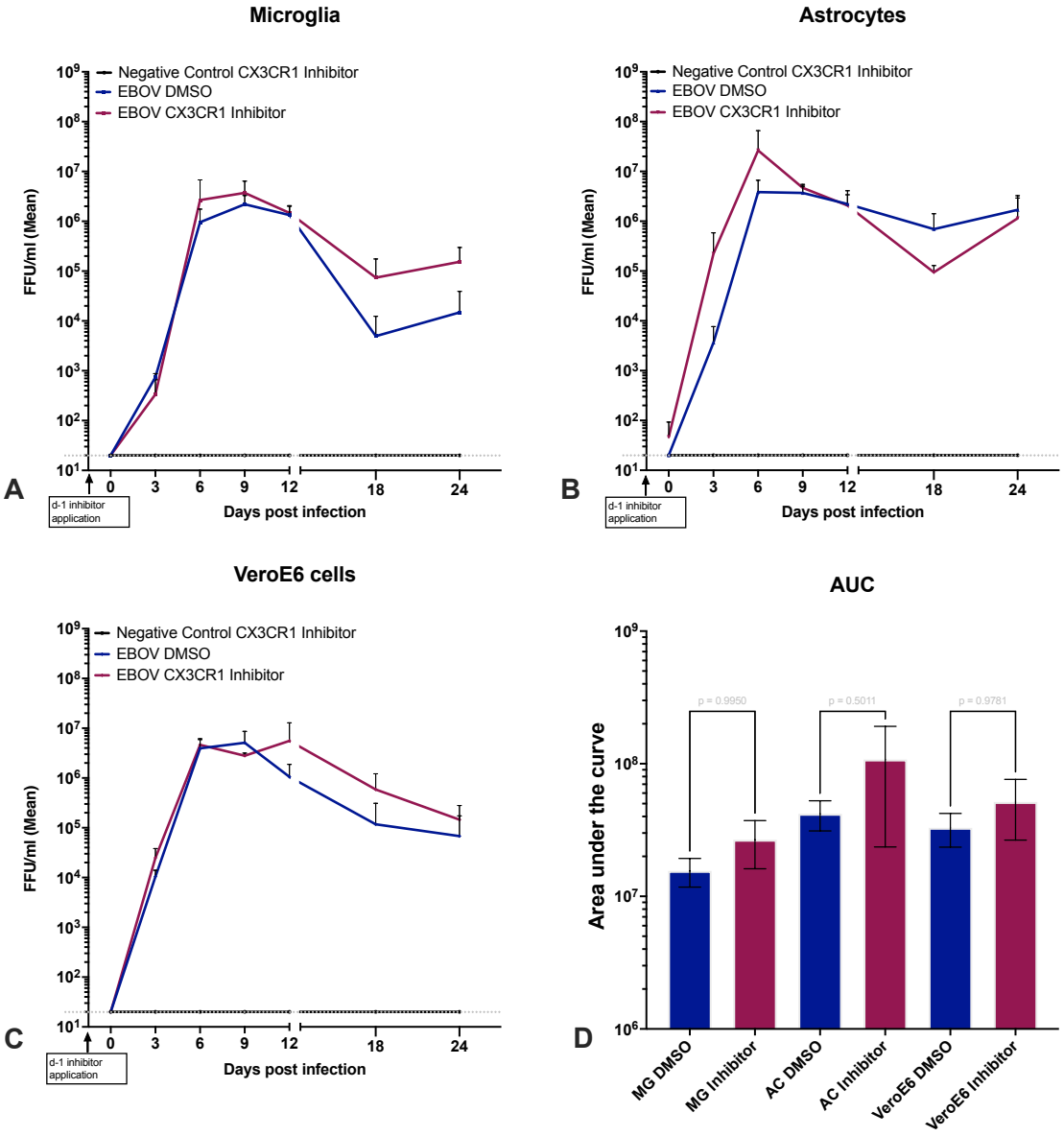


Figure 51: EBOV replication in human immortalized microglia, astrocytes, or VeroE6 cells under the influence of 1 µM CX3CR1 inhibition. Mean titer of EBOV (FFU/ml) after initial infection of microglia **(A)**, astrocytes **(B)**, or VeroE6 cells **(C)** with EBOV at MOI=0.0025. Inhibitor (maroon, 1 µM) / DMSO application (dark blue, 1:10.000) one day before infection and re-application every third day for the first two weeks and weekly after. Titration via immunofocus assay detecting EBOV NP expression. One experiment with n=3 replicates. LOD at 20 FFU/ml indicated as grey dotted line. **(D)** Area under the curve (AUC) calculations of total EBOV replication. One-way ANOVA and Sidak's Multiple Comparison for pair-wise comparisons. No significance.

6.4.3 Inhibition of CX3CR1 does not prevent EBOV persistence in choroid plexus organoids.

Given no reduction in replication or prevention of persistence was achieved upon inhibition of CX3CR1 in microglia in 2D, the influence of the CX3CR1 inhibition was queried in a 3D tissue context using human choroid plexus organoids. This was done as CX3CR1 expression appeared enriched in microglial dendrites upon infection, indicating a potential role in long-

range cell-cell transmission. Such cell-cell transmission is possibly more relevant in dense 3D tissues such as organoids, given limited contact with the media. Furthermore, choroid plexus organoids were selected, as the structure had been previously identified as a primary reservoir for EBOV persistence in NHP [183, 189]. As in cerebral organoids, infection was carried out at 10^4 FFU/organoid 100 days after organoid generation. Thereafter, the organoids were either treated with 1 µM CX3CR1 inhibitor AZD8797 the day prior (d-1) as well as daily until 15 dpi and weekly thereafter, or supplemented with 1:10.000 DMSO in the control group (Figure 52 (B)).

As is shown in Figure 52 (C), EBOV replicated and established persistence (48 days) in human choroid plexus organoids, whereby the replication pattern was similar to the one previously observed in cerebral organoids (Figure 26). In choroid plexus organoids, the range among the singular organoids was also large, possibly attributable to the high heterogeneity among the organoids. Irrespectively, mean titers peaked between 6 dpi and 15 dpi at approximately 10^6 FFU/ml before declining to longitudinal mean titers at roughly 10^4 FFU/ml in the EBOV-infected organoids without treatment. Notably, CX3CR1 inhibition did not influence the establishment of a persistent EBOV infection in human choroid plexus organoids. However, as indicated in Figure 52 (B, C), there was a minor trend particularly from 22 dpi onwards where mean titers were generally lower throughout the remainder of the experimental period in the treated group.

In the same experiment, it was further anticipated to harvest CSF-like fluids from the vacuolar compartments to determine the penetration of EBOV into the ventricular structure. Given that EBOV had been detected in the CSF of a human case of CNS persistence [139], it was aimed to reproduce this finding in vitro. As is depicted in Figure 52 (D), EBOV was detected in the CSF-like fluid in all time points as early as 3 dpi in both groups. However, it must be noted that organoid vacuoles were punctured using a pipette tip for the extraction. Therefore, the influence of minor tissue destruction and release of particles from the tissue cannot be excluded and these findings must be taken with caution. Hence, to determine the influence of general virus production within an organoid, titers measured in the CSF-like fluid were normalized to the titer measured in the respective choroid plexus organoid's supernatant (Figure 52 (E)). Here, normalized titers varied strongly amongst the groups and days, overall preventing any conclusions from being made regarding the penetration of EBOV into the ventricular structure of choroid plexus organoids.

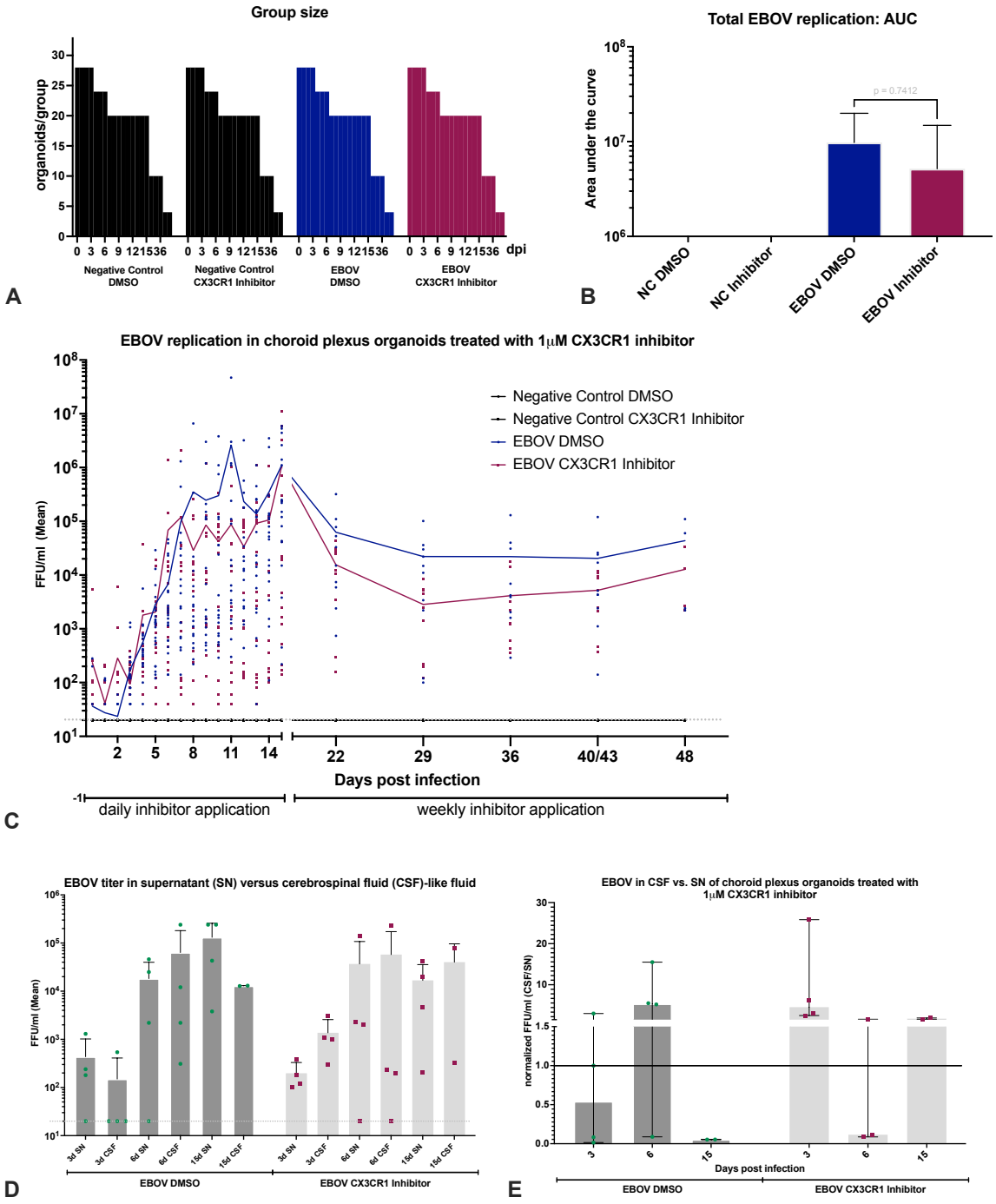


Figure 52: EBOV replication in human choroid plexus organoids treated with 1 µM CX3CR1 inhibitor. **(A)** Amount of choroid plexus organoids per group at the indicated time point. **(B)** Area under the curve (AUC) calculation using y=20 as baseline. Unpaired, two-tailed Student's T-test for the pairwise comparison performed for EBOV-infected DMSO control with EBOV-infected CX3CR1 inhibitor-treated group. Not significant. **(C)** Titers (Mean + Range) of EBOV in the supernatant of choroid plexus organoids after infection with 10^4 FFU EBOV/organoid at the indicated time point. EBOV control groups were treated with 1:10.000 DMSO in dark blue, and organoids were treated with 1µM AZD8797 CX3CR1 inhibitor in maroon. Pre-treatment the day prior, daily until 15 dpi, and weekly thereafter. N=10 organoids/group until day 36, longitudinal sampling at 48 dpi n=4 organoids per group. Organoids originated from two different batches and were used in two different experiments. **(D)** Mean virus titer in the supernatant versus vacuolar compartment (CSF-like fluid) in choroid plexus organoids at the indicated day post-infection with (maroon/light grey) or without (green/dark grey) inhibitor treatment. N=4 organoids per time point from one batch. **(E)** Normalized titer in CSF-like fluid versus supernatant of organoids treated with CX3CR1 inhibitor (maroon/light grey) or DMSO (green/dark grey) at the indicated time points.

6.5 Host response to EBOV persistence in the CNS

6.5.1 Transcriptome analysis of human immortalized microglia and astrocytes infected with EBOV reveals differential response at 12dpi.

A transcriptome analysis was performed using RNA sequencing to understand the cellular changes in the CNS at different stages after EBOV infection. This ultimately aimed at identifying host factors involved in the establishment or maintenance of EBOV CNS persistence, as described in the third objective of this thesis. Coherently, human immortalized microglia and astrocytes were infected with EBOV at a low MOI (MOI=0.0025) to capture stages of early (3 dpi), exponential (6 dpi) and saturated (12 dpi) viral propagation (Figure 53 (A)). However, the low MOI led to unsuccessful infection in some replicates and therefore subsequent exclusion from analysis (Table 6). As shown in Figure 53 (A), amongst the included replicates, early replication 3 dpi, exponential growth 6 dpi, and saturated/declining replication at the 12 dpi time point for EBOV infection in microglia and astrocytes were captured.

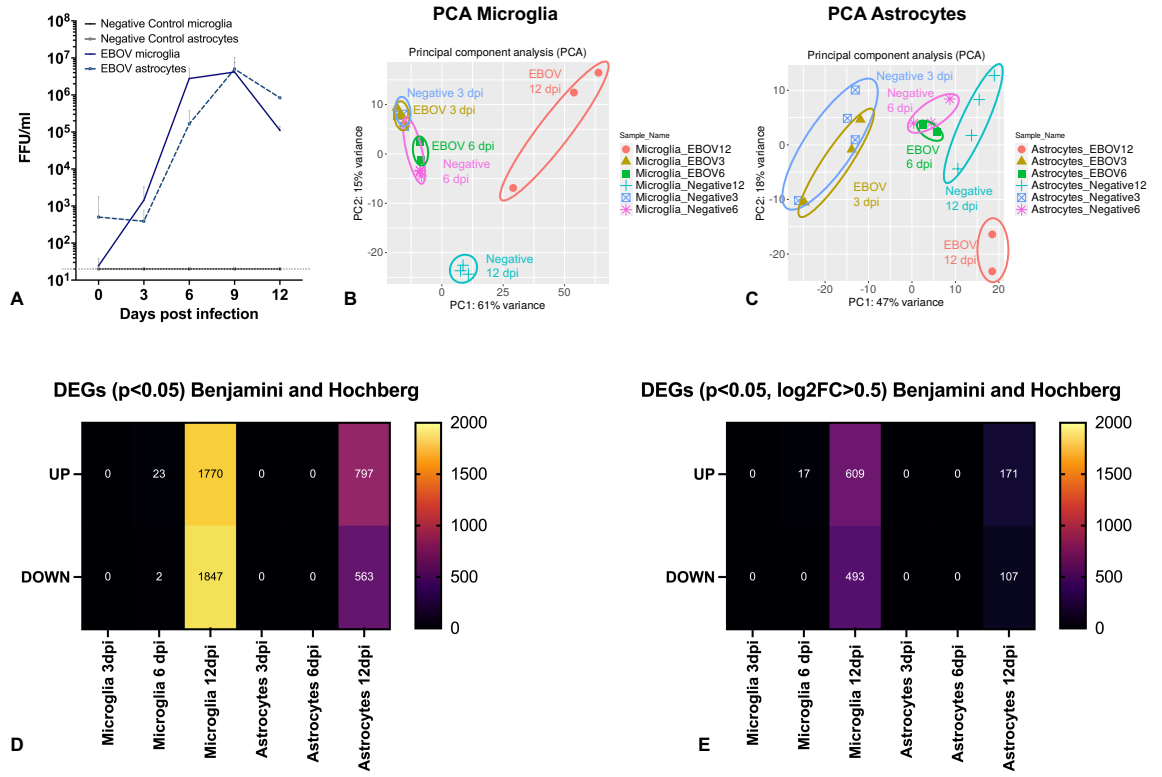


Figure 53: Replication, PCA, and DEGs in microglia and astrocytes infected with EBOV 3, 6, 12 dpi. (A) Mean virus titers (+SD) [FFU/ml] of microglia infected with EBOV (blue, full), astrocytes (blue, dotted) with a MOI=0.0025. LOD at 20 FFU/ml indicated as a grey dotted line. Removed non-infected outliers from analysis (Table 6). **(B)** Principal component analysis of included groups in the microglia subset. **(C)** Principal component analysis of included groups in the astrocyte subset. **(D)** Amount of differentially expressed genes in microglia and astrocytes infected with EBOV in comparison to the negative control for each time point (UP = upregulated genes, DOWN = downregulated genes). Benjamini-Hochberg (1995) FDR cutoff $p \leq 0.05$ and minimum absolute log2fold change $\log2FC \geq 0.5$ **(E)**.

Differential gene expression analysis using the limma-voom algorithm was thereafter performed for microglia and astrocytes infected with EBOV in comparison to the respective negative control (limma-voom details in the appendix). As underlined by the principal component analysis (PCA)s depicted in Figure 53 (B, C), early infection in either cell type 3 dpi at the low MOI=0.0025 did not reveal any differentially expressed genes (DEGs), whereby the infected groups clustered with the control groups in the PCA. Meanwhile, in microglia 6 dpi, only 17 genes were upregulated with Log2FC$\geq$0.5 (Table 9). No downregulated genes were noted 6 dpi with EBOV in microglia. In astrocytes, no DEGs were uncovered 6 dpi upon EBOV infection, either. In contrast, after 12 dpi with EBOV, microglia and astrocyte gene expression differed from the respective uninfected controls. Indeed, microglia 12 dpi upregulated 609 and downregulated 493 genes with a minimum Log2FC$\geq$0.5 (Table 10, Table 11). 12 dpi in astrocytes, a small number of genes were differentially expressed, amounting to 171 up- and 107 downregulated genes (Log2FC$\geq$0.5) (Table 12, Table 13).

At 6 dpi with EBOV in microglia, the top 10 upregulated genes comprised PDE5A (1.8 Log2FC), INSIG1, SDF2L1, CRELD2, HSPA5, MANF, IDI1, DNAJB11, HERPUD1, and HSD17B7 (0.6 Log2FC) (Table 9). No pathways were significantly enriched (GO Biological Process/KEGG). Amongst the top 10 upregulated genes in microglia 12 dpi, as listed in Table 10, most genes contributed to an type I interferon (IFN)-dependent antiviral response: IFI44 (8.5 Log2FC), IFI44L, IFIT3, IFIT2, IFIT1, IFI6, ISG15, DHX58, IFIH1, and OAS3 (5.9 Log2FC). Accordingly, GO-Term enrichment particularly identified the enrichment of ”negative regulation of viral processes”, ”regulation of viral life cycle”, ”regulation of viral processes”, ”defense response to virus”, and ”defense response to symbiont” (Figure 54 (A)). Meanwhile, KEGG mapping further revealed enrichment of ”p53 signaling pathway”, ”C-type lectin receptor signaling pathway” and several viral pathways as enriched (Figure 54 (B)).

Conversely, 12 dpi the most downregulated genes in microglia comprised LINC00641 (-1.6 Log2FC), MATK, EEF1A1, ABI3BP, SNORD141A, TNFRSF10D, PCDH18, CLUL1, ATP-SCKMT, and DNER (-1.2 Log2FC) (Table 11). As shown in Figure 54 (C), biological processes most downregulated in microglia 12 dpi were several pathways involved in gene expression and translation, including ”ribosomal small subunit assembly”, ”cytoplasmic translation”, or ”negative regulation of ubiquitin-protein ligase activity”. Enriched pathways identified by KEGG Mapping further supported this finding, whereby ”ribosome” was amongst the downregulated pathways (Figure 54 (D)). Notably, ”Coronavirus disease-COVID-19” was also decreased. Taken together, EBOV infection 12 dpi in microglia is determined by a strong proinflammatory and antiviral response. At the same time, gene expression on the level of translation was extensively downregulated.

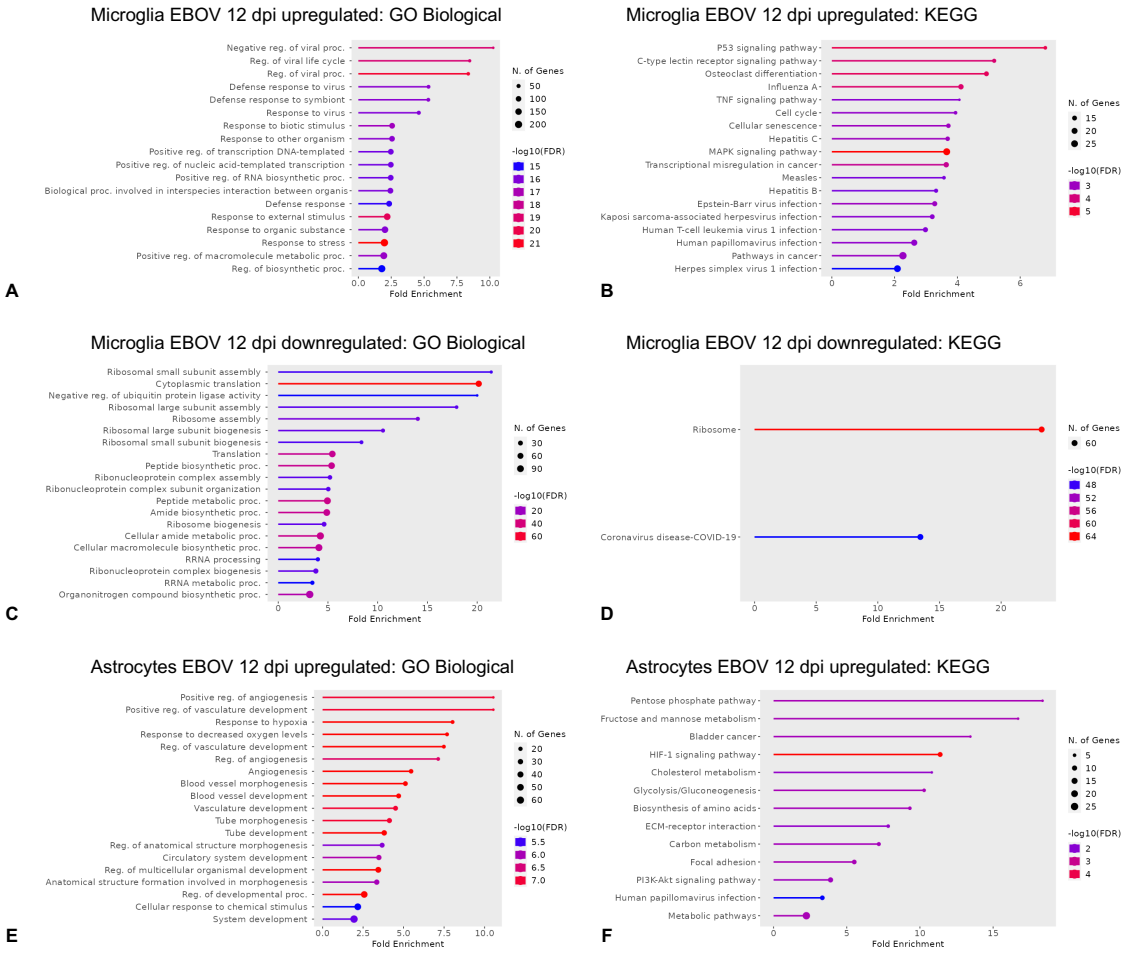


Figure 54: GO-Term and KEGG enrichment in microglia and astrocytes 12dpi with EBOV. GO-Term (Biological Process) and KEGG pathways enrichment in microglia and astrocytes 12dpi of genes significantly up- or downregulated Log2FC$\geq$0.5. **(A)** GO Biological for microglia 12dpi: upregulated genes, **(B)** KEGG for microglia 12dpi: upregulated genes, **(C)** GO Biological for microglia 12dpi: downregulated genes, **(D)** KEGG for microglia 12dpi: downregulated genes, **(E)** GO Biological for astrocytes 12dpi: upregulated genes, **(F)** KEGG for astrocytes 12dpi: upregulated genes.

Astrocytes that were infected for 12 days with EBOV upregulated to the greatest extent the following 10 genes: NDUFA4L2 (2.9 Log2FC), CA9, ANGPTL4, ALDOA, GDF15, CD68, RIMKLA, ALDOC, STC1, and CYGB (1 Log2FC) (Table 12). Among the most enriched biological processes ”positive regulation of angiogenesis”, ”positive regulation of vasculature development”, ”response to hypoxia”, ”response to decreased oxygen levels” as well as further developmental and morphogenic pathways were listed. Notably, only one pathway indicated infection in astrocytes, namely ”cellular response to chemical stimulus”, which was among the less enriched processes (Figure 54 (E)). KEGG pathway mapping further revealed an increase in the ”pentose phosphate pathway”, ”fructose and mannose metabolism”, ”HIF-1 signaling pathway” and other metabolic pathways. Notably, only ”human papilloma virus infection” enrichment was indicative of an infection (Figure 54 (F)).

The genes most downregulated in astrocytes 12 dpi with EBOV included LOC100506321

(-7.5 Log2FC), LRRC58-DT, LOC101448202, MYL12-AS1, ATP6V1C2, CERS6-AS1, ASB14, PRC1-AS1, Loc112268460, PLCG1-AS1 (-5.5 Log2FC) (Table 13). There were too few DEGs for pathway enrichment. Conclusively, while microglia presented with a strong proinflammatory response 12 dpi with EBOV, astrocytes seemingly reacted by regulation of their metabolism as well as morphogenic/developmental processes, without mounting as strong of an antiviral/proinflammatory response. Notably, this differential transcriptomic profile seemingly did not influence the replication of EBOV in either cell type at the applied MOI.

Table 9: All differentially expressed genes in microglia 6 dpi with EBOV: upregulation. All upregulated genes in microglia 6 dpi with EBOV as per limma-voom differential gene expression analysis. FDR (Benjamini and Hochberg) cut-off $\leq$0.05, Log2FC$\geq$0.5. Ordered by absolute Log2FC in expression.

GeneID	Genename	Gene symbol	log2FC	Average expression	adjusted p-Value
8654	phosphodiesterase 5A	PDE5A	1,854219707	8,64E+00	1,25E-04
3638	insulin induced gene 1	INSIG1	0,966052831	6,16E+00	9,89E-03
23753	stromal cell derived factor 2 like 1	SDF2L1	0,794662212	4,23E+00	5,08E-04
79174	cysteine rich with EGF like domains 2	CRELD2	0,73104559	5,11E+00	9,69E-04
3309	heat shock protein family A (Hsp70) member 5	HSPA5	0,725134719	9,11E+00	1,99E-03
7873	mesencephalic astrocyte derived neurotrophic factor	MANF	0,690394399	6,25E+00	1,99E-03
3422	isopentenyl-diphosphate delta isomerase 1	IDI1	0,65982881	5,95E+00	2,66E-02
51726	DnaJ heat shock protein family (Hsp40) member B11	DNAJB11	0,633145419	6,34E+00	1,99E-03
9709	homocysteine inducible ER protein with ubiquitin like domain 1	HERPUD1	0,633108832	5,33E+00	2,66E-02
51478	hydroxysteroid 17-beta dehydrogenase 7	HSD17B7	0,597887611	3,98E+00	7,72E-03
9871	SEC24 homolog D, COPII coat complex component	SEC24D	0,593922372	5,09E+00	7,50E-03
811	calreticulin	CALR	0,589798346	1,09E+01	2,60E-02
134429	StAR related lipid transfer domain containing 4	STARD4	0,56665109	5,80E+00	2,92E-02
25822	DnaJ heat shock protein family (Hsp40) member B5	DNAJB5	0,552621319	4,06E+00	3,04E-02
4189	DnaJ heat shock protein family (Hsp40) member B9	DNAJB9	0,547079815	4,76E+00	2,66E-02
2957	general transcription factor IIA subunit 1	GTF2A1	0,522108667	6,32E+00	1,95E-02
7184	heat shock protein 90 beta family member 1	HSP90B1	0,507755595	9,83E+00	4,43E-03

Table 10: Top 50 differentially expressed genes in microglia 12 dpi with EBOV: upregulation. Top 50 upregulated genes in microglia 12 dpi with EBOV as per limma-voom differential gene expression analysis. FDR (Benjamini and Hochberg) cut-off $\leq$0.05, Log2FC$\geq$0.5. Ordered by absolute Log2FC in expression.

GeneID	Genename	Gene symbol	log2FC	Average expression	adjusted p-Value
10561	interferon induced protein 44	IFI44	8,538481323	-1,37E+00	3,20E-03
10964	interferon induced protein 44 like	IFI44L	8,485411239	7,85E-01	9,71E-05
3437	interferon induced protein with tetratricopeptide repeats 3	IFIT3	7,851900478	2,26E+00	9,36E-04
3433	interferon induced protein with tetratricopeptide repeats 2	IFIT2	7,600843565	1,53E+00	1,57E-02
3434	interferon induced protein with tetratricopeptide repeats 1	IFIT1	7,342887671	3,15E+00	4,78E-05
2537	interferon alpha inducible protein 6	IFI6	6,397132813	3,85E+00	2,59E-07
9636	ISG15 ubiquitin like modifier	ISG15	6,279899898	3,59E+00	1,05E-03
79132	DExH-box helicase 58	DHX58	6,069247427	-1,83E+00	5,22E-02
64135	interferon induced with helicase C domain 1	IFIH1	5,938650633	1,53E+00	5,24E-03
4940	2'-5'-oligoadenylate synthetase 3	OAS3	5,924570368	4,82E+00	1,01E-04
219285	sterile alpha motif domain containing 9 like	SAMD9L	5,80324242	-2,67E-01	1,68E-02
91543	radical S-adenosyl methionine domain containing 2	RSAD2	5,49427424	1,56E+00	1,92E-02
10346	tripartite motif containing 22	TRIM22	5,289965036	1,82E+00	2,91E-02
10410	interferon induced transmembrane protein 3	IFITM3	4,985914197	4,70E+00	1,13E-04
4599	MX dynamin like GTPase 1	MX1	4,98573909	1,56E+00	1,85E-02
10202	dehydrogenase/reductase 2	DHRS2	4,953225245	3,71E+00	4,80E-02

Table 10: Top 50 differentially expressed genes in microglia 12 dpi with EBOV: upregulation. Top 50 upregulated genes in microglia 12 dpi with EBOV as per limma-voom differential gene expression analysis. FDR (Benjamini and Hochberg) cut-off $\leq$0.05, Log2FC$\geq$0.5. Ordered by absolute Log2FC in expression.

GeneID	Genename	Gene symbol	log2FC	Average expression	adjusted p-Value
25780	RAS guanyl releasing protein 3	RASGRP3	4,811139404	-1,51E+00	1,80E-02
84875	poly(ADP-ribose) polymerase family member 10	PARP10	4,770777391	1,99E+00	9,85E-03
105221694	BST2 interferon stimulated positive regulator	BISPR	4,62366596	3,56E-01	7,03E-03
8519	interferon induced transmembrane protein 1	IFITM1	4,610184419	4,29E+00	2,56E-05
684	bone marrow stromal cell antigen 2	BST2	4,596574576	3,15E+00	2,18E-04
23586	RNA sensor RIG-I	RIGI	4,52784362	4,09E+00	3,06E-04
3665	interferon regulatory factor 7	IRF7	4,526589324	5,18E-01	2,12E-03
105370363	uncharacterized LOC105370363	LOC105370363	4,47938088	7,18E-01	2,92E-02
105371346	cytoplasmic polyadenylated homeobox like	CPHXL	4,474012384	-2,00E+00	2,64E-02
250	alkaline phosphatase, placental	ALPP	4,471399481	-1,89E+00	4,34E-03
91351	DExD/H-box 60 like	DDX60L	4,37777563	2,29E+00	1,94E-03
2118	ETS variant transcription factor 4	ETV4	4,148634003	-2,20E-01	2,66E-02
284355	tetrapeptide repeat homeobox 1	TPRX1	4,123911444	-2,02E+00	1,37E-02
251	alkaline phosphatase, germ cell	ALPG	4,018740181	2,56E-01	4,94E-03
55138	family with sequence similarity 90 member A1	FAM90A1	3,997838306	-6,56E-01	5,87E-03
441581	FSHD region gene 2 family member B	FRG2B	3,958422341	-8,52E-01	9,52E-03
94240	epithelial stromal interaction 1	EPSTI1	3,932269777	2,91E+00	6,00E-04
729974	ret finger protein like 4A like 1	RFPL4AL1	3,856398941	-1,09E+00	7,01E-03
85441	helicase with zinc finger 2	HELZ2	3,826776467	5,94E+00	1,16E-06
105378952	Kruppel like factor 18	KLF18	3,825434278	-1,53E+00	1,91E-02
10568	solute carrier family 34 member 2	SLC34A2	3,805964864	1,48E+00	1,61E-03
7425	VGF nerve growth factor inducible	VGF	3,80357545	4,91E-01	1,65E-02
6772	signal transducer and activator of transcription 1	STAT1	3,765288315	6,75E+00	3,85E-09
9246	ubiquitin conjugating enzyme E2 L6	UBE2L6	3,67772421	1,63E+00	2,87E-02
54809	sterile alpha motif domain containing 9	SAMD9	3,675010537	4,42E+00	1,64E-04
342931	ret finger protein like 4A	RFPL4A	3,526326594	7,73E-01	6,93E-03
151636	deltex E3 ubiquitin ligase 3L	DTX3L	3,519889022	4,42E+00	2,43E-04
55601	DExD/H-box helicase 60	DDX60	3,517366875	4,52E+00	4,36E-05
8900	cyclin A1	CCNA1	3,514457299	1,85E+00	1,88E-03
10739	ret finger protein like 2	RFPL2	3,48767341	-1,57E-02	7,48E-03
196120	SSU72 like 5	SSU72L5	3,484717499	-8,97E-01	1,74E-03
442247	ret finger protein like 4B	RFPL4B	3,479342501	9,48E-01	4,80E-03
7098	toll like receptor 3	TLR3	3,46606555	-1,07E+00	3,59E-02
136157	SSU72 like 6	SSU72L6	3,449041622	-9,14E-01	3,53E-06

Table 11: Top 50 differentially expressed genes in microglia 12 dpi with EBOV: downregulation. Top 50 downregulated genes in microglia 12 dpi with EBOV as per limma-voom differential gene expression analysis. FDR (Benjamini and Hochberg) cut-off $\leq$0.05, Log2FC$\geq$0.5. Ordered by absolute Log2FC in expression.

GeneID	Genename	Gene symbol	log2FC	Average expression	adjusted p-Value
283624	long intergenic non-protein coding RNA 641	LINC00641	-1,604829047	4,72E+00	3,20E-03
4145	megakaryocyte-associated tyrosine kinase	MATK	-1,430988887	3,68E+00	1,13E-04
1915	eukaryotic translation elongation factor 1 alpha 1	EEF1A1	-1,357608707	1,37E+01	1,28E-03
25890	ABI family member 3 binding protein	ABI3BP	-1,339038404	1,65E+00	7,96E-04
106635683	small nucleolar RNA, C/D box 141A	SNORD141A	-1,32981985	3,36E+00	1,80E-03
8793	TNF receptor superfamily member 10d	TNFRSF10D	-1,284746358	6,33E+00	1,39E-02
54510	protocadherin 18	PCDH18	-1,23056165	4,34E+00	5,14E-04
27098	clusterin like 1	CLUL1	-1,222646476	2,03E+00	3,66E-03
134145	ATP synthase c subunit lysine N-methyltransferase	ATPSCKMT	-1,217754783	4,45E+00	3,57E-03
92737	delta/notch like EGF repeat containing	DNER	-1,19438323	3,22E+00	2,18E-04

Table 11: Top 50 differentially expressed genes in microglia 12 dpi with EBOV: downregulation. Top 50 downregulated genes in microglia 12 dpi with EBOV as per limma-voom differential gene expression analysis. FDR (Benjamini and Hochberg) cut-off $\leq$0.05, Log2FC$\geq$0.5. Ordered by absolute Log2FC in expression.

GeneID	Genename	Gene symbol	log2FC	Average expression	adjusted p-Value
92960	peroxisomal biogenesis factor 11 gamma	PEX11G	-1,167470408	2,25E+00	1,79E-03
5071	parkin RBR E3 ubiquitin protein ligase	PRKN	-1,136630814	1,83E+00	2,87E-03
6122	ribosomal protein L3	RPL3	-1,083502679	1,17E+01	4,71E-04
164832	LON peptidase N-terminal domain and ring finger 2	LONRF2	-1,05218763	6,28E+00	1,83E-02
127833	synaptotagmin 2	SYT2	-1,046142124	3,59E+00	7,49E-04
5126	proprotein convertase subtilisin/kexin type 2	PCSK2	-1,043528965	5,78E+00	1,01E-02
57291	differentiation antagonizing non-protein coding RNA	DANCR	-1,03773134	4,68E+00	1,94E-03
6146	ribosomal protein L22	RPL22	-1,037267951	8,46E+00	9,36E-04
222166	maturin, neural progenitor differentiation regulator homolog	MTURN	-1,03148659	6,62E+00	4,81E-04
23145	SCO-spondin, pseudogene	SSPOP	-1,027873986	2,59E+00	1,92E-02
6202	ribosomal protein S8	RPS8	-1,024837018	1,06E+01	1,71E-04
3646	eukaryotic translation initiation factor 3 subunit E	EIF3E	-1,016633271	8,76E+00	2,59E-03
6125	ribosomal protein L5	RPL5	-1,014346156	9,80E+00	4,47E-03
9349	ribosomal protein L23	RPL23	-1,009313491	9,50E+00	4,72E-05
112609	melanocortin 2 receptor accessory protein 2	MRAP2	-1,002950271	2,18E+00	7,81E-04
121053	NOP protein chaperone 1	NOPCHAP1	-0,989863741	4,44E+00	1,86E-03
139221	PWWP domain containing 3B	PWWP3B	-0,98402632	2,66E+00	1,22E-03
6194	ribosomal protein S6	RPS6	-0,978523299	1,07E+01	2,35E-04
55531	ELMO domain containing 1	ELMOD1	-0,963167176	2,43E+00	8,11E-04
100500804	microRNA 3654	MIR3654	-0,958206854	2,86E+00	4,19E-03
6129	ribosomal protein L7	RPL7	-0,957482459	9,98E+00	2,21E-03
9315	neuronal regeneration related protein	NREP	-0,952330287	7,12E+00	3,87E-03
375057	stum, mechanosensory transduction mediator homolog	STUM	-0,947988072	3,92E+00	1,16E-04
10233	leucine rich repeat containing 23	LRRC23	-0,947843056	2,31E+00	1,35E-03
728658	ribosomal protein L13a pseudogene 5	RPL13AP5	-0,946428472	4,86E+00	1,01E-04
79635	coiled-coil domain containing 121	CCDC121	-0,944065978	2,95E+00	2,48E-03
91893	ferredoxin-fold anticodon binding domain containing 1	FDXACB1	-0,940739624	1,97E+00	2,92E-02
6128	ribosomal protein L6	RPL6	-0,93236364	1,01E+01	6,23E-04
55277	FGGY carbohydrate kinase domain containing	FGGY	-0,929433091	2,08E+00	3,04E-03
6228	ribosomal protein S23	RPS23	-0,928656558	1,02E+01	1,02E-03
64798	DEP domain containing MTOR interacting protein	DEPTOR	-0,924535722	2,74E+00	5,60E-04
5859	glutaminyl-tRNA synthetase 1	QARS1	-0,923886852	8,54E+00	4,04E-04
3488	insulin like growth factor binding protein 5	IGFBP5	-0,920596442	7,24E+00	1,28E-03
100507032	TMCC1 divergent transcript	TMCC1-DT	-0,914255178	2,09E+00	7,57E-03
4673	nucleosome assembly protein 1 like 1	NAP1L1	-0,910770523	9,92E+00	2,91E-03
7102	tetraspanin 7	TSPAN7	-0,91042507	5,33E+00	1,25E-04
6229	ribosomal protein S24	RPS24	-0,908419905	9,83E+00	2,67E-04
4255	O-6-methylguanine-DNA methyltransferase	MGMT	-0,906583146	4,95E+00	4,59E-04
23521	ribosomal protein L13a	RPL13A	-0,904848946	1,16E+01	1,48E-04
64418	transmembrane protein 168	TMEM168	-0,903069071	5,06E+00	5,12E-03

Table 12: Top 50 differentially expressed genes in astrocytes 12 dpi with EBOV: upregulation. Top 50 upregulated genes in astrocytes 12 dpi with EBOV as per limma-voom differential gene expression analysis. FDR (Benjamini and Hochberg) cut-off $\leq$0.05, Log2FC$\geq$0.5. Ordered by absolute Log2FC in expression.

GeneID	Genename	Gene symbol	log2FC	Average expression	adjusted p-Value
56901	NDUFA4 mitochondrial complex associated like 2	NDUFA4L2	2,890895789	7,44E-01	2,96E-04
768	carbonic anhydrase 9	CA9	1,852219147	3,98E+00	4,29E-03
51129	angiopoietin like 4	ANGPTL4	1,579443255	7,11E-01	2,86E-02
226	aldolase, fructose-bisphosphate A	ALDOA	1,435386595	2,12E+00	2,66E-04

Table 12: Top 50 differentially expressed genes in astrocytes 12 dpi with EBOV: upregulation. Top 50 upregulated genes in astrocytes 12 dpi with EBOV as per limma-voom differential gene expression analysis. FDR (Benjamini and Hochberg) cut-off $\leq$0.05, Log2FC$\geq$0.5. Ordered by absolute Log2FC in expression.

GeneID	Genename	Gene symbol	log2FC	Average expression	adjusted p-Value
9518	growth differentiation factor 15	GDF15	1,43393341	2,64E+00	3,26E-04
968	CD68 molecule	CD68	1,21016345	4,93E+00	9,94E-04
284716	ribosomal modification protein rimK like family member A	RIMKLA	1,12088305	2,23E+00	3,67E-03
230	aldolase, fructose-bisphosphate C	ALDOC	1,120623814	6,88E+00	3,91E-03
6781	stanniocalcin 1	STC1	1,0739704	4,78E+00	5,52E-05
114757	cytoglobin	CYGB	1,031868089	2,85E+00	7,64E-04
64093	SPARC related modular calcium binding 1	SMOC1	1,025196977	3,51E+00	2,49E-04
10397	N-myc downstream regulated 1	NDRG1	1,020650029	6,58E+00	3,34E-03
3914	laminin subunit beta 3	LAMB3	1,013562798	3,09E+00	4,30E-04
9314	Kruppel like factor 4	KLF4	1,004700714	2,37E+00	2,18E-03
91584	plexin A4	PLXNA4	0,959547791	2,76E+00	5,12E-04
9235	interleukin 32	IL32	0,958814076	4,22E+00	1,35E-02
7851	mal, T cell differentiation protein like	MALL	0,931576257	3,00E+00	4,29E-03
8655	dynein light chain LC8-type 1	DYNLL1	0,930409738	8,10E+00	3,39E-03
2118	ETS variant transcription factor 4	ETV4	0,928762008	3,22E+00	1,67E-03
8794	TNF receptor superfamily member 10c	TNFRSF10C	0,921494339	2,05E+00	9,46E-03
8862	apelin	APLN	0,903588327	3,49E+00	3,18E-04
54541	DNA damage inducible transcript 4	DDIT4	0,894786301	6,05E+00	6,64E-03
79924	adrenomedullin 2	ADM2	0,889234086	2,42E+00	5,99E-03
8061	FOS like 1, AP-1 transcription factor subunit	FOSL1	0,889186812	4,85E+00	4,88E-03
5210	6-phosphofructo-2-kinase/fructose-2,6-biphosphatase 4	PFKFB4	0,876968618	5,45E+00	8,61E-04
1950	epidermal growth factor	EGF	0,871677389	2,22E+00	2,81E-03
11247	neurexophilin 4	NXPH4	0,848474547	3,03E+00	1,98E-03
3755	potassium voltage-gated channel modifier subfamily G member 1	KCNG1	0,84288904	1,83E+00	3,82E-02
8793	TNF receptor superfamily member 10d	TNFRSF10D	0,838183307	6,60E+00	2,74E-04
7052	transglutaminase 2	TGM2	0,828110798	5,77E+00	4,84E-03
1026	cyclin dependent kinase inhibitor 1A	CDKN1A	0,824959685	8,13E+00	3,47E-03
64073	chromosome 19 open reading frame 33	C19orf33	0,820424458	2,04E+00	1,84E-02
80274	signal peptide, CUB domain and EGF like domain containing 1	SCUBE1	0,802208451	1,27E+00	5,62E-02
1373	carbamoyl-phosphate synthase 1	CPS1	0,798324883	4,03E+00	1,93E-03
1893	extracellular matrix protein 1	ECM1	0,797598583	6,35E+00	3,90E-04
25789	transmembrane protein 59 like	TMEM59L	0,789342093	1,97E+00	1,84E-04
1890	thymidine phosphorylase	TYMP	0,774878683	8,54E-01	1,39E-02
610	hyperpolarization activated cyclic nucleotide gated potassium and sodium channel 2	HCN2	0,75165725	2,18E+00	3,82E-02
9610	Ras and Rab interactor 1	RIN1	0,749473499	3,71E+00	5,67E-04
80164	proline rich 36	PRR36	0,747092349	2,95E+00	1,69E-03
3783	potassium calcium-activated channel subfamily N member 4	KCNN4	0,745579593	2,22E+00	1,25E-02
6676	sperm associated antigen 4	SPAG4	0,744451174	2,33E+00	1,25E-02
23551	RASD family member 2	RASD2	0,744056517	2,57E+00	5,76E-03
9022	chloride intracellular channel 3	CLIC3	0,740064718	2,88E+00	3,56E-03
84331	MAPK regulated corepressor interacting protein 2	MCRIP2	0,738182074	2,33E+00	4,37E-03
220	aldehyde dehydrogenase 1 family member A3	ALDH1A3	0,727358429	3,05E+00	2,31E-02
57165	gap junction protein gamma 2	GJC2	0,718588497	2,22E+00	1,24E-02
79365	basic helix-loop-helix family member e41	BHLHE41	0,716604851	2,34E+00	2,01E-02
643988	fibronectin type III domain containing 10	FNDC10	0,712099535	2,89E+00	6,31E-03
3656	interleukin 1 receptor associated kinase 2	IRAK2	0,705103991	3,34E+00	5,73E-04

Table 13: Top 50 differentially expressed genes in astrocytes 12 dpi with EBOV: downregulation. Top 50 downregulated genes in astrocytes 12 dpi with EBOV as per limma-voom differential gene expression analysis. FDR (Benjamini and Hochberg) cut-off $\leq$0.05, Log2FC$\geq$0.5. Ordered by absolute Log2FC in expression.

GeneID	Genename	Gene symbol	log2FC	Average expression	adjusted p-Value
100506321	uncharacterized LOC100506321	LOC100506321	-7,596484189	1,52E+00	6,51E-14
100130701	LRRC58 divergent transcript	LRRC58-DT	-6,5034652	3,12E+00	6,41E-13
101448202	uncharacterized LOC101448202	LOC101448202	-6,22580544	1,53E+00	2,78E-06
104968399	MYL12A and MYL12B antisense RNA 1	MYL12-AS1	-6,148778835	2,18E+00	6,35E-07
245973	ATPase H+ transporting V1 subunit C2	ATP6V1C2	-6,027154223	1,36E+00	1,96E-07
100861402	CERS6 antisense RNA 1	CERS6-AS1	-5,992265955	1,56E+00	3,32E-11
142686	ankyrin repeat and SOCS box containing 14	ASB14	-5,749430058	1,57E+00	8,53E-06
100507118	PRC1 antisense RNA 1	PRC1-AS1	-5,734614235	2,78E+00	7,13E-11
112268460	uncharacterized LOC112268460	LOC112268460	-5,696429369	1,70E+00	4,06E-10
101927117	PLCG1 antisense RNA 1	PLCG1-AS1	-5,474605968	2,00E+00	7,13E-11
105371260	LIX1L antisense RNA 1	LIX1L-AS1	-5,353956123	1,52E+00	7,13E-11
107984340	uncharacterized LOC107984340	LOC107984340	-5,298796426	2,24E+00	1,27E-07
100874085	NUCB1 antisense RNA 1	NUCB1-AS1	-5,079884073	1,64E+00	8,19E-10
105369968	uncharacterized LOC105369968	LOC105369968	-4,606640267	2,44E+00	1,14E-08
109136579	TALAM1 transcript, MALAT1 antisense RNA	TALAM1	-3,996219983	1,40E+00	9,28E-07
107984643	uncharacterized LOC107984643	LOC107984643	-3,974915387	1,66E+00	3,02E-09
7439	bestrophin 1	BEST1	-3,811529709	4,47E+00	1,73E-04
284618	RUSC1 antisense RNA 1	RUSC1-AS1	-3,358565737	2,29E+00	2,01E-06
100302254	microRNA 1282	MIR1282	-3,311925433	3,38E+00	5,67E-04
107985034	uncharacterized LOC107985034	LOC107985034	-3,145134387	1,59E+00	2,01E-06
79856	sorting nexin 22	SNX22	-3,131959829	3,89E+00	2,83E-07
155185	archaelysin family metallopeptidase 1	AMZ1	-3,104539014	1,65E+00	2,76E-06
100128494	uncharacterized LOC100128494	LOC100128494	-3,081978662	2,48E+00	7,80E-05
84852	ATP1A1 antisense RNA 1	ATP1A1-AS1	-2,84113186	2,85E+00	1,98E-05
112268170	uncharacterized LOC112268170	LOC112268170	-2,809061115	1,93E+00	1,68E-06
112268030	uncharacterized LOC112268030	LOC112268030	-2,79693173	1,61E+00	2,01E-04
401944	low density lipoprotein receptor class A domain containing 2	LDLRAD2	-2,705479882	1,85E+00	1,27E-05
100129148	uncharacterized LOC100129148	LOC100129148	-2,575397674	1,86E+00	2,08E-05
100506755	mir-497-195 cluster host gene	MIR497HG	-2,572602763	1,61E+00	7,80E-05
400960	PCBP1 antisense RNA 1	PCBP1-AS1	-2,402117312	3,44E+00	2,23E-05
100507156	lysyl oxidase like 2 antisense RNA 1	LOXL2-AS1	-2,378322312	1,57E+00	6,94E-05
105371450	THBS3 antisense RNA 1	THBS3-AS1	-1,964654032	2,28E+00	2,78E-06
101927895	EMC1 antisense RNA 1	EMC1-AS1	-1,887189148	2,55E+00	3,18E-04
4541	NADH dehydrogenase subunit 6	ND6	-1,715629678	6,82E+00	1,86E-02
100507347	VIM antisense RNA 1	VIM-AS1	-1,556853725	4,43E+00	1,18E-02
100652758	uncharacterized LOC100652758	LOC100652758	-1,341764854	1,85E+00	8,96E-03
100286925	PPM1F antisense RNA 1	PPM1F-AS1	-1,286939762	1,99E+00	5,51E-04
9866	tripartite motif containing 66	TRIM66	-1,196485611	3,17E+00	2,00E-03
100861548	PINK1 antisense RNA	PINK1-AS	-1,155312791	3,21E+00	8,75E-05
107984950	uncharacterized LOC107984950	LOC107984950	-1,070302869	2,71E+00	6,94E-05
414149	acyl-CoA binding domain containing 7	ACBD7	-0,968856837	5,14E+00	2,78E-06
10734	stromal antigen 3	STAG3	-0,968252655	1,72E+00	1,77E-02
3077	homeostatic iron regulator	HFE	-0,958021811	4,37E+00	1,38E-04
348110	actin related protein 2/3 complex inhibitor	ARPIN	-0,94396579	6,25E+00	2,79E-06
6876	transgelin	TAGLN	-0,941183259	7,79E+00	4,63E-03
442582	stromal antigen 3-like 2 (pseudogene)	STAG3L2	-0,878743488	3,25E+00	4,50E-02
4166	carbohydrate sulfotransferase 6	CHST6	-0,835204462	2,21E+00	3,50E-03
3486	insulin like growth factor binding protein 3	IGFBP3	-0,830267745	5,56E+00	2,31E-02
347862	glutamine amidotransferase class 1 domain containing 1	GATD1	-0,818947459	6,68E+00	4,65E-04
3336	heat shock protein family E (Hsp10) member 1	HSPE1	-0,815480682	2,21E+00	1,65E-02

6.5.2 The transcriptome of microglia and astrocytes persistently infected with EBOV for 20 days.

Considering that the viability of microglia and astrocyte 2D cell cultures can be maintained until at least 25 dpi with EBOV, as well as the differential replication pattern upon LASV infection, further transcriptomic analyses were undertaken at 20 dpi with EBOV and LASV in immortalized human microglia and astrocytes. As shown in Figure 55, at 20 dpi when RNA was collected, EBOV replication had previously peaked in microglia, and based on previous results could represent the late-phase of persistent infection (Figure 40). Meanwhile, in astrocytes, the initial peak had also occurred, while at 20 dpi replication of EBOV was rising slowly during its persistent phase at the time of RNA collection (Figure 55). In LASV infected microglia, at 20 dpi, the virus had been cleared for over 7 days while in astrocytes infected with LASV, replication was at its second peak at the time of sample collection.

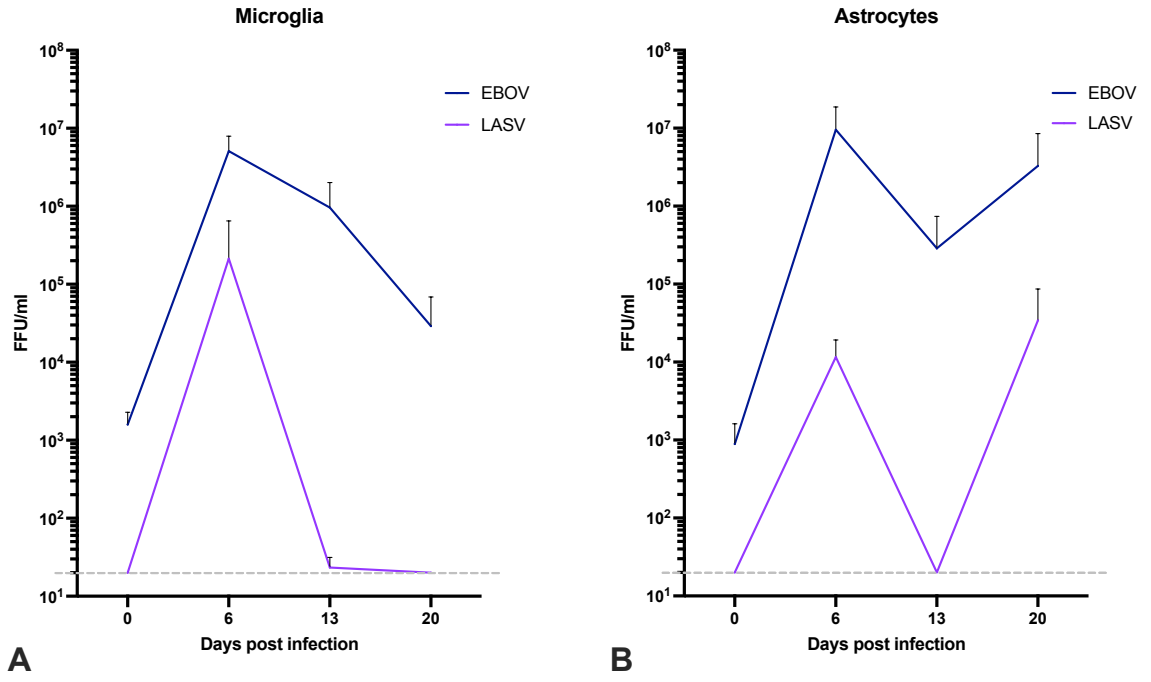


Figure 55: Replication of EBOV and LASV in microglia and astrocytes before sequencing 20dpi. Mean (+SD) viral titers [FFU/ml] of microglia and astrocytes infected with EBOV (blue) or LASV (purple) (n=6, MOI=0.0025). N=2 of each were pooled for total RNA sequencing of n=3 samples per group. LOD at 20 FFU/ml indicated as grey dotted line.

The transcriptome of the groups 20 dpi (n=3) was widely different, as is shown in the PCA in Figure 56 (A, B). Here, particularly EBOV-infected microglia clustered farthest away from the respective control, as well as LASV-infected microglia. Notably, LASV-infected microglia, that had cleared the virus, were seemingly at baseline regarding their gene expression. At the same time, astrocyte transcriptomic shifts upon EBOV or LASV infection were overall less pronounced than those observed in microglia, as shown by their close clustering in the first

two dimensions of the PCA (Figure 56 (A)). Besides this, EBOV-infected astrocytes at 20 dpi were more responsive than LASV-infected astrocytes, although LASV was still replicating at this time (Figure 56 (B)).

The lack of overall transcriptomic shifts upon LASV infection was reflected in the amount of DEGs, whereby microglia infected with LASV upregulated 14 and downregulated only one gene (ETV5 -0.8 Log2FC) above the Log2FC threshold of 0.5 (Figure 56 (C, D)). The top 10 upregulated genes comprised SAMD11 (1.0 Log2FC), LOC107985728, PGGHG, PLPPR3, GMPR, PCSK1N, WFDC2, LRRN2, KCNH2, and CDK18 (0.6 Log2FC). In astrocytes, there was only one gene significantly upregulated 20 dpi with LASV, namely WSB1 (0.5 Log2FC). No pathway enrichment was possible for the LASV-infected groups.

In microglia infected with EBOV, 2316 genes were upregulated and 1744 downregulated at 20 dpi (Log2FC$\geq$0.5). Among the top 10 of upregulated genes, mostly antiviral and proinflammatory genes clustered: OAS1 (12.6 Log2FC), OAS2, MX2, XAF1, PASL2, IFNB1, IFI44L, IFIT1, IFIT3, and IFI44 (7.7 Log2FC) (Table 14). Notably, unlike 12 dpi as previously described, GO Term enrichment of biological processes did not predominantly include an antiviral response (Figure 57 (A)). Most enriched pathways included ”circulatory system development”, ”cell migration”, ”positive regulation of signaling” and ”cell population proliferation” as well as further proliferative and developmental pathways. Only three enriched pathways ”cellular response to chemical stimulus”, ”response to organic substance”, and ”regulation of response to stimulus” were indicative of an ongoing infection. As further detailed via KEGG enrichment in microglia in Figure 57 (B), 20 dpi with EBOV pathways enriched were the ”p53 signaling pathway”, diverse cancer pathways as well as infection pathways with Human Papilloma virus (HPV) and Herpes Simplex virus 1 (HSV-1).

The top 10 downregulated genes in microglia 20 dpi with EBOV included KRTAP19-1 (-4.2 Log2FC), IL33, POSTN, TRNP, ABCA1, IGFN1, HIF3A, LOC105375222, PCSK2, and IGFBP5 (-2.6 Log2FC) (Table 20). Here, most downregulated biological processes, as shown in Figure 57 (C), comprised ”GPI anchor metabolic processes”, ”tRNA modification”, and ”mitochondrial translation” as well as further metabolic and biosynthesis processes. This was further underlined by KEGG enrichment, where ”GPI-anchor biosynthesis” was most downregulated followed by biosynthesis and metabolic pathways (Figure 57 (C)). Except for GPI-anchor regulation, this was mostly in line with findings made 12 dpi in microglia.

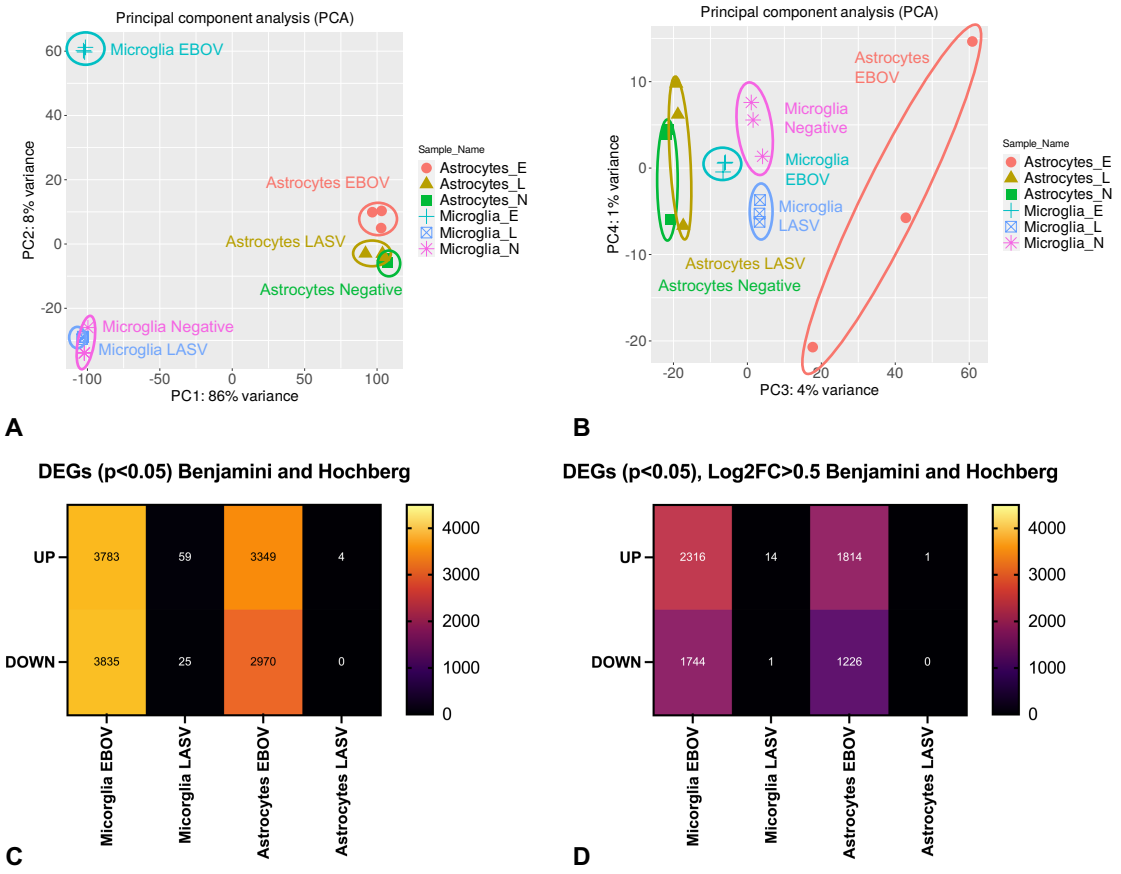


Figure 56: PCA and DEGs in microglia and astrocytes 20 dpi with EBOV, or LASV. (A) Principal component analysis (PCA) of transcriptomic data of microglia or astrocytes 20 dpi with EBOV or LASV. PC1 (86 % variance) and PC2 (8 % variance). **(B)** PCA plotting PC3 (4 % of variance) and PC4 (1 % of variance). **(C)** Differentially up- (UP) or downregulated (DOWN) genes (DEGs) reaching the FDR cut-off ($p \leq 0.05$). **(D)** Significantly up- or downregulated genes with a Log2FC$\geq$0.5. N=2 of each were pooled for total RNA sequencing of n=3 samples per group.

In astrocytes, EBOV infection for 20 days led to the upregulation of 1814 and downregulation of 1226 genes (Figure 56 (D)). The upregulated genes included the following top 10 genes: TMEM132B (7.4 Log2FC), IL1B, SBSN, CCND2, THBD, SHPA6, CDHR1, CXCL8, ADAMTS6, RPSAP52 (4.7 Log2FC) (Table 18). As shown via GO Term enrichment of biological processes, most enrichment occurred in regulatory, migratory, or morphogenic pathways as previously seen 12 dpi, for instance ”regulation of anatomical structure morphogenesis” and ”cell migration” (Figure 57 (E)). One ”regulation of response to stimulus” pathway was further enriched. Enriched KEGG pathways included ”steroid biosynthesis”, ”TNF signaling pathway” and ”IL-17 signaling pathway” as well as other signaling pathways and some parasitic and HPV pathway enrichment. Overall, this was similar to the transcriptomic shifts of astrocytes 12 dpi with EBOV (Figure 57 (F)).

The most downregulated genes in astrocytes 20 days after EBOV infection were COL15A1 (-4.7 Log2FC), TNFSF18, PLCE1-AS1, LYPD6B, HSD17B2, ANGPTL4, PDGFD, CPA4,

EDN2, and KCNH1 (-3.6 Log2FC) (Table 19). Biological processes most downregulated were ”renal system development”, and ”response to oxygen levels” as well as further developmental pathways (Figure 57 (G)). Meanwhile, KEGG mapping further revealed a decrease in ”fatty acid elongation”, ”biosynthesis of unsaturated fatty acids”, ”TGF-beta signaling pathway” as well as further signaling pathways and the ”regulation of actin cytoskeleton” (Figure 57 (H)).

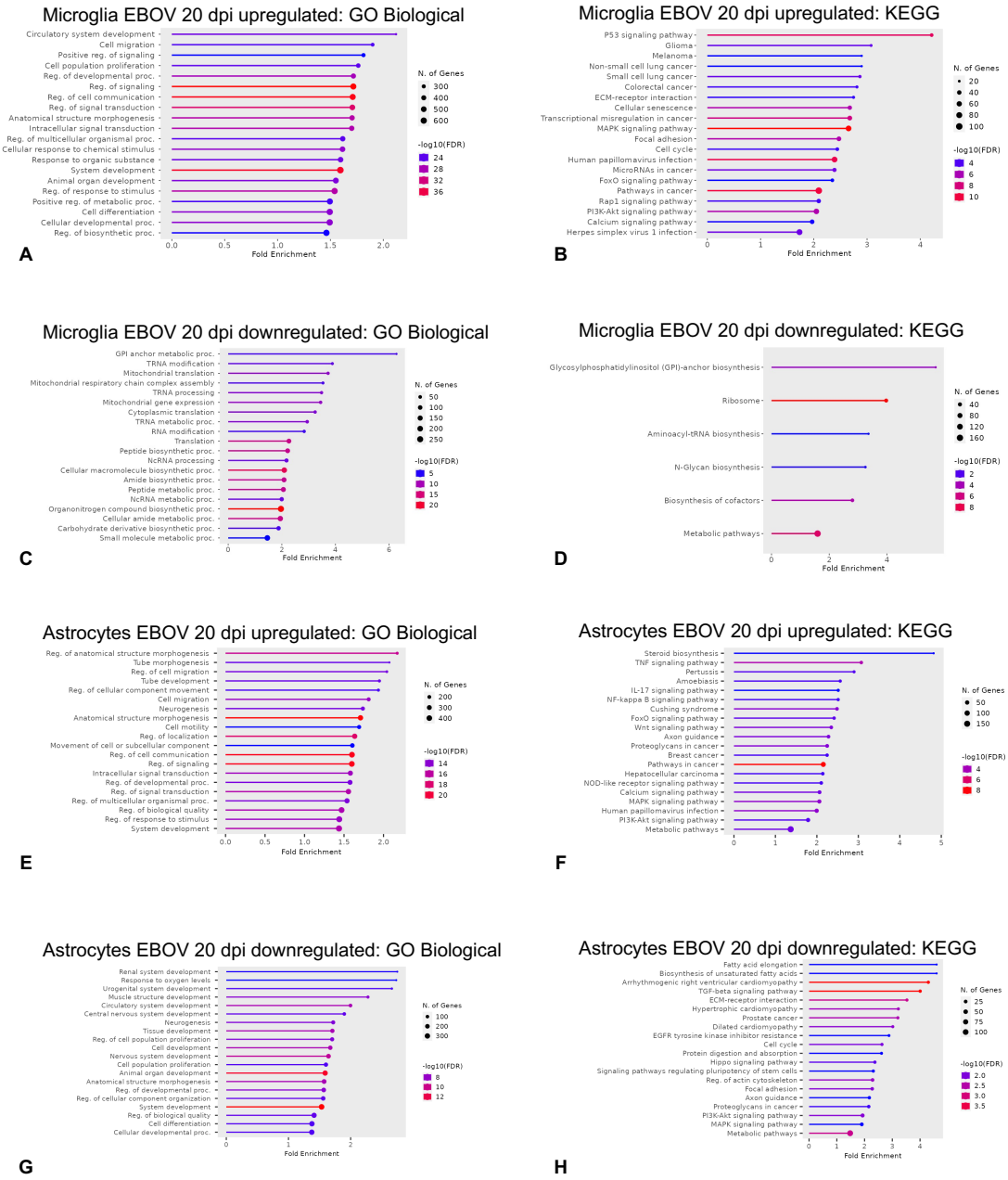


Figure 57: GO-Term and KEGG enrichment in microglia and astrocytes 20dpi with EBOV. GO-Term (Biological Process) and KEGG pathways enrichment in microglia or astrocytes 20dpi of genes significantly up- or downregulated Log2FC$\geq$0.5. **(A)** GO Biological EBOV upregulated genes microglia, **(B)** KEGG EBOV upregulated genes microglia, **(C)** GO Biological EBOV downregulated genes microglia, **(D)** KEGG EBOV downregulated genes microglia, **(E)** GO Biological EBOV upregulated genes astrocytes, **(F)** KEGG EBOV upregulated genes astrocytes, **(G)** GO Biological EBOV downregulated genes astrocytes, **(H)** KEGG EBOV downregulated genes astrocytes.

Taken together, it may therefore be concluded that 20 dpi, previously LASV-infected mi-

croglia or astrocytes were seemingly at baseline regarding their gene expression. In contrast, EBOV-infected astrocytes, like at 12 dpi, mostly responded via regulatory and morphogenic pathways. Notably, 20 dpi, proinflammatory genes were still highly upregulated in microglia, nevertheless, pathway enrichment additionally included regulatory response pathways comprising migratory and proliferative activity. Conclusively, long-term infection of microglia with EBOV seemingly provided more traces of a balanced antiviral response at later time points, which is more similar to the regulated astrocytes.

Table 14: Top 50 differentially expressed genes in microglia 20 dpi with EBOV: upregulation. Top 50 upregulated genes in microglia 20 dpi with EBOV as per limma-voom differential gene expression analysis. FDR (Benjamini and Hochberg) cut-off $\leq$0.05, Log2FC$\geq$0.5. Ordered by absolute Log2FC in expression.

GeneID	Genename	Gene symbol	log2FC	Average expression	adjusted p-Value
4938	2'-5'-oligoadenylate synthetase 1	OAS1	12,62444848	5,05E-01	3,03E-09
4939	2'-5'-oligoadenylate synthetase 2	OAS2	12,45417997	-4,49E-01	5,99E-12
4600	MX dynamin like GTPase 2	MX2	11,13163834	-1,09E+00	1,72E-10
54739	XIAP associated factor 1	XAF1	10,74924158	-1,94E+00	1,58E-09
8638	2'-5'-oligoadenylate synthetase like	OASL	9,869853857	3,91E-02	2,05E-10
3456	interferon beta 1	IFNB1	8,80915834	-3,83E+00	1,04E-09
10964	interferon induced protein 44 like	IFI44L	8,645614785	2,21E+00	2,64E-09
3434	interferon induced protein with tetratricopeptide repeats 1	IFIT1	8,306115466	3,37E+00	9,65E-16
3437	interferon induced protein with tetratricopeptide repeats 3	IFIT3	8,024603645	4,07E+00	5,18E-15
10561	interferon induced protein 44	IFI44	7,706435323	2,18E+00	2,90E-12
8542	apolipoprotein L1	APOL1	7,580258811	5,85E-01	2,66E-07
64135	interferon induced with helicase C domain 1	IFIH1	7,076762849	3,17E+00	4,53E-14
92736	otopetrin 2	OTOP2	7,067072292	-3,07E+00	7,29E-08
3433	interferon induced protein with tetratricopeptide repeats 2	IFIT2	7,055994879	3,51E+00	4,92E-13
91543	radical S-adenosyl methionine domain containing 2	RSAD2	7,005505447	-7,26E-01	7,95E-12
9636	ISG15 ubiquitin like modifier	ISG15	6,799044758	4,20E+00	1,88E-15
55281	transmembrane protein 140	TMEM140	6,753772848	-1,15E+00	6,80E-11
4940	2'-5'-oligoadenylate synthetase 3	OAS3	6,697137584	5,44E+00	3,20E-14
2537	interferon alpha inducible protein 6	IFI6	6,642583264	5,14E+00	6,23E-14
80830	apolipoprotein L6	APOL6	6,598177544	3,08E+00	8,98E-08
101928106	long intergenic non-protein coding RNA 2522	LINC02522	6,472855292	-2,37E+00	5,12E-07
400620	long intergenic non-protein coding RNA 2092	LINC02092	6,207740168	-3,11E+00	6,94E-10
124901177	uncharacterized LOC124901177	LOC124901177	6,150458762	-3,22E+00	1,67E-09
4599	MX dynamin like GTPase 1	MX1	6,149347847	3,03E+00	2,16E-12
2633	guanylate binding protein 1	GBP1	6,134744051	1,88E+00	1,88E-08
51296	solute carrier family 15 member 3	SLC15A3	6,0083414	1,11E+00	3,24E-06
105221694	BST2 interferon stimulated positive regulator	BISPR	6,008098351	8,51E-01	1,27E-11
219285	sterile alpha motif domain containing 9 like	SAMD9L	5,91272215	1,60E+00	1,41E-09
10346	tripartite motif containing 22	TRIM22	5,844565271	3,92E+00	2,08E-10
124901923	uncharacterized LOC124901923	LOC124901923	5,80547577	2,77E-01	3,54E-07
79132	DExH-box helicase 58	DHX58	5,739698967	-1,86E-01	1,74E-10
124903135	uncharacterized LOC124903135	LOC124903135	5,72594374	5,59E-02	1,26E-11
2635	guanylate binding protein 3	GBP3	5,677583542	1,42E+00	2,18E-07
684	bone marrow stromal cell antigen 2	BST2	5,658279176	4,75E+00	9,65E-11
124906099	uncharacterized LOC124906099	LOC124906099	5,65501721	-1,91E+00	4,88E-07
2118	ETS variant transcription factor 4	ETV4	5,600687632	4,31E+00	7,70E-12
23205	acyl-CoA synthetase bubblegum family member 1	ACSBG1	5,561326835	-2,92E-01	2,82E-08
84875	poly(ADP-ribose) polymerase family member 10	PARP10	5,508244616	3,87E+00	3,83E-12
1543	cytochrome P450 family 1 subfamily A member 1	CYP1A1	5,487234186	3,07E-01	6,18E-07
124903995	uncharacterized LOC124903995	LOC124903995	5,453280428	-2,58E+00	1,14E-09

Table 14: Top 50 differentially expressed genes in microglia 20 dpi with EBOV: upregulation. Top 50 upregulated genes in microglia 20 dpi with EBOV as per limma-voom differential gene expression analysis. FDR (Benjamini and Hochberg) cut-off $\leq$0.05, Log2FC$\geq$0.5. Ordered by absolute Log2FC in expression.

GeneID	Genename	Gene symbol	log2FC	Average expression	adjusted p-Value
649137	zinc finger and SCAN domain containing 5C	ZSCAN5C	5,411786073	-3,01E+00	6,44E-10
100134391	uncharacterized LOC100134391	LOC100134391	5,395892612	-2,49E+00	9,18E-10
81551	stathmin 4	STMN4	5,381159348	-1,66E+00	2,08E-11
7113	transmembrane serine protease 2	TMPRSS2	5,353246128	-2,44E+00	1,70E-08
124902696	uncharacterized LOC124902696	LOC124902696	5,275795938	3,56E-01	9,05E-11
5920	phospholipase A and acyltransferase 4	PLAAT4	5,220777772	5,07E-01	4,64E-03
55138	family with sequence similarity 90 member A1	FAM90A1	5,218014511	3,84E-01	8,81E-09
389384	BCL2 interacting protein 5	BNIP5	5,187696192	-2,16E+00	2,31E-08
124901385	uncharacterized LOC124901385	LOC124901385	5,151663758	-2,66E+00	5,08E-07
729083	CCDC13 antisense RNA 2	CCDC13-AS2	5,144760579	-2,71E+00	2,25E-09

Table 15: Top 50 differentially expressed genes in microglia 20 dpi with EBOV: downregulation. Top 50 downregulated genes in microglia 20 dpi with EBOV as per limma-voom differential gene expression analysis. FDR (Benjamini and Hochberg) cut-off $\leq$0.05, Log2FC$\geq$0.5. Ordered by absolute Log2FC in expression.

GeneID	Genename	Gene symbol	log2FC	Average expression	adjusted p-Value
337882	keratin associated protein 19-1	KRTAP19-1	-4,150302725	-1,13E+00	7,52E-06
90865	interleukin 33	IL33	-4,091751426	-1,63E+00	3,73E-07
10631	periostin	POSTN	-3,926643942	-4,99E-01	1,38E-06
4571	tRNA-Pro	TRNP	-3,919471151	-2,29E-01	2,06E-04
19	ATP binding cassette subfamily A member 1	ABCA1	-3,456860765	1,94E+00	6,05E-03
91156	immunoglobulin like and fibronectin type III domain containing 1	IGFN1	-3,425741747	7,38E-03	1,47E-03
64344	hypoxia inducible factor 3 subunit alpha	HIF3A	-3,041500068	8,71E-01	3,71E-05
105375222	uncharacterized LOC105375222	LOC105375222	-2,830153855	-1,26E+00	1,46E-08
5126	proprotein convertase subtilisin/kexin type 2	PCSK2	-2,708346922	9,85E-01	3,10E-09
3488	insulin like growth factor binding protein 5	IGFBP5	-2,614385711	5,10E+00	1,26E-04
54510	protocadherin 18	PCDH18	-2,530318319	3,52E+00	8,19E-06
54553	MIR4453 host gene	MIR4453HG	-2,445393381	1,92E+00	2,23E-09
55273	transmembrane protein 100	TMEM100	-2,436030527	2,14E+00	6,86E-04
284339	transmembrane protein 145	TMEM145	-2,389801846	8,35E-01	6,12E-08
30832	zinc finger protein 354C	ZNF354C	-2,347430304	6,66E-01	7,94E-03
5139	phosphodiesterase 3A	PDE3A	-2,340431472	2,28E+00	2,39E-04
2596	growth associated protein 43	GAP43	-2,335766885	-6,26E-01	6,02E-05
8641	protocadherin gamma subfamily B, 4	PCDHGB4	-2,308831772	1,07E+00	3,74E-03
60506	nyctalopin	NYX	-2,287195673	-1,13E+00	1,54E-08
200895	dihydrofolate reductase 2	DHFR2	-2,285259197	2,89E+00	3,92E-08
9315	neuronal regeneration related protein	NREP	-2,274318836	6,42E+00	6,03E-10
56892	transcriptional and immune response regulator	TCIM	-2,249779048	8,70E-01	1,61E-04
5105	phosphoenolpyruvate carboxykinase 1	PCK1	-2,225529518	-9,04E-01	4,76E-05
643866	cerebellin 3 precursor	CBLN3	-2,215810679	8,88E-01	5,69E-05
27098	clusterin like 1	CLUL1	-2,178215865	-6,10E-01	2,37E-06
11096	ADAM metallopeptidase with thrombospondin type 1 motif 5	ADAMTS5	-2,151700788	2,82E+00	1,06E-07
54331	G protein subunit gamma 2	GNG2	-2,125415275	3,79E+00	4,18E-08
646903	uncharacterized LOC646903	LOC646903	-2,125191802	8,84E-01	2,90E-07
254013	electron transfer flavoprotein subunit beta lysine methyltransferase	ETFBKMT	-2,122464949	1,14E+00	1,23E-06
283624	long intergenic non-protein coding RNA 641	LINC00641	-2,057771344	4,39E+00	2,08E-10
84812	phospholipase C delta 4	PLCD4	-2,022655759	1,91E+00	1,20E-03
132158	glycerate kinase	GLYCTK	-2,020551704	2,37E+00	7,05E-06
10161	lysophosphatidic acid receptor 6	LPAR6	-2,002441799	1,12E+00	6,76E-09

Table 15: Top 50 differentially expressed genes in microglia 20 dpi with EBOV: downregulation. Top 50 downregulated genes in microglia 20 dpi with EBOV as per limma-voom differential gene expression analysis. FDR (Benjamini and Hochberg) cut-off $\leq$0.05, Log2FC$\geq$0.5. Ordered by absolute Log2FC in expression.

GeneID	Genename	Gene symbol	log2FC	Average expression	adjusted p-Value
11191	phosphatase and tensin homolog pseudogene 1	PTENP1	-1,979043022	6,02E-01	4,15E-06
375519	gap junction protein beta 7	GJB7	-1,968954661	-1,85E+00	2,63E-04
84842	4-hydroxyphenylpyruvate dioxygenase like	HPDL	-1,962305227	1,80E+00	2,55E-07
2563	gamma-aminobutyric acid type A receptor subunit delta	GABRD	-1,944254647	3,73E-02	4,44E-06
4485	macrophage stimulating 1	MST1	-1,930272561	2,94E+00	5,69E-08
374907	UDP-GlcNAc:betaGal beta-1,3-N-acetylglucosaminyltransferase 8	B3GNT8	-1,920339034	1,71E+00	1,40E-08
64418	transmembrane protein 168	TMEM168	-1,908680008	4,73E+00	1,14E-09
56099	protocadherin gamma subfamily B, 7	PCDHGB7	-1,898651798	3,08E+00	2,70E-05
400960	PCBP1 antisense RNA 1	PCBP1-AS1	-1,88917342	2,76E+00	6,18E-06
133022	translocation associated membrane protein 1 like 1	TRAM1L1	-1,885766553	2,62E+00	5,46E-07
87769	gamma-glutamylamine cyclotransferase	GGACT	-1,869591294	2,25E+00	5,91E-06
26025	protocadherin gamma subfamily A, 12	PCDHGA12	-1,817507298	1,22E+00	3,15E-02
64714	protein disulfide isomerase family A member 2	PDIA2	-1,801650997	7,16E-01	2,87E-06
80270	hydroxy-delta-5-steroid dehydrogenase, 3 beta- and steroid delta-isomerase 7	HSD3B7	-1,794485216	3,14E+00	2,34E-06
9510	ADAM metallopeptidase with thrombospondin type 1 motif 1	ADAMTS1	-1,776447519	7,21E+00	1,14E-04
57547	zinc finger protein 624	ZNF624	-1,775900146	3,44E+00	4,28E-09
401588	ZNF674 antisense RNA 1 (head to head)	ZNF674-AS1	-1,767764432	3,07E+00	1,15E-08

Table 16: All differentially expressed genes in microglia 20 dpi with LASV: upregulation. All upregulated genes in microglia 20 dpi with LASV as per limma-voom differential gene expression analysis. FDR (Benjamini and Hochberg) cut-off $\leq$0.05, Log2FC$\geq$0.5. Ordered by absolute Log2FC in expression.

GeneID	Genename	Gene symbol	log2FC	Average expression	adjusted p-Value
148398	sterile alpha motif domain containing 11	SAMD11	0,975375228	3,40E+00	1,06E-02
107985728	collagen alpha-1(III) chain-like	LOC107985728	0,862740878	5,76E-01	4,32E-02
80162	protein-glucosylgalactosylhydroxylysine glucosidase	PGGHG	0,739333213	4,22E+00	1,06E-02
79948	phospholipid phosphatase related 3	PLPPR3	0,729276346	2,58E+00	1,06E-02
2766	guanosine monophosphate reductase	GMPR	0,725455526	3,70E+00	3,94E-02
27344	proprotein convertase subtilisin/kexin type 1 inhibitor	PCSK1N	0,703848553	3,20E+00	3,31E-02
10406	WAP four-disulfide core domain 2	WFDC2	0,689928986	8,26E-01	5,90E-02
10446	leucine rich repeat neuronal 2	LRRN2	0,676284596	2,69E+00	5,37E-02
3757	potassium voltage-gated channel subfamily H member 2	KCNH2	0,653225826	1,04E+00	5,38E-02
5129	cyclin dependent kinase 18	CDK18	0,642312264	4,76E+00	4,87E-02
29911	hook microtubule Tethering protein 2	HOOK2	0,563056301	4,49E+00	1,06E-02
146542	zinc finger protein 688	ZNF688	0,547475058	2,64E+00	3,94E-02
333	amyloid beta precursor like protein 1	APLP1	0,522059717	4,12E+00	1,06E-02
29801	zinc finger DHHC-type palmitoyltransferase 8	ZDHHC8	0,51331937	5,86E+00	4,78E-02

Table 17: All differentially expressed genes in microglia 20 dpi with LASV: downregulation. All down-regulated genes in microglia 20 dpi with LASV as per limma-voom differential gene expression analysis. FDR (Benjamini and Hochberg) cut-off $\leq$0.05, Log2FC$\geq$0.5. Ordered by absolute Log2FC in expression.

GeneID	Genename	Gene symbol	log2FC	Average expression	adjusted p-Value
2119	ETS variant transcription factor 5	ETV5	-0,794515506	5,98E+00	3,49E-02

Table 18: Top 50 differentially expressed genes in astrocytes 20 dpi with EBOV: upregulation. Top 50 upregulated genes in astrocytes 20 dpi with EBOV as per limma-voom differential gene expression analysis. FDR (Benjamini and Hochberg) cut-off $\leq$0.05, Log2FC$\geq$0.5. Ordered by absolute Log2FC in expression.

GeneID	Genename	Gene symbol	log2FC	Average expression	adjusted p-Value
114795	transmembrane protein 132B	TMEM132B	7,358827224	5,65E-01	1,07E-03
3553	interleukin 1 beta	IL1B	6,414069514	-3,54E-01	7,98E-04
374897	suprabasin	SBSN	6,141905812	-6,85E-01	5,21E-04
894	cyclin D2	CCND2	5,911649601	1,82E+00	4,35E-04
7056	thrombomodulin	THBD	5,7066203	-3,25E-02	3,60E-05
3310	heat shock protein family A (Hsp70) member 6	HSPA6	5,491092492	-5,47E-01	3,15E-06
92211	cadherin related family member 1	CDHR1	4,914286054	-3,97E-01	2,30E-04
3576	C-X-C motif chemokine ligand 8	CXCL8	4,69006464	4,77E+00	4,63E-04
11174	ADAM metallopeptidase with thrombospondin type 1 motif 6	ADAMTS6	4,679935266	6,02E-01	3,83E-04
204010	ribosomal protein SA pseudogene 52	RPSAP52	4,676601638	-2,00E+00	2,91E-04
3552	interleukin 1 alpha	IL1A	4,607079286	-9,01E-01	4,13E-03
4145	megakaryocyte-associated tyrosine kinase	MATK	4,53801441	1,61E-01	4,08E-04
6751	somatostatin receptor 1	SSTR1	4,27606144	-3,01E+00	1,64E-03
4884	neuronal pentraxin 1	NPTX1	4,071390797	2,93E+00	1,15E-03
220	aldehyde dehydrogenase 1 family member A3	ALDH1A3	4,007647718	3,95E+00	3,50E-05
26872	STEAP family member 1	STEAP1	3,939077545	2,27E-01	3,56E-03
768	carbonic anhydrase 9	CA9	3,926328309	-5,71E-01	5,84E-04
387755	INSC spindle orientation adaptor protein	INSC	3,904198636	-1,07E+00	2,47E-04
1437	colony stimulating factor 2	CSF2	3,89792472	-2,27E+00	3,70E-03
50486	G0/G1 switch 2	G0S2	3,83031816	2,16E+00	1,70E-04
8701	dynein axonemal heavy chain 11	DNAH11	3,819591845	-2,33E-01	9,09E-05
285	angiopoietin 2	ANGPT2	3,799082461	-6,75E-01	6,56E-04
399668	small integral membrane protein 10 like 2A	SMIM10L2A	3,77737879	8,36E-01	4,39E-04
5522	protein phosphatase 2 regulatory subunit Bgamma	PPP2R2C	3,75402407	1,12E+00	2,49E-04
121551	ankyrin repeat and BTB domain containing 3	ABTB3	3,739531383	1,67E+00	1,31E-03
643401	p53 upregulated regulator of p53 levels	PURPL	3,699626607	1,11E+00	4,39E-04
109729169	long intergenic non-protein coding RNA 2154	LINC02154	3,69645921	1,85E+00	1,39E-02
135398	chromosome 6 open reading frame 141	C6orf141	3,682433632	1,40E+00	2,38E-04
128209	KLF transcription factor 17	KLF17	3,661893281	-1,02E+00	8,01E-05
9388	lipase G, endothelial type	LIPG	3,650824075	-4,90E-01	8,75E-05
59284	calcium voltage-gated channel auxiliary subunit gamma 7	CACNG7	3,63393666	-5,77E-01	1,41E-03
100288152	SLC9A3 antisense RNA 1	SLC9A3-AS1	3,608608011	3,33E+00	6,34E-05
91156	immunoglobulin like and fibronectin type III domain containing 1	IGFN1	3,579426234	7,38E-03	6,96E-04
255738	proprotein convertase subtilisin/kexin type 9	PCSK9	3,570183234	1,23E+00	1,64E-07
83648	family with sequence similarity 167 member A	FAM167A	3,524874562	-3,21E-01	6,17E-05
4858	NOVA alternative splicing regulator 2	NOVA2	3,469388319	1,27E+00	3,79E-05
7482	Wnt family member 2B	WNT2B	3,439802683	1,63E+00	3,81E-05
63950	DMRT like family A2	DMRTA2	3,43557363	3,28E-01	1,75E-03
100133941	CD24 molecule	CD24	3,362487681	2,93E+00	7,22E-04
112464	caveolae associated protein 3	CAVIN3	3,349697788	-1,57E-01	2,94E-04
89795	neuron navigator 3	NAV3	3,34100435	3,11E-01	1,42E-04
6372	C-X-C motif chemokine ligand 6	CXCL6	3,310065438	-5,93E-01	2,55E-04
8912	calcium voltage-gated channel subunit alpha1 H	CACNA1H	3,256962767	2,10E+00	4,18E-03
124900605	uncharacterized LOC124900605	LOC124900605	3,158794688	3,00E-01	7,73E-05
7409	vav guanine nucleotide exchange factor 1	VAV1	3,14686224	-1,11E-01	6,99E-03
101928156	uncharacterized LOC101928156	LOC101928156	3,13437735	9,27E-01	1,27E-03
3742	potassium voltage-gated channel subfamily A member 6	KCNA6	3,133063062	5,52E-01	2,02E-04
5168	ectonucleotide pyrophosphatase/phosphodiesterase 2	ENPP2	3,108562767	1,51E+00	1,34E-05
284344	uncharacterized LOC284344	LOC284344	3,102386801	-1,27E+00	6,59E-03
3662	interferon regulatory factor 4	IRF4	3,028171574	-5,59E-01	4,51E-04

Table 19: Top 50 differentially expressed genes in astrocytes 20 dpi with EBOV: downregulation. Top 50 downregulated genes in astrocytes 20 dpi with EBOV as per limma-voom differential gene expression analysis. FDR (Benjamini and Hochberg) cut-off $\leq$0.05, Log2FC$\geq$0.5. Ordered by absolute Log2FC in expression.

GeneID	Genename	Gene symbol	log2FC	Average expression	adjusted p-Value
1306	collagen type XV alpha 1 chain	COL15A1	-4,722289941	1,05E+00	5,28E-05
8995	TNF superfamily member 18	TNFSF18	-4,635630034	-4,22E-01	1,24E-05
100128054	PLCE1 antisense RNA 1	PLCE1-AS1	-4,418568823	-1,20E+00	1,15E-06
130576	LY6/PLAUR domain containing 6B	LYPD6B	-4,076485954	2,84E+00	1,84E-05
3294	hydroxysteroid 17-beta dehydrogenase 2	HSD17B2	-4,056948733	-1,74E+00	1,68E-06
51129	angiopoietin like 4	ANGPTL4	-3,696374093	3,58E+00	1,59E-06
80310	platelet derived growth factor D	PDGFD	-3,640854496	1,79E+00	1,30E-04
51200	carboxypeptidase A4	CPA4	-3,462648895	2,56E+00	5,18E-06
1907	endothelin 2	EDN2	-3,395015374	4,15E-01	1,21E-05
3756	potassium voltage-gated channel subfamily H member 1	KCNH1	-3,35848234	5,81E-01	3,40E-07
388630	TraB domain containing 2B	TRABD2B	-3,281169369	9,97E-01	7,27E-04
2982	guanylate cyclase 1 soluble subunit alpha 1	GUCY1A1	-3,258975298	1,01E+00	3,88E-03
30820	potassium voltage-gated channel interacting protein 1	KCNIP1	-3,237224605	4,29E-01	1,90E-05
122319436	uncharacterized LOC122319436	LOC122319436	-3,039395175	-1,38E-01	2,18E-04
128434	V-set and transmembrane domain containing 2 like	VSTM2L	-3,024793408	1,88E+00	1,71E-07
284339	transmembrane protein 145	TMEM145	-2,977607559	8,35E-01	2,62E-03
4232	mesoderm specific transcript	MEST	-2,962552471	6,06E+00	3,25E-03
8470	sorbin and SH3 domain containing 2	SORBS2	-2,946605602	2,77E+00	1,00E-04
124903135	uncharacterized LOC124903135	LOC124903135	-2,84179563	5,59E-02	3,59E-03
80763	spexin hormone	SPX	-2,783765619	1,10E+00	1,26E-04
10529	nebulette	NEBL	-2,772886158	1,59E+00	3,21E-03
4239	microfibril associated protein 4	MFAP4	-2,730679258	3,57E+00	6,88E-04
10891	PPARG coactivator 1 alpha	PPARGC1A	-2,709281074	1,74E+00	3,93E-05
2042	EPH receptor A3	EPHA3	-2,660409524	8,03E-01	1,54E-02
9723	semaphorin 3E	SEMA3E	-2,637639273	3,12E-01	8,63E-03
7057	thrombospondin 1	THBS1	-2,573675924	5,53E+00	2,39E-04
387597	immunoglobulin like domain containing receptor 2	ILDR2	-2,542721662	2,03E+00	1,81E-04
64409	polypeptide N-acetylgalactosaminyltransferase 17	GALNT17	-2,535803148	2,72E-01	5,61E-03
101929074	PIK3CD antisense RNA 2	PIK3CD-AS2	-2,529537786	1,18E+00	1,18E-05
7504	X-linked Kx blood group antigen, Kell and VPS13A binding protein	XK	-2,506623659	1,61E-01	2,12E-02
5166	pyruvate dehydrogenase kinase 4	PDK4	-2,505389239	2,78E+00	1,33E-06
55273	transmembrane protein 100	TMEM100	-2,499955375	2,14E+00	4,85E-03
56062	kelch like family member 4	KLHL4	-2,478584428	2,76E+00	1,42E-04
120114	FAT atypical cadherin 3	FAT3	-2,428457771	3,73E+00	2,43E-05
4023	lipoprotein lipase	LPL	-2,414738104	9,68E-01	1,04E-03
7134	troponin C1, slow skeletal and cardiac type	TNNC1	-2,408480876	2,50E-01	9,50E-05
6578	solute carrier organic anion transporter family member 2A1	SLCO2A1	-2,38020559	2,65E+00	1,18E-03
283078	mohawk homeobox	MKX	-2,376139573	2,76E+00	3,31E-04
3759	potassium inwardly rectifying channel subfamily J member 2	KCNJ2	-2,359747046	2,30E+00	3,15E-06
4883	natriuretic peptide receptor 3	NPR3	-2,35380043	2,32E+00	2,93E-06
54510	protocadherin 18	PCDH18	-2,351772715	3,52E+00	8,27E-04
1124	chimerin 2	CHN2	-2,349045359	4,37E-01	5,03E-03
153020	RasGEF domain family member 1B	RASGEF1B	-2,347530589	4,59E-01	2,91E-02
64084	calsyntenin 2	CLSTN2	-2,34628281	5,23E+00	2,82E-07
440028	long intergenic non-protein coding RNA 2709	LINC02709	-2,340782655	1,23E+00	8,11E-04
84624	fibronectin type III domain containing 1	FNDC1	-2,335119553	3,49E+00	2,46E-04
388815	mir-99a-let-7c cluster host gene	MIR99AHG	-2,327670437	1,93E+00	1,09E-03
25878	matrix remodeling associated 5	MXRA5	-2,325076907	3,64E+00	3,10E-03
6335	sodium voltage-gated channel alpha subunit 9	SCN9A	-2,31737128	2,84E+00	3,14E-05
54504	carboxypeptidase vitellogenic like	CPVL	-2,316875923	3,65E+00	8,45E-06

Table 20: All differentially expressed genes in astrocytes 20 dpi with LASV: upregulation. All upregulated genes in microglia 20 dpi with LASV as per limma-voom differential gene expression analysis. FDR (Benjamini and Hochberg) cut-off ≤0.05, Log2FC≥0.5. Ordered by absolute Log2FC in expression.

GeneID	Genename	Gene symbol	log2FC	Average ex-pression	adjusted p-Value
26118	WD repeat and SOCS box containing 1	WSB1	0,525558567	6,24E+00	1,50E-02

6.5.3 The transcriptome of microglia passaged with EBOV for 10+3 passages.

EBOV persistently replicates over 13 passages (91 days) in human immortalized microglia (Figure 46). During this process, selection of both the host cells and viruses likely occurs. Therefore, to screen for host-cell-mediated adaptation to viral persistence, the transcriptome of the third passage after thawing (P10+3) was analyzed.

Figure 58 (A) depicts the PCA retrieved when analyzing the transcriptome of two separately passaged microglia lines persistently infected with EBOV at an inital MOI=1 for 10+3 passages (EBOV-A, EBOV-B, n=4 each) in contrast to a non-infected passage. Notably, despite EBOV-A and EBOV-B both having been infected with EBOV, they cluster widely differently from each other and the negative control.

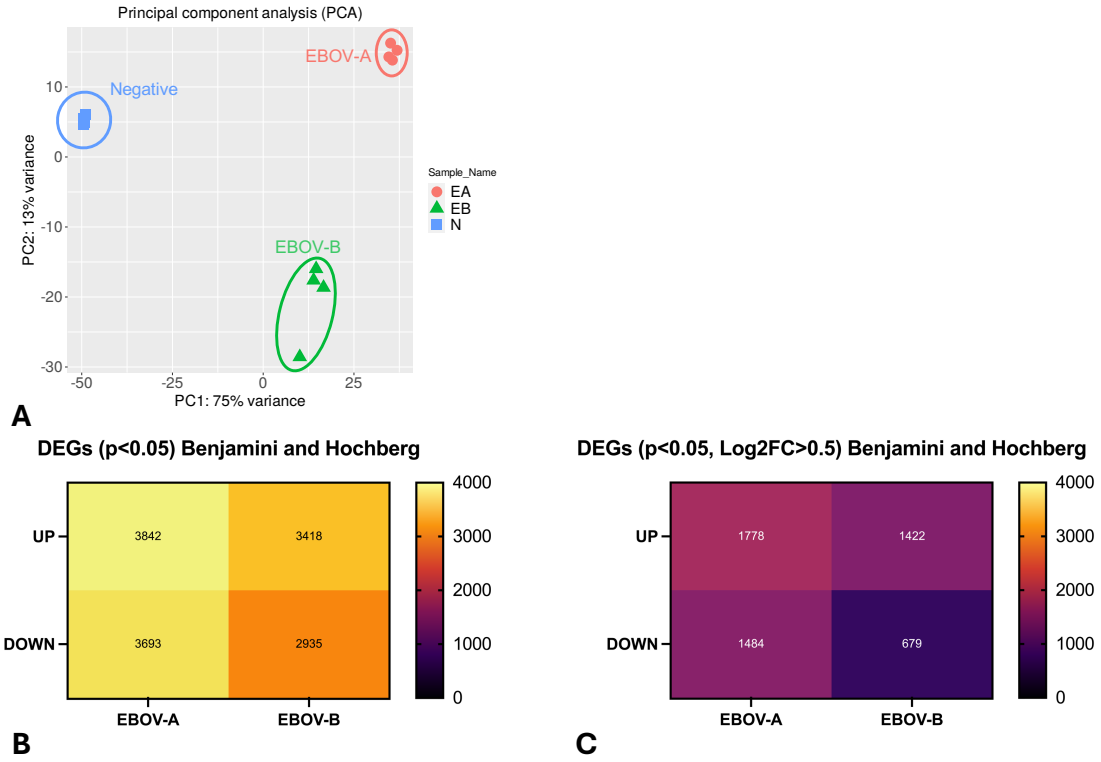


Figure 58: PCA and DEGs in microglia after passaging with EBOV. (A) Principal component analysis (PCA) of transcriptomic data of microglia after 10+3 passages with EBOV in two flasks (A, B). PC1 (75 % variance) and PC2 (13 % variance). **(B)** Differentially up- (UP) or downregulated (DOWN) genes (DEGs) reaching the FDR cut-off (p≤0.05). **(D)** Significantly up- or downregulated genes with a Log2FC≥0.5. N=4 samples per group.

Overall, in EBOV-A retrieved from the primary flask A in passage 10+3, 1778 genes were

up- and 1484 were downregulated with a Log2FC of at least 0.5 (Figure 58 (B, C)). In EBOV-B, 1422 genes were upregulated and 679 genes were downregulated. Notably, EBOV-B had slightly higher viral titers at the time of RNA harvest (Figure 46).

Among the top 10 upregulated genes in EBOV-A were OASL (12.8 Log2FC), OAS2, OAS1, IFIT2, IFNB1, IFI44, IFIT3, MX2, IFI44L, CXCL10 (8.9 Log2FC) (Table 21). Despite these being genes mostly associated with infection, GO enrichment of biological processes further revealed developmental and migratory as well as proliferation pathways to be enriched (Figure 59 (A)). ”Cellular response to chemical stimulus”, ”response to organic substance”, and ”regulation of response to stimulus” were nevertheless amongst enriched pathways. KEGG enrichment further revealed an increase in the ”p53 signaling pathway”, ”TNF signaling pathway”, ”NF-kappa B signaling pathway”, and ”apoptosis” as well as several cancer and viral infection pathways (Influenza A virus, Epstein-Barr virus (EBV), HSV-1, HPV) ((Figure 59 (B)). This is overall widely similar to microglia infected with EBOV for 20 days. The top 10 upregulated genes in the replicates originating from the second EBOV-infected flask (EBOV-B) passaged for 10+3 passages included OAS2 (11.7 Log2FC), OASL, OAS1, IFI44L, IFI44, IFNB1, IFIT2, MX2, IFIT3, and XAF1 (8.4 Log2FC) (Table 23). GO biological pathways enriched were mostly regulation of development and proliferation but also transcription and biosynthesis. No response to stimuli was listed among upregulated GO terms (Figure 59 (E)). KEGG pathway enrichment, similar to flask A, comprised ”p53 signaling pathway”, ”TNF signaling pathway”, ”NF-kappa B signaling pathway”, ”apoptosis” as well as multiple viral infections (Measles, Influenza A, EBV, Hepatitis B virus (HBV), HSV-1, HPV and ”Coronavirus disease”) (Figure 59 (F)). Despite clustering differentially in the PCA, this was still widely similar.

The downregulated top 10 genes in EBOV-A were KCNMA1 (-4.17 Log2FC), TMEM271, CXCL12, ITGA8, LGR5, STUM, MATK, THSD7A, PDCD4-AS1, and PCSK2 (-2.5 Log2FC) (Table 22). GO pathways enriched for downregulated genes comprised mostly ”cytoplasmic translation”, ”axon development”, ”axonogenesis”, morphogenic pathways of projections, and overall developmental pathways (Figure 59 (C)). KEGG pathways enriched among downregulation and passaging for 10+3 passages with EBOV were ”ribosome”, ”valine leucine and isoleucine degradation”, ”axon guidance”, several metabolic pathways as well as ”coronavirus disease-COVID-19”, overall indicating reduced gene expression and metabolic as well as phenotypic shifts in persistently infected microglia (Figure 59 (D)).

In EBOV-B, the top 10 downregulated genes were MATK (-1.9 Log2FC), LINC03061, SNHG19, TNFRSF10D, MAP1A, TNC, ESRRB, ST7-AS1, ZSCAN16-AS1, and CSPG5 (-1.3 Log2FC) (Table 24). These were associated with ”ribosome assembly”, ”cytoplasmic translation”, and further biogenesis and metabolic processes in GO Term enrichment (Figure 59 (G)), whereby KEGG enrichment revealed ”valine leucine and isoleucine degradation” as well as

”ribosome”, and general metabolic pathways, the splicosome as well as ”coronavirus disease - COVID-19” among the downregulated pathways (Figure 59 (H)). This was predominantly congruent with flask A.

Based on these findings, it can be summarized that upon persistent infection via EBOV passaging, the response of the microglia entailed a slight transcriptomic shift besides the overall antiviral response. Here, mostly metabolic, proliferative, and morphogenic pathways were differentially regulated in comparison to the negative control.

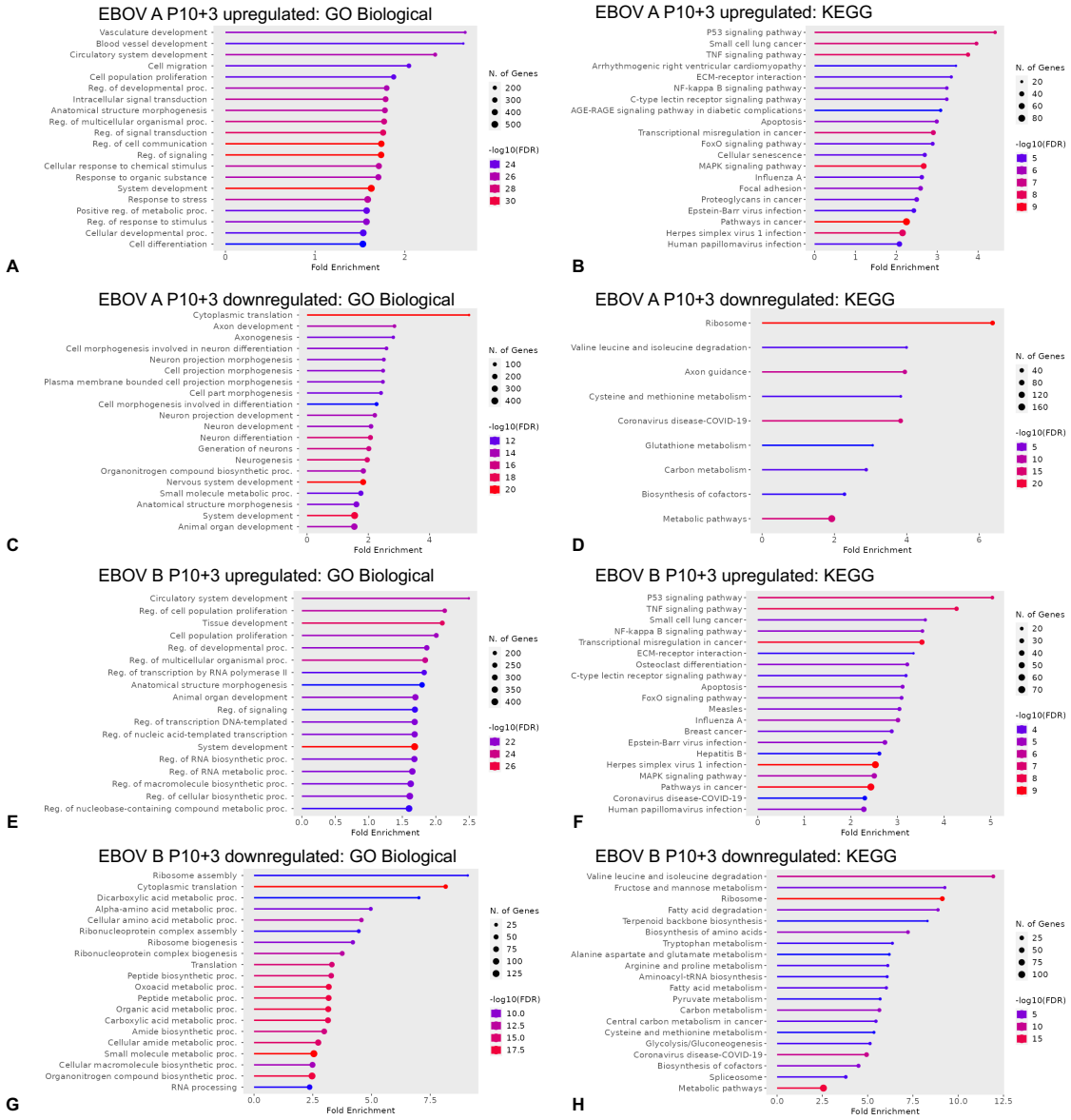


Figure 59: GO-Term and KEGG enrichment in microglia passaged with EBOV. GO-Term (Biological Process) and KEGG pathways enrichment in microglia after 10+3 passages with EBOV including genes significantly up- or downregulated Log2FC≥0.5. **(A)** GO Biological EBOV flask A upregulated genes, **(B)** KEGG EBOV flask A upregulated genes, **(C)** GO Biological EBOV flask A downregulated genes, **(D)** KEGG EBOV flask A downregulated genes, **(E)** GO Biological EBOV flask B upregulated genes, **(F)** KEGG EBOV flask B upregulated genes, **(G)** GO Biological EBOV flask B downregulated genes, **(H)** KEGG EBOV flask B downregulated genes.

Table 21: Top 50 differentially expressed genes in microglia after passaging with EBOV (A): upregulation. Top 50 upregulated genes after passaging with EBOV (A) as per limma-voom differential gene expression analysis. FDR (Benjamini and Hochberg) cut-off $\leq$0.05, Log2FC$\geq$0.5. Ordered by absolute Log2FC in expression.

GeneID	Genename	Gene symbol	log2FC	Average expression	adjusted p-Value
8638	2'-5'-oligoadenylate synthetase like	OASL	12,75070907	4,02E+00	1,60E-12
4939	2'-5'-oligoadenylate synthetase 2	OAS2	11,8541871	2,99E+00	7,62E-13
4938	2'-5'-oligoadenylate synthetase 1	OAS1	11,08787509	3,36E+00	8,78E-12
3433	interferon induced protein with tetratricopeptide repeats 2	IFIT2	10,37473178	7,16E+00	1,43E-13
3456	interferon beta 1	IFNB1	10,26434788	1,26E+00	2,22E-11
10561	interferon induced protein 44	IFI44	9,528440598	3,93E+00	1,27E-12
3437	interferon induced protein with tetratricopeptide repeats 3	IFIT3	9,316245101	7,05E+00	3,01E-15
4600	MX dynamin like GTPase 2	MX2	9,232626177	1,11E+00	4,06E-11
10964	interferon induced protein 44 like	IFI44L	9,227505972	4,33E+00	1,24E-11
3627	C-X-C motif chemokine ligand 10	CXCL10	8,891665645	1,71E+00	6,67E-10
8542	apolipoprotein L1	APOL1	8,375996633	3,21E-01	1,25E-10
115361	guanylate binding protein 4	GBP4	8,25942985	-7,67E-03	1,88E-10
3434	interferon induced protein with tetratricopeptide repeats 1	IFIT1	8,135717393	7,52E+00	5,55E-14
54739	XIAP associated factor 1	XAF1	8,118075755	2,44E-01	1,82E-13
399940	tripartite motif-containing 51E, pseudogene	TRIM51EP	7,964187958	-6,60E-01	3,72E-12
3872	keratin 17	KRT17	7,92604618	6,24E+00	1,49E-13
105378952	KLF transcription factor 18	KLF18	7,803599221	-1,54E-01	1,72E-09
80830	apolipoprotein L6	APOL6	7,737478619	1,47E+00	6,27E-12
6373	C-X-C motif chemokine ligand 11	CXCL11	7,601330715	2,64E-01	7,31E-09
2633	guanylate binding protein 1	GBP1	7,274236854	5,39E-01	3,55E-10
27063	ankyrin repeat domain 1	ANKRD1	7,074270696	4,03E+00	1,01E-11
102723546	uncharacterized LOC102723546	LOC102723546	7,043098774	-5,50E-01	4,79E-08
91543	radical S-adenosyl methionine domain containing 2	RSAD2	6,855728871	4,83E+00	1,95E-12
55281	transmembrane protein 140	TMEM140	6,754830634	7,37E-01	4,54E-09
9636	ISG15 ubiquitin like modifier	ISG15	6,610197899	6,85E+00	3,30E-11
10346	tripartite motif containing 22	TRIM22	6,539104849	3,76E+00	6,27E-12
345651	actin beta like 2	ACTBL2	6,464385534	2,53E+00	4,94E-11
284355	tetrapeptide repeat homeobox 1	TPRX1	6,380847816	-2,90E-01	4,15E-07
390999	PRAME family member 12	PRAMEF12	6,377370355	8,43E-01	1,63E-09
27012	potassium voltage-gated channel modifier subfamily V member 1	KCNV1	6,35906256	1,73E-01	2,24E-08
442247	ret finger protein like 4B	RFPL4B	6,351836237	1,95E+00	4,39E-10
107984375	uncharacterized LOC107984375	LOC107984375	6,343002328	7,90E-02	2,47E-07
64135	interferon induced with helicase C domain 1	IFIH1	6,255022554	6,10E+00	6,41E-14
79132	DExH-box helicase 58	DHX58	6,231364169	2,65E+00	1,68E-12
23586	RNA sensor RIG-I	RIGI	6,195187704	6,52E+00	1,10E-14
390245	lysine demethylase 4E	KDM4E	6,02666856	1,10E+00	3,97E-09
1490	cellular communication network factor 2	CCN2	6,013264302	4,16E+00	3,71E-12
2537	interferon alpha inducible protein 6	IFI6	5,991986898	7,12E+00	2,22E-11
91351	DExD/H-box 60 like	DDX60L	5,831949672	3,65E+00	2,41E-09
101928106	long intergenic non-protein coding RNA 2522	LINC02522	5,812212784	2,80E-01	1,15E-09
4940	2'-5'-oligoadenylate synthetase 3	OAS3	5,806078807	7,26E+00	8,22E-13
10739	ret finger protein like 2	RFPL2	5,800736157	6,62E-01	2,65E-06
10568	solute carrier family 34 member 2	SLC34A2	5,728501193	1,98E+00	5,05E-10
59272	angiotensin converting enzyme 2	ACE2	5,725220177	3,13E+00	1,52E-12
105370363	uncharacterized LOC105370363	LOC105370363	5,693033746	3,66E+00	1,44E-09
100129053	lysine demethylase 4F	KDM4F	5,668092363	5,37E-01	2,17E-09
1999	E74 like ETS transcription factor 3	ELF3	5,614193989	1,21E+00	3,08E-10
729974	ret finger protein like 4A like 1	RFPL4AL1	5,610801357	6,08E-01	4,08E-08
219285	sterile alpha motif domain containing 9 like	SAMD9L	5,542601081	2,52E+00	3,44E-10
105377581	uncharacterized LOC105377581	LOC105377581	5,520609483	7,54E-02	7,18E-07

Table 22: Top 50 differentially expressed genes in microglia after passaging with EBOV (A): downregulation. Top 50 downregulated genes after passaging with EBOV (A) as per limma-voom differential gene expression analysis. FDR (Benjamini and Hochberg) cut-off $\leq$0.05, Log2FC$\geq$0.5. Ordered by absolute Log2FC in expression.

GeneID	Genename	Gene symbol	log2FC	Average expression	adjusted p-Value
3778	potassium calcium-activated channel subfamily M alpha 1	KCNMA1	-4,1723344	1,68E+00	2,20E-06
112441426	transmembrane protein 271	TMEM271	-2,936941423	1,16E+00	6,95E-07
6387	C-X-C motif chemokine ligand 12	CXCL12	-2,735823944	2,45E+00	1,35E-08
8516	integrin subunit alpha 8	ITGA8	-2,644932814	1,82E+00	4,88E-08
8549	leucine rich repeat containing G protein-coupled receptor 5	LGR5	-2,624517427	4,67E+00	4,41E-10
375057	stum, mechanosensory transduction mediator homolog	STUM	-2,610125603	3,32E+00	3,35E-07
4145	megakaryocyte-associated tyrosine kinase	MATK	-2,561808159	3,60E+00	9,23E-11
221981	thrombospondin type 1 domain containing 7A	THSD7A	-2,561432749	1,93E+00	1,01E-04
282997	PDCD4 antisense RNA 1	PDCD4-AS1	-2,498654664	2,21E+00	1,40E-08
5126	proprotein convertase subtilisin/kexin type 2	PCSK2	-2,462223842	4,78E+00	1,43E-09
3642	INSM transcriptional repressor 1	INSM1	-2,438453624	3,24E+00	4,68E-09
3488	insulin like growth factor binding protein 5	IGFBP5	-2,376772214	6,38E+00	5,60E-10
63876	PBX/knotted 1 homeobox 2	PKNOX2	-2,334136868	2,42E+00	4,14E-09
80274	signal peptide, CUB domain and EGF like domain containing 1	SCUBE1	-2,327751748	2,30E+00	4,62E-07
91584	plexin A4	PLXNA4	-2,202739953	4,18E+00	7,06E-07
6092	roundabout guidance receptor 2	ROBO2	-2,15551801	4,19E+00	1,88E-07
5831	pyrroline-5-carboxylate reductase 1	PYCR1	-2,111028098	5,53E+00	1,39E-10
863	CBFA2/RUNX1 partner transcriptional co-repressor 3	CBFA2T3	-2,109389446	1,46E+00	1,22E-08
114795	transmembrane protein 132B	TMEM132B	-2,095167836	4,28E+00	4,88E-08
27132	copine 7	CPNE7	-2,09321037	2,84E+00	4,87E-09
64641	EBF transcription factor 2	EBF2	-2,082685684	3,91E+00	5,60E-10
284600	uncharacterized LOC284600	LOC284600	-2,071738172	3,09E+00	1,14E-06
9369	neurexin 3	NRXN3	-2,064833928	1,71E+00	1,58E-06
492	ATPase plasma membrane Ca2+ transporting 3	ATP2B3	-2,059675234	1,76E+00	3,16E-08
153478	pleckstrin homology and RhoGEF domain containing G4B	PLEKHG4B	-2,036616098	2,38E+00	2,38E-07
6586	slit guidance ligand 3	SLIT3	-2,015125068	5,31E+00	1,41E-08
347252	insulin like growth factor binding protein like 1	IGFBPL1	-1,944595477	4,46E+00	2,91E-09
196500	PILR alpha associated neural protein	PIANP	-1,914382532	4,08E+00	1,75E-08
93653	ST7 antisense RNA 1	ST7-AS1	-1,902278668	1,77E+00	5,78E-07
284339	transmembrane protein 145	TMEM145	-1,897859749	1,74E+00	4,99E-07
4857	NOVA alternative splicing regulator 1	NOVA1	-1,86445331	2,92E+00	1,17E-08
154215	sodium/potassium transporting ATPase interacting 2	NKAIN2	-1,846685026	1,77E+00	4,57E-07
56265	carboxypeptidase X, M14 family member 1	CPXM1	-1,830816186	4,56E+00	1,24E-09
79570	sodium/potassium transporting ATPase interacting 1	NKAIN1	-1,821044672	2,07E+00	1,14E-06
6666	SRY-box transcription factor 12	SOX12	-1,817948589	5,80E+00	6,00E-11
643988	fibronectin type III domain containing 10	FNDC10	-1,814139926	3,88E+00	8,57E-08
4833	NME/NM23 nucleoside diphosphate kinase 4	NME4	-1,808474242	7,14E+00	3,18E-07
23105	follistatin like 4	FSTL4	-1,80578691	2,74E+00	3,77E-07
91461	protein kinase domain containing, cytoplasmic	PKDCC	-1,800770623	3,81E+00	8,51E-09
7102	tetraspanin 7	TSPAN7	-1,790820742	4,80E+00	3,20E-09
5360	phospholipid transfer protein	PLTP	-1,771256972	4,20E+00	1,93E-08
170692	ADAM metallopeptidase with thrombospondin type 1 motif 18	ADAMTS18	-1,768544489	1,28E+00	2,36E-04
8793	TNF receptor superfamily member 10d	TNFRSF10D	-1,767739637	4,77E+00	5,00E-10
10736	SIX homeobox 2	SIX2	-1,766981217	2,43E+00	3,09E-07
6319	stearoyl-CoA desaturase	SCD	-1,753751223	8,30E+00	1,67E-10
10266	receptor activity modifying protein 2	RAMP2	-1,745167497	2,39E+00	3,32E-06
101060391	SNTG2 antisense RNA 1	SNTG2-AS1	-1,724101018	1,85E+00	5,39E-07
64943	5'-nucleotidase domain containing 2	NT5DC2	-1,723096289	7,30E+00	1,68E-08
3949	low density lipoprotein receptor	LDLR	-1,693287008	4,66E+00	2,15E-07
128553	teashirt zinc finger homeobox 2	TSHZ2	-1,688734954	3,50E+00	2,48E-06

Table 23: Top 50 differentially expressed genes in microglia after passaging with EBOV (B): upregulation. Top 50 upregulated genes after passaging with EBOV (B) as per limma-voom differential gene expression analysis. FDR (Benjamini and Hochberg) cut-off $\leq$0.05, Log2FC$\geq$0.5. Ordered by absolute Log2FC in expression.

GeneID	Genename	Gene symbol	log2FC	Average expression	adjusted p-Value
4939	2'-5'-oligoadenylate synthetase 2	OAS2	11,71784918	2,99E+00	1,15E-12
8638	2'-5'-oligoadenylate synthetase like	OASL	11,53613614	4,02E+00	6,83E-12
4938	2'-5'-oligoadenylate synthetase 1	OAS1	10,65354739	3,36E+00	2,36E-11
10964	interferon induced protein 44 like	IFI44L	9,58188042	4,33E+00	1,66E-11
10561	interferon induced protein 44	IFI44	9,460972027	3,93E+00	2,46E-12
3456	interferon beta 1	IFNB1	9,297512478	1,26E+00	1,11E-10
3433	interferon induced protein with tetratricopeptide repeats 2	IFIT2	9,008950632	7,16E+00	6,18E-13
4600	MX dynamin like GTPase 2	MX2	8,681772907	1,11E+00	1,46E-10
3437	interferon induced protein with tetratricopeptide repeats 3	IFIT3	8,558645544	7,05E+00	7,86E-15
54739	XIAP associated factor 1	XAF1	8,403318197	2,44E-01	2,05E-13
3627	C-X-C motif chemokine ligand 10	CXCL10	7,918390582	1,71E+00	4,60E-09
115361	guanylate binding protein 4	GBP4	7,511658014	-7,67E-03	1,24E-09
3434	interferon induced protein with tetratricopeptide repeats 1	IFIT1	7,227748932	7,52E+00	2,05E-13
8542	apolipoprotein L1	APOL1	7,186482714	3,21E-01	1,66E-09
80830	apolipoprotein L6	APOL6	7,160123412	1,47E+00	2,69E-11
6373	C-X-C motif chemokine ligand 11	CXCL11	6,873202145	2,64E-01	5,59E-08
55281	transmembrane protein 140	TMEM140	6,575818656	7,37E-01	1,31E-08
2537	interferon alpha inducible protein 6	IFI6	6,413795645	7,12E+00	2,23E-11
105378952	KLF transcription factor 18	KLF18	6,34063092	-1,54E-01	5,68E-08
10346	tripartite motif containing 22	TRIM22	6,181505869	3,76E+00	2,23E-11
107984375	uncharacterized LOC107984375	LOC107984375	6,111584775	7,90E-02	7,63E-07
2633	guanylate binding protein 1	GBP1	6,012088074	5,39E-01	7,44E-09
9636	ISG15 ubiquitin like modifier	ISG15	5,901534165	6,85E+00	1,47E-10
399940	tripartite motif-containing 51E, pseudogene	TRIM51EP	5,841575501	-6,60E-01	5,43E-10
684	bone marrow stromal cell antigen 2	BST2	5,809718579	6,02E+00	2,64E-11
338440	anoctamin 9	ANO9	5,723393899	1,01E+00	1,13E-07
91543	radical S-adenosyl methionine domain containing 2	RSAD2	5,672318737	4,83E+00	2,23E-11
284355	tetrapeptide repeat homeobox 1	TPRX1	5,607039768	-2,90E-01	3,81E-06
79132	DExH-box helicase 58	DHX58	5,556641665	2,65E+00	9,79E-12
219285	sterile alpha motif domain containing 9 like	SAMD9L	5,467621566	2,52E+00	7,69E-10
124905145	uncharacterized LOC124905145	LOC124905145	5,461625017	2,27E+00	1,31E-08
84875	poly(ADP-ribose) polymerase family member 10	PARP10	5,419249438	4,09E+00	5,65E-11
4940	2'-5'-oligoadenylate synthetase 3	OAS3	5,394012538	7,26E+00	2,09E-12
105221694	BST2 interferon stimulated positive regulator	BISPR	5,355622539	2,74E+00	7,08E-10
284344	uncharacterized LOC284344	LOC284344	5,272435918	4,44E-01	4,33E-09
91351	DExD/H-box 60 like	DDX60L	5,239322247	3,65E+00	1,45E-08
3783	potassium calcium-activated channel subfamily N member 4	KCNN4	5,235252342	1,20E+00	2,61E-09
64135	interferon induced with helicase C domain 1	IFIH1	5,200264103	6,10E+00	5,66E-13
390999	PRAME family member 12	PRAMEF12	5,162329174	8,43E-01	4,29E-08
23586	RNA sensor RIG-I	RIGI	5,147067226	6,52E+00	8,13E-14
124904632	uncharacterized LOC124904632	LOC124904632	5,145475055	6,57E+00	2,48E-14
10410	interferon induced transmembrane protein 3	IFITM3	5,122832603	7,91E+00	3,69E-12
4051	cytochrome P450 family 4 subfamily F member 3	CYP4F3	5,003276575	3,32E+00	5,88E-09
102723546	uncharacterized LOC102723546	LOC102723546	4,998038766	-5,50E-01	7,36E-06
442247	ret finger protein like 4B	RFPL4B	4,934597427	1,95E+00	1,31E-08
101928106	long intergenic non-protein coding RNA 2522	LINC02522	4,875824357	2,80E-01	2,02E-08
105374117	uncharacterized LOC105374117	LOC105374117	4,810741928	7,04E-01	6,63E-08
10202	dehydrogenase/reductase 2	DHRS2	4,742490171	6,05E+00	7,01E-13
729974	ret finger protein like 4A like 1	RFPL4AL1	4,732141512	6,08E-01	6,24E-07
390245	lysine demethylase 4E	KDM4E	4,725083297	1,10E+00	1,45E-07

Table 24: Top 50 differentially expressed genes in microglia after passaging with EBOV (B): downregulation. Top 50 downregulated genes after passaging with EBOV (B) as per limma-voom differential gene expression analysis. FDR (Benjamini and Hochberg) cut-off $\leq$0.05, Log2FC$\geq$0.5. Ordered by absolute Log2FC in expression.

GeneID	Genename	Gene symbol	log2FC	Average expression	adjusted p-Value
4145	megakaryocyte-associated tyrosine kinase	MATK	-1,877237304	3,60E+00	1,20E-09
127379752	long intergenic non-protein coding RNA 3061	LINC03061	-1,860991213	4,86E-01	4,96E-06
100507303	small nucleolar RNA host gene 19	SNHG19	-1,543332778	3,22E+00	2,15E-07
8793	TNF receptor superfamily member 10d	TNFRSF10D	-1,520089553	4,77E+00	3,33E-09
4130	microtubule associated protein 1A	MAP1A	-1,495945611	3,05E+00	1,87E-06
3371	tenascin C	TNC	-1,384837727	6,80E+00	3,39E-07
2103	estrogen related receptor beta	ESRRB	-1,367734224	1,73E+00	1,15E-05
93653	ST7 antisense RNA 1	ST7-AS1	-1,310198968	1,77E+00	1,29E-05
100129195	ZSCAN16 antisense RNA 1	ZSCAN16-AS1	-1,306088525	3,32E+00	2,34E-06
10675	chondroitin sulfate proteoglycan 5	CSPG5	-1,302281967	3,88E+00	9,83E-08
127833	synaptotagmin 2	SYT2	-1,301893398	1,69E+00	7,80E-05
282997	PDCD4 antisense RNA 1	PDCD4-AS1	-1,299790379	2,21E+00	1,88E-06
283624	long intergenic non-protein coding RNA 641	LINC00641	-1,277872193	4,11E+00	7,50E-07
1728	NAD(P)H quinone dehydrogenase 1	NQO1	-1,26864715	2,64E+00	5,36E-06
100129387	GABPB1 antisense RNA 1	GABPB1-AS1	-1,263275699	2,80E+00	2,89E-07
56099	protocadherin gamma subfamily B, 7	PCDHGB7	-1,259479297	1,61E+00	1,70E-02
54331	G protein subunit gamma 2	GNG2	-1,246822166	2,40E+00	6,25E-08
63876	PBX/knotted 1 homeobox 2	PKNOX2	-1,24393169	2,42E+00	6,09E-07
3949	low density lipoprotein receptor	LDLR	-1,224042869	4,66E+00	5,02E-06
138649	ankyrin repeat domain 19, pseudogene	ANKRD19P	-1,17822168	3,86E+00	3,18E-05
5176	serpin family F member 1	SERPINF1	-1,177059842	3,09E+00	4,93E-07
9568	gamma-aminobutyric acid type B receptor subunit 2	GABBR2	-1,165623759	2,19E+00	4,82E-06
1535	cytochrome b-245 alpha chain	CYBA	-1,165464323	5,82E+00	1,67E-06
3488	insulin like growth factor binding protein 5	IGFBP5	-1,156594087	6,38E+00	6,49E-07
6320	C-type lectin domain containing 11A	CLEC11A	-1,138814543	3,15E+00	7,45E-05
6124	ribosomal protein L4	RPL4	-1,115639958	1,08E+01	3,06E-07
254102	EH domain binding protein 1 like 1	EHBP1L1	-1,112123727	3,92E+00	1,36E-04
9028	rhomboid like 1	RHBDL1	-1,107709504	2,50E+00	1,04E-06
2822	glycosylphosphatidylinositol specific phospholipase D1	GPLD1	-1,095027638	3,11E+00	1,40E-05
441150	chromosome 6 open reading frame 226	C6orf226	-1,090854596	1,96E+00	2,10E-04
84264	hydroxyacylglutathione hydrolase like	HAGHL	-1,090007898	1,66E+00	2,75E-06
26227	phosphoglycerate dehydrogenase	PHGDH	-1,088634512	7,71E+00	1,87E-08
6652	sorbitol dehydrogenase	SORD	-1,087716534	5,13E+00	1,54E-08
284119	caveolae associated protein 1	CAVIN1	-1,080377754	5,90E+00	3,42E-08
1757	sarcosine dehydrogenase	SARDH	-1,077597037	2,63E+00	1,19E-06
56105	protocadherin gamma subfamily A, 11	PCDHGA11	-1,073274951	4,10E+00	3,16E-03
5831	pyrroline-5-carboxylate reductase 1	PYCR1	-1,069338005	5,53E+00	1,10E-07
80274	signal peptide, CUB domain and EGF like domain containing 1	SCUBE1	-1,05389618	2,30E+00	1,35E-04
284339	transmembrane protein 145	TMEM145	-1,048775593	1,74E+00	5,59E-05
724102	small nucleolar RNA host gene 4	SNHG4	-1,047907221	3,84E+00	2,28E-07
4833	NME/NM23 nucleoside diphosphate kinase 4	NME4	-1,045042089	7,14E+00	6,66E-05
112441426	transmembrane protein 271	TMEM271	-1,038517475	1,16E+00	6,50E-04
445	argininosuccinate synthase 1	ASS1	-1,036184862	5,38E+00	2,86E-07
55809	transcriptional regulating factor 1	TRERF1	-1,033038677	2,76E+00	8,73E-06
585	Bardet-Biedl syndrome 4	BBS4	-1,030875794	5,02E+00	5,04E-08
23741	EP300 interacting inhibitor of differentiation 1	EID1	-1,030559722	7,26E+00	2,14E-07
586	branched chain amino acid transaminase 1	BCAT1	-1,03017215	4,33E+00	3,10E-08
6666	SRY-box transcription factor 12	SOX12	-1,020336353	5,80E+00	2,24E-08
400745	SH2 domain containing 5	SH2D5	-1,01825849	2,40E+00	5,77E-06
64714	protein disulfide isomerase family A member 2	PDIA2	-1,016796424	2,85E+00	9,59E-05

6.5.4 Transcriptomic trends in Ebola virus CNS persistence.

To compare overall transcriptomic trends in microglia and astrocytes at different time points of EBOV infection, some key genes of interest (GOIs) most differentially regulated amongst the datasets are presented in the following.

As depicted in Figure 60, ISG involved in the antiviral response and PRR sensing were particularly elevated in microglia upon EBOV infection, but not in astrocytes. These included genes such as OAS1, OAS2, MX2, XF1, OASL, IFNB1, IFI44L, IFIT1, IFIT3, IFI44, IFIH (MDA-5), IFIT2, RSAD2 (Viperin), ISG15, OASS2, IFI6, MX1, SAMD9L, TRIM22, TRIM5, DHx58, BST2 (Tetherin), RIGI, or Toll-like receptor 3 (TLR-3). Genes encoding cytokines that were upregulated upon EBOV infection in microglia comprised IL11, IL1B, IL15, IL31, IL12A, and IL1A. Here, IL32 was particularly elevated upon passaging. Notably, 20 dpi in astrocytes, IL1B, IL1A, and IL6 were increased. Moreover, IL18 and IL33 were substantially decreased in microglia 20 dpi but elevated in astrocytes. Host factors involved in EBOV entry, NPC1, CatB (CTSB), and CatL (CTSL) were expressed in all groups, whereby an elevation of NPC1 was observed in microglia 20 dpi and upon passage as well as 20 dpi in astrocytes. CatL expression was additionally increased in astrocytes 20 dpi. IRF-7, as downstream signaling factor of diverse PRR, was significantly upregulated in microglia infected with EBOV 12 dpi. In contrast, the expression of the host factor completely ceased in microglia 20 dpi and upon passage. IRF-7 was generally not expressed in astrocytes. IRF-3 expression did not substantially vary among the groups and time points and was neither elevated nor decreased upon infection with EBOV. Upon LASV infection, host factors with minor changes were TMPRSS2 and TMPRSS9 in microglia 20 dpi as well as XAF1 and RSAD2 (viperin) in astrocytes. No further distinctive observations were made.

Based on the observed increase in regulatory response in microglia at late stages of EBOV infection, GOIs involved in the dampening of inflammation were additionally selected. As is shown in Figure 61, in microglia from 12 dpi onwards, particularly USP18, a negative regulator of type I IFN signaling, was elevated. Furthermore, TGFB1 expression was increased 20 dpi in microglia, while TGFB2 was increased upon passaging of EBOV in flask A. 20 dpi in astrocytes, type I IFN signaling inhibitor SOCS2 was particularly upregulated, while TGFB2 was suppressed. Earlier time points did not reveal any distinct signatures. In summary, astrocytes and microglia seemingly differentially regulate their antiviral immune responses upon EBOV infection.

Finally, to elucidate the direct interactions of host enzymes with the EBOV genome, RNA editing and modifying enzymes were queried. Figure 62 depicts how these enzymes were in part differentially expressed in microglia upon infection with EBOV. Here, particularly PARP10 was elevated 12 dpi with EBOV onwards. Moreover, adenosine deaminase acting

on RNA (ADAR)B2 was enriched both in microglia and astrocytes 20 dpi with EBOV as well as in astrocyte infection with LASV. ADAR was further slightly elevated in infected microglia, as well as some members of the APOBEC family.

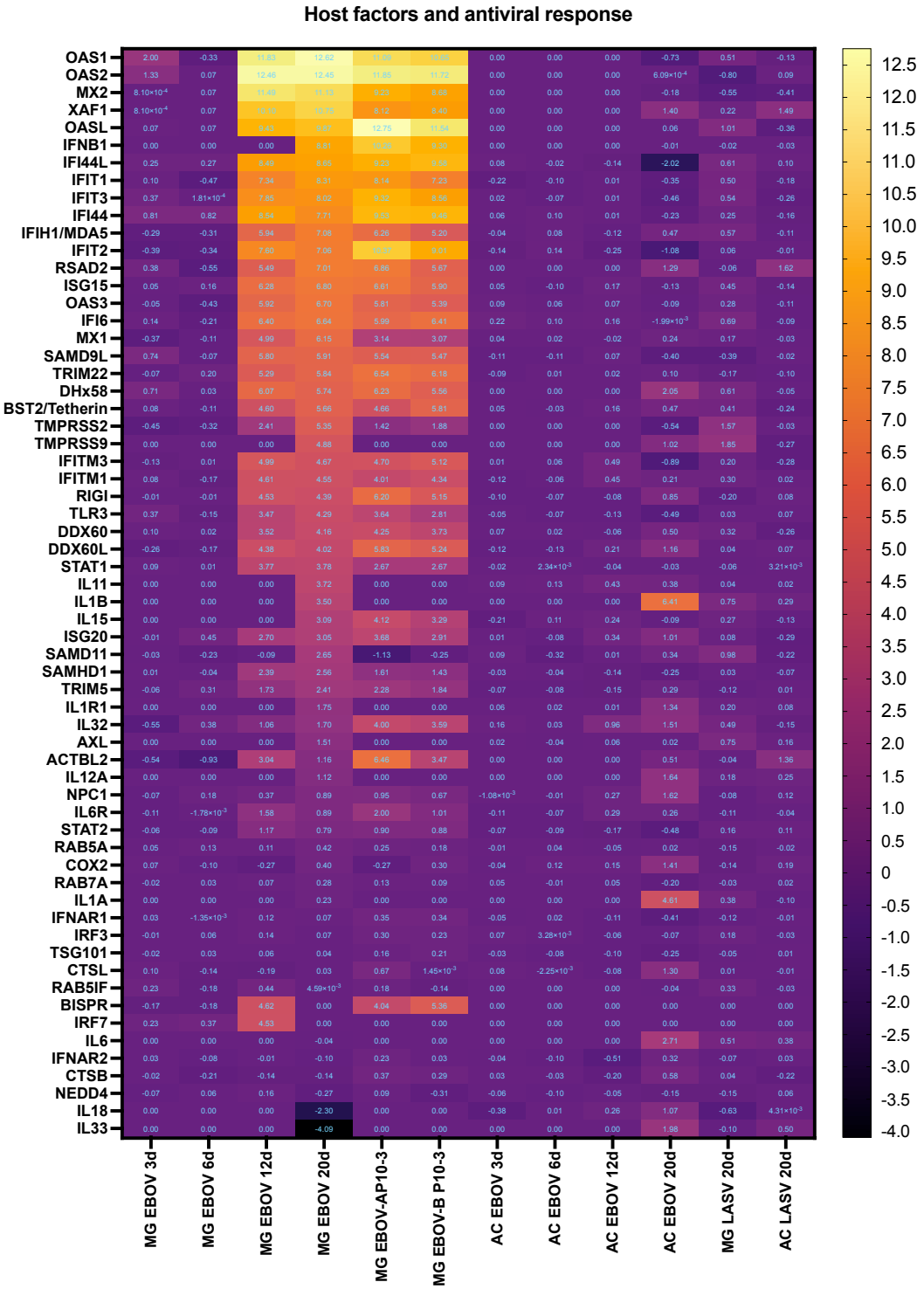


Figure 60: Heatmap of Log2FC in the expression of selected host factors in EBOV infections. Heatmap summarizing the Log2FC in the expression of all datasets in comparison to the respective negative control in selected Heatmap of Log2FC in the expression of selected GOIs involved in EBOV infections. MG = microglia, AC = astrocytes. 0 = not expressed in this cell type (≥5counts/million reads).

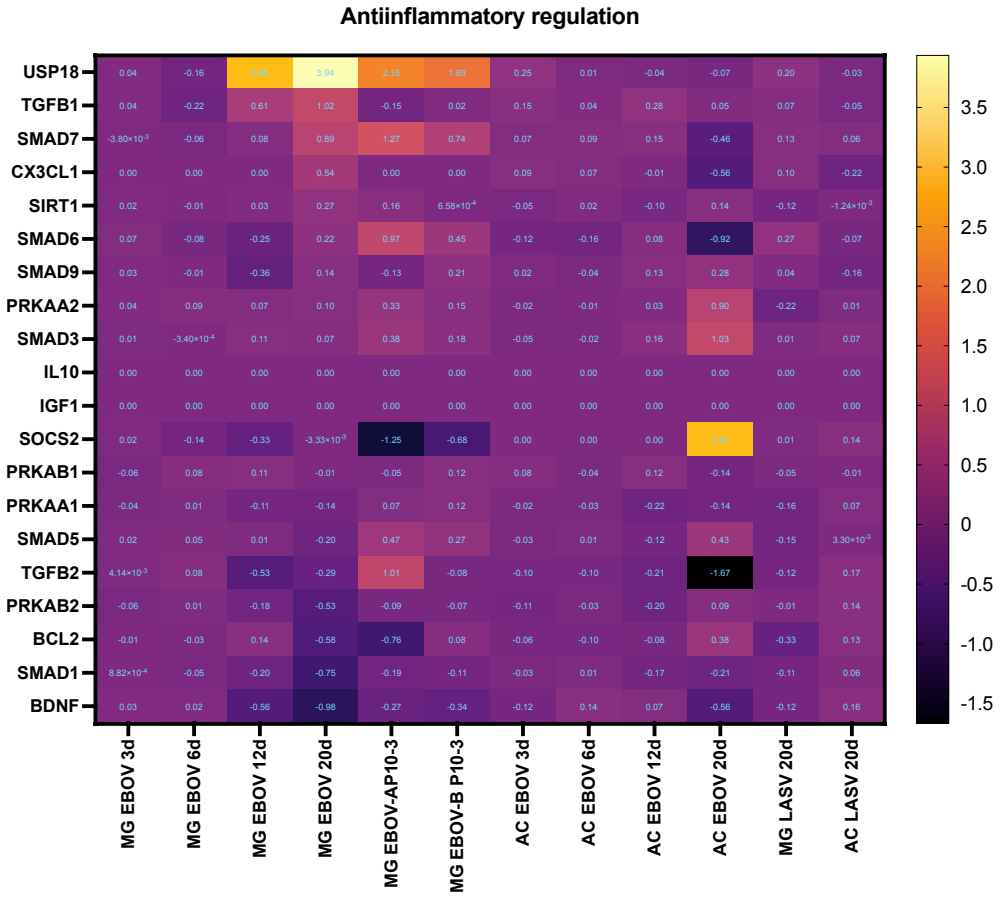


Figure 61: Heatmap of Log2FC in the expression of selected host factors in antiinflammatory pathways. Heatmap summarizing the Log2FC in the expression of all datasets in comparison to the respective negative control in selected Heatmap of Log2FC in the expression of selected GOIs involved in antiinflammatory pathways. MG = microglia, AC = astrocytes. 0 = not expressed in this cell type (≥5counts/million reads).

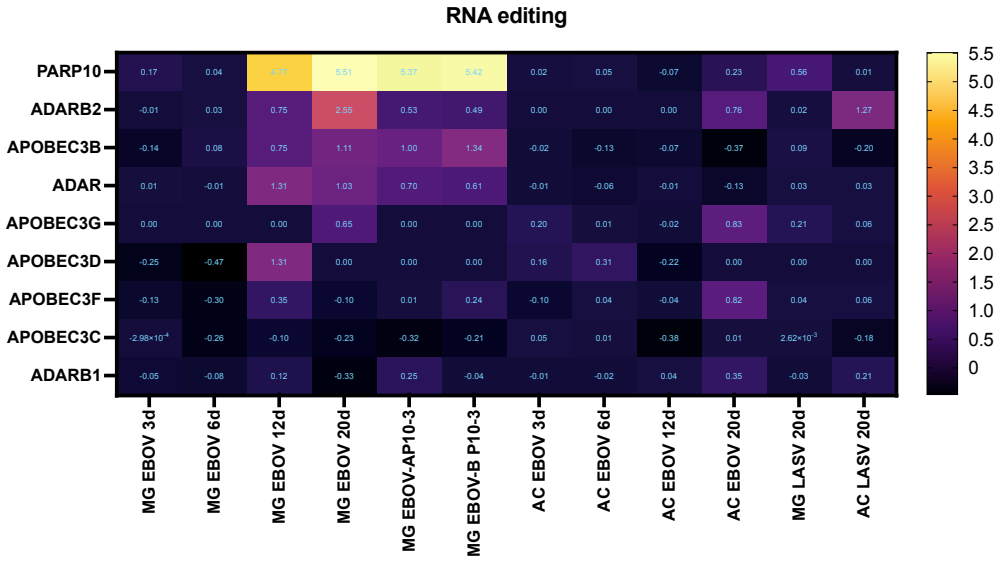


Figure 62: Heatmap of Log2FC in RNA editing. Heatmap summarizing the Log2FC in the expression of all datasets compared to the respective negative control in selected Heatmap of Log2FC in the expression of selected GOIs involved in RNA editing. MG = microglia, AC = astrocytes. 0 = not expressed in this cell type (≥5counts/million reads).

6.6 EBOV variants in persistent CNS infections.

6.6.1 EBOV gene expression during persistent microglia and astrocyte infection.

Studies on the host-pathogen interface in CNS persistence of EBOV further require the investigation of viral gene expression during different stages of infection, as per objective four of this study. To determine the expression of EBOV genes as well as maintenance of the viral (-) RNA genome during different stages of infection, the stranded (+ = mRNA, - = genome) EBOV RNA from infected microglia or astrocytes 3, 6, 12, 20 dpi, and after 10+3 passages (P10+3) was analyzed.

As is depicted in Figure 63 (A,B), the expression (mRNA) of EBOV genes generally followed the reported scheme [257] according to their position in the viral genome – NP - VP35 - VP40 - GP - VP30 - VP24 - L – in microglia and astrocytes during all stages of infection. Here, NP had the most normalized maps and L the least. Furthermore, during early infection, EBOV gene expression peaked 6 dpi in microglia and astrocytes before decreasing (Figure 63 A, B). Notably, 20 dpi and at P10+3, trends in microglia gene expression increased again, while in astrocytes 20 dpi gene expression was still in decline. In microglia, as is shown in Figure 63 (C), the presence of the EBOV (-) RNA genome peaked 6 dpi and was thereafter reduced at 12 dpi, although a slight increase towards 20 dpi occurred as well. EBOV genomes upon P10+3 in microglia were relatively low in contrast to the increase in gene expression (mRNA). The normalization of the gene expression to the presence of the viral genome, depicted in Figure 63 (E), furthermore showed that gene expression per genome copies generally decreased over time in microglia without passaging. In contrast, for microglia passaged with EBOV, pronouncedly more viral mRNA per genome copies was detected. Thus, fewer viral genomes yield higher levels of gene expression in persistently infected, passaged human microglia at P10+3. Notably, all EBOV genes followed the same overall trends in microglia regarding their expression.

In astrocytes, the EBOV gene expression slowly declined after its initial peak at 6 dpi. The same trend was observed for the presence of EBOV genome maps (Figure 63 (D)). Hence, as depicted in Figure 63 (F), for most genes, NP, VP35, VP40, GP, and VP30, the gene expression per genome did not decrease until 12 dpi, where a slight drop at 20 dpi was observed. Meanwhile, VP24 mRNA expression/genome copies were relatively reduced 3 dpi and 20 dpi in comparison to the other genes. Strikingly, median EBOV RdRp-encoding L protein expression/genome copies declined constantly from 3 dpi onwards, reaching a minimum at 20 dpi. Thus, the overall trend was different from all other EBOV genes in astrocytes but very similar to the trends observed in microglia 3 dpi to 20 dpi.

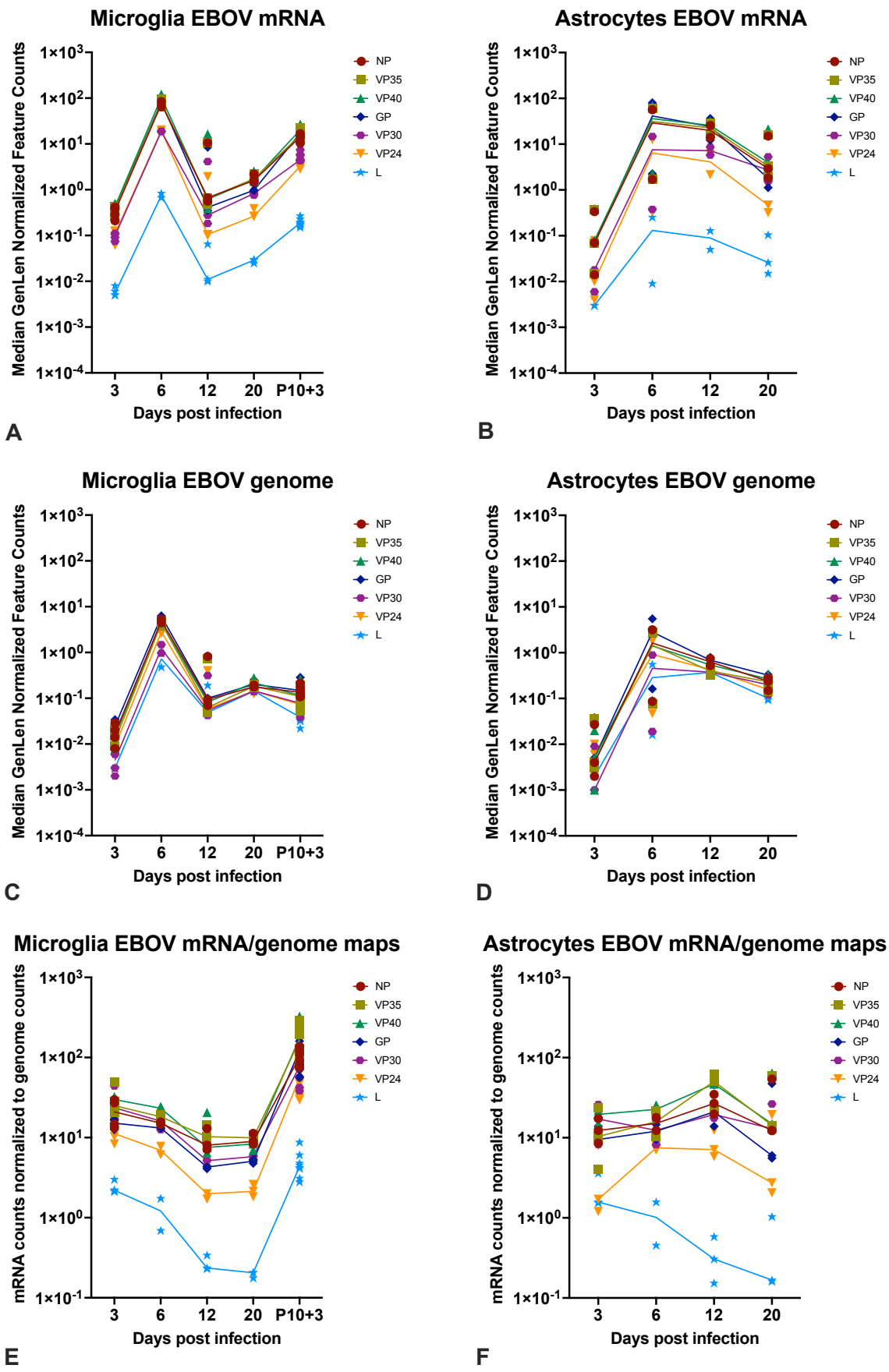


Figure 63: EBOV gene expression in microglia and astrocytes. Median gene counts normalized to the gene length at the indicated time points post-infection. **(A)** EBOV mRNA counts in microglia, **(B)** EBOV mRNA counts in astrocytes, **(C)** EBOV genome counts in microglia, **(D)** EBOV genome counts in astrocytes. Normalization of EBOV mRNA counts (second strand, (+)) to genome counts (first strand, (-)) for EBOV gene expression per genome in **(E)** microglia or **(F)** astrocytes. Line through the median.

6.6.2 Accumulation of SNP in EBOV serially passaged in microglia.

Via passaging of microglia upon infection with EBOV, a 70 d ongoing viral replication was achieved (Figure 46 (A)). Moreover, the release of infectious viral particles into the supernatant was recovered after freezing of the persistently infected cells (Figure 46 (B)). During the passaging process, every second passage was collected to isolate total RNA for strand-specific sequencing of the viral swarm within that sample to determine whether certain genomic mutations accumulated over time. The SNP uncovered in comparison to the stock used for the infection are listed in Table 25. Neither in VP35 nor VP40 any predominant SNP were recovered. Meanwhile, for NP, one SNP (S587A) was uncovered and GP predominantly encoded two (S12P, T293P). In VP30, three SNP accumulated, namely E33K, D269E, A241T, whereas in VP24 one SNP dominated: P147L. In L, two SNP were detected, C1092Y and K1157R. Notably, the listed SNP are those dominating the viral swarm being present in >60 % of mapped reads.

Table 25: SNP in EBOV passaging at the indicated passage.

Viral protein	SNP (coding>60%)	Occurence
NP	S587A	EBOV MOI=1 P2, P6, P10
VP35	none	none
VP40	none	none
GP	S12P	EBOV MOI=1 P6, P8, P10; EBOV MOI=10 P6, P10
GP	T293P	EBOV MOI=10 P8
VP30	E33K	EBOV MOI=1 P2, P6, P10
VP30	D269E	EBOV MOI=1 P2, P6, P8, P10; EBOV MOI=10 P6, P10
VP30	A241T	EBOV MOI=10 P8
VP24	P147L	EBOV MOI=1 P1, P2, P10; EBOV MOI=10 P1, P2, P4, P6, P10
L	C1092Y	EBOV MOI=1 P6
L	K1157R	EBOV MOI=1 P6

6.6.3 Isolation of naturally occurring EBOV$_{n120}$ variants grown for 120 days in human cerebral organoids via limited dilution assay.

To isolate viral variants of EBOV which occurred naturally by growing EBOV for 120 days in human cerebral organoids, limited dilution assays were performed. As shown in Figure 64, the LDA was successful, indicating that singular viral quasi-species had infected a certain well. These isolate variants, in the following referred to as EBOV$_{n120}$, comprised 46 EBOV variants to be screened for differences in their capacity to infect certain cellular targets, their replication kinetics, and potential viral mutations causing these in the following.

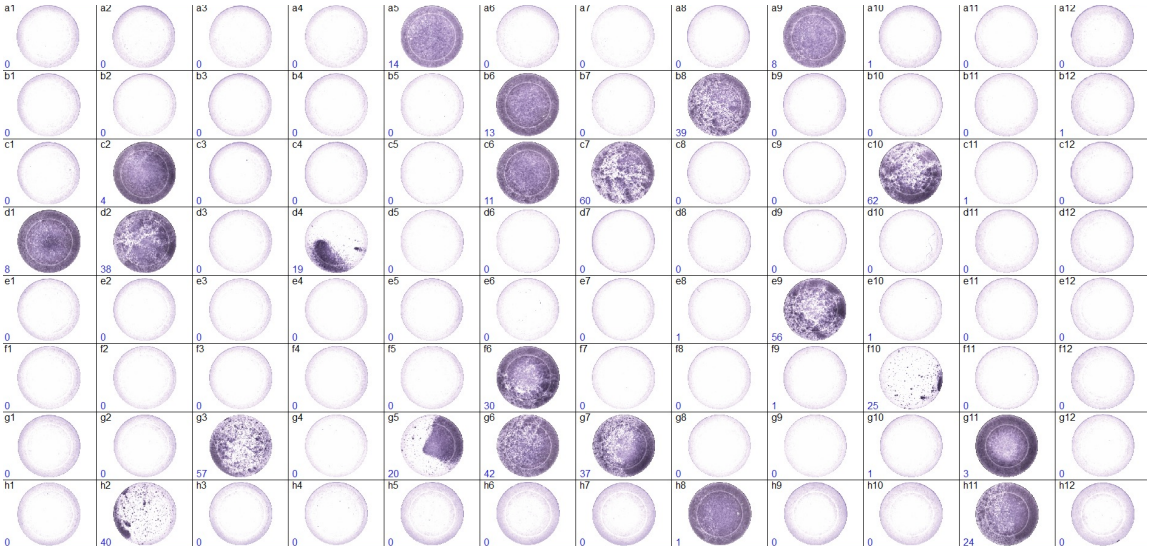


Figure 64: Limited dilution assay. Example of a read-out for a positive limited dilution assay (LDA) with various wells tested positive via antigen staining for isolates.

6.6.4 Replication of EBOV$_{n120}$ variants in immortalized microglia and astrocytes reveals distinct replication profiles.

The EBOV$_{n120}$ isolates retrieved by LDA, later referred to via Greek nomenclature, were subsequently used in an initial screen regarding their replicative behavior in VeroE6 cells versus immortalized microglia for 13 days (n=2, MOI=0.01), as shown in Figure 65. This was performed before sequencing to limit downstream candidates. While all isolates showed similar replication profiles in both VeroE6 cells and microglia, some deviations were detected, particularly 13 dpi. Cohesively, as shown in Figure 65 (A), some EBOV$_{n120}$ isolates replicated to lower titers at the later time points (EBOV gamma, EBOV delta, EBOV sigma). Some of these showed a pronounced CPE which was not observed in the original EBOV variant or other variants. Conversely, other EBOV$_{n120}$ isolates had notably higher longitudinal titers (EBOV alpha, EBOV beta, EBOV omega, EBOV epsilon, EBOV kappa, EBOV lambda) than the original EBOV. After normalizing the titers measured in microglia to VeroE6 titers, whereby normalized titers >1 were considered as increased replication in microglia, further groups were chosen (Figure 65 (B)). Here, EBOV$_{n120}$ early increased replication was observed in EBOV gamma, EBOV delta, EBOV kappa, and EBOV sigma, particularly in comparison to the EBOV stock isolate. Moreover, some had longitudinally decreased replication in microglia, in comparison to VeroE6 cells, namely EBOV epsilon and EBOV omega. Lastly, four variants with relatively elevated long-term (13 dpi) replication capacity were detected (EBOV alpha, EBOV beta, EBOV kappa, EBOV lambda).

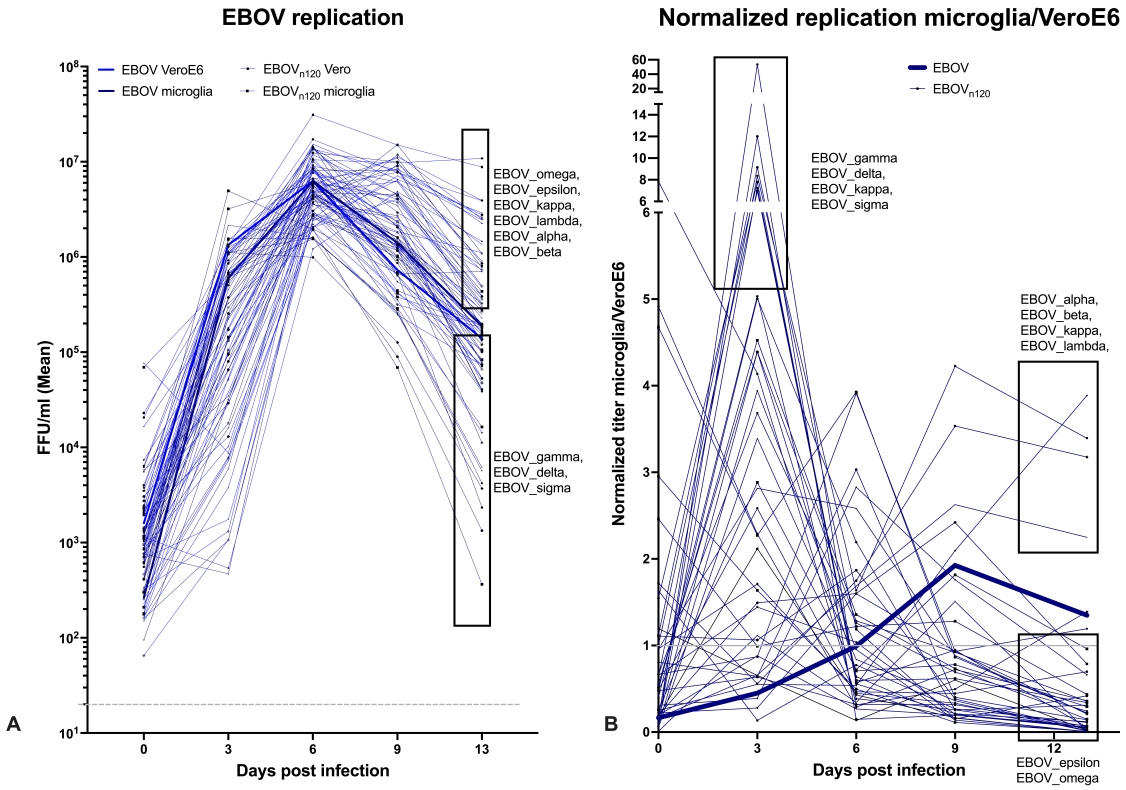


Figure 65: Replication of EBOV$_{n120}$ variants in VeroE6 cells and microglia. (A) Mean viral titers [FFU/ml] of an MRA in VeroE6 cells or immortalized human microglia of EBOV$_{n120}$ virus isolates generated via LDA from the respective 120d longitudinal cerebral organoid supernatants. Infection of n=2 replicates at MOI=0.01. EBOV (original virus: thick) and EBOV$_{n120}$ in thin. Sampling every three days until day 13. Distinct candidates are marked in boxes. LOD=20FFU/ml marked as a grey dotted line. **(B)** Mean virus titers of each variant in microglia normalized to the respective mean titers of the VeroE6 infected samples. The Grey dotted line indicates y=1. Distinct candidates are marked in boxes.

Based on this, nine naturally occurring EBOV$_{n120}$ variants (EBOV alpha, beta, gamma, delta, epsilon, omega, kappa, lambda, sigma) (Table 26) were selected for further replication kinetics in VeroE6 and Huh7 cells, microglia, or astrocytes over a 25 days period (MOI=0.01, n=4 in one experiment) (note: same stock virus as Figure 40).

For all EBOV$_{n120}$ isolates, replication in VeroE6 cells did not present in a grossly altered manner in comparison to the original variant regarding the overall replication course (Figure 66 (A)). In general, mean titers peaked 8 dpi and subsequently slightly decreased for all but one isolate, EBOV alpha, which remained at its peak until 12 dpi before declining to the overall lowest longitudinal titer. Indeed, titers were 10 to 100 fold elevated in EBOV alpha at 12 dpi in comparison to some other variants, particularly EBOV beta and delta. In general, EBOV epsilon and EBOV omega presented with the highest overall titers in the EBOV group upon VeroE6 infection (Figure 67 (A)). Moreover, 4 dpi, both EBOV gamma and EBOV sigma showed the lowest levels of virus replication. Moreover, as seen in Figure 68, while EBOV, EBOV alpha, beta, kappa, and lambda did not display any CPE, EBOV gamma, delta, epsilon, omega, and sigma infection led to extensively damaged monolayers with large clusters of

cell clumps 25 dpi in VeroE6 cells. No cells remained viable in case of EBOV sigma infection.

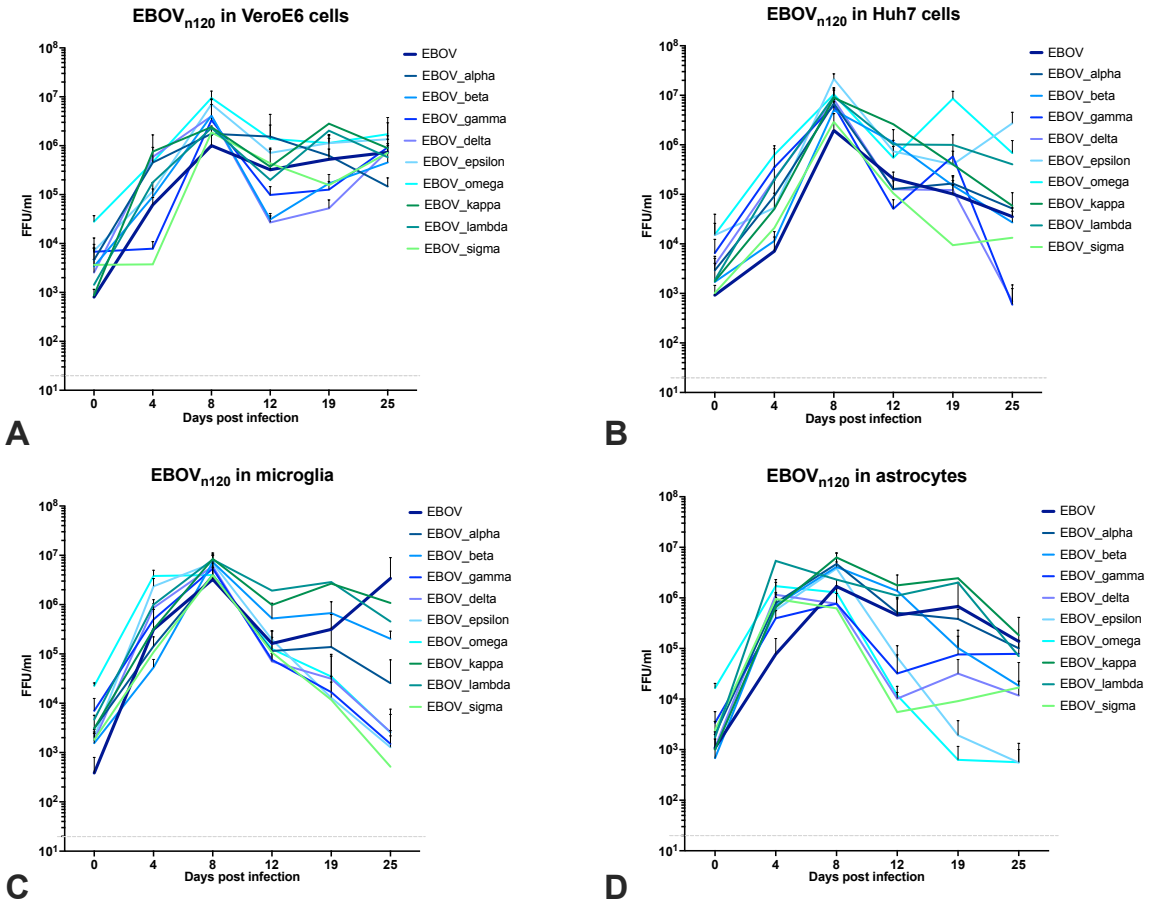


Figure 66: Multicycle-replication of EBOV$_{n120}$ in VeroE6 cells, Huh7 cells, microglia and astrocytes. Mean (+SD) titers [FFU/ml] of EBOV (blue, thick) in comparison to EBOV$_{n120}$ isolates (MOI=0.01, n=4 in one experiment) run in the same experiment as Figure 40. LOD=20FFU/ml marked as a grey dotted line. **(A)** VeroE6 cells + EBOV (isolates) **(B)** Huh7 cells + EBOV (isolates), **(C)** microglia + EBOV (isolates), **(D)** astrocytes + EBOV (isolates).

The replication of EBOV in all other cell types such as Huh7 cells, microglia, and astrocytes, was less cohesive. In this context, EBOV stock virus replication in Huh7 cells peaked 8 dpi before decreasing throughout the remainder of the queried time frame (Figure 66 (B)). This is also true for EBOV alpha, beta, and lambda variants. Conversely, EBOV gamma and delta variant titers crashed after 19 dpi towards 25 dpi to mean titers below 10^3 FFU/ml. Moreover, EBOV sigma titers were also longitudinally low. This was not observed in the VeroE6 cells. In contrast, EBOV epsilon, lambda, and omega variants, which – similar to VeroE6 cells – remained the highest overall in the Huh7 cell infection (Figure 67 (B)). Regarding the observed CPE in Huh7 cells, neither EBOV (variant) led to the destruction of the monolayers, as seen in Figure 68, however, EBOV epsilon and omega with highest overall titers manifested with increased cellular clumping 25 dpi. Additionally, CPE appeared more pronounced in EBOV sigma, where replication was longitudinally low. In contrast, EBOV gamma and delta, whose late-stage replication was even lower than observed for EBOV sigma, decreased longitudinally and did not extensively establish a CPE in Huh7 cells.

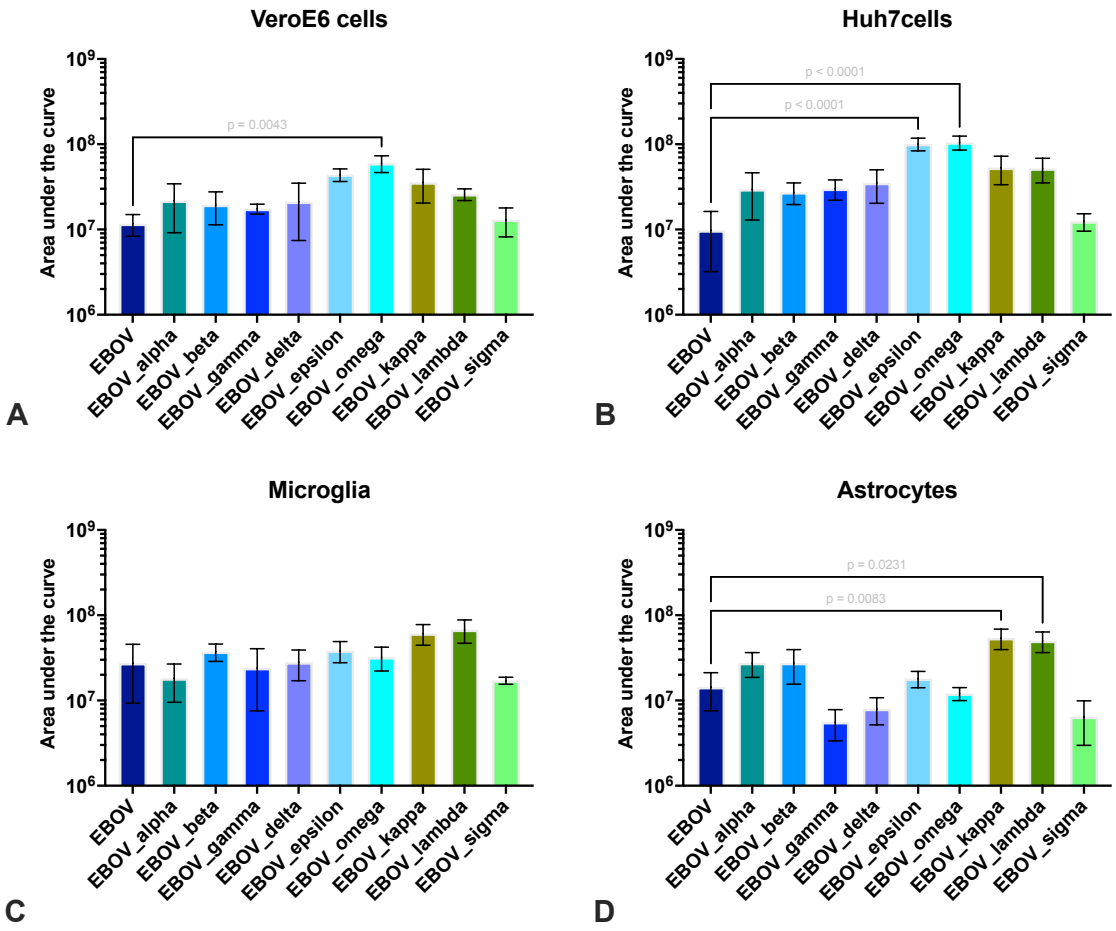


Figure 67: AUC for EBOV$_{n120}$ variants in CNS cells. Area under the curve (AUC) calculations for EBOV$_{n120}$ variants in **(A)** VeroE6 cells, **(B)** Huh7 cells, **(C)** microglia, and **(D)** astrocytes. Baseline =20. One-way ANOVA with Dunnet's Multiple comparisons against the respective EBOV stock. Significance reported.

In immortalized microglia, early EBOV replication, as shown in Figure 66 (C), did not differ amongst the original variant and the CNS-isolated variants until 8–12 dpi. Here, after the initial peak at 8 dpi, all mean titers decreased, although to a variable extent. Only EBOV beta, kappa, and lambda remained at mean titers >10^5 FFU/ml at 12 dpi as well as the highest viral titers longitudinally, except for the original stock. Notably, the CPE observed for the EBOV stock and beta, kappa, and lambda variants were similar (Figure 68). In contrast, EBOV epsilon and omega, which were overall strongest at replicating longitudinally in VeroE6 and Huh7 cells (Figure 66 (A, B), diminished towards mean titers of <10^4 FFU/ml at 25 dpi in microglia. This was further observed for EBOV gamma, delta, and sigma (Figure 66 (E), which were also lowest longitudinally in the Huh7 cells. EBOV alpha replication in microglia clustered in between the more plateaued, persistent replication of the EBOV beta, kappa, and lambda variants but showed a decreasing trend at late stages. Notably, in variants with largely declining longitudinal titers (EBOV gamma, delta, epsilon, omega, sigma) the CPE was most pronounced, as depicted in Figure 68, although clumps of cells were still observable in some. Therefore, this is in line with the CPE observed in VeroE6 and astrocytes but not in

Huh7 cells.

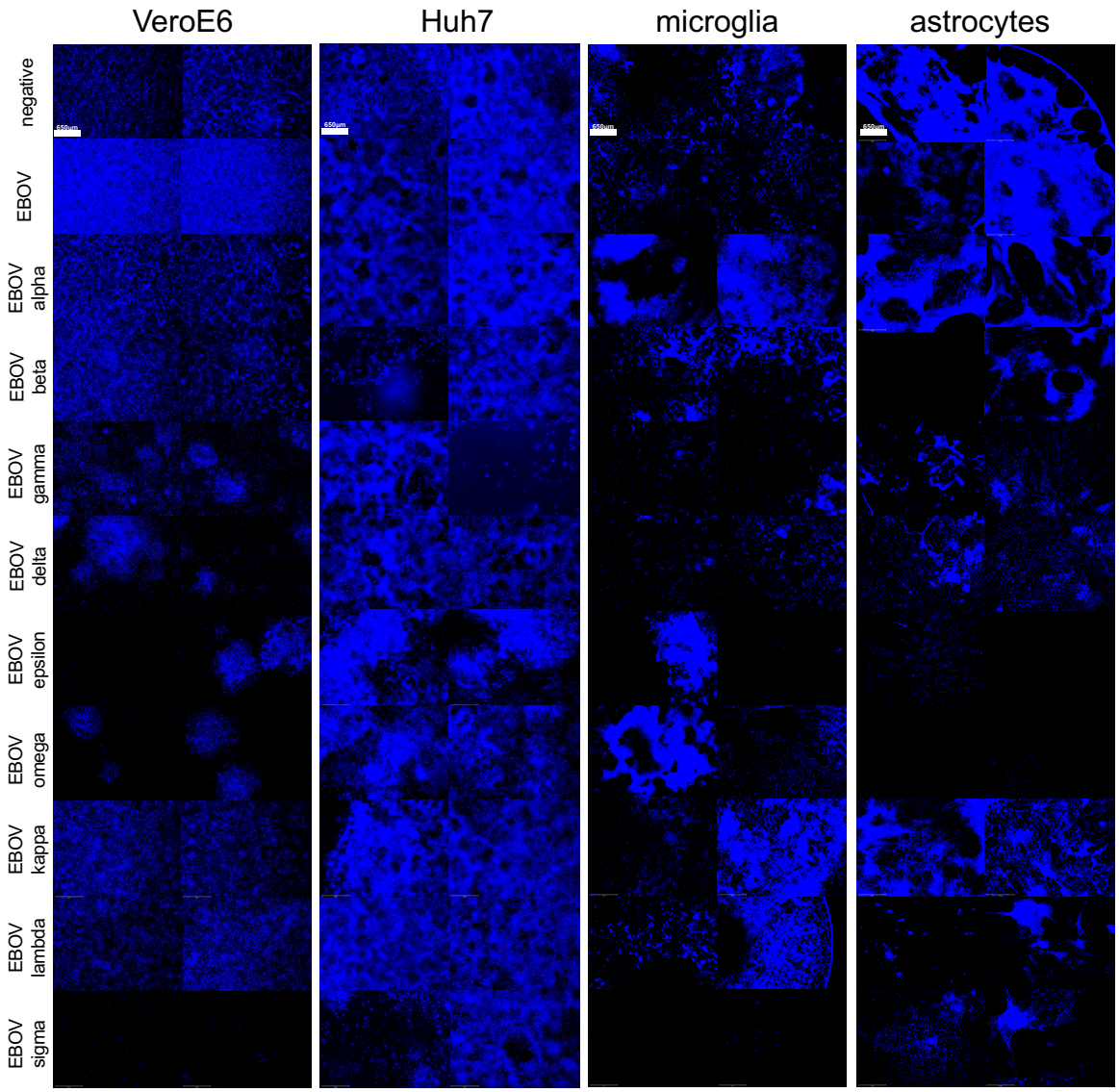


Figure 68: Monolayers of immortalized cells 25dpi with EBOV$_{n120}$ variants. Immunofluorescence microscopy images 25 dpi with EBOV or its isolated variants of VeroE6, Huh7, microglia, and astrocytes stained with DAPI and imaged at 4x magnification. Scale bar indicates 650 µ, n=2 representative replicates each. Image contrast is maximized for purposes of visualization.

Finally, the replication kinetics within the astrocytes was only similar to the EBOV stock until the initial peak of the respective EBOV isolate (Figure 66 (D)). Four variants, EBOV delta, omega, lambda, and sigma, reached this peak already at 6 dpi, while other variants and the EBOV original stock peaked at 8 dpi as seen in VeroE6, Huh7 cells, and microglia. Again, as seen in microglia but in stark contrast to VeroE6 and Huh7 cells, EBOV epsilon and omega declined towards the overall lowest viral titer at 19–25 dpi (<10^3 FFU/ml). This was reflected in the state of the astrocyte monolayer, where only in EBOV epsilon and omega destruction occurred (Figure 68). Among the other early peaking isolates, EBOV delta and sigma, replicated similarly, declining after the initial early peak and subsequently plateauing

19–25 dpi at a low-level titer. Furthermore, EBOV gamma and delta, which presented with a pronounced decline in viral replication in Huh7 cells and microglia, did not follow this pronounced trend in the astrocytes. Both plateaued after 12 dpi and sustained the same level of replication until day 25. Indeed, EBOV gamma clustered close by the original variant and EBOV alpha regarding the longitudinal replication (Figure 66 (G)). The CPE in EBOV gamma and delta was present, although seemingly not as strong as in microglia (Figure 68). EBOV alpha, kappa, and lambda replicated like the original stock in astrocytes, although EBOV alpha continuously, but not as drastically as EBOV epsilon and omega, declined from 8 dpi onwards. In this case, CPE was observable and more pronounced in astrocytes than all other cell types. Meanwhile, EBOV kappa and lambda replicated highest until 19 dpi, whereby titers 25 dpi were comparable to the original stock. As per AUC, replication in astrocytes was overall highest by EBOV kappa and lambda (Figure 67 (D)). While there was barely any CPE in EBOV kappa at 25 dpi, EBOV lambda infection at 25 dpi was accompanied with CPE comparable to EBOV beta.

To conclude, the replication of EBOV in human cerebral organoids for 120 days and subsequent isolation of quasi-species revealed the presence of viruses with distinct replication profiles. While all EBOV$_{n120}$ isolates sustained their broad range in cellular targets in all four cell lines tested, especially later time points of replication uncovered differences in their replication profile. However, this distinction was only really reflected in Huh7 cells, microglia, and astrocytes, while the VeroE6 cells could not seemingly discern the different isolates, despite displaying differential monolayer damage 25 dpi. Overall, EBOV alpha, beta, kappa, and lambda replication appeared least distinct and caused the least CPE in all cell types, while EBOV gamma and delta had especially low-level replication during late stages in Huh7 and microglia. This was reflected in a more extensive CPE. Finally, EBOV epsilon and omega infection resulted in the most drastic changes, which were established by the highest overall longitudinal titers in Huh7 cells, where cell clusters formed, and the opposite effect in both microglia and astrocytes, where the monolayers were extensively damaged. Here, EBOV epsilon and omega titers were more than 100-fold lower at 25 dpi, thereby breaking the pattern of a long-term plateau as seen for the original EBOV variant. Finally, such loss of long-term higher-level replication further occurred for EBOV sigma, where a strong reduction in microglia, Huh7 cells, and astrocyte replication, in line with elevated CPE, was observed.

Notably, enlarged plaque sizes, as revealed by immunofocus assay, were widely similar for EBOV alpha, beta, kappa, and lambda, depicted in Figure 69. In contrast, EBOV epsilon formed mixed-sized plaques, while in EBOV gamma, delta, omega, and sigma, the CPE was more pronounced on the VeroE6 cell monolayer.

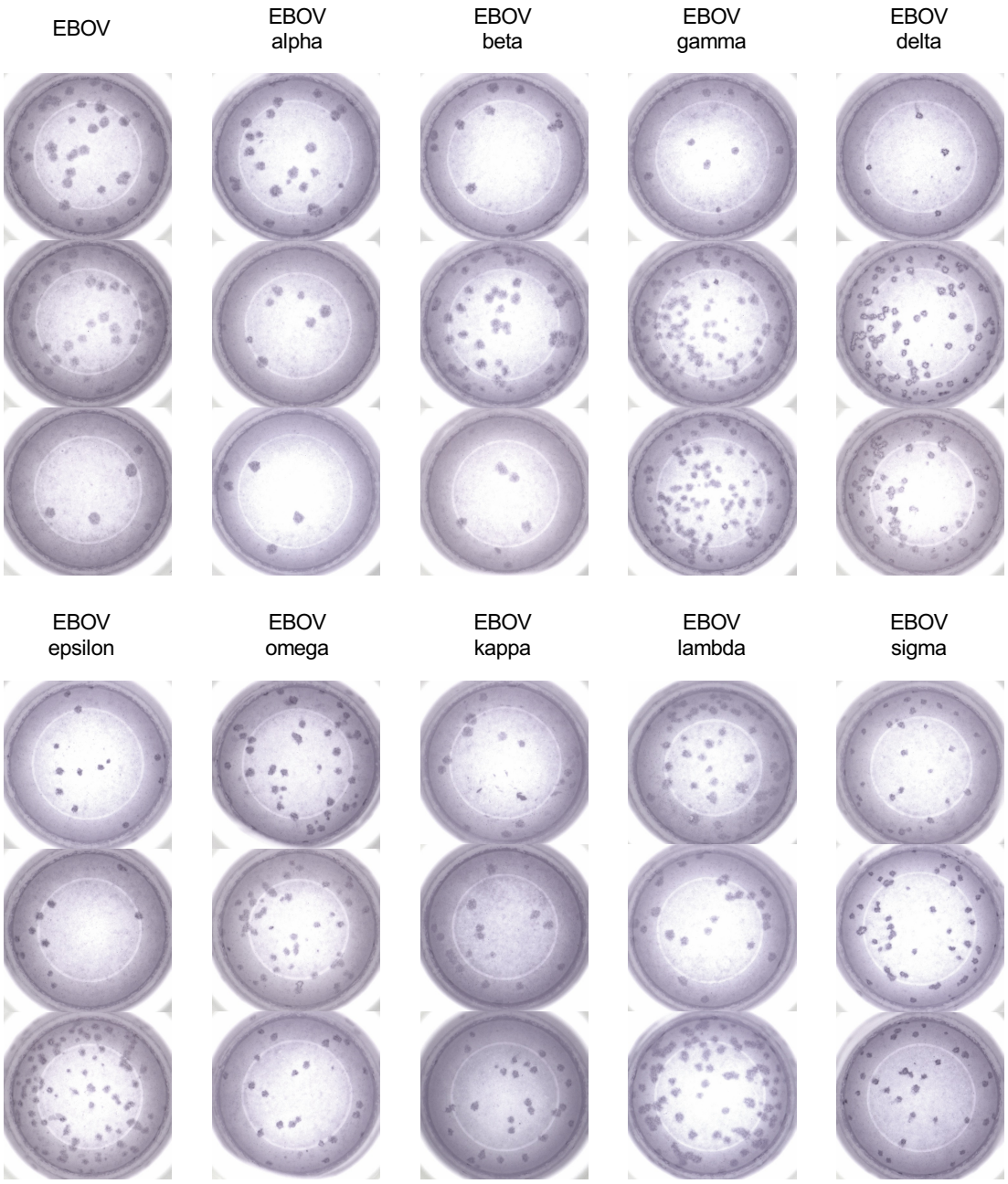


Figure 69: Plaque size in EBOV$_{n120}$. Plaque size during immunofocus assay of EBOV$_{n120}$ in comparison to the original stock, three exemplary images each taken in a 96-well plate. Virus variants indicated above.

6.6.5 Viral RNA sequencing reveals accumulations of coding SNPs across EBOV genome upon CNS selection.

To determine whether EBOV variants are selected in the CNS once it establishes persistence, the isolates that presented with differential replication in diverse immortalized cells were subsequently sequenced. Indeed, all isolates had a varied amount of coding changes ($\geq$60 % of reads) in their genome compared to the stocks used for the infection (Table 26). Some of these SNPs were consistent across the variants isolated from the same and different

cerebral organoid supernatants. Regarding the origins, EBOV alpha + beta, EBOV gamma + delta, EBOV epsilon + omega, and EBOV kappa + lambda each came from the same organoid's supernatant. Notably, most uncovered mutations clustered in NP, GP, VP30, and the L-protein (Figure 70). No conserved mutations were uncovered in the matrix and budding protein VP40. In addition, only one mutation was detected in immunosuppressive VP35 and two in VP24. Lastly, among the SNP meeting the threshold, EBOV kappa and lambda encoded the same.

Table 26: EBOV$_{n120}$ SNP and replication summary. Plaque sizes retrieved from Figure 69.

Virus	Plaque size/CPE	Name (i.a.)	SNP (coding>60%)	25dpi replication
EBOV	large	EBOV$_{n120}$ alpha	NP(R612G)	Huh7: medium, Microglia: medium, Astrocytes: high, CerOrg: high
EBOV	large	EBOV$_{n120}$ beta	NP(S581N), NP(R612G), L(P401L)	Huh7: medium, Microglia: high, Astrocytes: medium, CerOrg: high
EBOV	mixed, CPE	EBOV$_{n120}$ gamma	NP(R612I), VP35(R19K), GP(N257K), GP (E283D), VP30(R196H)	Huh7: medium, Microglia: low, Astrocytes: high, CerOrg: low
EBOV	CPE	EBOV$_{n120}$ delta	NP(D445G), NP(S581G), NP(E590G), NP(R612G), GP(T77I), GP(N257K), L(Y32S), L(R1522G)	Huh7: low, Microglia: low, Astrocytes: medium, CerOrg: low
EBOV	mixed, CPE	EBOV$_{n120}$ epsilon	GP(S12P), GP(H59Y), VP30(S221R), VP30(M237I), VP30(D269E), VP24(P147L), L(L915S), L(C1092Y)	Huh7: high, Microglia: low, Astrocytes: low, CerOrg: high
EBOV	mixed, CPE	EBOV$_{n120}$ omega	GP(S12P), VP30(M237I), VP30(D269E), VP24(P147L), L(L915S), L(C1092Y)	Huh7: high, Microglia: low, Astrocytes: low, CerOrg: medium
EBOV	large	EBOV$_{n120}$ kappa	NP (P428S), NP (A605V), GP (S46N), GP (I249T), GP (D257N), VP30 (S234P)	Huh7: medium, Microglia: high, Astrocytes: high, CerOrg: medium
EBOV	large	EBOV$_{n120}$ lambda	NP (P428S), NP (A605V), GP (S46N), GP (I249T), VP30 (S234P)	Huh7: high, Microglia: high, Astrocytes: high, CerOrg: medium
EBOV	mixed, CPE	EBOV$_{n120}$ sigma	NP (P428S), NP (N500K), GP (S46N), GP (I249T), GP (D257N), VP30 (E205V), VP24 (R140H), L (R1644G), L (H1754Y)	Huh7: low, Microglia: low, Astrocytes: low, CerOrg: low

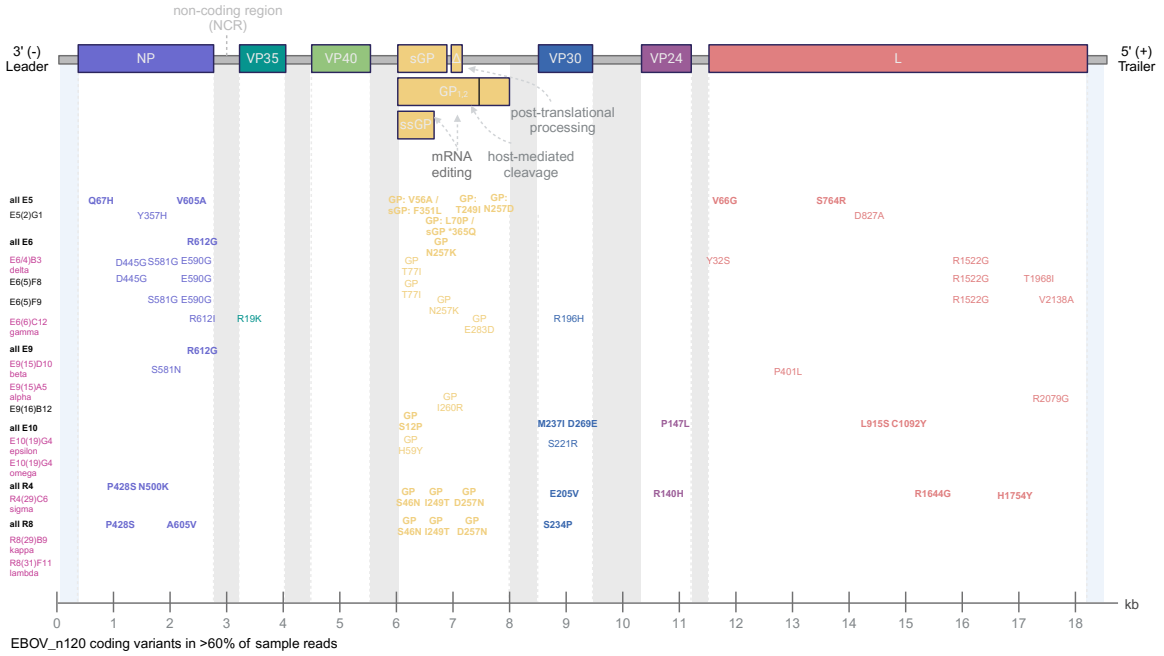


Figure 70: Coding SNPs in EBOV$_{n120}$. Coding SNPs occurring in $\geq$60 % of reads in EBOV$_{n120}$ variants in the displayed genomic region.

6.6.6 Naturally occurring EBOV$_{n120}$ variants display the same persistence profile in human cerebral organoids.

Next, the limited set of naturally occurring CNS variants was used to infect human cerebral organoids (n=6, 1 batch, 10^4 FFU/organoid), to determine whether their replication profile has changed after their long-term replication in CNS tissue. It must be noted that initial titers of infection of the original EBOV were seemingly lower, given the day of infection titers in comparison to the variants. This was likely caused by the re-use of the original stock to ensure sequence identity. Moreover, this experiment was only performed in one cerebral organoid batch and therefore requires further repetition.

Despite these technical limitations, the replication assay in the cerebral organoid, as depicted in Figure 71, demonstrated that all EBOV$_{n120}$ variants retained a similar replication profile in human cerebral organoids. The EBOV$_{n120}$ variants were able to establish a persistent infection without clearance in 100 % of infected organoids, as previously seen with EBOV in Figure 26 (A).

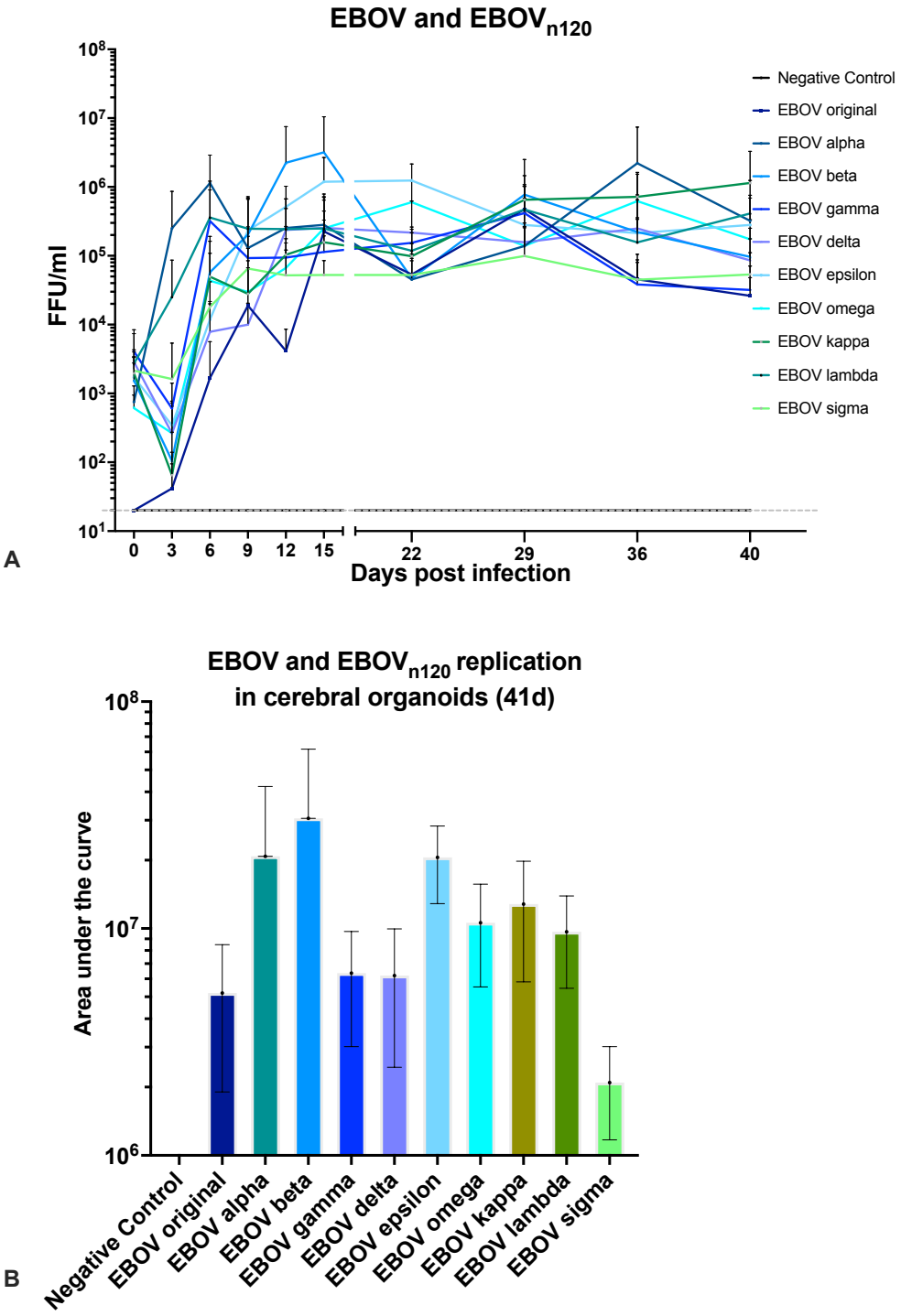


Figure 71: Replication of EBOV$_{n120}$ in human cerebral organoids. (A) Mean titers [FFU/ml] of EBOV in comparison to EBOV$_{n120}$ isolates in human cerebral organoids. Infection with 10^4 FFU/organoid, with 6 organoids per group originating from one batch. LOD=20FFU/ml marked as a grey dotted line. **(B)** Area under the curve (AUC) calculation of EBOV and EBOV$_{n120}$ titers in human cerebral organoid supernatants for 41 days. LOD was used as a baseline. Plotted are mean and SEM. One-way ANOVA with Dunnet's Multiple comparisons: no significance.

Amongst the EBOV$_{n120}$ variants, EBOV alpha established a strong replication the earliest, peaking already at 3–6 dpi before declining and peaking longitudinally again. Together with EBOV beta and epsilon, AUC calculations overall revealed their replication the highest

throughout (Figure 71 (B)). Additionally, EBOV lambda replication peaked 6 dpi before remaining stable until 41 dpi. Meanwhile, EBOV epsilon seemingly replicated to the highest extent from 15–22 dpi in the range from 10^5 to 10^6 FFU/ml before longitudinally remaining at a high level of 10^5 to 10^6 FFU/ml, together with EBOV omega, alpha, beta, lambda, and delta. Meanwhile, EBOV gamma and sigma clustered at overall slightly lower titers longitudinally. Notably, EBOV sigma had overall lowest titers throughout, as per AUC, whereby EBOV gamma and delta were among the lower group as well. Notably, all EBOV$_{n120}$ variants with low replication regarding their AUC in cerebral organoids were those with smaller and mixed-plaque populations as well as CPE in a plaque assay shown in Figure 69.

6.6.7 Staining for NP and GP in EBOV$_{n120}$ variants reveals distinct antigenic distribution and infection phenotype.

25 dpi with the respective EBOV$_{n120}$ variants, immunofluorescence microscopy staining was performed, staining for F-actin as well as either EBOV NP or GP. Here, the following observations were made but not quantified. EBOV alpha, which encoded one dominant mutation NP(R612G), formed large plaques and overall replicated well longitudinally in 2D and cerebral organoids. Upon infection, immunofluorescence staining did not reveal a particular difference regarding the viral protein expression in astrocytes and Huh7 cells. No images were attained for microglia (Figure 72).

EBOV beta carried SNPs in NP(S581N), NP(R612G), and L(P401L) and formed large plaques in the immunofocus assay (Figure 69). This variant replicated overall well at late stages in all measured cell types and particularly in cerebral organoids. As is depicted in Figure 73, EBOV beta infection in microglia led to a pronounced formation of long-range cellular connections as previously described for original EBOV (Figure 49). Here, EBOV GP was located, infecting via the cell-to-cell route. Infection rates in microglia and astrocytes were additionally elevated in EBOV beta when comparing to images of the original stock infection previously presented in Figure 44 and Figure 45.

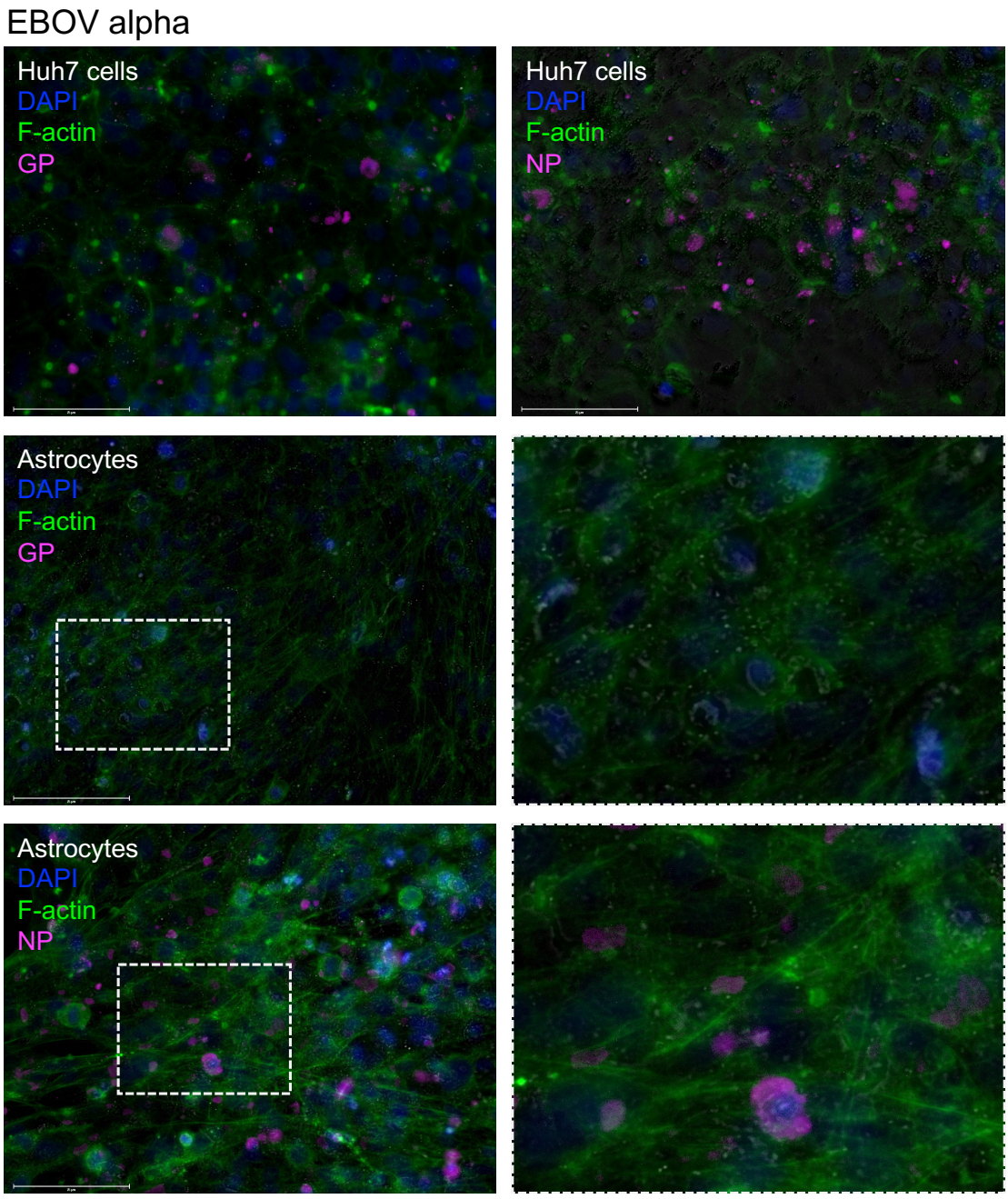


Figure 72: Expression of EBOV NP and GP in EBOV alpha. Immunofluorescence microscopy images of Huh7 cells and astrocytes infected for 25 days with EBOV alpha. NP(R612G). Staining for F-actin (green), and EBOV NP / GP (magenta). Counter-staining using DAPI (blue). The scale bar indicates 75 µm.

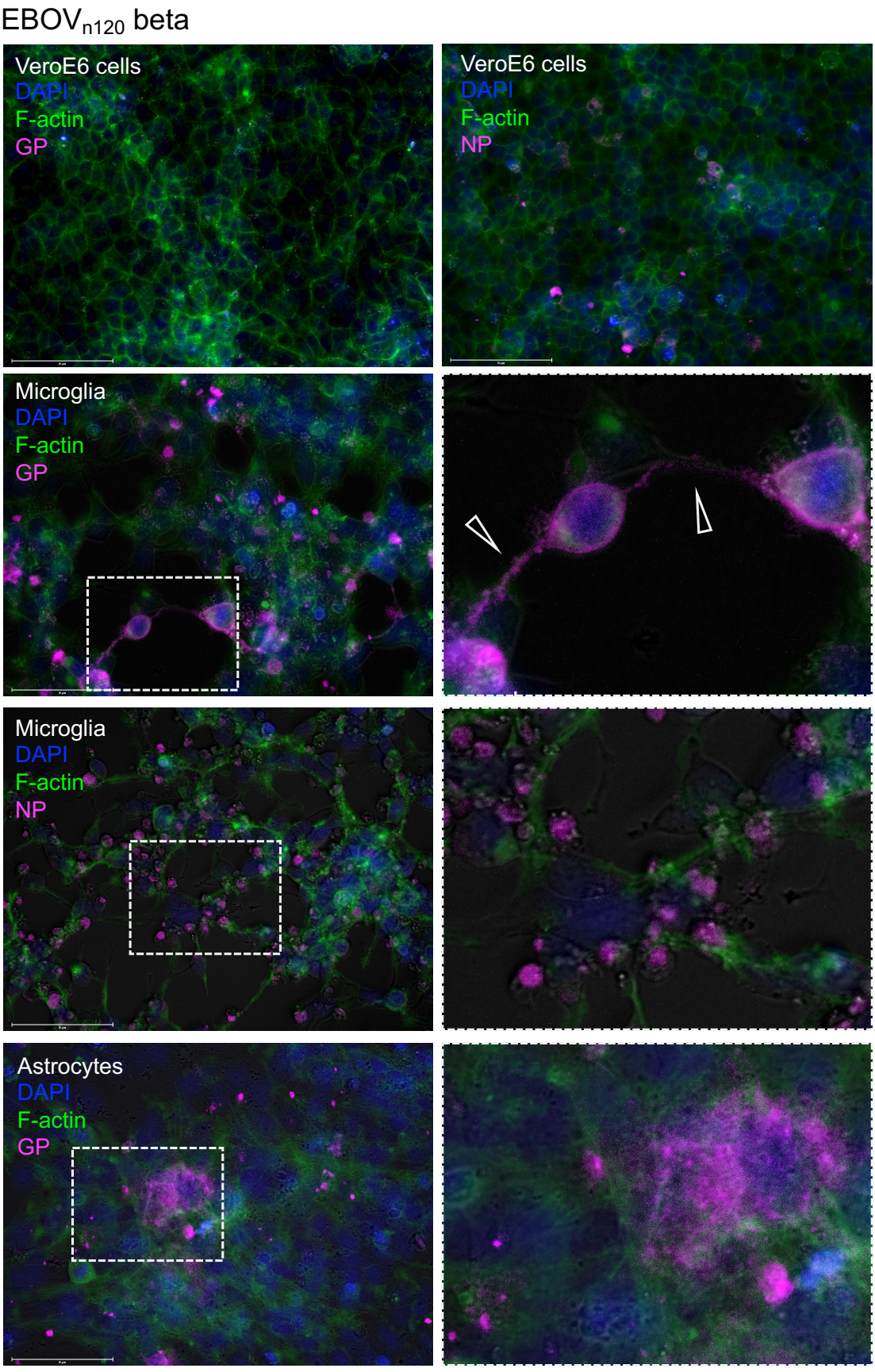


Figure 73: Expression of EBOV NP and GP in EBOV beta. Immunofluorescence microscopy images of VeroE46 cells, and microglia infected for 25 days with EBOV beta. NP(S581N), NP(R612G), L(P401L). Staining for F-actin (green), and EBOV NP / GP (magenta). Counter-staining using DAPI (blue). The scale bar indicates 75 µm. Boxed areas zoomed in on the right side.

EBOV gamma was mutated in multiple loci: NP(R612I), VP35(R19K), GP(N257K), GP-(E283D), and VP30(R196H). This variant formed mixed-sized plaques with signs of CPE on the VeroE6 monolayer used for the plaque assay (Figure 69). Furthermore, EBOV gamma behaved differently in astrocytes and microglia, whereby longitudinal replication in microglia was low due to extensive CPE but remained high in astrocytes. Replication in cerebral organoids was low. Immunofluorescence microscopy of EBOV NP and GP expression upon EBOV gamma infection of microglia, displayed in Figure 74, depicts the formation of long-range cell-cell connections in which EBOV NP and GP staining was positive. Additionally, long-range connections between astrocyte-bundles, containing EBOV NP, were further detected. Expression of viral protein, also in Huh7 cells, was more pronounced than upon infection with the original EBOV stock for 25 days (previously shown in Figure 43, Figure 44 and Figure 45).

Eight predominant, coding SNP were found in EBOV delta. These were NP(D445G), NP(S581G), NP(E590G), NP(R612G), GP(T77I), GP(N257K), L(Y32S), and L(R1522G). The naturally occurring EBOV$_{n120}$ variant formed the most pronounced CPE in plaque assays (Figure 69), whereby CPE in VeroE6 cells and microglia was observed (Figure 68). EBOV delta replicated minimally in Huh7 cells and microglia at late stages. Replication in astrocytes was in the medium group longitudinally and among the lowest replication in cerebral organoids. Immunofluorescence microscopy of EBOV NP and GP expression in microglia revealed an elevated expression of EBOV GP (Figure 75). Furthermore, in astrocytes, localization of GP to the actin cytoskeleton and in cellular connections was observed.

EBOV epsilon, encoding GP(S12P), GP(H59Y), VP30(S221R), VP30(M237I), VP30(D269E), VP24(P147L), L(L915S), L(C1092Y) mutations, was further observed in immunofluorescence microscopy staining for EBOV antigens GP and NP. The variant had previously been shown to result in mixed-sized plaques and CPE in all but Huh7 cells. Replication was longitudinally low in microglia and astrocytes, however highest in Huh7 cells and cerebral organoids. As per immunofluorescence microscopy in Figure 76, Huh7 cells presented with high expression of both viral antigens. This was also true for microglia, where the CPE was high. In astrocytes, EBOV NP staining further revealed the formation of large NP inclusion bodies-like structures within the cytoplasm.

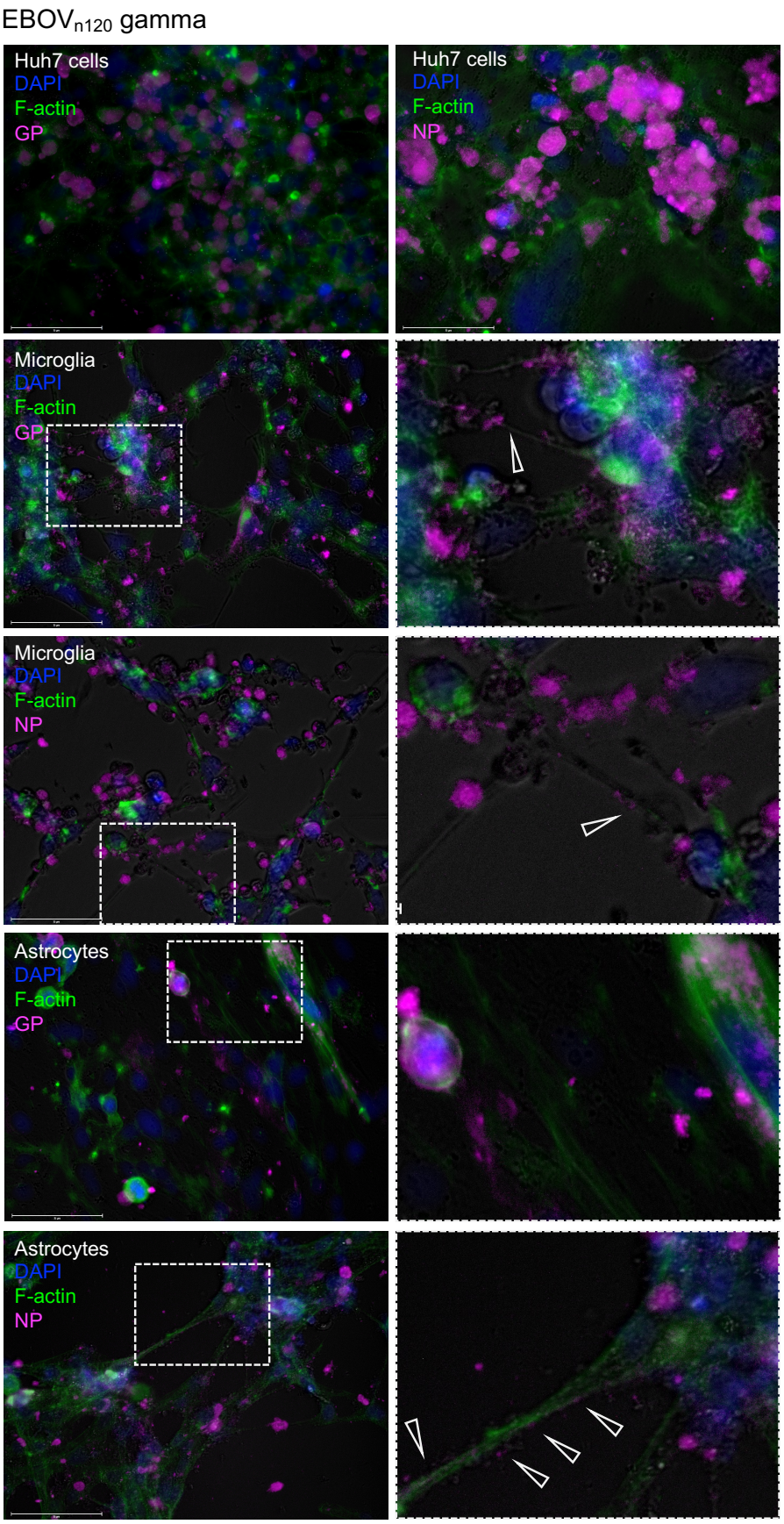


Figure 74: Expression of EBOV NP and GP in EBOV gamma. Immunofluorescence microscopy images of Huh7 cells, microglia, and astrocytes infected for 25 days with EBOV gamma. NP(R612I), VP35(R19K), GP(N257K), GP(E283D), VP30(R196H). Staining for F-actin (green), and EBOV NP / GP (magenta). Counter-staining using DAPI (blue). Scale bar indicates 75 µm. Boxed areas zoomed in on the right side.

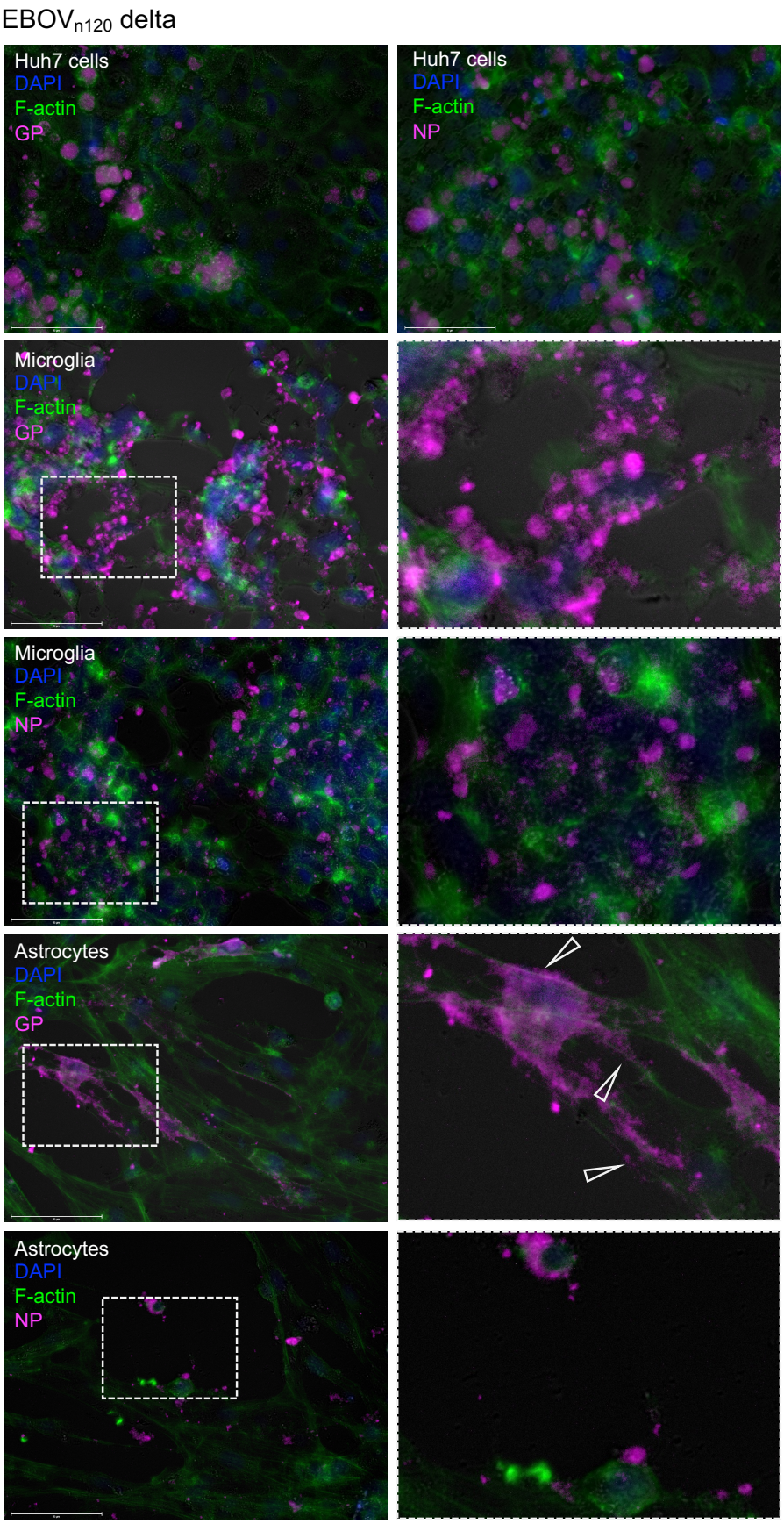


Figure 75: Expression of EBOV NP and GP in EBOV delta. Immunofluorescence microscopy images of Huh7 cells, microglia, and astrocytes infected for 25 days with EBOV delta. NP(D445G), NP(S581G), NP(E590G), NP(R612G), GP(T77I), GP(N257K), L(Y32S), L(R1522G). Staining for F-actin (green), and EBOV NP / GP (magenta). Counter-staining using DAPI (blue). Scale bar indicates 75 µm. Boxed areas zoomed in on the right side.

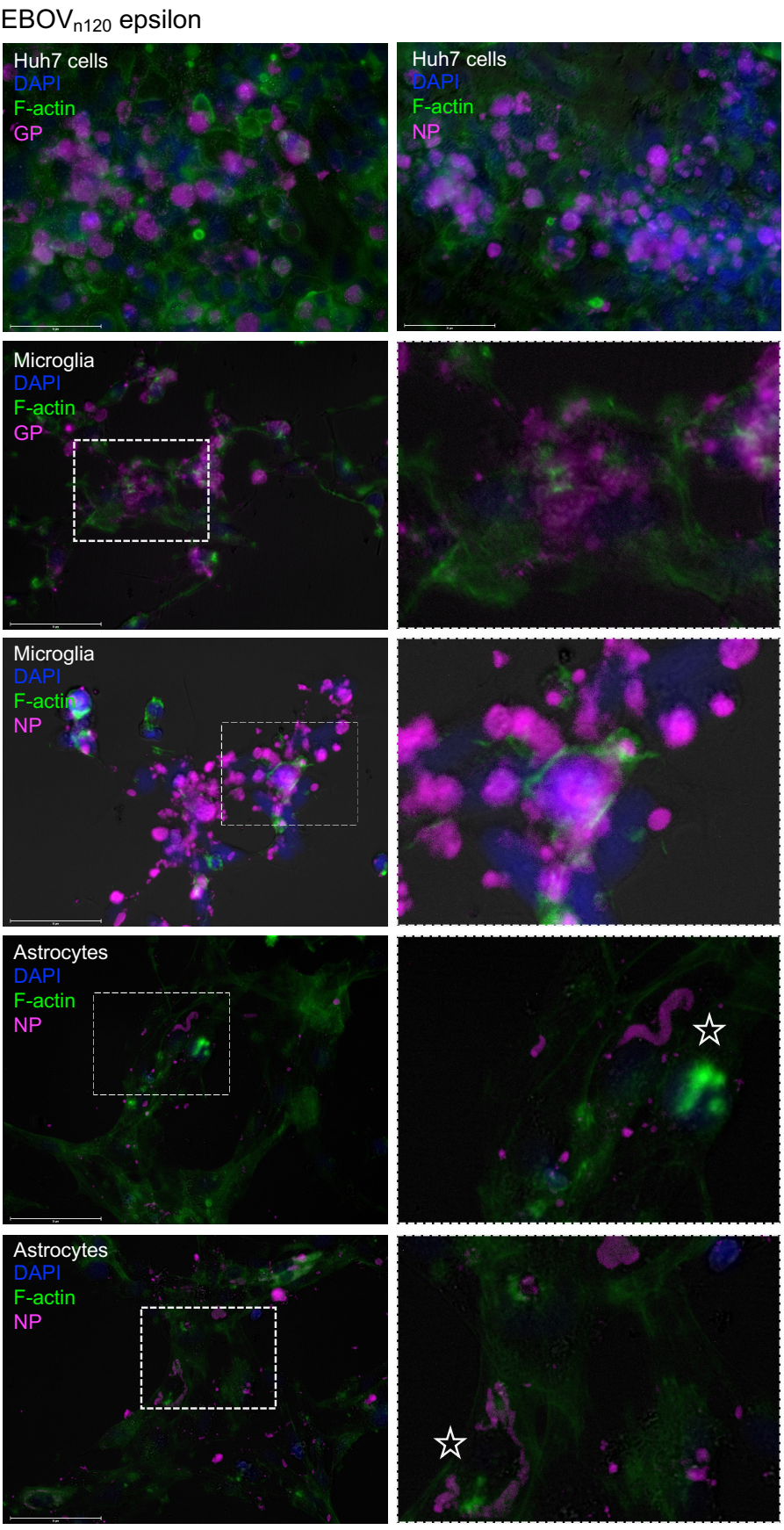


Figure 76: Expression of EBOV NP and GP in EBOV epsilon. Immunofluorescence microscopy images of Huh7 cells, microglia, and astrocytes infected for 25 days with EBOV epsilon. GP(S12P), GP(H59Y), VP30(S221R), VP30(M237I), VP30(D269E), VP24(P147L), L(L915S), L(C1092Y). Staining for F-actin (green), and EBOV NP / GP (magenta). Counter-staining using DAPI (blue). Scale bar indicates 75 µm. Boxed areas zoomed in on the right side.

The EBOV omega variant, encoding GP(S12P), VP30(M237I), VP30(D269E), VP24(P147L), L(L915S), L(C1092Y), formed mixed-sized plaques with CPE in plaque assays (Figure 69). Furthermore, a high level of replication in Huh7 cells was contrasted with low replication in astrocytes and microglia 25 dpi. CPE was observed in all but Huh7 cells. Images were only retrieved for microglia, where EBOV GP and NP expression were less pronounced than in other variants. Notably, expression of viral proteins was high in Huh7 cells upon EBOV omega infection 25 dpi (Figure 77).

The following mutations were encoded in EBOV kappa: NP (P428S), NP (A605V), GP (S46N), GP (I249T), GP (D257N), VP30 (S234P). In the plaque assay, the variant formed large plaques, while long-term replication in either cell type and cerebral organoids was overall in the medium-range. In Figure 78, the immunofluorescence staining of EBOV NP and GP upon 25 days of EBOV kappa infection are depicted. Here, viral protein expression was strong, particularly in Huh7 cells. In microglia and astrocytes, no particular observations were made.

EBOV lambda, with the same SNP as EBOV kappa in NP (P428S), NP (A605V), GP (S46N), GP (I249T), GP (D257N), VP30 (S234P), was found to also form large plaques. The variant replicated to overall high titers at late stages in all cell types and cerebral organoids. Via immunofluorescence microscopy, representative images shown in Figure 79, it was furthermore found that EBOV lambda infection came with particularly pronounced long-range cellular connections, both in microglia and astrocytes. Indeed, cell-cell connections between singular ramified microglia contained EBOV GP and NP. In astrocytes, cellular bulks formed large-scale actin-stabilized connections of more than 750 µm in length, containing large amounts of EBOV GP.

The last tested EBOV$_{n120}$ variant, EBOV sigma, encoded NP (P428S), NP (N500K), GP (S46N), GP (I249T), GP (D257N), VP30 (E205V), VP24 (R140H), L (R1644G), L (H1754Y). Here, an overall strong CPE and mixed-sized plaques were observed (Figure 69, Figure 68). The variant replicated highly in Huh7 cells and overall least in cerebral organoids. However, replication was drastically lower in astrocytes and microglia at 25 dpi, where pronounced CPE was observed. In Figure 80, the expression of GP and NP of EBOV sigma are exemplified. Notably, in astrocytes, EBOV GP localized to the cellular connections, while NP formed large inclusion body-like accumulations, as previously observed for EBOV epsilon.

In conclusion, the naturally occurring variants retrieved from 120 days-infected human cerebral organoids not only presented with differential replication in diverse cell types but also distinct antigenic distribution upon infection. Concluding the fourth objective, it can be surmised that EBOV variants are likely selected based on the host environment in persistent CNS infections in humans. Moreover, this can be captured using the herein-presented, novel human cerebral organoid model for EBOV infections.

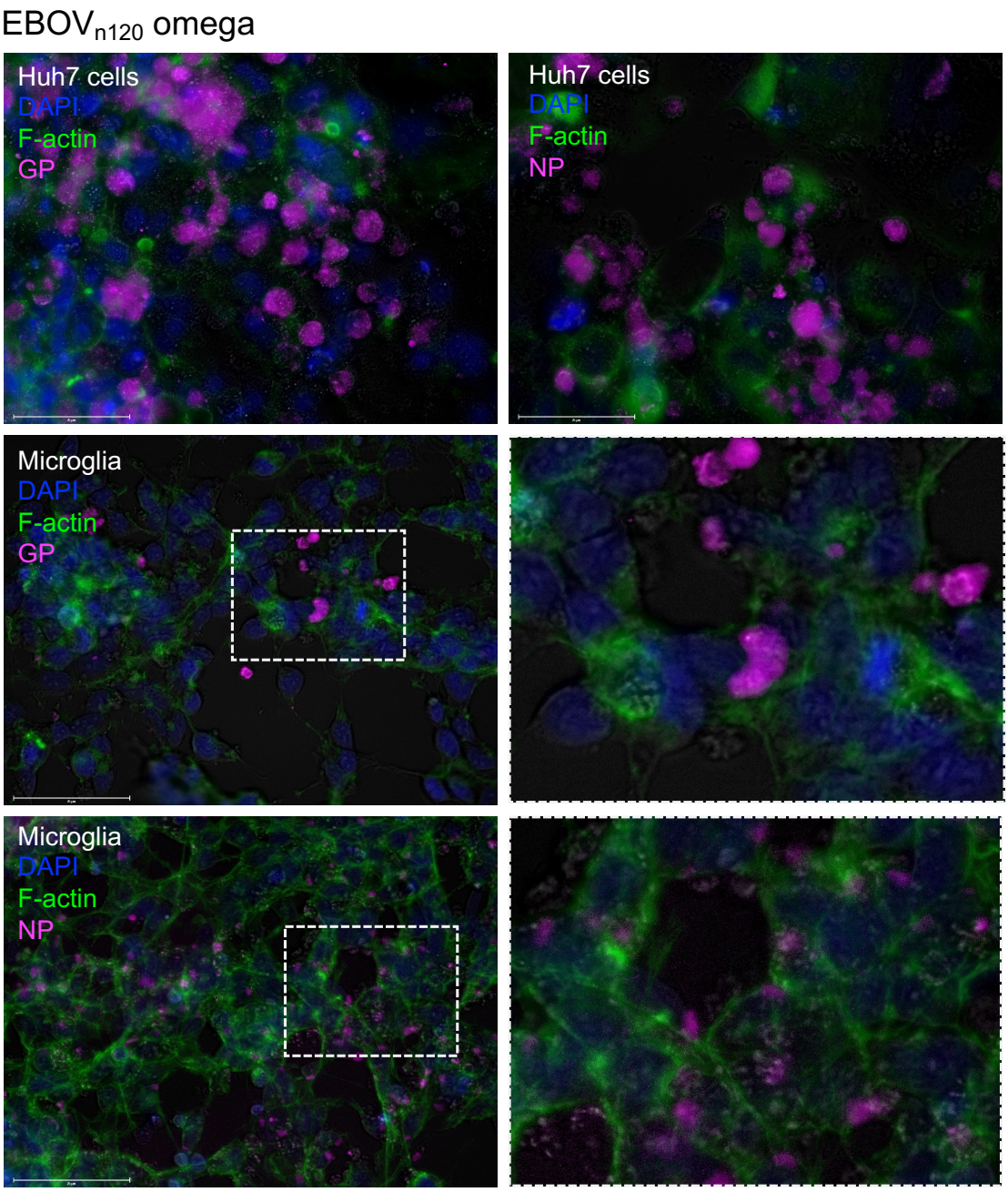


Figure 77: Expression of EBOV NP and GP in EBOV omega. Immunofluorescence microscopy images of Huh7 cells and microglia infected for 25 days with EBOV omega. GP(S12P), VP30(M237I), VP30(D269E), VP24(P147L), L(L915S), L(C1092Y). Staining for F-actin (green), and EBOV NP / GP (magenta). Counter-staining using DAPI (blue). Scale bar indicates 75 µm. Boxed areas zoomed in on the right side.

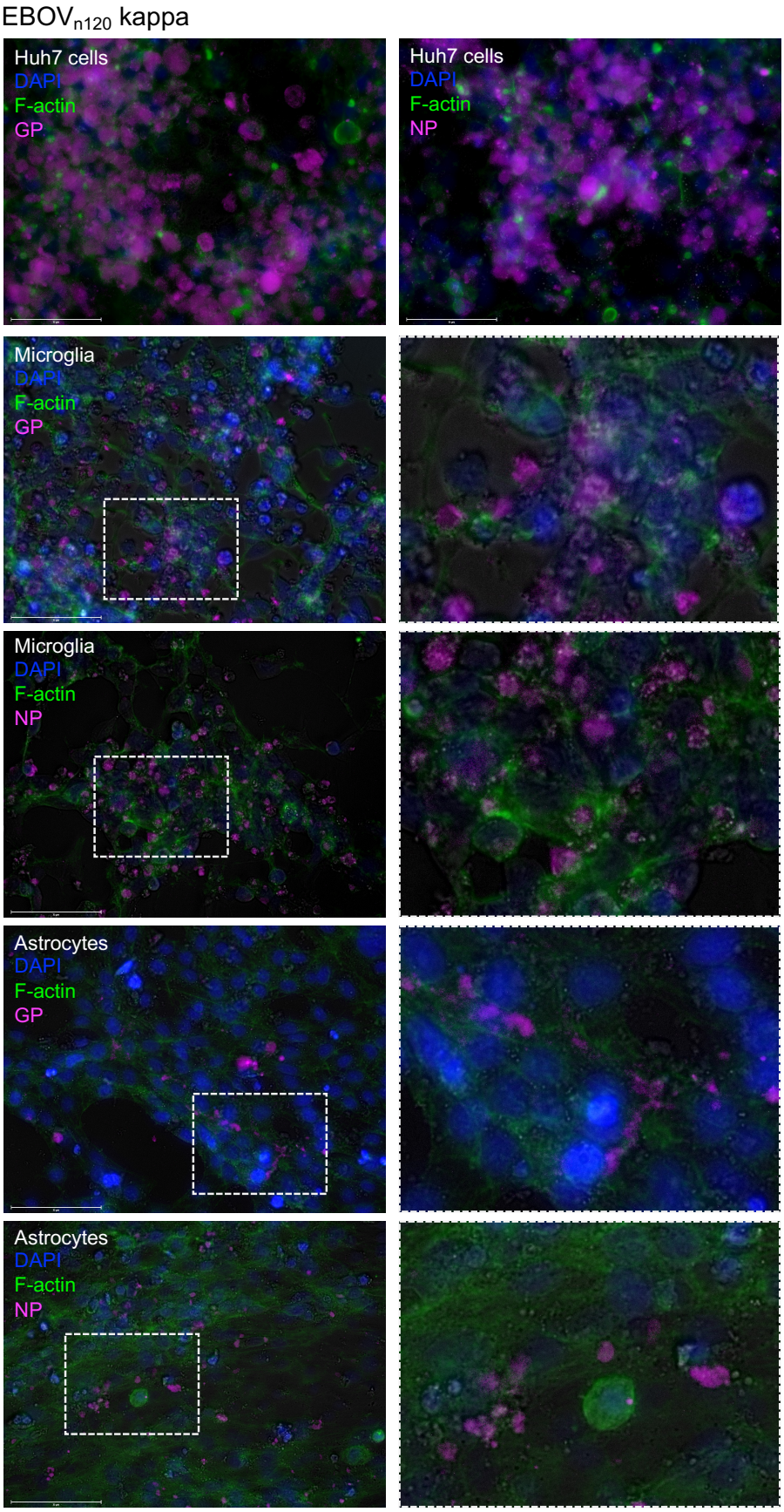


Figure 78: Expression of EBOV NP and GP in EBOV kappa. Immunofluorescence microscopy images of Huh7 cells, microglia, and astrocytes infected for 25 days with EBOV kappa. NP (P428S), NP (A605V), GP (S46N), GP (I249T), GP (D257N), VP30 (S234P). Staining for F-actin (green), and EBOV NP / GP (magenta). Counter-staining using DAPI (blue). Scale bar indicates 75 µm. Boxed areas zoomed in on the right side.

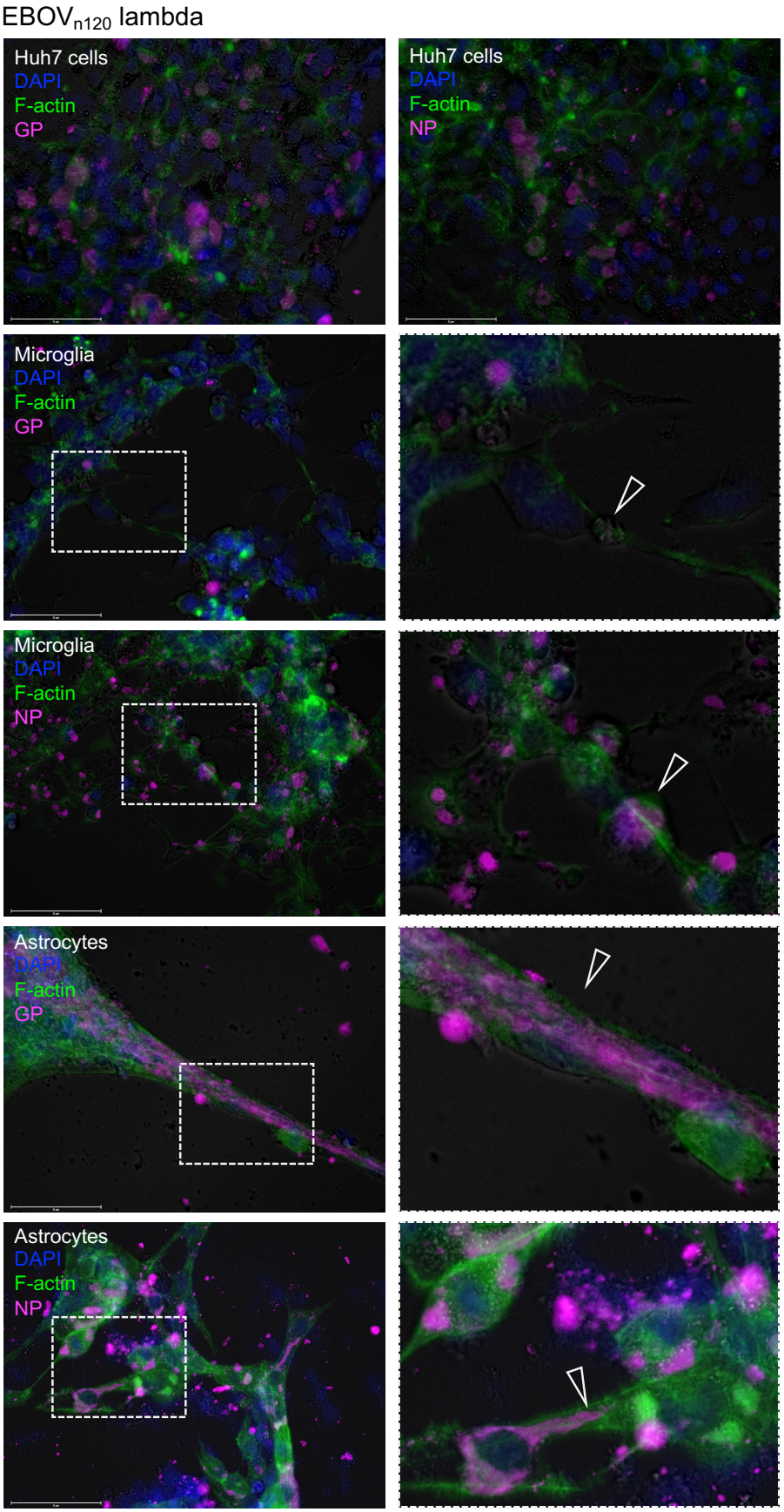


Figure 79: Expression of EBOV NP and GP in EBOV lambda. Immunofluorescence microscopy images of Huh7 cells, microglia, and astrocytes infected for 25 days with EBOV lambda. NP (P428S), NP (A605V), GP (S46N), GP (I249T), GP (D257N), VP30 (S234P). Staining for F-actin (green), and EBOV NP / GP (magenta). Counter-staining using DAPI (blue). Scale bar indicates 75 µm. Boxed areas zoomed in on the right side.

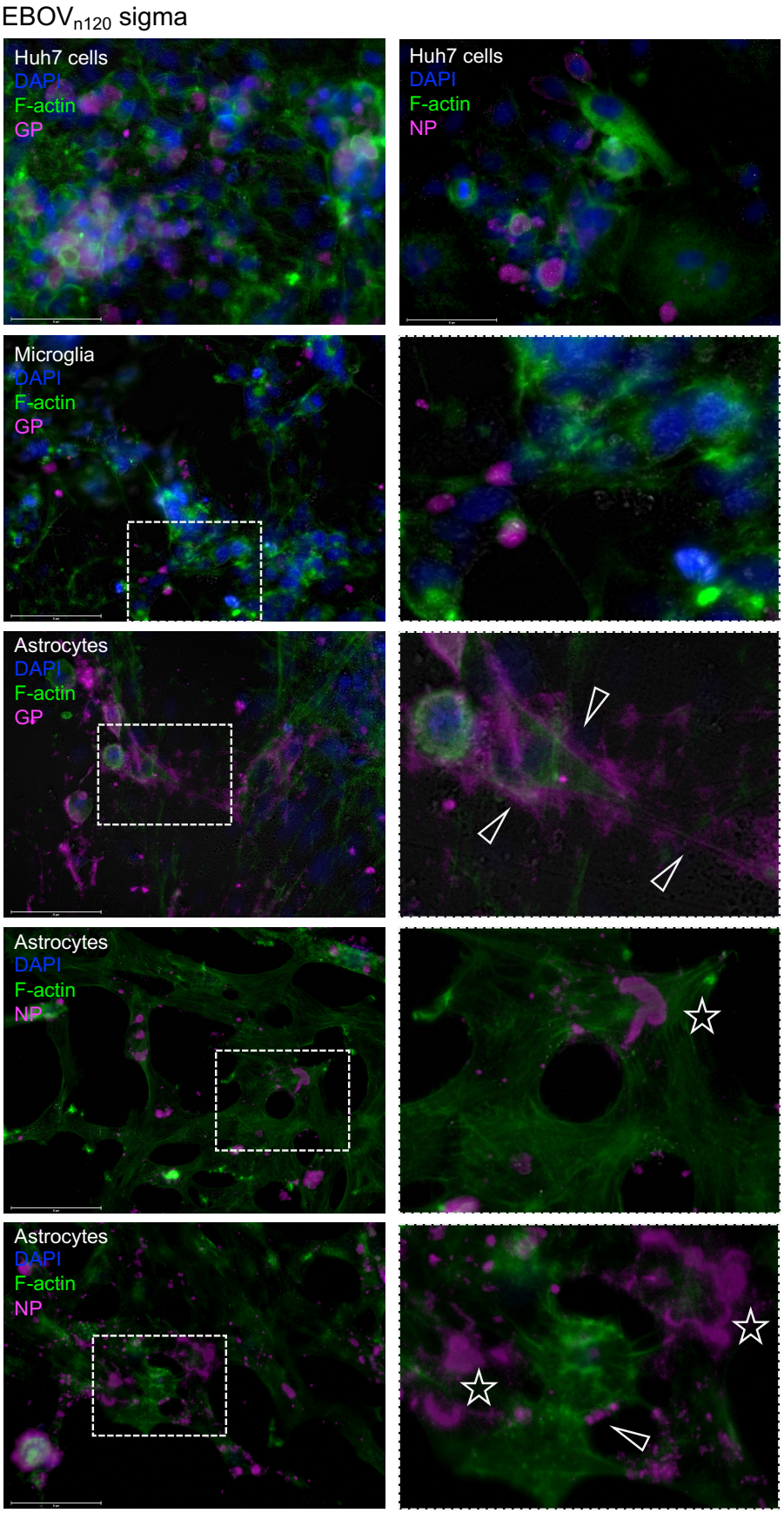


Figure 80: Expression of EBOV NP and GP in EBOV sigma. Immunofluorescence microscopy images of Huh7 cells, microglia, and astrocytes infected for 25 days with EBOV sigma. NP (P428S), NP (N500K), GP (S46N), GP (I249T), GP (D257N), VP30 (E205V), VP24 (R140H), L (R1644G), L (H1754Y). Staining for F-actin (green), and EBOV NP / GP (magenta). Counter-staining using DAPI (blue). Scale bar indicates 75 µm. Boxed areas zoomed in on the right side.

7 Summary of results

In this study, EBOV persistence in the human CNS was investigated using a novel human cerebral organoid infection model that captures host-pathogen interactions during long-term infections.

Accordingly, in the scope of the first objective, human cerebral organoids and choroid plexus organoids as well as long-term in vitro cultures were generated. As part of the second objective, the human cerebral organoids were used to demonstrate that EBOV specifically establishes a persistent infection of at least 120 days in human CNS tissue, including long-term viral replication and viral shedding. Notably, during EBOV persistence, non-infectious viral RNA was increasingly shed, whereby an increase in 5'cb-DVG diversity was furthermore observed. As early and prolonged targets of EBOV CNS infection, the neuronal mass making up the organoid was identified. Furthermore, astrocytes were infected particularly during late stages, while microglia migrated towards areas of infection. Finally, as revealed by multiplex cytokine assays, EBOV persistence led to some degree of neuroinflammation at late stages of infection, which was to be differentiated from a more acute LASV CNS infection. Importantly, the establishment of EBOV CNS persistence in the human cerebral organoid model was confirmed in a choroid plexus organoid model and found to be conserved across (recombinant) orthoebolaviruses, including RESTV-GFP. RESTV-GFP, in this study, replicated to a lower extent than EBOV-GFP in human cerebral organoids.

As a third objective, the host response to EBOV persistence was investigated using 2D cell culture models of long-term infection. Here, previous works by Calain *et al*. were successfully reproduced, leading to the generation of a persistently EBOV-infected microglia cell line via serial passaging. Here, productive infection was maintained for 91 days. Moreover, long-term infection of microglia and astrocyte cell lines was achieved for 25 days without passaging, whereby the establishment of persistence concomitant with viral release was viral load-independent and specific to EBOV (in comparison to LASV). Importantly, CPE was revealed as a major limiting factor in the establishment of viral persistence in 2D cultures.

In microglia, the infection with EBOV-GFP led to an increase in CX3CR1 surface expression, as determined by flow cytometry. This was located to the microglial ramifications. Importantly, inhibition of CX3CR1 via an allosteric inhibitor did not affect EBOV replication in microglia, however, a slight trend towards reduced replication was observed in choroid plexus organoids in 3D. Notwithstanding this, EBOV persistence was achieved and maintained with and without CX3CR1 activity in choroid plexus organoids, microglia, and astrocytes.

In transcriptome screens using RNA sequencing, the response of microglia and astrocytes to persistent EBOV infection was analyzed. In these experiments, it was overall observed that while astrocytes do not respond with a strong antiviral response, microglia strongly responded

to the inoculation with EBOV by upregulation of the interferon and antiviral response. At the same time, translation was increasingly downregulated. Astrocytes overall remained at a more regulatory state in which morphogenic and regenerative pathways were more enriched. Notably, at later stages of EBOV infection in microglia, proliferative and migratory pathways were additionally elevated.

Finally, to fulfill the scope of the fourth objective, EBOV genomics during persistent CNS infection were analyzed. Here, EBOV genome replication versus gene expression in microglia and astrocytes revealed distinct profiles. In addition, naturally occurring EBOV variants were analyzed regarding their replicative capacity in diverse cell types and human cerebral organoids. Taken together, these experiments covering the viral side of the host-pathogen interface revealed a likely selection of EBOV variants in the CNS upon persistence.

In summary, in this thesis, suitable in vitro models for the studies on EBOV persistence in the CNS were established. These were further employed to uncover future targets within the intricate interplay occurring at the host-pathogen interface between EBOV and human CNS cells during viral persistence.

8 Discussion

8.1 Studies on Ebola virus CNS persistence in a tissue context using human cerebral and choroid plexus organoids

8.1.1 Partially immunocompetent human cerebral and choroid plexus organoids

In this study, partially immunocompetent human cerebral organoids [214, 217] as well as choroid plexus organoids [223] were successfully generated to investigate the mechanisms and physiology of EBOV persistence. For the generation of human cerebral organoids, an unguided differentiation protocol was chosen, which resulted in organoids containing mesoderm-derived, tissue-resident $CD68^+$ microglia. At the same time, further major populations presence including $GFAP^+$ astrocytes as well as mature neurons ($NeuN^+$/$Map2^+$) were characterized. One observed feature of the model was the heterogeneity among the generated organoids/batches as well as the development of vacuolar structures in the unguided cerebral organoids. This was expected with the unguided cerebral organoid differentiation protocol first established by Lancaster *et al*. [214]. To reduce the influence of these heterogeneities, cerebral organoids presenting with vacuolar structures were not included in downstream experiments that did not pertain to the choroid plexus. Conversely, organoids generated using the choroid plexus protocol [223], all developed ventricular structures and were as such included in the choroid plexus infection studies. Furthermore, key experiments were performed with two independent organoid batches to reduce batch effects. Besides the observed heterogeneity, cortical layering, as described by Lancaster *et al*. [214, 258], was not as pronounced in the cerebral organoids generated herein. This may be explained with the herein used iPSC line (HMGU-1) as well as the differentiation protocol employed. Different iPSC inherently harbor preferences for certain lineages [259, 260]. This is possibly caused by the finding that although the original somatic cells are re-programmed and thus regain their pluripotency [261], epigenetic re-programming does not occur in all iPSC to the same extent [259, 260]. At the same time, regeneration of the tissue-specific epigenetic landscape is not always regained upon differentiation [262].

Cerebral organoid protocols with more stringent differentiation, as employed for organoids of specific regional identity of the brain, develop more pronounced cortical layering more robustly than unguided protocols [263, 264]. These, however, rely on dual SMAD inhibition to limit the organoids to the neuroectodermal development, therefore, no microglial population (mesoderm-derived) would develop [217]. Alternative protocols to achieve the population of such organoids with microglia would necessitate the ”spiking” of the microglia after initial organoid generation during early maturation by generating a co-culture [265]. The co-cultured microglia would ideally be derived from the same iPSC line as the region-specific brain organoids [265]. This however requires the laborious differentiation either across their meso-

dermal yolk-sac origin [266, 267], which takes more than 40 days [267]. Alternatively, microglia may be differentiated from iPSC across the hematopoietic lineage, whereby hematopoietic progenitor cells are generated and subsequently driven towards microglial phenotype [268]. The differentiation takes approximately 30 to 60 days [268, 269]. One complication of microglia spiking is the adaptation of the culturing media to meet the components suitable for both microglia and cerebral organoid culture [265]. Due to the increasing complexity of such spiked models, in this thesis the unguided differentiation protocol of human cerebral organoids, in which $CD68^+$, $CD11b^+$, IBA-1^+, $CD45^+$, $CX3CR1^+$, $CD14^+$, HLA-DR^+ microglia develop [217], was employed. Notably, organoid-derived microglia are more similar to adult microglia than those generated externally in vitro [217]. Thus, the limitations of the reduced cortical layering were taken into account for the interpretation of results but it was finally decided to employ the unguided protocol in the following studies.

8.1.2 Ebola virus persistence in human cerebral and choroid plexus organoids

Human cerebral organoids were explored as models for EBOV persistence in the CNS. EBOV productively infected human cerebral organoids and established persistent replication for at least 120 days, providing the first in vitro evidence for the phenomenon in 3D cultures. Persistence manifested as ongoing replication including the release of infectious viral particles. This meets the criteria of viral persistence rather than latency [141]. At 120 dpi, the experiment was terminated, although replication had not ceased and cerebral organoids overall did not appear affected by more CPE or necrosis than negative control cerebral organoids. Hence, 120 days is likely not the upper limit of EBOV persistence in this model. In human choroid plexus organoids, EBOV persistence was furthermore confirmed for at least 48 days.

As EBOV successfully established persistence in human cerebral organoids, the same was tested using recombinant orthoebolaviruses EBOV-GFP and RESTV-GFP. Here, it was found that both established persistence as well, indicating that CNS persistence is possibly conserved across orthoebolaviruses, including the seemingly human apathogenic RESTV [7]. However, differences were observed both between the recombinant EBOV-GFP and EBOV as well as between EBOV-GFP and RESTV-GFP. Firstly, while EBOV established a stable, plateaued infection following an initial peak 15 dpi, EBOV-GFP infection in human cerebral organoids initially ceased early before establishing long-term persistence. Since this was only observed in one batch of human cerebral organoids, a technical error or batch effect cannot be excluded. Thus, a repetition of this experiment is needed. Notably, the same was observed for RESTV-GFP. Besides this, at the last time point 68 dpi, some EBOV-GFP- and RESTV-GFP-infected organoids did not release infectious particles above the LOD. While still three out of five cerebral organoids per group were producing infectious particles, this still was strikingly different to 100 % productive infection with wild-type EBOV. EBOV-GFP-infected organoids

furthermore presented with larger CPE 68 dpi than wild-type infected cerebral organoids 120 dpi. Consequently, this leaves the question of whether the overexpression of GFP as an individual viral gene in the context of the recombinant viruses might influence the viability of the cerebral organoids or the fitness of the recombinant viruses during late-stage persistence. Indeed, high expression of GFP can be cytotoxic by activation of apoptosis [270–272]. Thus, it may be concluded that in the context of in vitro studies on viral persistence, recombinant viruses overexpressing potentially cytotoxic reporter genes should be side-by-side compared with their wild-type counterparts to exclude the modification as possible confounders. The increased putative cytotoxicity of EBOV-GFP was also observed in immortalized microglia as described later on.

RESTV-GFP replicated 10 to 100 fold lower than EBOV-GFP throughout the 68 days of human cerebral organoid infection, resulting in overall significantly lower viral particles being released in comparison to EBOV-GFP. As this experiment was only performed with one batch of organoids, these findings must be taken with caution. However, RESTV is considered apathogenic in humans [7] and less pathogenic in a humanized mouse model of filovirus infection [177]. Therefore, the finding that RESTV-GFP seemingly replicates slower in human cerebral organoid models is in line with the current understanding of the differential pathogenicity of the orthoebolaviruses in humans [7]. Taken together, it may be surmised that the establishment of CNS persistence is conserved across orthoebolaviruses and may capture genus-specific differences.

To exclude that the observed finding of EBOV persistence is a general consequence of the cerebral organoid infection model, LASV was used as a control in this study. In contrast to EBOV, infectious LASV particles were only released during early time points of infection in the majority of organoids. Only in the supernatant of one cerebral organoid, the LASV titer was above the LOD past 48 dpi. Importantly, LASV RNA was detected until 120 dpi in the supernatant of all LASV-infected cerebral organoids, this indicates that while infectious particles were not released, viral genome or defective parts thereof had remained within the tissue [273]. Hence, LASV persistence within the CNS tissue cannot be excluded per se, as the virus might still replicate within the tissue without being released [141]. In agreement with this, antigen staining of organoids 120 dpi further revealed expression of LASV NP in the organoids and only appeared located at the surface in the case of the particular organoid that still released low levels of infectious particles. To understand putative LASV CNS persistence in human cerebral organoids, further studies on the viral RNA genome integrity and replicative capacity within the tissue are needed [141]. These however were not in the scope of this study.

8.1.3 Cellular reservoirs of Ebola virus in the CNS

As EBOV was found to persist in the human cerebral organoid model, its cellular targets were observed over time. EBOV NP expression was detected in the neuronal mass as well as in astrocytes particularly at late stages of infection 48 dpi and 120 dpi. Generally, an outside-in infection was uncovered, thus neurons were the most exposed cell types in this model. Coherently, this might have influenced the cells targeted by EBOV. The overall outside-in infection pattern further eludes to the fact that persistence in this model is possibly driven by both the constant reinfection from the media as well as deeper tissue penetration of the infection herds over time. Thus, in this model EBOV seems to continuously spread through the tissue rather than persist in one particular cell, as observed for neurons in persistent Borna disease virus 1 (BoDV-1) infection [274]. Of note, based on the scarce case reports in humans [127, 139], it is unknown whether EBOV persistence in vivo is maintained intracellularly or at the tissue level via constant re-infection. However, the release of infectious virus into the CSF of the patients during recrudescent inflammatory disease [127, 139] suggests that virus may be released from persistently infected tissues at certain times. Whether this is limited to instances of ”re-activation” or was only captured late with the recrudescence of disease, remains to be determined. In future studies, this limitation could be addressed by leveraging the human cerebral organoid model. For instance, by performing live-cell immunofluorescence microscopy of the ongoing, persistent infection using EBOV-GFP. Besides this, constant re-infection from the media could be prevented by neutralizing the virus in the supernatant using antibodies [275]. However, such experiments would drive the establishment of escape variants and should therefore be considered with caution. Alternatively, these might be performed with the human apathogenic RESTV [7], or using novel virus-neutralizing strategies not employed by the human immune response, such as RNases or deoxyribonucleic acid (DNA)-origami shells [275–278].

Zeng *et al*. exclusively pinpointed EBOV CNS replication in persistent EBOV infection in NHP to histiocytic foci (glial nodules) containing $CD68^+$ microglia [189]. Notably, this was only observed in one natural NHP survivor 36 days after EBOV challenge [189]. Nevertheless, $CD68^+$ macrophages are targets in choroid plexus, testicular, and ocular EBOV persistence in NHP as well [183, 189], highlighting their overall importance in EBOV persistence. The accumulation of microglia in glial nodules at the site where EBOV antigen was detected observed by Zeng *et al*. [189], was confirmed in the herein employed human cerebral organoid model at 15 dpi to 48 dpi. However, microglia presence had ceased 120 dpi. Although the reduction of microglia was possibly not caused by the infection with EBOV, as it was also observed in LASV-challenged cerebral organoids (and negative controls), $CD68^+$ microglia-based long-term persistence of EBOV in the cerebral organoid model could not be confirmed.

In further contrast to NHP, astrocytes were found to be long-term targets of human cerebral organoids. Notably, although astrocytes were not particularly infected in NHP, they were close to the infection in the choroid plexus of NHP [183].

Neither Liu *et al*. nor Zeng *et al*. detected EBOV in neurons at persistent stages of infection in retrospective screenings in NHP [183, 189]. In contrast, Schreiber-Stainthorp *et al*. longitudinally assessed the consequences of acute EBOV infection for the brain and identified endothelial cells, microglia, and particularly neurons as targets [186]. This is in contrast to many other reports which exclude acute CNS infection in NHP in general [182–184, 188, 189] as well as the persistent infection of neurons [183, 189]. Nevertheless, neuronal infection was observed in the human cerebral organoid model herein. This raises the question of whether this model, with ongoing but lower-level replication from 22 to 120 dpi, may capture an earlier stage of EBOV CNS persistence than the one observed in NHP [183, 189] or differences between the NHP and human exist. To address the raised species differences between humans and NHP, a side-by-side comparison of human and NHP cerebral organoids would be necessary.

8.1.4 Limitations of human cerebral and choroid plexus organoids: barrier function and adaptive immune compartment in Ebola virus persistence

The lack of tissue vascularization and the distinct route of infection using human cerebral organoids must be mentioned. EBOV easily infects human cerebral organoids when supplied in the medium as done in this study. And, as previously mentioned, continuous re-infection due the the maintenance in the media is likely. This may not be representative for the natural route of EBOV infection or dissemination to the CNS in humans which entails the passage of the BBB.

Considering the sites of EBOV persistence in humans (and NHP) are seemingly those classically considered ”immune privileged” [279], dissemination into a site via the passage of a barrier, such as the BBB and blood-CSF-barrier (choroid plexus), may be relevant to the downstream cells infected. Importantly, it was found that EBOV possibly breaks down and thereby overcomes the BBB during acute disease in NHP [186], which is supported by findings of Liu *et al*. who have found EBOV to infect the endothelium of the choroid plexus, followed by perivascular infection in proximity [183]. In a case of human meningoencephalitis upon EBOV infection, Bosworth *et al*. have evidenced that EBOV possibly penetrated the BBB of the patient 12 dpi during acute disease [139, 169].

In the scope of the thesis, the penetration of the blood-CSF-barrier by EBOV was investigated using human choroid plexus organoids. For reasons of safe handling in the high containment laboratory, it was attempted to sample the CSF-like fluid from the vacuoles [223] using a pipette tip instead of a syringe. Indeed, in some organoids, EBOV titers in the

CSF-like fluid were elevated in comparison to those retrieved from the supernatant from the same organoid, indicative of penetration into this compartment. However, mechanical force was applied to penetrate the tight barrier, leading to its collapse and the ability to sample the fluid. Therefore, it cannot be definitively excluded whether the virus had originated from the partially homogenized tissue of the ventricle-like structure. Moreover, histology to confirm the presence of viral protein expression in the barrier structure could not be subsequently performed. Notwithstanding this, the finding that mechanical force had to be applied to open the vacuoles in the first place, could be indicative of the general integrity of the blood-CSF-barrier in the context of EBOV infection in choroid plexus organoids.

In summary, the consequences of the differential route of passage and downstream dissemination of EBOV in sites of low immunological responsiveness remain to be determined. Therefore, this may be addressed in the choroid plexus or cerebral organoid model in the future.

8.1.5 Neuroinflammation in persistently infected human cerebral organoids

Some of the NHP with persistent EBOV infection of the CNS in the study by Liu *et al*. showed signs of meningoencephalitis, ventriculitis, choroiditis, and vasculitis after initial convalescence [183], which is overall similar to the recrudescent inflammatory disease that has been observed in human EBOV persistence [139]. Meningoencephalitis signs were furthermore observed in multiple other NHP studies [182, 184, 188]. In this study, in the supernatant of persistently infected cerebral organoids, proinflammatory mediators such as IL-6, IL-18, sTREM-1, CCL-2, and CX3CL1 slightly accumulated towards late timepoints. In contrast, CCL-2 and IL-18 were increased early upon LASV infection, but not with EBOV at 6 dpi. Although uninfected organoids also increased the release of proinflammatory mediators, these findings cautiously indicate differential neuroinflammatory profiles during different viral infections in the cerebral organoid model. Moreover, antiinflammatory mediators such as BDNF were increased in LASV-infected organoids after cessation of viral particle release, while in EBOV-infected organoids bNGF was increased compared to LASV infection.

In humans, the neuroinflammatory signature of human CNS persistence has not been explored. However, in one persistently infected survivor with EBOV in the CNS [139], the acute blood transcriptome up until 12 days after the initial presentation has been reported [169]. Notably, this survivor had recrudescent inflammatory disease (meningoencephalitis) nine months after initial convalescence [139, 169]. Overall, several T cell recruiting, and chemotactic transcripts were elevated, namely CXCL2, CXCL9, CXCL12, and CXCL11 [169]. Meanwhile, CTLA4, which has been reported in the dysfunctional T cell response in fatal EVD [118], and CCL-2 were further elevated [169].

Besides this, no information on possible (neuro-)inflammatory signatures in cases of human

CNS persistence of EBOV is available. However, the immune signature of acute EVD has been reported. In fatal or severe cases of EVD, higher levels of proinflammatory cytokines such as TNF-α and IL-8 as well as chemokines macrophage inflammatory protein (MIP)-1α, MIP-1β, CCL-2, CX3CL1, and M-CSF compared to survivors and moderate cases have been uncovered [109, 110, 280]. Moreover, antiinflammatory IL-10 and IL-1RA were elevated, possibly due to ongoing compensatory mechanisms [109]. Potentially compensatory release of antiinflammatory marker bNGF was also observed in the human cerebral model during persistent EBOV replication. Notably, in those individuals with EBOV persistence and subsequent recrudescence in the CNS, biomarkers of disease were indicative of a severe disease [139, 169]. In conclusion, in the supernatant of EBOV-infected human cerebral organoids, several pro-inflammatory markers (IL-6, CX3CL1, CCL-2) accumulated. These have been associated with fatal EVD and severity [280].

8.2 Studies on Ebola virus persistence on the cellular level

8.2.1 Ebola virus infection in microglia

When infecting human cerebral organoids with EBOV, CD68$^+$ microglia migrated towards the sites of infection. To evidence the susceptibility of human microglia to EBOV infection and investigate their role in EBOV persistence, various 2D cell culture models were explored. Initially, a primary cell culture model for human microglia was anticipated. To that end, MDMi were used.

To generate MDMi, a protocol published by Ryan *et al*. was employed, in which human monocytes are differentiated by supplying IL-34, GM-CSF, M-CSF, and bNGF [226]. Microglia of monocytic origin are often considered more similar to a subset re-populating the CNS upon damage [226]. The application of IL-34, which is mainly produced by neurons in the CNS, has been shown to drive the development of microglia in mice [281]. Therefore, differentiation protocols supplying IL-34 have been used to skew the MDMi towards a phenotype more similar to resident microglia [226, 282, 283]. These MDMi present with a ramified phenotype, whereby a small soma and radial ramifications can be observed [283]. Coherently, the MDMi phenotype using IL-34 has been described as CD11b$^+$, CD45^{int}, Iba-1$^+$, CX3CR1$^+$, transmembrane protein 119 (TMEM119)$^+$, transcription factor PU.1 (PU.1)$^+$, and purinergic receptor P2Y, G-protein coupled 12 (P2RY12)$^+$ [281, 282].

As previously published [226, 283], MDMi generated in this study displayed the typical ramified phenotype of resident microglia and expressed relevant surface markers including CD11b, CD45, CD14, and CX3CR1. In MDMi, EBOV replicated and established a plateaued infection of 12 days, evidencing the capacity of EBOV to infect human microglia. It must be noted that in this experiment, a high MOI=10 was used. In primary moDC and bone

marrow-derived DC, others have used an MOI=1 or MOI=3 to achieve infection with EBOV [116, 174, 255]. Although the MOI used in this study was higher, the strong replication in the MRA provides sufficient evidence to confirm the productive EBOV infection in MDMi.

A limitation for subsequent persistence studies was the finding that MDMi culture generally did not remain viable for more than two weeks. Hence, this primary microglia model was not suitable for longer infection periods as necessary for persistence studies. As a consequence, subsequent studies were mostly performed in immortalized human microglia and corresponding other cell types.

Previously, Wool-Lewis *et al*. have shown that pseudotyped Murine Leukemia virus (MLV) expressing EBOV GP replicates in the immortalized U81 microglia line [284]. This was confirmed in this study, where immortalized microglia were found to be susceptible to authentic EBOV infection.

Furthermore, upon infection of immortalized human microglia with EBOV-GFP, it was uncovered that these increase the surface expression of CX3CR1. As this increase was also observed within the uninfected cells of the EBOV-stimulated sample, it is possibly not driven directly by virus infection. Nevertheless, it was a distinct feature compared to the negative control. Furthermore, this increase in CX3CR1 was not observed in RESTV-GFP infected immortalized human microglia either, although this could also be attributable to the generally lower infection rate of RESTV-GFP at the measured time points. Importantly, immortalized human microglia infected with MOI=0.0025 EBOV-GFP were not persistently infected, as all cells were dead 9 dpi. As this was not observed with EBOV wild-type infection at the same MOI, this was attributed to the previously hypothesized cytotoxicity of GFP upon overexpression in vitro [270]. As a consequence, recombinant viruses were not used in long-term infection studies.

The phenotype of MDMi infection with EBOV-GFP was further explored using the same flow cytometry panel. Although MDMi were not positive for EBOV-GFP 6 dpi (MOI=1), a small CX3CR1^{++} population was also observed, confirming the finding of the immortalized cell line. A higher MOI or later timepoint is advisable to capture the effects of the infection of particular cells.

The increase of CX3CR1 on the surface of microglia, as measured via flow cytometry, was further observed using immunofluorescence microscopy in immortalized human microglia and wild-type EBOV infection. Thus, artefacts driven by the recombinant expression of GFP can be excluded. In addition, it must be noted that while CX3CR1 expression in immortalized human microglia was generally hard to capture using immunofluorescence microscopy, upon infection, the marker was increasingly present on the surface of the microglia. In fact, the CX3CR1 signal appeared enriched in the microglial ramifications in which EBOV NP was furthermore detected. Besides this, neither CX3CR1 nor its ligand CX3CL1 (fractalkine) were

among the top regulated genes identified using RNA sequencing, indicating that the perceived increase in CX3CR1 surface presence is not mediated on the level of gene expression. Further mechanistic implications of the increase in surface CX3CR1 as well as the presence of the marker and EBOV NP in the microglial dendrites will be addressed in subsection 8.3.3.

8.2.2 Ebola virus infection in astrocytes and neuroblastoma cells

In this study, it was broadly established that EBOV not only infects immortalized human microglia but also astrocytes, as well as undifferentiated neuroblastoma cells (SH-SY5Y). In addition, productive infection of all three cell types was further achieved using LASV, EBOV-GFP as well as RESTV-GFP.

In the human cerebral organoid model, astrocytes were infected with EBOV at later stages of infection upon exposure to EBOV in deeper layers. Thus, infection of immortalized astrocytes is in line with the findings of this model. Besides this, astrocytes were the only cell line tested that were not productively infected with EBOV at the lowest tested MOI=0.001, which suggests they may be less susceptible to infection than microglia, VeroE6 cells or Huh7 cells. Notably, as for the early developmental astrocytes that develop in the human cerebral organoid model, the herein-used astrocyte cell line was generated from fetal astrocytes. Hence, primary astrocytes from an adult, human donor would further add value to the findings herein. Astrocyte infection with EBOV has not been previously reported in the literature. Merely, in an organ-on-chip model of the blood-retina-barrier, retinal astrocytes were included and inoculated with EBOV-virus-like particle (VLP) [285]. However, the authors did not elaborate further on astrocyte infection [285].

The productive infection of the neuroblastoma cell line is in line with the observation that in the human cerebral organoid model, the neuronal mass was infected throughout the experiment. However, Zapatero-Belinchón *et al*. have published that the same cell line, SH-SY5Y, is resistant to EBOV (Mayinga) infection [286]. In the study presented herein, SH-SY5Y cells were infected with EBOV (Mayinga) at MOI=0.1 or EBOV-GFP/RESTV-GFP at MOI=1 for 1 h with subsequent growth of 5 days. Here, the lowest increase between the day 0 and day 5 sample was observed upon RESTV-GFP infection, although titers still increased by 3Log_{10}, evidencing productive infection of the orthoebolaviruses in the neuroblastoma cells. Zaptero-Belinchón *et al*. initially found SH-SY5Y cells resistant to EBOV in a replicon assay system, with equally low activity as observed in the T cell line Jurkat [286]. T cells are known to not be productively infected by EBOV and to undergo apoptosis upon infection [60, 61, 284]. The authors further infected the neuroblastoma cell line with authentic EBOV (Mayinga) MOI=0.1 for 1 h and 72 h viral growth [286]. After three days, EBOV protein expression was not detected in SH-SY5Y via immunofluorescence microscopy or western blot in authentic EBOV infection, although no titrations were performed [286]. The

authors attributed the resistance of these neuroblastoma cells to the inability of GP-mediated entry, as evidenced by multiple entry assays using diverse filoviral recombinant Vesicular Stomatitis virus expressing EBOV GP (VSV-G) pseudoviruses. Notably, SH-SY5Y cells express functional NPC1, CatB, and CatL [286], which are the limiting factors of the filovirus tropism [53, 56–59]. Overexpression of EBOV attachment factors rescued the entry of VSV-G into neuroblastoma cells [286]. Based on this, it may be speculated that differences observed among the results by Zaptero-Belinchón *et al*. and the findings of this study might have been caused by differential expression of EBOV attachment factors.

Besides these contradictory findings, SH-SY5Y neuroblastoma cells represent non-polarized neuroblastoma cells, which may be differentiated to a more mature neuron-like phenotype using retinoic acid [287]. Mature SH-SY5Y cells form neurite processes, synapses, and express mature neuronal markers including MAP2 and NeuN [287]. Hence, in future studies, a previous maturation step, and its influence on the susceptibility to EBOV infection, may be considered to elucidate the neuronal infection capacity of orthoebolaviruses further.

8.2.3 Persistent replication of Ebola virus in microglia and astrocytes

2D cell culture models of persistent infection were anticipated and subsequently further investigated for host mechanisms important for the establishment or maintenance of EBOV persistence. As the studies in the SH-SY5Y cell line led to contradictory results, further studies on EBOV persistence via long-term replication kinetics in 2D were limited to immortalized human microglia and astrocytes. To ensure virus-specific effects were uncovered, LASV was used as a control.

EBOV persistently replicated in human immortalized microglia and astrocytes for 25 days without necessitating passage of the cells. During this time, the CPE observed in microglia and astrocytes upon EBOV infection was similar to the negative control but was strikingly reduced compared to LASV infection. Nevertheless, reduced confluency and cellular rounding were observed. Meanwhile, LASV did not establish persistence in microglia, possibly due to the destruction of the monolayer. Moreover, astrocytes infected with LASV, as well as Huh7 cells, amplified the virus in a wave-like pattern with viral titers at the LOD at local minima. The implications of this replication pattern will be addressed in subsection 8.4.1.

Unlike LASV, EBOV established persistence in all cell lines and at all tested MOI (0.1, 0.01, and 0.001) if a productive infection was initially achieved. Here, astrocytes seemed less susceptible, based on the finding that the lowest MOI did not result in productive infection. Nevertheless, long-term replication was achieved at MOI=0.1 and 0.01. Moreover, a minor wave-like pattern of EBOV replication was uncovered in microglia infected with the highest of the three MOI=0.1. This was however not comparable to the temporary clearance observed in LASV-infected astrocytes and Huh7 cells. Besides, persistent EBOV replication was further

established in VeroE6 cells and Huh7 cells at the same MOI, whereby no excessive CPE (i.e. loss of the monolayer) was observed 25 dpi, either. Notably, in these classical target cells, minor CPE in the sense of cellular rounding and clumping was observed. This was however also true for microglia and astrocytes. To confirm the persistence of EBOV infection further, in all cell lines, EBOV GP and NP expression was investigated via immunofluorescence microscopy 25 dpi. Indeed, the antigens remained expressed in all immortalized cells, although the infection rate varied and appeared particularly low in VeroE6 cells. This was however not quantified.

Besides this, an alternative protocol for the generation of EBOV persistence in microglia via passaging was employed. This was based on an early publication by Calain *et al*., who had passaged EBOV at MOI=1 in VeroE6 cells and thereby achieved viral persistence in the sense that they maintained the culture for 10 passages [190] (subsection 8.4.1). In this study, the microglia culture however established strong CPE after three passages, including cellular rounding, clumping, as well as death. To adapt to protocols by Calain *et al*., a higher MOI (MOI=10, MOI=1), than previously (0.1, 0.01, 0.001) was employed, thus the elevated CPE observed in microglia upon passage in comparison to cells not passaged but long-term infected with EBOV could be caused by this. However, CPE only occurred upon the third passage. Thus, it is more likely that the passaging process using Trypsin-EDTA was possibly too harsh to the culture upon infection. To achieve persistence despite this limitation, naïve microglia were supplied during each passaging from passage three to passage nine onwards. This way, the culture was kept viable and infectious viral particles were released until the by Calain *et al*. defined time point of persistence (passage 10) [190]. Notably, the phenomenon of EBOV persistence upon passaging is maintained on a tissue level and likely not intracellularly, particularly when novel target cells are supplied and infection through the supernatant is not excluded [190]. In addition to this, Calain *et al*. attributed the establishment of tissue-culture level persistence in part to the high MOI (MOI=1) employed in their study [190]. The authors reason this with the presence of DVG, which will be discussed in subsection 8.4.1. However, in this study, EBOV infection with both MOI=1 and MOI=10 manifested similarly regarding the achieved persistence as well as observed CPE, thus viral load-dependency is unclear. This is in line with previous experiments herein where EBOV persistence also established viral load-independently in unpassaged microglia and astrocytes.

In other studies, human cells isolated from sites of low immunological responsiveness or immortalized cell lines thereof, such as fibroblast-like synoviocytes, retinal pigment cells, Leydig and Sertoli cells (testicle), have been studied in their capacity to differentially respond to EBOV infection or potentially establish a persistent infection [179, 195, 288]. To that end, Cooper *et al*. determined that EBOV-infected fibroblast-like synoviocytes do not develop a CPE in vitro [179], although no long-term infection was queried by the authors. Nevertheless,

lack of CPE might cautiously indicate that EBOV could be able to inherently establish a persistent infection in these cells. At the same time, Smith *et al*. found human retinal pigment cells to be susceptible to EBOV infection [288]. The authors did not assay long-term replication. Meanwhile, Webb *et al*. infected human immortalized cells derived from the testicle, namely Sertoli and Leydig cells, with EBOV-GFP (Makona) MOI=0.1 [195]. In this case, a productive infection of 28 days was achieved in Sertoli cells, whereby (uninfected) Leydig cells could not be cultured beyond 14 days [195]. The length of EBOV replication in Sertoli cells by Webb *et al*. is similar to the one observed in microglia and astrocytes in this study. Notably, the authors found replication in Sertoli cells to be slower than the one observed in Leydig cells, which infection-independently lost viability at 14 dpi [195]. Notably, the authors did not infect with wild-type EBOV, hence, the effect of the GFP expression cannot be addressed.

Besides these findings in human cell lines originating from low immunological responsiveness niches, EBOV also establishes persistent infections in (primary) bat cell lines [9, 289–291]. As the EBOV suspected reservoir hosts, bats have been shown to tolerate the infection with EBOV, and the virus replicates without causing disease in vivo [9]. The exact mechanism for such low pathogenesis and lack of CPE in vitro is widely unknown [9, 292, 293]. However, in bat cells, a tightly orchestrated type I and III interferon response are mounted, and seroconversion as well as a T cell response can be observed in vivo [9, 292, 293].

8.3 Molecular mechanisms of Ebola virus CNS persistence

8.3.1 The role of the antiviral response in Ebola virus persistence

To investigate potential alterations in the antiviral response upon EBOV persistence, RNA sequencing was performed on microglia and astrocytes after various lengths of infection with EBOV. Here, in comparison to the respective negative control, no CPE was observed at the time of harvest.

Notably, no pronounced differential gene expression was retrieved for astrocytes and microglia infected with EBOV at 3 dpi or 6 dpi with MOI=0.0025. This is likely based on the finding that as per flow cytometry, many cells were possibly not infected at the time of harvest. Given the suspected slightly decreased susceptibility of astrocytes, the infection rate was possibly even lower. Thus, bulk RNA sequencing, which averages the gene expression across a sample, could not retrieve conclusive information on dysregulated genes within EBOV-infected cells at early time points. Indeed, these early infection samples clustered with the negative controls in the PCA. In the future, a higher MOI may be needed to capture earlier time points of infection. Irrespectively, differentially expressed genes were uncovered 12 dpi, which is representative of the peak viral titer in microglia and astrocytes, as well as

20 dpi corresponding to persistence in 2D cultures. Furthermore, differential gene expression was measured in microglia infected with EBOV for 10+3 passages which is equal to 91 days of infection.

Above all, the RNA sequencing performed herein revealed that EBOV-infected microglia mount a strong antiviral response throughout the queried time frames as well as upon passaging with EBOV. This is unsurprising, given microglia are the innate immune cell population in the CNS [294]. Antiviral genes that were strongly upregulated included OAS1, OAS2, MX2, XAF1, OASL, IFNB1, IFI44L, IFIT1, IFIT3, IFI44, IFIH (MDA-5), IFIT2, RSAD2 (Viperin), ISG15, OASS2, IFI6, MX1, SAMD9L, SAMHD1, TRIM22, TRIM5, DHx58, BST2 (Tetherin), RIGI, or TLR-3. Amongst these, PRR TLR-3, IFI-H (MDA-5), RIGI, and DHx58 are involved in the sensing of viral RNA within a host cell and are known to be targets of EBOV VP35 antagonism during acute infection [99, 101, 104, 105, 295]. Meanwhile, many other upregulated genes in microglia are ISG that are increased upon the sensing of viral RNA within a cell. In the case of a survivor with CNS persistence, the transcripts of antiviral genes were measured in the blood during the acute phase [139, 169]. Here, OAS2, IFIT1, STAT1, IFITM3, IFI6, IFI16, IFI44L, RSAD2, IFITM, MX1, and MX2 were elevated [169]. In general, the appearance of these ISG observed during the acute phase that led to later persistence are similar to the ones detected in the microglia upon EBOV infection. All of these markers decline later on in the same patient [139, 169].

Notably, the in microglia upregulated antiviral TRIM-5, to which TRIM-22 is closely related [296, 297], has been found to cause susceptibility to EBOV infection in collaborative cross mice [298]. Moreover, ISG15 is known to block EBOV VP40-mediated budding [299]. However, from 12 dpi onwards, particularly USP18, which is a negative regulator of type I interferon signaling but also disables ISG15 function [300], was elevated. Importantly, USP18 is also upregulated in Leydig and retinal pigment cells upon EBOV infection [195, 288]. Whether this may be a specific mechanism in certain cell types or ubiquitous in EBOV infection is unknown. Tetherin (BST-2), a major antagonist of EBOV particle release [89, 90, 96, 301, 302], was furthermore highly upregulated in microglia. In Leydig cells infected with EBOV, antivral OASL2, OAS1A, IFIH1 (MDA-5), DDx60, Dhx58, OASL1, ISG15, RIGI, STAT1, IRF7, and IFIT3 are also upregulated 14 dpi [195]. Meanwhile, persistently infected Sertoli cells upregulate XAF1, IRF7, BST2, OAS2, OAS1, OASL, IFIT3, RSAD2, and MX1, thereby also exhibiting a strong antiviral response 28 dpi [195], as observed for persistently infected human microglia herein.

Besides this, in microglia, IRF-3 was expressed at baseline, whereby IRF-7 was significantly upregulated 12 dpi. Whether the phosphorylation status of IRF-3, and thus its activity, changed upon infection cannot be captured using RNA sequencing. Besides this, the expression of IRF-7 had ceased below the threshold of $\geq$5 counts per million reads 20 dpi and upon passage

of EBOV in microglia. IRF-7 was generally not expressed in astrocytes. The translocation of transcription factors IRF-3 and IRF-7 to the nucleus, which regulates the production of type I interferons, is robustly antagonized by VP35 in EBOV infection [99, 101, 105, 295]. It may therefore be hypothesized that the lack of IRF-7 expression in astrocytes is favorable to the infection with EBOV. Furthermore, the peak of IRF-7 during the peak of EBOV replication in microglia and its decrease 20 dpi might hint towards an EBOV antagonism of the antiviral response in microglia. Importantly, other viruses in the *Mononegavirales* order that can establish persistence in vitro, such as Sendai virus (SeV) and Measles virus (MeV) target processes within the intracellular antiviral response to maintain or establish persistence. Here, the ablation of IRF-3 by SeV prevents apoptosis and is a necessary step for the establishment of persistence [303].

The cytokine response in EBOV-infected microglia comprised IL11, IL1B, IL15, IL31, IL12A, and IL1A, whereby IL32 was particularly elevated upon passaging. Thus, the response of microglia to EBOV infection overall appears proinflammatory. However, it must be noted that at later time points, GO-Term enrichment further revealed regulatory, proliferative, and morphogenic activity in the microglia. Indeed, tumor growth factor (TGF)-β1 (TGFB1) expression was increased 20 dpi, while TGF-β2 (TGFB2) was increased upon passaging of EBOV in microglia. Notably, during the acute infection of retinal pigment cells by Smith *et al.*, programmed cell death ligand-1 (PD-L1) and programmed cell death ligand-1 (PD-L2) were upregulated, although classical immunomodulatory markers such as TGF-β, interleukin 10 (IL-10), and Fas ligand (FasL) remained at baseline levels [288].

In opposition to the findings in microglia, it was overall apparent that astrocytes did not mount a strong antiviral response upon early and late EBOV infection. While the major antiviral genes were not increasingly expressed, XAF1, RSAD2, and DHx58 were elevated 20 dpi but not 12 dpi. Notably, IFI44L was strongly suppressed in astrocytes 20 dpi. This overall signifies a low responsiveness to both early and late EBOV infection in astrocytes. Only 20 dpi, the upregulation of some proinflammatory cytokines like IL1B, IL1A, IL6, IL-18, IL-33 occured. Notably, in microglia, IL-18 and IL-33 were particularly suppressed 20 dpi. Lastly, upon LASV persistence in astrocytes for 20 days, no substantial changes in the transcriptome were observed, while microglia that had cleared the infection had returned to their baseline transcriptome. Besides this, the quality of the microglia culture, after ceased viral particle release, was comparable to the negative control as observed via light microscopy. Minor CPE (cell rounding) but no loss of monolayer was observed in the astrocytes. This was not captured in the transcriptome analysis.

In conclusion, the antiviral response in microglia and astrocytes upon peak and long-term EBOV infection differed drastically. Microglia strongly responded with an antiviral response and proinflammatory profile, which at later time points included some traces of regulation. In

contrast, astrocytes remained in a regulatory state, barely upregulating antiviral factors and proinflammatory cytokines. In both cell types, EBOV established persistence. With such an opposed antiviral response that does not translate to a distinct replication profile, it cannot be concluded which state is more favorable to the establishment of persistence. Moreover, it may even be speculated that the establishment of the persistence cannot be prevented by the host antiviral response. At the same time, the traces of more regulatory and regenerative activity in microglia at late stages of EBOV infection might cautiously elude to the notion that this might be favorable to the maintenance of the microglia culture and thus possibly EBOV persistence. Targeted studies are needed on the key factors presented herein to understand this process further.

8.3.2 Ebola virus gene expression in persistence

Limitation of gene expression is a mechanism by which viruses modulate the presence of viral proteins and thus recognition by the host cell during persistence [141]. Upon acute infection, EBOV specifically enables gene expression via the suppression of the host restriction factor PKR through VP35 [76, 102, 107]. Coherently, viral gene expression was also studied.

Here, via immunofluorescence microscopy, it was found that in microglia, astrocytes, Huh7 cells, and VeroE6 cells 25 dpi with EBOV, GP and NP remain expressed. Furthermore, EBOV gene expression patterns in microglia but not astrocytes overall decreased, measured by EBOV mRNA per genome present over time. Meanwhile, in astrocytes, a decrease in viral mRNA was only observed with the L polymerase gene, whereas all other viral genes remained more constant in their expression. Passaging of microglia led to a comparably high mRNA expression, as seen in astrocytes. The reduction observed in microglia without passaging might be explained by the fact that upon infection with EBOV, translation and gene expression pathways were robustly downregulated. However, this was also true upon passaging of microglia.

Except for the uncovered irregularity with EBOV L in astrocytes, the gene expression analysis further revealed that all EBOV genes remained expressed linearly across the filoviral genome [13, 257]. Conclusively, no traces regarding altered gene expression programs in the context of EBOV persistence in microglia or astrocytes were uncovered by the methodology employed herein.

8.3.3 Altered infection dynamics during persistence: from entry to exit

The expression of the cholesterol transporter NPC1 is tropism-restricting and, together with the expression of CatB and CatL, rate-limiting in EBOV infection [53, 56, 57, 304]. Coherently, in primary bat cells, persistence of EBOV has been associated with a low expression of NPC1

[290]. It may therefore be hypothesized that this limits the rate of EBOV infection upon persistence.

Importantly, NPC1 but also CatB (CTSB) and CatL (CTSL) were expressed in microglia and astrocytes at baseline as well as upon infection with EBOV. Strikingly, an elevation of NPC1 was observed in microglia 20 dpi and upon passage with EBOV as well as 20 dpi in astrocytes. Moreover, CatL expression was additionally increased in astrocytes 20 dpi. While this confirms the general permissiveness of the cell lines to EBOV infection, it stands in contrast to decreased NPC1 expression in persistently infected bat cells [290]. Indeed, due to the rate-limiting nature of their expression [53, 56, 57, 304], it might be speculated that the uptake of EBOV is increased during the late stages of EBOV infection in microglia and astrocytes.

In MeV infection, Doi *et al*. further found the switch from lytic to persistent infection to be self-regulated via the ectopic accumulation of the MeV nucleoprotein [305]. This way, MeV replication is suppressed [305], a known strategy in viral persistence [141]. In the context of this study, it may be speculated that observations made via immunofluorescence microscopy using the EBOV$_{n120}$ variants showed signs of ectopic EBOV NP accumulation. However, this was not quantified and requires more detailed attention which was out of the scope of the thesis. Here, in particular, the integrity of the EBOV IBs which serve as viral factories during replication [73–77], may be explored in the context of persistence.

Besides this, there are multiple switches within the EBOV lifecycle which may be exploited in the context of persistence. On the one hand, the phosphorylation status of VP30 determines whether the viral genome is transcribed or replicated [63–66]. On the other hand, VP24 has been suggested to inhibit EBOV transcription and replication, which ultimately allows for the switch towards viral packaging [306]. Whether these play a role in the persistence observed at hand, warrants further attention. Notably, in astrocytes, the L gene was decreasingly expressed, which may be indicative of regulation of either viral transcription or replication since this viral gene encodes the RdRp [101]. At the same time, VP24 contributes to the viral matrix, virion assembly, and suppression of the antiviral response [101, 106, 306], showed a minor trend towards decreased expression in astrocytes 20 dpi as well.

Upon assembly, EBOV buds from the host membrane and is released in novel infectious particles. This makes the virions vulnerable to detection as well as neutralization by the host immune response [89, 301, 302]. Moreover, it has been shown that the ISG Tetherin (BST2) traps egressing EBOV particles to the host membrane, preventing their release [89, 90, 96, 301, 302]. Importantly, in the context of this study, Tetherin was highly upregulated in microglia upon EBOV infection but not in astrocytes. In the studies of Webb *et al*., Tetherin was furthermore only increased in persistently infected Sertoli cells [195]. The Tetherin-mediated mechanism of EBOV trapping is counteracted by GP via direct interference [90].

Thus, an increase in Tetherin expression could interfere with particle release.

In other viruses that switch from a lytic to persistent infection, such as MeV, persistence is intracellularly maintained via cell-to-cell or trans-synaptical spread [307–309]. This way, years-long CNS persistence of MeV is achieved, while the CNS immune response and clearance is successfully evaded [307, 308]. Recent findings of Djurkovic *et al*. as well as Santos *et al*. to that end confirm that EBOV spreads cell-cell both via long-range intercellular connections termed TNT as well as via a GP-TIM-1-mediated fusion [91, 94]. Furthermore, syncytia formation has been reported [92, 95]. Not only does this way of spread overcome the Tetherin-mediated antagonism of orthoebolaviral budding [94], it further might hide the virus from the host immune response [91] and overcome boundaries of the EBOV tropism, such as the expression of NPC1 or attachment factors [94]. Importantly, cell-to-cell spread has been observed in this study, whereby in microglia EBOV NP and GP were both located to long-range connectors (EBOV, EBOV beta, EBOV gamma, EBOV lambda), both with EBOV and naturally occurring EBOV$_{n120}$ variants. Notably, the connectors in which EBOV has been observed are made up of actin, as observed by Djurkovic *et al*. [94]. Cell-cell spread within large astrocyte bundles was furthermore observed with naturally occurring EBOV$_{n120}$ variants (EBOV gamma, EBOV delta, EBOV lambda).

Notably, the CX3CR1-CX3CL1 axis in the CNS mediates the cross-talk between microglia and neurons by chemotaxis via soluble CX3CL1 as well as direct binding to membrane-bound CX3CL1 [45, 310]. This way, the CX3CR1-CX3CL1 interaction is involved in diverse neuroinflammatory diseases and neurotropic infections (rev. in [275, 311]). As revealed by this study, in microglial connectors and ramifications, upon EBOV infection, CX3CR1 was enriched. Importantly, in Japanese Encephalitis virus (JEV) infections in vitro, cell-cell-spread is dependent on the CX3CR1-CX3CL1-axis [275, 312]. The authors demonstrated that the neurotropic virus spreads cell-to-cell between JEV-harboring monocyte-derived microglia and baby hamster kidney cells [275]. Here, JEV infection of microglia causes a transient increase in CX3CR1 surface expression which is downstream exploited for the cell-to-cell transfer of infectious JEV (+)-sense RNA genome to susceptible cells [275, 312]. Upon CX3CR1 inhibitor treatment, long-range cell-cell connections and cell fusions were reportedly substantially decreased [275].

Based on the observed surface upregulation of CX3CR1, it was initially hypothesized that this could affect EBOV infection or persistence. In an initial experiment, it was therefore tested whether the application of an allosteric CX3CR1 inhibitor (AZD8797, 1 µM) would influence EBOV replication in microglia. However, no differences in replication or the establishment of persistence were observed in 2D. This is in line with the later hypothesized cell-cell implications of CX3CR1 [275]. Besides this, the applied inhibitor concentration was also lower than in the works by Lannes *et al*. (10 µM) [275] and no positive control for the functionality of the

inhibitor like the comparison to JEV was performed. However, a previous screening of the inhibitor had revealed cytotoxicity (cellular rounding) in the immortalized microglia at the highest concentration but not in the mock control.

As no effects were seen in 2D, the inhibition was carried out in 3D, as it was hypothesized that the 3D environment would favor cell-cell infection. Strikingly, in choroid plexus organoids, a slight reduction of EBOV replication was observed upon the application of the CX3CR1 inhibitor. This was not statistically significant and must therefore be taken with caution. However, this also invites the speculation that the inhibition of CX3CR1 might influence the tissue spread of EBOV in a human choroid plexus model. To address this hypothesis in the future, studies that prohibit infection via the media in microglia and organoids are necessary. To that end, one could observe the plaque size in EBOV-infected microglia cultured in overlay media where no viral spread through the media occurs. Alternatively, the use of neutralizing antibodies or RNase treatment of the supernatant [275] could be explored. Importantly, as previously discussed, in the context of EBOV infections, strategies that do not exhibit an evasion pressure on the virus are favorable.

8.4 Naturally occurring Ebola virus variants in CNS persistence

8.4.1 Defective viral genomes and defective interfering particles in Ebola virus persistence

Calain *et al*. have demonstrated that EBOV DVG are formed if the virus is passaged in infected cells [190]. Indeed, the authors have evidenced that this way, persistence may be established, as the overall presence of DVG coincided with the viability of the long-term culture [190]. This was possibly achieved by preferential replication of defective genomes over viable RNA [190, 194]. Moreover, Johnson *et al*. have uncovered the formation of EBOV DVG in acute infection in NHP [192], while in cases of EBOV persistence in humans, short deletions and the presence of minor DVG populations were furthermore suggested [162, 169].

Based on this, in this study it was anticipated to reproduce the findings of Calain *et al*. in microglia cells, to determine whether the formation of DVG upon EBOV passaging occurs and coincides with viral persistence. Indeed, it was shown that microglia passaged with EBOV become persistently infected with the virus. Moreover, the presence of DVG species diversity within the cell and supernatant was observed. Notably, no increase in diversity was observed throughout the passaging. Meanwhile, DVG-species diversity in the supernatant of human cerebral organoids had increased over time in persistent EBOV or EBOV-GFP infection. Although the absolute quantity of the DVG was not assessed, this might cautiously hint at a putative role of the DVG in EBOV CNS persistence, confirming findings by Calain *et al*..

Importantly, in the case of LASV infection, the lack of infectious viral particle release in contrast to the sustained presence of viral RNA in the cerebral organoid supernatant was also apparent. This might indicate that LASV also forms DVG which are released from cerebral organoids. Notably, a striking wave-like replication pattern was observed in Huh7 cells and astrocytes upon long-term infection with LASV as well as slightly in microglia upon EBOV infection. Such waves, in other viruses, are indicative of alternating accumulation of DVG and functional viral RNA [193, 313]. Indeed, accumulation of DVG reduces viral replication, whereby the tissue culture recovers. In return, this further allows for the re-infection and replication of viable progeny, whereby viral replication increases again and causes novel CPE [190, 193, 194, 313]. Notably, DVG and DIP have been implicated in the context of persistent infection of LASV-reassortant vaccine candidates [314, 315]. Moreover, passaging of LASV in VeroE6 cells leads to the establishment of viral persistence, driven by the accumulation of DVG and reduction of infectious viral particle release [273]. In this context, future studies on a differential mechanism of LASV persistence in the human cerebral organoid model would be of interest.

8.4.2 Low-level viral replication and evolutionary dynamics in Ebola virus persistence

In the scope of this study, the EBOV replication during its persistence in diverse cell culture models was studied. It is widely accepted that high-level viral replication leads to cell lysis or detection by the immune system [316]. To persist, viruses might reduce their replication or utilize less efficient replication programs, thereby evading antiviral activity and cellular responses [169]. In line with this, low-level viral replication is used by the paramyxovirus parainfluenza virus type 5 as a mode of persistence [316].

In the human cerebral organoid and choroid plexus model, the release of infectious EBOV particles over time was maintained but had decreased after an initial peak to approximately 10^3-10^4 FFU/ml. Peak levels were 10^5-10^6 FFU/ml. In coherence with this, the level of EBOV release in passaged microglia at P10+3 was lower than at its maximum peak. 25 dpi in unpassaged cells, titers were however still relatively high, although minor waves with lower replication were also observed. Importantly, detection of the EBOV genome in microglia and astrocytes over time revealed a peak in genomic maps 6 dpi and subsequent reduction towards 20 dpi, as well as upon passaging in microglia. All of this overall supports the hypothesis that EBOV replicates during its persistence in CNS tissue. Moreover, this replication might be slightly reduced in comparison to the initial acute phase.

High viral replication further leads to the accumulation of mutations. EBOV approximately mutates with a modeled rate of 0.96x10^{-3} to 1.42x10^{-3} substitutions per site per year [162, 169], resulting in roughly 16 to 25 nucleotide changes across the genome per year. Meanwhile, in atypical transmission chains during EVD outbreaks EBOV replicate is seemingly

at a reduced level, generating 3.7 to 6-fold fewer mutations than the modeled rate [28, 29, 31, 33, 140]. Importantly, in the case of an EVD patient with meningoencephalitis [139], Bosworth *et al*. cautiously suggest that low-level replication might be a mechanism of EBOV persistence in this particular case [169]. This is in line with the results in the human cerebral organoid.

In this study, sequencing of EBOV after passaging in microglia revealed a multitude of SNP, which maintained their dominance throughout the passages or independently arose in different cultures. Meanwhile, Calain *et al*. did not reveal any adaptive mutations of EBOV upon passaging in VeroE6 cells [190]. It must however be noted that sequencing technology has since improved. Strikingly, upon passaging in microglia, only in VP35 and VP40 no dominant SNP occurred or accumulated. Thus, it can be surmised that the VP35 interferon antagonism remains intact and budding is likely not impaired [78, 85–88, 101]. Besides this, one SNP (S587A) accumulated in EBOV NP from passage 2 onwards and remained dominant until passage 10. This is located in the central domain of NP, which is crucial to its interaction with VP30 [77, 232]. Meanwhile, in VP30, three dominant mutations arose, whereby E33K and D269E accumulated and A241T was only present in one passage. They all lie in proximity to a cleft highly conserved across orthoebolaviruses which maintains the VP30-NP-interaction necessary for transcription and replication [317]. However, neither have been identified as the crucial interaction partners [317]. Of note, D269E also accumulated in the supernatant of human cerebral organoids. Besides this, two SNP were uncovered in GP, S12P and T293P, whereby the former accumulated throughout and the latter was only predominant in one passage. S12P has not been specifically reported on, but as described in the following, also accumulated upon natural variant selection in the cerebral organoid. T293P did not show up in the cerebral organoids. The SNP is located in the glycan cap region of GP1 [318]. Meanwhile, in VP24, one dominant SNP, P147L, was uncovered. This was also observed for human cerebral organoids and will be discussed below. Lastly, L encoded two dominant SNP, which however only popped up in one passage and were thus probably not selected. C1092Y and K1157R are within the GDP polyribonucleotidyltransferase (PRNTase) domain [319, 320].

Naturally occurring variants of EBOV upon 120 days of growth in human cerebral organoids revealed that most SNP in this study locate to EBOV NP, GP, VP30, or L. In contrast, VP40 was completely devoid of mutations, suggesting intact viral budding capacity as observed for the passaging [78, 84–88]. In VP35 and VP24, few mutations were uncovered (VP35(R19K), VP24(P147L), VP24(R140H)). This is also similar to the overall trends in EBOV passaging. The VP35 R19K substitution has not been published in the literature. It is not located within a specific domain associated with nucleoprotein-chaperoning or interferon inhibition [321]. Meanwhile, the amino acid in position 147 of VP24 has been associated with the

adaptation for guinea pig-adapted EBOV, whereby proline would allow growth in guinea pig cells [322, 323]. R140H has been extensively studied by Ramanathan *et al*. [324]. The SNP is positioned in the VP24-karyopherin alpha interphase employed during the antagonism of nuclear STAT-1 translocation [324, 325]. Strikingly, in BDBV position 140 also encodes histidine (H) as seen for the SNP herein [326]. Alanine substitutions in this position (R140A) interferon-independently reduce viral growth, whereby amounts of viral genomic RNA and mRNA are reduced [324]. Importantly, this SNP was only dominant in EBOV sigma, which grew least efficiently in human cerebral organoids. Further single-mutant studies in the context of persistence are needed to elaborate on this mutation further. Besides this, the results strongly suggest that the interferon antagonism of EBOV is likely intact after its growth in human cerebral organoids.

Among the EBOV$_{n120}$, polymerase-cofactor VP30 encoded the following SNP: VP30(R196H), VP30 (E205V), VP30(S221R), VP30(S234P) VP30(M237I), VP30(D269E). Notably, these are positioned in proximity to a cleft highly conserved across orthoebolaviruses which maintains the VP30-NP-interaction [317]. This is similar to the passaged EBOV. Except for S234, SNP of this study have not been specifically evaluated regarding their consequences for the interaction [317]. Kirchdoerfer *et al*. found SNP S234R to be detrimental to the interaction of VP30 and NP [317, 327]. The VP30(S234P) of this study occurs in EBOV kappa/lambda. These however replicated strongly in all tested models. Further studies are necessary to conclusively elucidate this. Lastly, polymorphisms in position 221 of VP30, which is otherwise a highly conserved region in orthoebolaviruses, have been attributed to different genera, although their substitution is not predicted to strongly impact NP binding [317].

In EBOV NP, the following SNP were enriched among the naturally occurring variants: NP(P428S), NP(D445G), NP(N500K) NP(S581N/G), NP(E590G), NP (A605V), and NP-(R612G/I). Strikingly, the SNP (pos. 581-590) are in proximity to the SNP S587A retrieved upon passaging. Besides this, the first, D445G, lies outside regions associated with crucial domains involved in VP35 interaction, inclusion body, or particle formation [77]. However, N500K borders the intrinsically disordered region of NP which has been associated with inclusion body formation [74]. In contrast, positions 581 to 590 comprise the central domain of NP, which is involved in VP30 and host factor (SET and MYND domain containing 3 (SMYD3)) interaction via a SxPxLE motif [77, 232]. Depletion of SMYD3 has been associated with reduced EBOV mRNA transcription [328]. NP(S581N/G) (EBOV beta, delta) and NP(E590G) (EBOV delta) single and double mutations could thus be relevant in the context of EBOV persistence. At the same time, A605 (EBOV kappa, lambda) and R612 (EBOV beta, gamma, delta) lie in the interaction domain with VP30, which is crucial for transcription [77, 317, 327]. Here, the PPxPxY motif is needed for the interaction, whereby the addition of multiple (but not single) residues adjacent to position 612 completely abrogates the binding of VP30 to NP and

leads to limited replication in a minigenome assay [77, 317, 327]. The specific consequences of the substitutions uncovered herein, concerning the functionality of the VP30-NP interaction, might overall be a valuable target to explore in the context of viral persistence.

Throughout EBOV L, several SNP were enriched among the naturally occurring EBOV$_{n120}$ variants, namely L(Y32S), L(P401L), L(L915S), L(C1092Y) L(R1522G),L(R1644G), L(H1754Y). None of them has been specifically reported upon in the literature. While Y32 lies in the N-terminal domain, P401 is positioned in the finger domain of the RdRp, and L915 as well as C1092 are located within the PRNTase domain [319, 320]. R1522, R1644, and H1754 are in the C-terminal domain of the L protein [319, 320]. Further studies are needed to evaluate the consequences of these SNP [319, 320].

No escape mutations targeted by antiviral or monoclonal antibody treatment were detected in two cases of EBOV persistence in which monoclonal antibody (mAB) treatment was administered [162, 169]. Moreover, in the only case of EVD relapse, a coding mutation in GP(E280G) did not result in antibody escape [140]. In this study, naturally occurring EBOV variants also accumulated several mutations within the EBOV GP locus: GP(S12P), GP(S46N), GP(H59Y), GP(T77I), GP(I249T), GP(N257K), and GP(E283D). Many SNP have not been specifically reported on in the literature. However, S46N (EBOV kappa/lambda), which is conserved in EBOV and BDBV but not SUDV, is a critical residue for the mAB EBOV-786 interaction [329]. EBOV-786 is a neutralizing public clonotype that targets only GP$_{CL}$ [329]. Moreover, position T77 (EBOV delta), which is highly conserved across orthoebolaviruses, has been described to be involved in the binding of the mAB rEBOV-520 against the GP base region [318]. Importantly, the substitutions both occurred without any selection pressure in the context of this study. Besides this, position N257 (EBOV gamma, delta, sigma) is highly conserved across orthoebolaviruses and constitutes an N-glycan binding motif (N-X-S/T) [330]. Upon deglycosylation of such motifs, infection efficiency and endosomal protease sensitivity may be altered [330]. Based on this, this SNP may be an interesting target in future persistence studies. No mutations were obtained in the GP2 subunit.

Among the naturally occurring EBOV$_{n120}$ variants, different replicative capacities were uncovered in VeroE6 cells, Huh7 cells, astrocytes, and microglia. Importantly, all replicated in human cerebral organoids and established persistence, but some seemingly lost this capacity in microglia and astrocytes where more CPE was present. Notably, variants that formed large plaques in the immunofocus assay seemingly were those highly replicating in human cerebral organoids. Based on this, it may be speculated that cell-to-cell infection may be favored, as previously discussed in subsection 8.3.3. Indeed, via immunofluorescence microscopy, many events of cell-cell infection were observed amongst the EBOV$_{n120}$ variants (EBOV beta, gamma, delta, lambda, sigma). This must however be taken with caution since this was not quantified and infection via the media was not excluded in the experimental

setup. Other variants, such as EBOV sigma, showed signs of low-level replication in human cerebral organoids. Since naturally occurring variants herein mostly encoded multiple SNP, the causality of the mutations in the context of replicative behavior cannot be pinpointed. Future studies should include single mutant replicon assays [331], as discussed above.

Finally, it must be noted that the accumulation of SNP upon passaging in microglia and during long-term culture in human cerebral organoids might not be due to selection pressure but could also be due to a lack of constraints or enzymatic activity [162]. Moreover, SNP in non-coding regions might further have occurred but were not highlighted in the scope of this study. As such, U-to-C hyperediting events of the viral genome were enriched in persistent EBOV isolates in two survivors with paired acute samples in which ADAR1 enzyme activity was elevated [162, 332]. To elucidate the direct interactions of host enzymes with the EBOV genome in this study, the expression of RNA editing and modifying enzymes was queried within the RNA sequencing datasets retrieved from persistently infected microglia and astrocytes. Strikingly, some enzymes were in part differentially expressed upon long-term infection with EBOV. Here, particularly PARP10 was elevated 12 dpi with EBOV onwards. PARP10 ADP-ribosylates RNA, which has been shown to aid RNA stability but has also been exploited by viruses for capping of the viral mRNA [333, 334]. Notably, PARP10 inhibits Venezuelan equine encephalitis virus (VEEV) replication [335]. ADAR RNA editing enzymes [332] were further altered in EBOV persistence. As such, ADAR mostly targets the 3'UTRs of filoviral mRNA and thereby positively influences translation [336]. ADAR was elevated in microglia upon infection. Moreover, ADARB2 was enriched both in microglia and astrocytes 20 dpi with EBOV as well as in astrocyte infection with LASV. Notably, besides its editing activity, ADARB2 has been shown to reduce self-non-self-recognition of RNA species by inducing A-to-I mutations [332]. In persistent BoDV-1 infection, such modifications lead to BoDV-1 RNA being recognized as self and thus enables evasion of PRR-sensing [337]. Some members of the RNA-editing APOBEC family [338] were further enriched in microglia upon EBOV infection. Importantly, in EBOV-infected bat cells, upon passage, an accumulation of mutations in the GP glycan shield and mucin-rich domain was linked to elevated ADAR1 activity in the cell line [291]. Conclusively, the interaction of these RNA editing enzymes, which are only enriched in microglia and less in astrocytes, may be interesting targets to study in the context of EBOV persistence in the human CNS.

Besides the evolutionary dynamics observed within a host/tissue upon EBOV persistence, inter-evolutionary dynamics further play a role during outbreaks. At the same time, a low accumulation of coding changes in humans with confirmed persistence confirms this notion [138, 139, 162, 169]. No definitive proof for site-specific selection pressure and replication dynamics has been provided so far [13, 162]. In this study, several candidate mutations were uncovered, some of which have already been reported before. Further studies are needed

to further assess their consequences for EBOV persistence as well as potential viral gene signature in site-specific EBOV persistence tracing [13].

9 Outlook

This thesis proposes a novel human cerebral organoid model that can be used in studies of the EBOV CNS persistence. Together with the exploration of various cell culture models of CNS cells, multiple putative mechanisms for the establishment and maintenance of EBOV CNS persistence were investigated.

In the future, mechanistic studies can expand upon the findings of this work. In particular, cerebral organoids may be incorporated into an organ-on-chip device with a selective barrier [339] to study the role of the infection across the BBB for the downstream targets of EBOV in the CNS. In addition, such a BBB could further be used to address the role of further innate and adaptive immune cell populations in human cerebral organoids and the consequences for EBOV clearance as well as CNS inflammation [339, 340]. This could be particularly done as avatar models of EVD survivors and individuals with (former) EBOV persistence to elucidate host-specific contributors to EBOV CNS persistence.

Furthermore, the cerebral organoid model may be employed in intervention studies that anticipate the clearance of a persistent EBOV infection. In this context, more targeted approaches focusing on the herein-identified host factors, such as the CX3CR1-CX3CL1-axis in the context of cell-cell infection, or regulatory players of the antiviral response, may be applied. In this context, the generation of specific knock outs in the human cerebral organoid model might be used.

Lastly, the role of the uncovered, naturally occurring CNS variants might further be addressed in minireplicon screens, thereby elucidating possibly targetable weak points within the EBOV genome in the context of the CNS niche.

References

[1] Fairhead J, Leach M, Millimouno D. Spillover or endemic? Reconsidering the origins of Ebola virus disease outbreaks by revisiting local accounts in light of new evidence from Guinea. BMJ Glob Health. 2021 Apr;6(4).

[2] Salmanton-García J, Wipfler P, Leckler J, Nauclér P, Mallon PW, Bruijning-Verhagen PCJL, et al. Predicting the next pandemic: VACCELERATE ranking of the World-Health Organization's Blueprint forAction toPreventEpidemics. Travel Med Infect Dis. 2024;57:102676.

[3] Jacob ST, Crozier I, Fischer WA, Hewlett A, Kraft CS, Vega MA, et al. Ebola virus disease. Nat Rev Dis Primers. 2020 Feb;6(1):13.

[4] Gorbalenya AE, Krupovic M, Mushegian A, Kropinski AM, Siddell SG, Varsani A, et al. The new scope of virus taxonomy: partitioning the virosphere into 15 hierarchical ranks. Nat Microbiol. 2020 05;5(5):668-74.

[5] Walker PJ, Siddell SG, Lefkowitz EJ, Mushegian AR, Adriaenssens EM, Alfenas-Zerbini P, et al. Changes to virus taxonomy and to the International Code of Virus Classification and Nomenclature ratified by the International Committee on Taxonomy of Viruses (2021). Arch Virol. 2021 Sep;166(9):2633-48.

[6] Biedenkopf N, Bukreyev A, Chandran K, Di Paola N, Formenty PBH, Griffiths A, et al. Renaming of genera Ebolavirus and Marburgvirus to Orthoebolavirus and Orthomarburgvirus, respectively, and introduction of binomial species names within family Filoviridae. Arch Virol. 2023 Aug;168(8):220.

[7] Miranda ME, Miranda NL. Reston ebolavirus in humans and animals in the Philippines: a review. J Infect Dis. 2011 Nov;204:757-60.

[8] CDC. History of Ebola Disease Outbreaks; 2024. Available from: https://www.cdc.gov/vhf/ebola/history/chronology.html.

[9] Riesle-Sbarbaro SA, Wibbelt G, x A, Kouakou V, Bokelmann M, Hansen-Kant K, et al. Selective replication and vertical transmission of Ebola virus in experimentally infected Angolan free-tailed bats. Nat Commun. 2024 Jan;15(1):925.

[10] Forbes KM, Webala PW, Jääskeläinen AJ, Abdurahman S, Ogola J, Masika MM, et al. Bombali Virus in Mops condylurus Bat, Kenya. Emerg Infect Dis. 2019 05;25(5):955-7.

[11] Goldstein T, Anthony SJ, Gbakima A, Bird BH, Bangura J, Tremeau-Bravard A, et al. Author Correction: The discovery of Bombali virus adds further support for bats as hosts of ebolaviruses. Nat Microbiol. 2018 12;3(12):1486.

[12] Karan LS, Makenov MT, Korneev MG, Sacko N, Boumbaly S, Yakovlev SA, et al. Bombali Virus in Mops condylurus Bats, Guinea. Emerg Infect Dis. 2019 09;25(9).

[13] Di Paola N, Sanchez-Lockhart M, Zeng X, Kuhn JH, Palacios G. Viral genomics in Ebola virus research. Nature Reviews Microbiology. 2020;18(7):365-78.

[14] Amman BR, Carroll SA, Reed ZD, Sealy TK, Balinandi S, Swanepoel R, et al. Seasonal pulses of Marburg virus circulation in juvenile Rousettus aegyptiacus bats coincide with periods of increased risk of human infection. PLoS Pathog. 2012;8(10):e1002877.

[15] Amman BR, Bird BH, Bakarr IA, Bangura J, Schuh AJ, Johnny J, et al. Isolation of Angola-like Marburg virus from Egyptian rousette bats from West Africa. Nat Commun. 2020 01;11(1):510.

[16] Paweska JT, Jansen van Vuren P, Kemp A, Storm N, Grobbelaar AA, Wiley MR, et al. Marburg Virus Infection in Egyptian Rousette Bats, South Africa, 2013–2014. Emerg Infect Dis. 2018 Jun;24(6):1134-7.

[17] Towner JS, Amman BR, Sealy TK, Carroll SA, Comer JA, Kemp A, et al. Isolation of genetically diverse Marburg viruses from Egyptian fruit bats. PLoS Pathog. 2009 Jul;5(7):e1000536.

[18] Bechtelsheimer H, Jacob H, Solcher H. Zur Neuropathologie der durch grüne Meerkatzen (Cercopithecus aethiops) übertragenen Infektionskrankheiten in Marburg. Dt Med Wschr. 1969;93(12a):602-4.

[19] Kajihara M, Hang'ombe BM, Changula K, Harima H, Isono M, Okuya K, et al. Marburgvirus in Egyptian Fruit Bats, Zambia. Emerg Infect Dis. 2019 08;25(8):1577-80.

[20] Barrette RW, Metwally SA, Rowland JM, Xu L, Zaki SR, Nichol ST, et al. Discovery of swine as a host for the Reston ebolavirus. Science. 2009 Jul;325(5937):204-6.

[21] Belyi VA, Levine AJ, Skalka AM. Unexpected inheritance: multiple integrations of ancient bornavirus and ebolavirus/marburgvirus sequences in vertebrate genomes. PLoS Pathog. 2010 Jul;6(7):e1001030.

[22] Taylor DJ, Dittmar K, Ballinger MJ, Bruenn JA. Evolutionary maintenance of filovirus-like genes in bat genomes. BMC Evol Biol. 2011 Nov;11:336.

[23] Taylor DJ, Leach RW, Bruenn J. Filoviruses are ancient and integrated into mammalian genomes. BMC Evol Biol. 2010 Jun;10:193.

[24] Bermejo M, Rodríguez-Teijeiro JD, Illera G, Barroso A, Vilà C, Walsh PD. Ebola outbreak killed 5000 gorillas. Science. 2006 Dec;314(5805):1564.

[25] Leroy EM, Rouquet P, Formenty P, Souquière S, Kilbourne A, Froment JM, et al. Multiple Ebola virus transmission events and rapid decline of central African wildlife. Science. 2004 Jan;303(5656):387-90.

[26] Wittmann TJ, Biek R, Hassanin A, Rouquet P, Reed P, Yaba P, et al. Isolates of Zaire ebolavirus from wild apes reveal genetic lineage and recombinants. Proc Natl Acad Sci U S A. 2007 Oct;104(43):17123-7.

[27] Grubaugh ND, Ladner JT, Lemey P, Pybus OG, Rambaut A, Holmes EC, et al. Tracking virus outbreaks in the twenty-first century. Nat Microbiol. 2019 01;4(1):10-9.

[28] Keita M, Duraffour S, Loman NJ, Rambaut A, Diallo B, Magassouba N, et al. Unusual Ebola Virus Chain of Transmission, Conakry, Guinea, 2014-2015. Emerg Infect Dis. 2016 Dec;22(12):2149-52.

[29] Blackley DJ, Wiley MR, Ladner JT, Fallah M, Lo T, Gilbert ML, et al. Reduced evolutionary rate in reemerged Ebola virus transmission chains. Sci Adv. 2016 Apr;2(4):e1600378.

[30] Christie A, Davies-Wayne GJ, Cordier-Lassalle T, Blackley DJ, Laney AS, Williams DE, et al. Possible sexual transmission of Ebola virus - Liberia, 2015. MMWR Morb Mortal Wkly Rep. 2015 May;64(17):479-81.

[31] Diallo B, Sissoko D, Loman NJ, Bah HA, Bah H, Worrell MC, et al. Resurgence of Ebola Virus Disease in Guinea Linked to a Survivor With Virus Persistence in Seminal Fluid for More Than 500 Days. Clin Infect Dis. 2016 Nov;63(10):1353-6.

[32] Mate SE, Kugelman JR, Nyenswah TG, Ladner JT, Wiley MR, Cordier-Lassalle T, et al. Molecular Evidence of Sexual Transmission of Ebola Virus. N Engl J Med. 2015 Dec;373(25):2448-54.

[33] Keita AK, Koundouno FR, Faye M, Düx A, Hinzmann J, Diallo H, et al. Resurgence of Ebola virus in 2021 in Guinea suggests a new paradigm for outbreaks. Nature. 2021 Sep;597(7877):539-43.

[34] Brauburger K, Boehmann Y, Krähling V, Mühlberger E. Transcriptional Regulation in Ebola Virus: Effects of Gene Border Structure and Regulatory Elements on Gene Expression and Polymerase Scanning Behavior. J Virol. 2016 Feb;90(4).

[35] Sanchez A, Kiley MP, Holloway BP, Auperin DD. Sequence analysis of the Ebola virus genome: organization, genetic elements, and comparison with the genome of Marburg virus. Virus Res. 1993 Sep;29(3):215-40.

[36] Volchkova VA, Klenk HD, Volchkov VE. Delta-peptide is the carboxy-terminal cleavage fragment of the nonstructural small glycoprotein sGP of Ebola virus. Virology. 1999 Dec;265(1):164-71.

[37] de La Vega MA, Wong G, Kobinger GP, Qiu X. The multiple roles of sGP in Ebola pathogenesis. Viral Immunol. 2015 Feb;28(1):3-9.

[38] Brindley MA, Hunt CL, Kondratowicz AS, Bowman J, Sinn PL, McCray PB, et al. Tyrosine kinase receptor Axl enhances entry of Zaire ebolavirus without direct interactions with the viral glycoprotein. Virology. 2011 Jul;415(2):83-94.

[39] Hunt CL, Kolokoltsov AA, Davey RA, Maury W. The Tyro3 receptor kinase Axl enhances macropinocytosis of Zaire ebolavirus. J Virol. 2011 Jan;85(1):334-47.

[40] Ji X, Olinger GG, Aris S, Chen Y, Gewurz H, Spear GT. Mannose-binding lectin binds to Ebola and Marburg envelope glycoproteins, resulting in blocking of virus interaction with DC-SIGN and complement-mediated virus neutralization. J Gen Virol. 2005 Sep;86(Pt 9):2535-42.

[41] Marzi A, Akhavan A, Simmons G, Gramberg T, Hofmann H, Bates P, et al. The signal peptide of the ebolavirus glycoprotein influences interaction with the cellular lectins DC-SIGN and DC-SIGNR. J Virol. 2006 Jul;80(13):6305-17.

[42] Moller-Tank S, Maury W. Phosphatidylserine receptors: enhancers of enveloped virus entry and infection. Virology. 2014 Nov;468-470:565-80.

[43] Simmons G, Reeves JD, Grogan CC, Vandenberghe LH, Baribaud F, Whitbeck JC, et al. DC-SIGN and DC-SIGNR bind ebola glycoproteins and enhance infection of macrophages and endothelial cells. Virology. 2003 Jan;305(1):115-23.

[44] Perez-Zsolt D, Erkizia I, Pino M, a Gallo M, Martin MT, Benet S, et al. Anti-Siglec-1 antibodies block Ebola viral uptake and decrease cytoplasmic viral entry. Nat Microbiol. 2019 Sep;4(9):1558-70.

[45] Lee JE, Saphire EO. Ebolavirus glycoprotein structure and mechanism of entry. Future Virol. 2009;4(6):621-35.

[46] Sanchez A. Analysis of filovirus entry into vero e6 cells, using inhibitors of endocytosis, endosomal acidification, structural integrity, and cathepsin (B and L) activity. J Infect Dis. 2007 Nov;196:251-8.

[47] Rasmussen AL. Host Factors in Ebola Infection. Annu Rev Genomics Hum Genet. 2016 Aug;17:333-51.

[48] Nanbo A, Imai M, Watanabe S, Noda T, Takahashi K, Neumann G, et al. Ebolavirus is internalized into host cells via macropinocytosis in a viral glycoprotein-dependent manner. PLoS Pathog. 2010 Sep;6(9):e1001121.

[49] Martin B, Hoenen T, Canard B, Decroly E. Filovirus proteins for antiviral drug discovery: A structure/function analysis of surface glycoproteins and virus entry. Antiviral Res. 2016 Nov;135:1-14.

[50] Ito H, Watanabe S, Sanchez A, Whitt MA, Kawaoka Y. Mutational analysis of the putative fusion domain of Ebola virus glycoprotein. J Virol. 1999 Oct;73(10):8907-12.

[51] Durham ND, Howard AR, Govindan R, Senjobe F, Fels JM, Diehl WE, et al. Real-Time Analysis of Individual Ebola Virus Glycoproteins Reveals Pre-Fusion, Entry-Relevant Conformational Dynamics. Viruses. 2020 Jan;12(1).

[52] Brecher M, Schornberg KL, Delos SE, Fusco ML, Saphire EO, White JM. Cathepsin cleavage potentiates the Ebola virus glycoprotein to undergo a subsequent fusion-relevant conformational change. J Virol. 2012 Jan;86(1):364-72.

[53] Odongo L, Habtegebrael BH, Kiessling V, White JM, Tamm LK. system of supported planar endosomal membranes (SPEMs) reveals an enhancing role for cathepsin B in the final stage of Ebola virus fusion and entry. Microbiol Spectr. 2023 Sep;11(5):e0190823.

[54] Yuan S, Cao L, Ling H, Dang M, Sun Y, Zhang X, et al. TIM-1 acts a dual-attachment receptor for Ebolavirus by interacting directly with viral GP and the PS on the viral envelope. Protein Cell. 2015 Nov;6(11):814-24.

[55] Winter SL, Golani G, Lolicato F, Vallbracht M, Thiyagarajah K, Ahmed SS, et al. The Ebola virus VP40 matrix layer undergoes endosomal disassembly essential for membrane fusion. EMBO J. 2023 Jun;42(11):e113578.

[56] Martinez O, Ndungo E, Tantral L, Miller EH, Leung LW, Chandran K, et al. A Mutation in the Ebola Virus Envelope Glycoprotein Restricts Viral Entry in a Host Species- and Cell-Type-Specific Manner. Journal of Virology. 2013;87(6):3324-34.

[57] Mingo RM, Simmons JA, Shoemaker CJ, Nelson EA, Schornberg KL, D'Souza RS, et al. Ebola virus and severe acute respiratory syndrome coronavirus display late cell entry kinetics: evidence that transport to NPC1+ endolysosomes is a rate-defining step. J Virol. 2015 Mar;89(5):2931-43.

[58] Ahmad I, Fatemi SN, Ghaheri M, Rezvani A, Khezri DA, Natami M, et al. An overview of the role of Niemann-pick C1 (NPC1) in viral infections and inhibition of viral infections through NPC1 inhibitor. Cell Commun Signal. 2023 Dec;21(1):352.

[59] Carette JE, Raaben M, Wong AC, Herbert AS, Obernosterer G, Mulherkar N, et al. Ebola virus entry requires the cholesterol transporter Niemann-Pick C1. Nature. 2011 Aug;477(7364):340-3.

[60] Younan P, Santos RI, Ramanathan P, Iampietro M, Nishida A, Dutta M, et al. Ebola virus-mediated T-lymphocyte depletion is the result of an abortive infection. PLoS Pathog. 2019 Oct;15(10):e1008068.

[61] Younan P, Iampietro M, Nishida A, Ramanathan P, Santos RI, Dutta M, et al. Ebola Virus Binding to Tim-1 on T Lymphocytes Induces a Cytokine Storm. mBio. 2017 Sep;8(5).

[62] Rasmussen AL. Host Factors Involved in Ebola Virus Replication. Curr Top Microbiol Immunol. 2018;419:113-50.

[63] Martinez MJ, Biedenkopf N, Volchkova V, Hartlieb B, Alazard-Dany N, Reynard O, et al. Role of Ebola virus VP30 in transcription reinitiation. J Virol. 2008 Dec;82(24):12569-73.

[64] Martinez MJ, Volchkova VA, Raoul H, Alazard-Dany N, Reynard O, Volchkov VE. Role of VP30 phosphorylation in the Ebola virus replication cycle. J Infect Dis. 2011 Nov;204:934-40.

[65] Modrof J, Mühlberger E, Klenk HD, Becker S. Phosphorylation of VP30 impairs ebola virus transcription. J Biol Chem. 2002 Sep;277(36):33099-104.

[66] Ilinykh PA, Tigabu B, Ivanov A, Ammosova T, Obukhov Y, Garron T, et al. Role of protein phosphatase 1 in dephosphorylation of Ebola virus VP30 protein and its targeting for the inhibition of viral transcription. J Biol Chem. 2014 Aug;289(33):22723-38.

[67] Garcia-Dorival I, Wu W, Armstrong SD, Barr JN, Carroll MW, Hewson R, et al. Elucidation of the Cellular Interactome of Ebola Virus Nucleoprotein and Identification of Therapeutic Targets. J Proteome Res. 2016 Dec;15(12):4290-303.

[68] Sztuba-Solinska J, Diaz L, Kumar MR, Kolb G, Wiley MR, Jozwick L, et al. A small stem-loop structure of the Ebola virus trailer is essential for replication and interacts with heat-shock protein A8. Nucleic Acids Res. 2016 Nov;44(20):9831-46.

[69] Smith DR, McCarthy S, Chrovian A, Olinger G, Stossel A, Geisbert TW, et al. Inhibition of heat-shock protein 90 reduces Ebola virus replication. Antiviral Res. 2010 Aug;87(2):187-94.

[70] Yamayoshi S, Noda T, Ebihara H, Goto H, Morikawa Y, Lukashevich IS, et al. Ebola virus matrix protein VP40 uses the COPII transport system for its intracellular transport. Cell Host Microbe. 2008 Mar;3(3):168-77.

[71] Takahashi K, Halfmann P, Oyama M, Kozuka-Hata H, Noda T, Kawaoka Y. DNA topoisomerase 1 facilitates the transcription and replication of the Ebola virus genome. J Virol. 2013 Aug;87(16):8862-9.

[72] Zhang J, Wang B, Gao X, Peng C, Shan C, Johnson SF, et al. RNF185 regulates proteostasis in Ebolavirus infection by crosstalk between the calnexin cycle, ERAD, and reticulophagy. Nat Commun. 2022 Oct;13(1):6007.

[73] Hoenen T, Shabman RS, Groseth A, Herwig A, Weber M, Schudt G, et al. Inclusion bodies are a site of ebolavirus replication. J Virol. 2012 Nov;86(21):11779-88.

[74] Bodmer BS, Vallbracht M, Ushakov DS, Wendt L, Chlanda P, Hoenen T. Ebola virus inclusion bodies are liquid organelles whose formation is facilitated by nucleoprotein oligomerization. Emerg Microbes Infect. 2023 Dec;12(2):2223727.

[75] Fang J, Castillon G, Phan S, McArdle S, Hariharan C, Adams A, et al. Spatial and functional arrangement of Ebola virus polymerase inside phase-separated viral factories. Nat Commun. 2023 Jul;14(1):4159.

[76] Zhu L, Gao T, Huang Y, Jin J, Wang D, Zhang L, et al. Ebola virus VP35 hijacks the PKA-CREB1 pathway for replication and pathogenesis by AKIP1 association. Nat Commun. 2022 Apr;13(1):2256.

[77] Miyake T, Farley CM, Neubauer BE, Beddow TP, Hoenen T, Engel DA. Ebola Virus Inclusion Body Formation and RNA Synthesis Are Controlled by a Novel Domain of Nucleoprotein Interacting with VP35. J Virol. 2020 Jul;94(16).

[78] Nanbo A, Ohba Y. Budding of Ebola Virus Particles Requires the Rab11-Dependent Endocytic Recycling Pathway. J Infect Dis. 2018 Nov;218:388-96.

[79] Han Z, Madara JJ, Liu Y, Liu W, Ruthel G, Freedman BD, et al. ALIX Rescues Budding of a Double PTAP/PPEY L-Domain Deletion Mutant of Ebola VP40: A Role for ALIX in Ebola Virus Egress. J Infect Dis. 2015 Oct;212:138-45.

[80] Martin-Serrano J, Zang T, Bieniasz PD. HIV-1 and Ebola virus encode small peptide motifs that recruit Tsg101 to sites of particle assembly to facilitate egress. Nat Med. 2001 Dec;7(12):1313-9.

[81] Silvestri LS, Ruthel G, Kallstrom G, Warfield KL, Swenson DL, Nelle T, et al. Involvement of vacuolar protein sorting pathway in Ebola virus release independent of TSG101 interaction. J Infect Dis. 2007 Nov;196:264-70.

[82] Yasuda J, Nakao M, Kawaoka Y, Shida H. Nedd4 regulates egress of Ebola virus-like particles from host cells. J Virol. 2003 Sep;77(18):9987-92.

[83] Lu J, Qu Y, Liu Y, Jambusaria R, Han Z, Ruthel G, et al. Host IQGAP1 and Ebola virus VP40 interactions facilitate virus-like particle egress. J Virol. 2013 Jul;87(13):7777-80.

[84] Acciani MD, Lay Mendoza MF, Havranek KE, Duncan AM, Iyer H, Linn OL, et al. Ebola Virus Requires Phosphatidylserine Scrambling Activity for Efficient Budding and Optimal Infectivity. J Virol. 2021 Sep;95(20):e0116521.

[85] Younan P, Iampietro M, Santos RI, Ramanathan P, Popov VL, Bukreyev A. Role of Transmembrane Protein 16F in the Incorporation of Phosphatidylserine Into Budding Ebola Virus Virions. J Infect Dis. 2018 Nov;218:335-45.

[86] Soni SP, Adu-Gyamfi E, Yong SS, Jee CS, Stahelin RV. The Ebola virus matrix protein deeply penetrates the plasma membrane: an important step in viral egress. Biophys J. 2013 May;104(9):1940-9.

[87] Soni SP, Stahelin RV. The Ebola virus matrix protein VP40 selectively induces vesiculation from phosphatidylserine-enriched membranes. J Biol Chem. 2014 Nov;289(48):33590-7.

[88] Adu-Gyamfi E, Johnson KA, Fraser ME, Scott JL, Soni SP, Jones KR, et al. Host Cell Plasma Membrane Phosphatidylserine Regulates the Assembly and Budding of Ebola Virus. J Virol. 2015 Sep;89(18):9440-53.

[89] Vande Burgt NH, Kaletsky RL, Bates P. Requirements within the Ebola Viral Glycoprotein for Tetherin Antagonism. Viruses. 2015 Oct;7(10):5587-602.

[90] Kaletsky RL, Francica JR, Agrawal-Gamse C, Bates P. Tetherin-mediated restriction of filovirus budding is antagonized by the Ebola glycoprotein. Proc Natl Acad Sci U S A. 2009 Feb;106(8):2886-91.

[91] Santos RI, Ilinykh PA, Pietzsch CA, Ronk AJ, Huang K, Kuzmina NA, et al. Blocking of ebolavirus spread through intercellular connections by an MPER-specific antibody depends on BST2/tetherin. Cell Rep. 2023 Oct;42(10):113254.

[92] Miao C, Li M, Zheng YM, Cohen FS, Liu SL. Cell-cell contact promotes Ebola virus GP-mediated infection. Virology. 2016 Jan;488:202-15.

[93] Bär S, Takada A, Kawaoka Y, Alizon M. Detection of cell-cell fusion mediated by Ebola virus glycoproteins. J Virol. 2006 Mar;80(6):2815-22.

[94] Djurkovic MA, Leavitt CG, Arnett E, Kriachun V, nez Sobrido L, Titone R, et al. Ebola Virus Uses Tunneling Nanotubes as an Alternate Route of Dissemination. J Infect Dis. 2023 Nov;228:522-35.

[95] Markosyan RM, Miao C, Zheng YM, Melikyan GB, Liu SL, Cohen FS. Induction of Cell-Cell Fusion by Ebola Virus Glycoprotein: Low pH Is Not a Trigger. PLoS Pathog. 2016 Jan;12(1):e1005373.

[96] Nehls J, Businger R, Hoffmann M, Brinkmann C, Fehrenbacher B, Schaller M, et al. Release of Immunomodulatory Ebola Virus Glycoprotein-Containing Microvesicles Is Suppressed by Tetherin in a Species-Specific Manner. Cell Reports. 2019;26(7):1841-53.e6.

[97] Pleet ML, Mathiesen A, DeMarino C, Akpamagbo YA, Barclay RA, Schwab A, et al. Corrigendum: Ebola VP40 in Exosomes Can Cause Immune Cell Dysfunction. Front Microbiol. 2018;9:692.

[98] Basler CF. Innate immune evasion by filoviruses. Virology. 2015 May;479-480:122-30.

[99] Basler CF, Amarasinghe GK. Evasion of interferon responses by Ebola and Marburg viruses. J Interferon Cytokine Res. 2009 Sep;29(9):511-20.

[100] Cardenas WB, Loo YM, Gale M, Hartman AL, Kimberlin CR, Martínez-Sobrido L, et al. Ebola virus VP35 protein binds double-stranded RNA and inhibits alpha/beta interferon production induced by RIG-I signaling. J Virol. 2006 Jun;80(11):5168-78.

[101] Basler CF, Mikulasova A, Martinez-Sobrido L, Paragas J, mühlberger E, Bray M, et al. The Ebola virus VP35 protein inhibits activation of interferon regulatory factor 3. J Virol. 2003 Jul;77(14):7945-56.

[102] Schümann M, Gantke T, Mühlberger E. Ebola virus VP35 antagonizes PKR activity through its C-terminal interferon inhibitory domain. J Virol. 2009 Sep;83(17):8993-7.

[103] Hartman AL, Bird BH, Towner JS, Antoniadou ZA, Zaki SR, Nichol ST. Inhibition of IRF-3 activation by VP35 is critical for the high level of virulence of ebola virus. J Virol. 2008 Mar;82(6):2699-704.

[104] Luthra P, Ramanan P, Mire CE, Weisend C, Tsuda Y, Yen B, et al. Mutual antagonism between the Ebola virus VP35 protein and the RIG-I activator PACT determines infection outcome. Cell Host Microbe. 2013 Jul;14(1):74-84.

[105] Zhu L, Jin J, Wang T, Hu Y, Liu H, Gao T, et al. Ebola virus sequesters IRF3 in viral inclusion bodies to evade host antiviral immunity. Elife. 2024 Jan;12(RP88122).

[106] He FB, Khan H, Huttunen M, Kolehmainen P, n K, Maljanen S, et al. Filovirus VP24 Proteins Differentially Regulate RIG-I and MDA5-Dependent Type I and III Interferon Promoter Activation. Front Immunol. 2021;12:694105.

[107] Fabozzi G, Nabel CS, Dolan MA, Sullivan NJ. Ebolavirus proteins suppress the effects of small interfering RNA by direct interaction with the mammalian RNA interference pathway. J Virol. 2011 Mar;85(6):2512-23.

[108] Longet S, Mellors J, Carroll MW, Tipton T. Ebolavirus: Comparison of Survivor Immunology and Animal Models in the Search for a Correlate of Protection. Front Immunol. 2020;11:599568.

[109] Ruibal P, Oestereich L, Lüdtke A, Becker-Ziaja B, Wozniak DM, Kerber R, et al. Unique human immune signature of Ebola virus disease in Guinea. Nature. 2016 May;533(7601):100-4.

[110] McElroy AK, Erickson BR, Flietstra TD, Rollin PE, Nichol ST, Towner JS, et al. Ebola hemorrhagic Fever: novel biomarker correlates of clinical outcome. J Infect Dis. 2014 Aug;210(4):558-66.

[111] Vernet MA, Reynard S, Fizet A, Schaeffer J, Pannetier D, Guedj J, et al. Clinical, virological, and biological parameters associated with outcomes of Ebola virus infection in Macenta, Guinea. JCI Insight. 2017 Mar;2(6):e88864.

[112] Henao-Restrepo AM, Longini IM, Egger M, Dean NE, Edmunds WJ, Camacho A, et al. Efficacy and effectiveness of an rVSV-vectored vaccine expressing Ebola surface glycoprotein: interim results from the Guinea ring vaccination cluster-randomised trial. Lancet. 2015 Aug;386(9996):857-66.

[113] Mulangu S, Dodd LE, Davey RT, Tshiani Mbaya O, Proschan M, Mukadi D, et al. A Randomized, Controlled Trial of Ebola Virus Disease Therapeutics. N Engl J Med. 2019 Dec;381(24):2293-303.

[114] CDC. Treatment; 2024. Available from: https://www.cdc.gov/vhf/ebola/treatment/index.html.

[115] McElroy AK, Akondy RS, McIlwain DR, Chen H, Bjornson-Hooper Z, Mukherjee N, et al. Immunologic timeline of Ebola virus disease and recovery in humans. JCI Insight. 2020 May;5(10).

[116] Bosio CM, Aman MJ, Grogan C, Hogan R, Ruthel G, Negley D, et al. Ebola and Marburg viruses replicate in monocyte-derived dendritic cells without inducing the production of cytokines and full maturation. J Infect Dis. 2003 Dec;188(11):1630-8.

[117] McElroy AK, Akondy RS, Davis CW, Ellebedy AH, Mehta AK, Kraft CS, et al. Human Ebola virus infection results in substantial immune activation. Proc Natl Acad Sci U S A. 2015 Apr;112(15):4719-24.

[118] Speranza E, Ruibal P, Port JR, Feng F, Burkhardt L, Grundhoff A, et al. T-Cell Receptor Diversity and the Control of T-Cell Homeostasis Mark Ebola Virus Disease Survival in Humans. J Infect Dis. 2018 Nov;218:508-18.

[119] Baize S, Leroy EM, Georges-Courbot MC, Capron M, Lansoud-Soukate J, Debré P, et al. Defective humoral responses and extensive intravascular apoptosis are associated with fatal outcome in Ebola virus-infected patients. Nat Med. 1999 Apr;5(4):423-6.

[120] Dahlke C, Lunemann S, Kasonta R, Kreuels B, Schmiedel S, Ly ML, et al. Comprehensive Characterization of Cellular Immune Responses Following Ebola Virus Infection. J Infect Dis. 2017 Jan;215(2):287-92.

[121] Wauquier N, Becquart P, Padilla C, Baize S, Leroy EM. Human fatal Zaire ebola virus infection is associated with an aberrant innate immunity and with massive lymphocyte apoptosis. PLoS Neglected Tropical Diseases. 2010;4(10).

[122] Adekanmbi O, Ilesanmi O, Lakoh S. Ebola: A review and focus on neurologic manifestations. Journal of the Neurological Sciences. 2021;421(January):117311.

[123] Billioux BJ, Smith B, Nath A. Neurological Complications of Ebola Virus Infection. Neurotherapeutics. 2016;13(3):461-70.

[124] Aylward B, Barboza P, Bawo L, Bertherat E, Bilivogui P, Blake I, et al. Ebola virus disease in West Africa–the first 9 months of the epidemic and forward projections. N Engl J Med. 2014 10;371(16):1481-95.

[125] Mohammed H, Vandy AO, Stretch R, Otieno D, Prajapati M, Calderon M, et al. Sequelae and Other Conditions in Ebola Virus Disease Survivors, Sierra Leone, 2015. Emerg Infect Dis. 2017 01;23(1):66-73.

[126] West TE, von Saint André-von Arnim A. Clinical presentation and management of severe Ebola virus disease. Ann Am Thorac Soc. 2014 Nov;11(9):1341-50.

[127] Howlett PJ, Walder AR, Lisk DR, Fitzgerald F, Sevalie S, Lado M, et al. Case Series of Severe Neurologic Sequelae of Ebola Virus Disease during Epidemic, Sierra Leone. Emerg Infect Dis. 2018 08;24(8):1412-21.

[128] Sagui E, Janvier F, Baize S, Foissaud V, Koulibaly F, Savini H, et al. Severe Ebola Virus Infection With Encephalopathy: Evidence for Direct Virus Involvement. Clin Infect Dis. 2015 Nov;61(10):1627-8.

[129] Bwaka MA, Bonnet MJ, Calain P, Colebunders R, De Roo A, Guimard Y, et al. Ebola hemorrhagic fever in Kikwit, Democratic Republic of the Congo: clinical observations in 103 patients. J Infect Dis. 1999 Feb;179 Suppl 1:1-7.

[130] Howlett P, Brown C, Helderman T, Brooks T, Lisk D, Deen G, et al. Ebola Virus Disease Complicated by Late-Onset Encephalitis and Polyarthritis, Sierra Leone. Emerg Infect Dis. 2016 Jan;22(1):150-2.

[131] Chertow DS, Nath A, Suffredini AF, Danner RL, Reich DS, Bishop RJ, et al. Severe Meningoencephalitis in a Case of Ebola Virus Disease: A Case Report. Ann Intern Med. 2016 Aug;165(4):301-4.

[132] Sneller MC, Reilly C, Badio M, Bishop RJ, Eghrari AO, Moses SJ, et al. A Longitudinal Study of Ebola Sequelae in Liberia. N Engl J Med. 2019 03;380(10):924-34.

[133] Higgs ES, Gayedyu-Dennis D, Fischer Ii WA, Nason M, Reilly C, Beavogui AH, et al. PREVAIL IV: A Randomized, Double-Blind, 2-Phase, Phase 2 Trial of Remdesivir vs Placebo for Reduction of Ebola Virus RNA in the Semen of Male Survivors. Clin Infect Dis. 2021 Nov;73(10):1849-56.

[134] Vetter P, Kaiser L, Schibler M, Ciglenecki I, Bausch DG. Sequelae of Ebola virus disease: the emergency within the emergency. Lancet Infect Dis. 2016 06;16(6):e82-91.

[135] Epstein L, Wong KK, Kallen AJ, Uyeki TM. Post-Ebola Signs and Symptoms in U.S. Survivors. N Engl J Med. 2015 Dec;373(25):2484-6.

[136] Scott JT, Sesay FR, Massaquoi TA, Idriss BR, Sahr F, Semple MG. Post-Ebola Syndrome, Sierra Leone. Emerg Infect Dis. 2016 Apr;22(4):641-6.

[137] Wilson HW, Amo-Addae M, Kenu E, Ilesanmi OS, Ameme DK, Sackey SO. Post-Ebola Syndrome among Ebola Virus Disease Survivors in Montserrado County, Liberia 2016. Biomed Res Int. 2018;2018:1909410.

[138] Varkey JB, Shantha JG, Crozier I, Kraft CS, Lyon GM, Mehta AK, et al. Persistence of Ebola Virus in Ocular Fluid during Convalescence. New England Journal of Medicine. 2015;372(25):2423-7.

[139] Jacobs M, Rodger A, Bell DJ, Bhagani S, Cropley I, Filipe A, et al. Late Ebola virus relapse causing meningoencephalitis: a case report. The Lancet. 2016;388(10043):498-503.

[140] Mbala-Kingebeni P, Pratt C, Mutafali-Ruffin M, Pauthner MG, Bile F, Nkuba-Ndaye A, et al. Ebola Virus Transmission Initiated by Relapse of Systemic Ebola Virus Disease. N Engl J Med. 2021 Apr;384(13):1240-7.

[141] Randall RE, Griffin DE. Within host RNA virus persistence: mechanisms and consequences. Curr Opin Virol. 2017 04;23:35-42.

[142] Martini GA, Schmidt HA. [Spermatogenic transmission of the ”Marburg virus”. (Causes of ”Marburg simian disease”)]. Klin Wochenschr. 1968 Apr;46(7):398-400.

[143] Ristanović ES, Crozier I, Kuhn JH, Gligić AS. A Forgotten Episode of Marburg Virus Disease: Belgrade, Yugoslavia, 1967. Microbiol Mol Biol Rev. 2020 May;84(2).

[144] Gear JS, Cassel GA, Gear AJ, Trappler B, Clausen L, Meyers AM, et al. Outbreake of Marburg virus disease in Johannesburg. Br Med J. 1975 Nov;4(5995):489-93.

[145] Smith DH, Johnson BK, Isaacson M, Swanapoel R, Johnson KM, Killey M, et al. Marburg-virus disease in Kenya. Lancet. 1982 Apr;1(8276):816-20.

[146] Nikiforov VV, ĭ IuI, Kalinin PP, Akinfeeva LA, Katkova LR, Barmin VS, et al. Transl.[A case of a laboratory infection with Marburg fever]. Zh Mikrobiol Epidemiol Immunobiol. 1994;(3):104-6.

[147] Emond RT, Evans B, Bowen ET, Lloyd G. A case of Ebola virus infection. Br Med J. 1977 Aug;2(6086):541-4.

[148] Rodriguez LL, De Roo A, Guimard Y, Trappier SG, Sanchez A, Bressler D, et al. Persistence and genetic stability of Ebola virus during the outbreak in Kikwit, Democratic Republic of the Congo, 1995. J Infect Dis. 1999 Feb;179:170-6.

[149] Rowe AK, Bertolli J, Khan AS, Mukunu R, Muyembe-Tamfum JJ, Bressler D, et al. Clinical, Virologic, and Immunologic Follow-Up of Convalescent Ebola Hemorrhagic Fever Patients and Their Household Contacts, Kikwit, Democratic Republic of the Congo. J Infect Dis. 1999 Feb;179 Suppl 1:28-35.

[150] Uyeki TM, Erickson BR, Brown S, McElroy AK, Cannon D, Gibbons A, et al. Ebola Virus Persistence in Semen of Male Survivors. Clin Infect Dis. 2016 Jun;62(12):1552-5.

[151] Purpura LJ, Rogers E, Baller A, White S, Soka M, Choi MJ, et al. Ebola Virus RNA in Semen from an HIV-Positive Survivor of Ebola. Emerg Infect Dis. 2017 Apr;23(4):714-5.

[152] Dyal J, Kofman A, Kollie JZ, Fankhauser J, Orone R, Soka MJ, et al. Risk Factors for Ebola Virus Persistence in Semen of Survivors in Liberia. Clin Infect Dis. 2023 Feb;76(3):e849-56.

[153] Sow MS, Etard JF, Baize S, Magassouba N, Faye O, Msellati P, et al. New Evidence of Long-lasting Persistence of Ebola Virus Genetic Material in Semen of Survivors. J Infect Dis. 2016 Nov;214(10):1475-6.

[154] Barnes KG, Kindrachuk J, Lin AE, Wohl S, Qu J, Tostenson SD, et al. Evidence of Ebola Virus Replication and High Concentration in Semen of a Patient During Recovery. Clin Infect Dis. 2017 Oct;65(8):1400-3.

[155] Sissoko D, Duraffour S, Kerber R, Kolie JS, Beavogui AH, Camara AM, et al. Persistence and clearance of Ebola virus RNA from seminal fluid of Ebola virus disease survivors: a longitudinal analysis and modelling study. Lancet Glob Health. 2017 Jan;5(1):e80-8.

[156] Subtil F, Delaunay C, Keita AK, Sow MS, Touré A, Leroy S, et al. Dynamics of Ebola RNA Persistence in Semen: A Report From the Postebogui Cohort in Guinea. Clin Infect Dis. 2017 Jun;64(12):1788-90.

[157] Keita AK, Vidal N, Toure A, Diallo MSK, Magassouba N, Baize S, et al. A 40-Month Follow-Up of Ebola Virus Disease Survivors in Guinea (PostEbogui) Reveals Long-Term Detection of Ebola Viral Ribonucleic Acid in Semen and Breast Milk. Open Forum Infect Dis. 2019 Dec;6(12):ofz482.

[158] Keita AK, Toure A, Sow MS, Raoul H, Magassouba N, Delaporte E, et al. Extraordinary long-term and fluctuating persistence of Ebola virus RNA in semen of survivors in Guinea: implications for public health. Clin Microbiol Infect. 2017 Jun;23(6):412-3.

[159] Soka MJ, Choi MJ, Baller A, White S, Rogers E, Purpura LJ, et al. Prevention of sexual transmission of Ebola in Liberia through a national semen testing and counselling programme for survivors: an analysis of Ebola virus RNA results and behavioural data. Lancet Glob Health. 2016 Oct;4(10):e736-43.

[160] Deen GF, Broutet N, Xu W, Knust B, Sesay FR, McDonald SLR, et al. Ebola RNA Persistence in Semen of Ebola Virus Disease Survivors - Final Report. N Engl J Med. 2017 Oct;377(15):1428-37.

[161] Thorson AE, Deen GF, Bernstein KT, Liu WJ, Yamba F, Habib N, et al. Persistence of Ebola virus in semen among Ebola virus disease survivors in Sierra Leone: A cohort study of frequency, duration, and risk factors. PLoS Med. 2021 Feb;18(2):e1003273.

[162] Whitmer SLM, Ladner JT, Wiley MR, Patel K, Dudas G, Rambaut A, et al. Active Ebola Virus Replication and Heterogeneous Evolutionary Rates in EVD Survivors. Cell Reports. 2018;22(5):1159-68.

[163] Fischer WA, Brown J, Wohl DA, Loftis AJ, Tozay S, Reeves E, et al. Ebola Virus Ribonucleic Acid Detection in Semen More Than Two Years After Resolution of Acute Ebola Virus Infection. Open Forum Infect Dis. 2017;4(3):ofx155.

[164] Schindell BG, Webb AL, Kindrachuk J. Persistence and sexual transmission of filoviruses. Viruses. 2018;10(12).

[165] Nordenstedt H, Bah EI, de la Vega MA, Barry M, N'Faly M, Crahay B, et al. Ebola Virus in Breast Milk in an Ebola Virus-Positive Mother with Twin Babies, Guinea, 2015. Emerg Infect Dis. 2016 Apr;22(4):759-60.

[166] Bower H, Grass JE, Veltus E, Brault A, Campbell S, Basile AJ, et al. Delivery of an Ebola Virus-Positive Stillborn Infant in a Rural Community Health Center, Sierra Leone, 2015. Am J Trop Med Hyg. 2016 Feb;94(2):417-9.

[167] Liu WJ, Sesay FR, Coursier A, Knust B, Marrinan JE, Whitmer S, et al. Comprehensive Clinical and Laboratory Follow-up of a Female Patient With Ebola Virus Disease: Sierra Leone Ebola Virus Persistence Study. Open Forum Infect Dis. 2019 Mar;6(3):ofz068.

[168] Shantha JG, Mattia JG, Goba A, Barnes KG, Ebrahim FK, Kraft CS, et al. Ebola Virus Persistence in Ocular Tissues and Fluids (EVICT) Study: Reverse Transcription-Polymerase Chain Reaction and Cataract Surgery Outcomes of Ebola Survivors in Sierra Leone. EBioMedicine. 2018 Apr;30:217-24.

[169] Bosworth A, Rickett NY, Dong X, Ng LFP, García-Dorival I, Matthews DA, et al. Analysis of an Ebola virus disease survivor whose host and viral markers were predictive of death indicates the effectiveness of medical countermeasures and supportive care. Genome Medicine. 2021;13(1):1-18.

[170] Widerspick L, Steffen JF, Tappe D, oz Fontela C. Animal Model Alternatives in Filovirus and Bornavirus Research. Viruses. 2023 Jan;15(1).

[171] Durant O, Marzi A. Ebola virus disease sequelae and viral persistence in animal models: Implications for the future. PLoS Pathog. 2024 Mar;20(3):e1012065.

[172] Kozak R, He S, Kroeker A, de La Vega MA, Audet J, Wong G, et al. Ferrets Infected with Bundibugyo Virus or Ebola Virus Recapitulate Important Aspects of Human Filovirus Disease. J Virol. 2016 Oct;90(20):9209-23.

[173] Watson RJ, Tree J, Fotheringham SA, Hall Y, Dong X, Steeds K, et al. Dose-Dependent Response to Infection with Ebola Virus in the Ferret Model and Evidence of Viral Evolution in the Eye. J Virol. 2021 Nov;95(24):e0083321.

[174] Rottstegge M, Tipton T, Oestereich L, Ruibal P, Nelson EV, Olal C, et al. Avatar Mice Underscore the Role of the T Cell-Dendritic Cell Crosstalk in Ebola Virus Disease and Reveal Mechanisms of Protection in Survivors. J Virol. 2022 Sep;96(18):e0057422.

[175] Lüdtke A, Ruibal P, Wozniak DM, Pallasch E, Wurr S, Bockholt S, et al. Ebola virus infection kinetics in chimeric mice reveal a key role of T cells as barriers for virus dissemination. Sci Rep. 2017 Mar;7:43776.

[176] Lüdtke A, Oestereich L, Ruibal P, Wurr S, Pallasch E, Bockholt S, et al. Ebola virus disease in mice with transplanted human hematopoietic stem cells. J Virol. 2015 Apr;89(8):4700-4.

[177] Escudero-Pérez B, Ruibal P, Rottstegge M, Lüdtke A, Port JR, Hartmann K, et al. Comparative pathogenesis of Ebola virus and Reston virus infection in humanized mice. JCI Insight. 2019 Nov;4(21).

[178] Clancy CS, Smart G, Rhoderick JF, O'Donnell KL, Rosenke R, Schäfer A, et al. Establishing a Mouse Model for Sexual Transmission and Male Reproductive Tract Persistence of Ebola Virus. J Infect Dis. 2023 Nov;228:554-8.

[179] Cooper TK, Sword J, Johnson JC, Bonilla A, Hart R, Liu DX, et al. New Insights Into Marburg Virus Disease Pathogenesis in the Rhesus Macaque Model. J Infect Dis. 2018 Nov;218:423-33.

[180] Nakayama E, Saijo M. Animal models for Ebola and Marburg virus infections. Front Microbiol. 2013 Sep;4:267.

[181] Gupta M, Mahanty S, Greer P, Towner JS, Shieh WJ, Zaki SR, et al. Persistent infection with ebola virus under conditions of partial immunity. J Virol. 2004 Jan;78(2):958-67.

[182] Larsen T, Stevens EL, Davis KJ, Geisbert JB, Daddario-DiCaprio KM, Jahrling PB, et al. Pathologic findings associated with delayed death in nonhuman primates experimentally infected with Zaire Ebola virus. J Infect Dis. 2007 Nov;196:323-8.

[183] Liu J, Trefry JC, Babka AM, Schellhase CW, Coffin KM, Williams JA, et al. Ebola virus persistence and disease recrudescence in the brains of antibody-treated nonhuman primate survivors. Sci Transl Med. 2022 Feb;14(631):eabi5229.

[184] Banadyga L, Zhu W, Kailasan S, Howell KA, Franaszek K, He S, et al. Atypical ebola virus disease in a nonhuman primate following monoclonal antibody treatment is associated with glycoprotein mutations within the fusion loop. mBio. 2021;12(1):1-22.

[185] Feldmann H, Geisbert TW. Ebola haemorrhagic fever. The Lancet. 2011;377(9768):849-62.

[186] Schreiber-Stainthorp W, Solomon J, Lee JH, Castro M, Shah S, Martinez-Orengo N, et al. Longitudinal in vivo imaging of acute neuropathology in a monkey model of Ebola virus infection. Nat Commun. 2021 May;12(1):2855.

[187] Qiu X, Wong G, Fernando L, Audet J, Bello A, Strong J, et al. mAbs and Ad-vectored IFN-α therapy rescue Ebola-infected nonhuman primates when administered after the detection of viremia and symptoms. Sci Transl Med. 2013 Oct;5(207):207ra143.

[188] Alves DA, Honko AN, Kortepeter MG, Sun M, Johnson JC, Lugo-Roman LA, et al. Necrotizing Scleritis, Conjunctivitis, and Other Pathologic Findings in the Left Eye and Brain of an Ebola Virus-Infected Rhesus Macaque (Macaca mulatta) With Apparent Recovery and a Delayed Time of Death. J Infect Dis. 2016 Jan;213(1):57-60.

[189] Zeng X, Blancett CD, Koistinen KA, Schellhase CW, Bearss JJ, Radoshitzky SR, et al. Identification and pathological characterization of persistent asymptomatic Ebola virus infection in rhesus monkeys. Nature Microbiology. 2017;2(July):1-11.

[190] Calain P, Monroe MC, Nichol ST. Ebola virus defective interfering particles and persistent infection. Virology. 1999 Sep;262(1):114-28.

[191] Calain P, Roux L, Kolakofsky D. Defective interfering genomes and Ebola virus persistence. The Lancet. 2016;388(10045):659-60.

[192] Johnson RI, Boczkowska B, Alfson K, Weary T, Menzie H, Delgado J, et al. Identification and Characterization of Defective Viral Genomes in Ebola Virus-Infected Rhesus Macaques. J Virol. 2021 Aug;95(17):e0071421.

[193] Vignuzzi M, López CB. Defective viral genomes are key drivers of the virus-host interaction. Nat Microbiol. 2019 Jul;4(7):1075-87.

[194] Smither SJ, Garcia-Dorival I, Eastaugh L, Findlay JS, O'Brien LM, Carruthers J, et al. An Investigation of the Effect of Transfected Defective, Ebola Virus Genomes on Ebola Replication. Front Cell Infect Microbiol. 2020;10:159.

[195] Webb AL, Schindell BG, Soule G, Siddik AB, Abrenica B, Memon H, et al. Characterizing changes in transcriptome and kinome responses in testicular cells during infection by Ebola virus. npj Viruses. 2024 Apr;2(12).

[196] Oliver GF, Orang AV, Appukuttan B, Marri S, Michael MZ, Marsh GA, et al. Expression of microRNA in human retinal pigment epithelial cells following infection with Zaire ebolavirus. BMC Research Notes. 2019;12(1):1-7.

[197] Garry RF. Lassa fever - the road ahead. Nat Rev Microbiol. 2023 Feb;21(2):87-96.

[198] Günther S, Lenz O. Lassa virus. Crit Rev Clin Lab Sci. 2004;41(4):339-90.

[199] Okokhere P, Colubri A, Azubike C, Iruolagbe C, Osazuwa O, Tabrizi S, et al. Clinical and laboratory predictors of Lassa fever outcome in a dedicated treatment facility in Nigeria: a retrospective, observational cohort study. Lancet Infect Dis. 2018 Jun;18(6):684-95.

[200] Monath TP, Newhouse VF, Kemp GE, Setzer HW, Cacciapuoti A. Lassa virus isolation from Mastomys natalensis rodents during an epidemic in Sierra Leone. Science. 1974 Jul;185(4147):263-5.

[201] Fichet-Calvet E, Becker-Ziaja B, Koivogui L, Günther S. Lassa serology in natural populations of rodents and horizontal transmission. Vector Borne Zoonotic Dis. 2014 Sep;14(9):665-74.

[202] Fichet-Calvet E, Lecompte E, Koivogui L, Daffis S, ter Meulen J. Reproductive characteristics of Mastomys natalensis and Lassa virus prevalence in Guinea, West Africa. Vector Borne Zoonotic Dis. 2008;8(1):41-8.

[203] Hoffmann C, Krasemann S, Wurr S, Hartmann K, Pallasch E, Bockholt S, et al. Lassa virus persistence with high viral titers following experimental infection in its natural reservoir host, Mastomys natalensis. PREPRINT Version 1 on Research Square. Accessed: 04-04-2024. Available from: https://doi.org/10.21203/rs.3.rs-4157727/v1.

[204] Thielebein A, Ighodalo Y, Taju A, Olokor T, Omiunu R, Esumeh R, et al. Virus persistence after recovery from acute Lassa fever in Nigeria: a 2-year interim analysis of a prospective longitudinal cohort study. Lancet Microbe. 2022 Jan;3(1):e32-40.

[205] Okokhere PO, Bankole IA, Iruolagbe CO, Muoebonam BE, Okonofua MO, Dawodu SO, et al. Aseptic Meningitis Caused by Lassa Virus: Case Series Report. Case Rep Neurol Med. 2016;2016:1978461.

[206] Okohere PO, Akpede GO. Central nervous system manifestations of lassa fever in Nigeria and the effect on martality. Journal of the Neurological Sciences. 2017;333(e604).

[207] Günther S, Weisner B, Roth A, Grewing T, Asper M, Drosten C, et al. Lassa fever encephalopathy: Lassa virus in cerebrospinal fluid but not in serum. J Infect Dis. 2001 Aug;184(3):345-9.

[208] Cummins D, Bennett D, Fisher-Hoch SP, Farrar B, Machin SJ, McCormick JB. Lassa fever encephalopathy: clinical and laboratory findings. J Trop Med Hyg. 1992 Jun;95(3):197-201.

[209] Johnson KM, McCormick JB, Webb PA, Smith ES, Elliott LH, King IJ. Clinical virology of Lassa fever in hospitalized patients. J Infect Dis. 1987 Mar;155(3):456-64.

[210] Duvignaud A, Doutchi M, Abejegah C, Etafo I, Jaspard M, Serra B, et al. Delayed-onset paraparesis in Lassa fever: A case report. Int J Infect Dis. 2020 Mar;92:49-52.

[211] Ezeomah C, Adoga A, Ihekweazu C, Paessler S, Cisneros I, Tomori O, et al. Sequelae of Lassa Fever: Postviral Cerebellar Ataxia. Open Forum Infect Dis. 2019 Dec;6(12):ofz512.

[212] Li AL, Grant D, Gbakie M, Kanneh L, Mustafa I, Bond N, et al. Ophthalmic manifestations and vision impairment in Lassa fever survivors. PLoS One. 2020;15(12):e0243766.

[213] Penisson M, Ladewig J, Belvindrah R, Francis F. Genes and Mechanisms Involved in the Generation and Amplification of Basal Radial Glial Cells. Front Cell Neurosci. 2019;13:381.

[214] Lancaster MA, Renner M, Martin CA, Wenzel D, Bicknell LS, Hurles ME, et al. Cerebral organoids model human brain development and microcephaly. Nature. 2013;501(7467):373-9.

[215] Markey KM, Saunders JC, Smuts J, von Reyn CR, Garcia ADR. Astrocyte development-More questions than answers. Front Cell Dev Biol. 2023;11:1063843.

[216] Lawrence JM, Schardien K, Wigdahl B, Nonnemacher MR. Roles of neuropathology-associated reactive astrocytes: a systematic review. Acta Neuropathol Commun. 2023 Mar;11(1):42.

[217] Ormel PR, Vieira de Sá R, van Bodegraven EJ, Karst H, Harschnitz O, Sneeboer MAM, et al. Microglia innately develop within cerebral organoids. Nature Communications. 2018;9(1).

[218] Qian X, Song H, Ming GL. Brain organoids: advances, applications and challenges. Development. 2019 Apr;146(8).

[219] Hattori Y. The behavior and functions of embryonic microglia. Anat Sci Int. 2022 Jan;97(1):1-14.

[220] Du P, Wu J. Hallmarks of totipotent and pluripotent stem cell states. Cell Stem Cell. 2024 Mar;31(3):312-33.

[221] Beumer J, Clevers H. Hallmarks of stemness in mammalian tissues. Cell Stem Cell. 2024 Jan;31(1):7-24.

[222] Englund C, Fink A, Lau C, Pham D, Daza RA, Bulfone A, et al. Pax6, Tbr2, and Tbr1 are expressed sequentially by radial glia, intermediate progenitor cells, and postmitotic neurons in developing neocortex. J Neurosci. 2005 Jan;25(1):247-51.

[223] Pellegrini L, Bonfio C, Chadwick J, Begum F, Skehel M, Lancaster MA. Human CNS barrier-forming organoids with cerebrospinal fluid production. Science. 2020 Jul;369(6500).

[224] Lun MP, Monuki ES, Lehtinen MK. Development and functions of the choroid plexus-cerebrospinal fluid system. Nat Rev Neurosci. 2015 Aug;16(8):445-57.

[225] Chiavari M, Ciotti GMP, Navarra P, Lisi L. Pro-inflammatory activation of a new immortalized human microglia cell line. Brain Sciences. 2019;9(5).

[226] Ryan KJ, White CC, Patel K, Xu J, Olah M, Replogle JM, et al. A human microglia-like cellular model for assessing the effects of neurodegenerative disease gene variants. Science Translational Medicine. 2017;9(421):1-13.

[227] Hoenen T, Groseth A, Callison J, Takada A, Feldmann H. A novel Ebola virus expressing luciferase allows for rapid and quantitative testing of antivirals. Antiviral Res. 2013 Sep;99(3):207-13.

[228] Lecompte E, Fichet-Calvet E, Daffis S, Koulémou K, Sylla O, Kourouma F, et al. Mastomys natalensis and Lassa fever, West Africa. Emerg Infect Dis. 2006 Dec;12(12):1971-4.

[229] Hufert FT, Lüdke W, Schmitz H. Epitope mapping of the Lassa virus nucleoprotein using monoclonal anti-nucleocapsid antibodies. Arch Virol. 1989;106(3-4):201-12.

[230] Amanat F, Duehr J, Oestereich L, Hastie KM, Ollmann Saphire E, Krammer F. Antibodies to the Glycoprotein GP2 Subunit Cross-React between Old and New World Arenaviruses. mSphere. 2018;3(3).

[231] Rueden CT, Schindelin J, Hiner MC, DeZonia BE, Walter AE, Arena ET, et al. ImageJ2: ImageJ for the next generation of scientific image data. BMC Bioinformatics. 2017 Nov;18(1):529.

[232] Chen Y, Chen Y, Shi C, Huang Z, Zhang Y, Li S, et al. SOAPnuke: a MapReduce acceleration-supported software for integrated quality control and preprocessing of high-throughput sequencing data. Gigascience. 2018 Jan;7(1):1-6.

[233] Afgan E, Baker D, Batut B, van den Beek M, Bouvier D, Cech M, et al. The Galaxy platform for accessible, reproducible and collaborative biomedical analyses: 2018 update. Nucleic Acids Res. 2018 Jul;46(W1):W537-44.

[234] Afgan E, Nekrutenko A, Grüning BA, Blankenberg D, Goecks J, Schatz MC, et al. The Galaxy platform for accessible, reproducible and collaborative biomedical analyses: 2022 update. Nucleic Acids Res. 2022 Apr;50(W1):W345-51.

[235] Bolger AM, Lohse M, Usadel B. Trimmomatic: a flexible trimmer for Illumina sequence data. Bioinformatics. 2014 Aug;30(15):2114-20.

[236] Andrews, S. (n.d.).FastQC A Quality Control tool for High Throughput Sequence Data.;. Accessed: February 2023. Available from: http://www.bioinformatics.babraham.ac.uk/projects/fastqc/.

[237] Dobin A, Davis CA, Schlesinger F, Drenkow J, Zaleski C, Jha S, et al. STAR: ultrafast universal RNA-seq aligner. Bioinformatics. 2013 Jan;29(1):15-21.

[238] Li H, Handsaker B, Wysoker A, Fennell T, Ruan J, Homer N, et al. The Sequence Alignment/Map format and SAMtools. Bioinformatics. 2009 Aug;25(16):2078-9.

[239] AnnotateMyIDs, Dunning M.;. Accessed: February 2023. Available from: https://github.com/markdunning/galaxy-annotateMyIDs.

[240] Liu R, Holik AZ, Su S, Jansz N, Chen K, Leong HS, et al. Why weight? Modelling sample and observational level variability improves power in RNA-seq analyses. Nucleic Acids Res. 2015 Sep;43(15):e97.

[241] Smyth GK. In: Gentleman R, Carey VJ, Huber W, Irizarry RA, Dudoit S, editors. limma: Linear Models for Microarray Data. New York, NY: Springer New York; 2005. p. 397-420.

[242] Ritchie ME, Diyagama D, Neilson J, van Laar R, Dobrovic A, Holloway A, et al. Empirical array quality weights in the analysis of microarray data. BMC Bioinformatics. 2006 May;7:261.

[243] Law CW, Chen Y, Shi W, Smyth GK. voom: Precision weights unlock linear model analysis tools for RNA-seq read counts. Genome Biol. 2014 Feb;15(2):R29.

[244] Robinson MD, Smyth GK. Moderated statistical tests for assessing differences in tag abundance. Bioinformatics. 2007 Nov;23(21):2881-7.

[245] Robinson MD, Smyth GK. Small-sample estimation of negative binomial dispersion, with applications to SAGE data. Biostatistics. 2008 Apr;9(2):321-32.

[246] Robinson MD, McCarthy DJ, Smyth GK. edgeR: a Bioconductor package for differential expression analysis of digital gene expression data. Bioinformatics. 2010 Jan;26(1):139-40.

[247] McCarthy DJ, Chen Y, Smyth GK. Differential expression analysis of multifactor RNA-Seq experiments with respect to biological variation. Nucleic Acids Res. 2012 May;40(10):4288-97.

[248] Ge SX, Son EW, Yao R. iDEP: an integrated web application for differential expression and pathway analysis of RNA-Seq data. BMC Bioinformatics. 2018 Dec;19(1):534.

[249] Thomas PD, Ebert D, Muruganujan A, Mushayahama T, Albou LP, Mi H. PANTHER: Making genome-scale phylogenetics accessible to all. Protein Sci. 2022 Jan;31(1):8-22.

[250] Ge SX, Jung D, Yao R. ShinyGO: a graphical gene-set enrichment tool for animals and plants. Bioinformatics. 2020 Apr;36(8):2628-9.

[251] Langmead B, Salzberg SL. Fast gapped-read alignment with Bowtie 2. Nat Methods. 2012 Mar;9(4):357-9.

[252] Castellano S, Cestari F, Faglioni G, Tenedini E, Marino M, Artuso L, et al. iVar, an Interpretation-Oriented Tool to Manage the Update and Revision of Variant Annotation and Classification. Genes (Basel). 2021 Mar;12(3).

[253] Chua KB, Bellini WJ, Rota PA, Harcourt BH, Tamin A, Lam SK, et al. Nipah virus: a recently emergent deadly paramyxovirus. Science. 2000 May;288(5470):1432-5.

[254] Guenther S, Weisner B, Roth A, Grewing T, Asper M, Drosten C, et al. Lassa fever encephalopathy: Lassa virus in cerebrospinal fluid but not in serum. J Infect Dis. 2001 Aug;184(3):345-9.

[255] Niemetz L, Bodmer BS, Olal C, Escudero-Pérez B, Hoeh K, Bencsik A, et al. Ebola virus infection of Flt3-dependent, conventional dendritic cells and antigen cross-presentation leads to high levels of T-cell activation. PREPRINT Version 1 on BioRxiv. Accessed: 09-06-2024.

[256] Grünvogel O, Esser-Nobis K, Windisch MP, Frese M, Trippler M, Bartenschlager R, et al. Type I and type II interferon responses in two human liver cell lines (Huh-7 and HuH6). Genom Data. 2016 Mar;7:166-70.

[257] Shabman RS, Jabado OJ, Mire CE, Stockwell TB, Edwards M, Mahajan M, et al. Deep sequencing identifies noncanonical editing of Ebola and Marburg virus RNAs in infected cells. mBio. 2014 Nov;5(6):e02011.

[258] Lancaster MA, Corsini NS, Wolfinger S, Gustafson EH, Phillips AW, Burkard TR, et al. Guided self-organization and cortical plate formation in human brain organoids. Nat Biotechnol. 2017 Jul;35(7):659-66.

[259] Chehelgerdi M, Behdarvand Dehkordi F, Kabiri H, Salehian-Dehkordi H, Abdolvand M, Salmanizadeh S, et al. Exploring the promising potential of induced pluripotent stem cells in cancer research and therapy. Mol Cancer. 2023 Nov;22(1):189.

[260] Kyttälä A, Moraghebi R, Valensisi C, Kettunen J, Andrus C, Pasumarthy KK, et al. Genetic Variability Overrides the Impact of Parental Cell Type and Determines iPSC Differentiation Potential. Stem Cell Reports. 2016 Feb;6(2):200-12.

[261] Takahashi K, Yamanaka S. Induction of pluripotent stem cells from mouse embryonic and adult fibroblast cultures by defined factors. Cell. 2006 Aug;126(4):663-76.

[262] Frobel J, Hemeda H, Lenz M, Abagnale G, Joussen S, Denecke B, et al. Epigenetic rejuvenation of mesenchymal stromal cells derived from induced pluripotent stem cells. Stem Cell Reports. 2014 Sep;3(3):414-22.

[263] Zhang B, He Y, Xu Y, Mo F, Mi T, Shen QS, et al. Differential antiviral immunity to Japanese encephalitis virus in developing cortical organoids. Cell Death Dis. 2018 Jun;9(7):719.

[264] Qian X, Nguyen HN, Song MM, Hadiono C, Ogden SC, Hammack C, et al. Brain-Region-Specific Organoids Using Mini-bioreactors for Modeling ZIKV Exposure. Cell. 2016 May;165(5):1238-54.

[265] Sabate-Soler S, Nickels SL, Saraiva C, Berger E, Dubonyte U, Barmpa K, et al. Microglia integration into human midbrain organoids leads to increased neuronal maturation and functionality. Glia. 2022 Jul;70(7):1267-88.

[266] Ginhoux F, Greter M, Leboeuf M, Nandi S, See P, Gokhan S, et al. Primitive Macrophages. Science. 2010;701(November):841-5.

[267] Muffat J, Li Y, Yuan B, Mitalipova M, Omer A, Corcoran S, et al. Efficient derivation of microglia-like cells from human pluripotent stem cells. Nat Med. 2016 Nov;22(11):1358-67.

[268] Abud EM, Ramirez RN, Martinez ES, Healy LM, Nguyen CHH, Newman SA, et al. iPSC-Derived Human Microglia-like Cells to Study Neurological Diseases. Neuron. 2017 Apr;94(2):278-93.

[269] Chichagova V, Georgiou M, Carter M, Dorgau B, Hilgen G, Collin J, et al. Incorporating microglia-like cells in human induced pluripotent stem cell-derived retinal organoids. J Cell Mol Med. 2023 Feb;27(3):435-45.

[270] Ansari AM, Ahmed AK, Matsangos AE, Lay F, Born LJ, Marti G, et al. Cellular GFP Toxicity and Immunogenicity: Potential Confounders in in Vivo Cell Tracking Experiments. Stem Cell Rev Rep. 2016 Oct;12(5):553-9.

[271] Liu HS, Jan MS, Chou CK, Chen PH, Ke NJ. Is green fluorescent protein toxic to the living cells? Biochem Biophys Res Commun. 1999 Jul;260(3):712-7.

[272] Ganini D, Leinisch F, Kumar A, Jiang J, Tokar EJ, Malone CC, et al. Fluorescent proteins such as eGFP lead to catalytic oxidative stress in cells. Redox Biol. 2017 Aug;12:462-8.

[273] Lukashevich IS, Mar'iankova RF, Fidarov FM. Acute and chronic Lassa virus infection of Vero cells. Vopr Virusol. 1981;(4):452-6.

[274] Hans A, Syan S, Crosio C, Sassone-Corsi P, Brahic M, Gonzalez-Dunia D. Borna disease virus persistent infection activates mitogen-activated protein kinase and blocks neuronal differentiation of PC12 cells. J Biol Chem. 2001 Mar;276(10):7258-65.

[275] Lannes N, Garcia-Nicolàs O, Démoulins T, Summerfield A, Filgueira L. CX 3 CR1-CX 3 CL1-dependent cell-to-cell Japanese encephalitis virus transmission by human microglial cells. Scientific Reports. 2019;9(1):1-13.

[276] Monferrer A, Kretzmann JA, Sigl C, Sapelza P, Liedl A, Wittmann B, et al. Broad-Spectrum Virus Trapping with Heparan Sulfate-Modified DNA Origami Shells. ACS Nano. 2022 Dec;16(12):20002-9.

[277] Monferrer A, Kohler F, Sigl C, Schachtner M, Peterhoff D, Asbach B, et al. DNA origami traps for large viruses. Cell Reports Physical Science. 2023;4(1):101237.

[278] Zeng YC, Young OJ, Si L, Ku MW, Isinelli G, Rajwar A, et al. DNA origami vaccine (DoriVac) nanoparticles improve both humoral and cellular immune responses to infectious diseases. PREPRINT available from bioRxiv. 2024. Available from: https://www.biorxiv.org/content/early/2024/01/02/2023.12.29.573647.full.pdf.

[279] Forrester JV, Xu H, Lambe T, Cornall R. Immune privilege or privileged immunity? Mucosal Immunol. 2008 Sep;1(5):372-81.

[280] McElroy AK, Harmon JR, Flietstra TD, Campbell S, Mehta AK, Kraft CS, et al. Kinetic Analysis of Biomarkers in a Cohort of US Patients With Ebola Virus Disease. Clin Infect Dis. 2016 Aug;63(4):460-7.

[281] Wang Y, Szretter KJ, Vermi W, Gilfillan S, Rossini C, Cella M, et al. IL-34 is a tissue-restricted ligand of CSF1R required for the development of Langerhans cells and microglia. Nat Immunol. 2012 Jun;13(8):753-60.

[282] Sellgren CM, Sheridan SD, Gracias J, Xuan D, Fu T, Perlis RH. Patient-specific models of microglia-mediated engulfment of synapses and neural progenitors. Mol Psychiatry. 2017 Feb;22(2):170-7.

[283] Ohgidani M, Kato TA, Setoyama D, Sagata N, Hashimoto R, Shigenobu K, et al. Direct induction of ramified microglia-like cells from human monocytes: dynamic microglial dysfunction in Nasu-Hakola disease. Sci Rep. 2014 May;4:4957.

[284] Wool-Lewis RJ, Bates P. Characterization of Ebola virus entry by using pseudotyped viruses: identification of receptor-deficient cell lines. J Virol. 1998 Apr;72(4):3155-60.

[285] Gao J, Guo Z, Li W, Zhang X, Zhang XE, Cui Z. Ebola virus disrupts the inner blood-retinal barrier by induction of vascular endothelial growth factor in pericytes. PLoS Pathog. 2023 Jan;19(1):e1011077.

[286] Zapatero-Belinchón FJ, Dietzel E, Dolnik O, Döhhner K, Costa R, Hertel B, et al. Characterization of the Filovirus-Resistant Cell Line SH-SY5Y Reveals Redundant Role of Cell Surface Entry Factors. Viruses. 2019 Mar;11(3).

[287] Kovalevich J, Langford D. Considerations for the use of SH-SY5Y neuroblastoma cells in neurobiology. Methods Mol Biol. 2013;1078:9-21.

[288] Smith JR, Todd S, Ashander LM, Charitou T, Ma Y, Yeh S, et al. Retinal Pigment Epithelial Cells are a Potential Reservoir for Ebola Virus in the Human Eye. Transl Vis Sci Technol. 2017 Jul;6(4):12.

[289] Strong JE, Wong G, Jones SE, Grolla A, Theriault S, Kobinger GP, et al. Stimulation of Ebola virus production from persistent infection through activation of the Ras/MAPK pathway. Proc Natl Acad Sci U S A. 2008 Nov;105(46):17982-7.

[290] Bokelmann M, Vogel U, Debeljak F, Düx A, Riesle-Sbarbaro S, Lander A, et al. Tolerance and persistence of ebola virus in primary cells from mops condylurus, a potential ebola virus reservoir. Viruses. 2021 Oct;13(11).

[291] Whitfield ZJ, Prasad AN, Ronk AJ, Kuzmin IV, Ilinykh PA, Andino R, et al. Species-Specific Evolution of Ebola Virus during Replication in Human and Bat Cells. Cell Rep. 2020 Aug;32(7):108028.

[292] Jayaprakash AD, Ronk AJ, Prasad AN, Covington MF, Stein KR, Schwarz TM, et al. Marburg and Ebola Virus Infections Elicit a Complex, Muted Inflammatory State in Bats. Viruses. 2023 Jan;15(2).

[293] Kuzmin IV, Schwarz TM, Ilinykh PA, Jordan I, Ksiazek TG, Sachidanandam R, et al. Innate Immune Responses of Bat and Human Cells to Filoviruses: Commonalities and Distinctions. J Virol. 2017 Apr;91(8).

[294] Castellani G, Croese T, Peralta Ramos JM, Schwartz M. Transforming the understanding of brain immunity. Science. 2023 Apr;380(6640):eabo7649.

[295] Chang TH, Kubota T, Matsuoka M, Jones S, Bradfute SB, Bray M, et al. Ebola Zaire virus blocks type I interferon production by exploiting the host SUMO modification machinery. PLoS Pathog. 2009 Jun;5(6):e1000493.

[296] Sawyer SL, Emerman M, Malik HS. Discordant evolution of the adjacent antiretroviral genes TRIM22 and TRIM5 in mammals. PLoS Pathog. 2007 Dec;3(12):e197.

[297] Fernandes AP, gueda Pinto A, Pinheiro A, Rebelo H, Esteves PJ. Evolution of TRIM5 and TRIM22 in Bats Reveals a Complex Duplication Process. Viruses. 2022 Feb;14(2).

[298] Schäfer A, Marzi A, Furuyama W, Catanzaro NJ, Nguyen C, Haddock E, et al. Mapping of susceptibility loci for Ebola virus pathogenesis in mice. Cell Rep. 2024 May;43(5):114127.

[299] Okumura A, Pitha PM, Harty RN. ISG15 inhibits Ebola VP40 VLP budding in an L-domain-dependent manner by blocking Nedd4 ligase activity. Proc Natl Acad Sci U S A. 2008 Mar;105(10):3974-9.

[300] Malakhov MP, Malakhova OA, Kim KI, Ritchie KJ, Zhang DE. UBP43 (USP18) specifically removes ISG15 from conjugated proteins. J Biol Chem. 2002 Mar;277(12):9976-81.

[301] Brinkmann C, Nehlmeier I, Walendy-Gnirß K, Nehls J, González Hernández M, Hoffmann M, et al. The Tetherin Antagonism of the Ebola Virus Glycoprotein Requires an Intact Receptor-Binding Domain and Can Be Blocked by GP1-Specific Antibodies. Journal of Virology. 2016;90(24):11075-86.

[302] González-Hernández M, Hoffmann M, Brinkmann C, Nehls J, Winkler M, Schindler M, et al. A GXXXA Motif in the Transmembrane Domain of the Ebola Virus Glycoprotein Is Required for Tetherin Antagonism. Journal of Virology. 2018;92(13):1-12.

[303] Peters K, Chattopadhyay S, Sen GC. IRF-3 activation by Sendai virus infection is required for cellular apoptosis and avoidance of persistence. J Virol. 2008 Apr;82(7):3500-8.

[304] Martinez O, Johnson JC, Honko A, Yen B, Shabman RS, Hensley LE, et al. Ebola Virus Exploits a Monocyte Differentiation Program To Promote Its Entry. Journal of Virology. 2013;87(7):3801-14.

[305] Doi T, Kwon HJ, Honda T, Sato H, Yoneda M, Kai C. Measles virus induces persistent infection by autoregulation of viral replication. Sci Rep. 2016 Nov;6:37163.

[306] Watanabe S, Noda T, Halfmann P, Jasenosky L, Kawaoka Y. Ebola virus (EBOV) VP24 inhibits transcription and replication of the EBOV genome. J Infect Dis. 2007 Nov;196 Suppl 2:S284-90.

[307] Sato Y, Watanabe S, Fukuda Y, Hashiguchi T, Yanagi Y, Ohno S. Cell-to-Cell Measles Virus Spread between Human Neurons Is Dependent on Hemagglutinin and Hyper-fusogenic Fusion Protein. J Virol. 2018 Mar;92(6).

[308] Griffin DE. Measles virus persistence and its consequences. Curr Opin Virol. 2020 Apr;41:46-51.

[309] Robinzon S, Dafa-Berger A, Dyer MD, Paeper B, Proll SC, Teal TH, et al. Impaired cholesterol biosynthesis in a neuronal cell line persistently infected with measles virus. J Virol. 2009 Jun;83(11):5495-504.

[310] Harrison JK, Jiang Y, Chen S, Xia Y, Maciejewski D, McNamara RK, et al. Role for neuronally derived fractalkine in mediating interactions between neurons and CX3CR1-expressing microglia. Proc Natl Acad Sci U S A. 1998 Sep;95(18):10896-901.

[311] Lee M, Lee Y, Song J, Lee J, Chang SY. CR1 Expressing Immune Cells and Their Relationships with Human Disease. Immune Netw. 2018 Feb;18(1):e5.

[312] Lannes N, Neuhaus V, Scolari B, Kharoubi-Hess S, Walch M, Summerfield A, et al. Interactions of human microglia cells with Japanese encephalitis virus. Virol J. 2017 Jan;14(1):8.

[313] Xu J, Sun Y, Li Y, Ruthel G, Weiss SR, Raj A, et al. Replication defective viral genomes exploit a cellular pro-survival mechanism to establish paramyxovirus persistence. Nat Commun. 2017 Oct;8(1):799.

[314] Johnson DM, Cubitt B, Pfeffer TL, de la Torre JC, Lukashevich IS. Lassa Virus Vaccine Candidate ML29 Generates Truncated Viral RNAs Which Contribute to Interfering Activity and Attenuation. Viruses. 2021 Jan;13(2).

[315] Johnson DM, Jokinen JD, Lukashevich IS. Mice. Pathogens. 2019 Jan;8(1).

[316] Young DF, Wignall-Fleming EB, Busse DC, Pickin MJ, Hankinson J, Randall EM, et al. The switch between acute and persistent paramyxovirus infection caused by single amino acid substitutions in the RNA polymerase P subunit. PLoS Pathog. 2019 02;15(2):e1007561.

[317] Kirchdoerfer RN, Moyer CL, Abelson DM, Saphire EO. The Ebola Virus VP30-NP Interaction Is a Regulator of Viral RNA Synthesis. PLoS Pathog. 2016 Oct;12(10):e1005937.

[318] Gilchuk P, Murin CD, Milligan JC, Cross RW, Mire CE, Ilinykh PA, et al. Analysis of a Therapeutic Antibody Cocktail Reveals Determinants for Cooperative and Broad Ebolavirus Neutralization. Immunity. 2020 Feb;52(2):388-403.

[319] Peng Q, Yuan B, Cheng J, Wang M, Gao S, Bai S, et al. Molecular mechanism of de novo replication by the Ebola virus polymerase. Nature. 2023 Oct;622(7983):603-10.

[320] Yuan B, Peng Q, Cheng J, Wang M, Zhong J, Qi J, et al. Structure of the Ebola virus polymerase complex. Nature. 2022 Oct;610(7931):394-401.

[321] Di Palma F, Daino GL, Ramaswamy VK, Corona A, Frau A, Fanunza E, et al. Relevance of Ebola virus VP35 homo-dimerization on the type I interferon cascade inhibition. Antivir Chem Chemother. 2019;27:2040206619889220.

[322] Mateo M, Carbonnelle C, Reynard O, Kolesnikova L, Nemirov K, Page A, et al. VP24 is a molecular determinant of Ebola virus virulence in guinea pigs. J Infect Dis. 2011 Nov;204 Suppl 3:S1011-20.

[323] Subbotina E, Dadaeva A, Kachko A, Chepurnov A. Genetic factors of Ebola virus virulence in guinea pigs. Virus Res. 2010 Oct;153(1):121-33.

[324] Ramanathan P, Tigabu B, Santos RI, Ilinykh PA, Kuzmina N, Vogel OA, et al. Ebolavirus Species-Specific Interferon Antagonism Mediated by VP24. Viruses. 2023 Apr;15(5).

[325] Xu W, Edwards MR, Borek DM, Feagins AR, Mittal A, Alinger JB, et al. Ebola virus VP24 targets a unique NLS binding site on karyopherin alpha 5 to selectively compete with nuclear import of phosphorylated STAT1. Cell Host Microbe. 2014 Aug;16(2):187-200.

[326] Schwarz TM, Edwards MR, Diederichs A, Alinger JB, Leung DW, Amarasinghe GK, et al. VP24-Karyopherin Alpha Binding Affinities Differ between Ebolavirus Species, Influencing Interferon Inhibition and VP24 Stability. J Virol. 2017 Feb;91(4).

[327] Xu W, Luthra P, Wu C, Batra J, Leung DW, Basler CF, et al. Ebola virus VP30 and nucleoprotein interactions modulate viral RNA synthesis. Nat Commun. 2017 Jun;8:15576.

[328] Chen J, He Z, Yuan Y, Huang F, Luo B, Zhang J, et al. Host factor SMYD3 is recruited by Ebola virus nucleoprotein to facilitate viral mRNA transcription. Emerg Microbes Infect. 2019;8(1):1347-60.

[329] Chen EC, Gilchuk P, Zost SJ, Ilinykh PA, Binshtein E, Huang K, et al. Systematic analysis of human antibody response to ebolavirus glycoprotein shows high prevalence of neutralizing public clonotypes. Cell Rep. 2023 Apr;42(4):112370.

[330] Lennemann NJ, Rhein BA, Ndungo E, Chandran K, Qiu X, Maury W. Comprehensive functional analysis of N-linked glycans on Ebola virus GP1. mBio. 2014 Jan;5(1):e00862-13.

[331] Hoenen T, Watt A, Mora A, Feldmann H. Modeling the lifecycle of ebola virus under biosafety level 2 conditions with virus-like particles containing tetracistronic minigenomes. Journal of Visualized Experiments. 2014;(91):1-10.

[332] Keegan LP, Hajji K, O'Connell MA. Adenosine Deaminase Acting on RNA (ADAR) Enzymes: A Journey from Weird to Wondrous. Acc Chem Res. 2023 Nov;56(22):3165-74.

[333] Munnur D, Bartlett E, Mikolcević P, Kirby IT, Rack JGM, Mikoč A, et al. Reversible ADP-ribosylation of RNA. Nucleic Acids Res. 2019 Jun;47(11):5658-69.

[334] Weixler L, Feijs KLH, Zaja R. ADP-ribosylation of RNA in mammalian cells is mediated by TRPT1 and multiple PARPs. Nucleic Acids Res. 2022 Sep;50(16):9426-41.

[335] Atasheva S, Frolova EI, Frolov I. Interferon-stimulated poly(ADP-Ribose) polymerases are potent inhibitors of cellular translation and virus replication. J Virol. 2014 Feb;88(4):2116-30.

[336] Khadka S, Williams CG, Sweeney-Gibbons J, Basler CF. Marburg and Ebola Virus mRNA 3' Untranslated Regions Contain Negative Regulators of Translation That Are Modulated by ADAR1 Editing. J Virol. 2021 Sep;95(19):e0065221.

[337] Yanai M, Kojima S, Sakai M, Komorizono R, Tomonaga K, Makino A. ADAR2 Is Involved in Self and Nonself Recognition of Borna Disease Virus Genomic RNA in the Nucleus. J Virol. 2020 Feb;94(6).

[338] Salter JD, Bennett RP, Smith HC. The APOBEC Protein Family: United by Structure, Divergent in Function. Trends Biochem Sci. 2016 Jul;41(7):578-94.

[339] Song J, Bang S, Choi N, Kim HN. Brain organoid-on-a-chip: A next-generation human brain avatar for recapitulating human brain physiology and pathology. Biomicrofluidics. 2022 Dec;16(6):061301.

[340] Nair AL, Groenendijk L, Overdevest R, Fowke TM, Annida R, Mocellin O, et al. Human BBB-on-a-chip reveals barrier disruption, endothelial inflammation, and T cell migration under neuroinflammatory conditions. Front Mol Neurosci. 2023;16:1250123.

10 Appendix

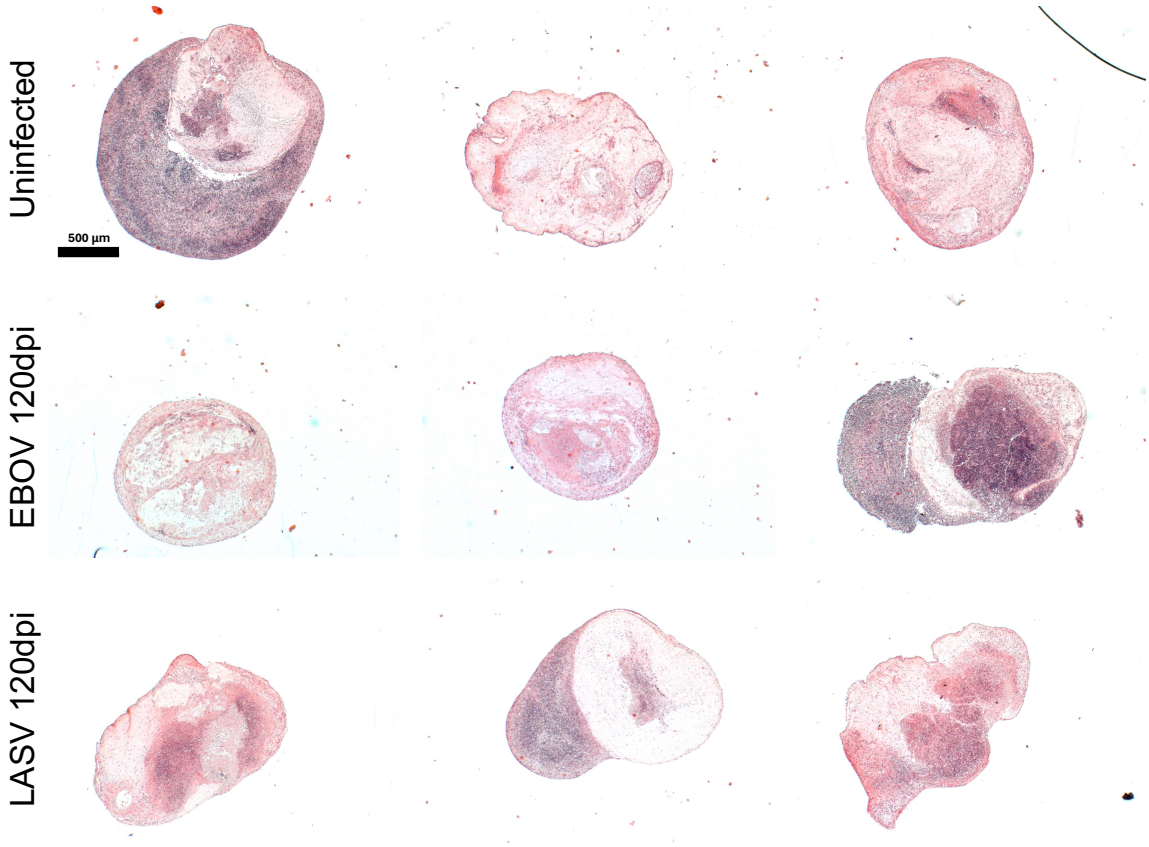


Figure 81: HE staining of 220 days old cerebral organoids. HE staining of three representative human cerebral organoids cultured for 220 days (120 without shaking), either uninfected, EBOV-infected, or LASV-infected for 120 days. The scale bar indicates 500 µm.

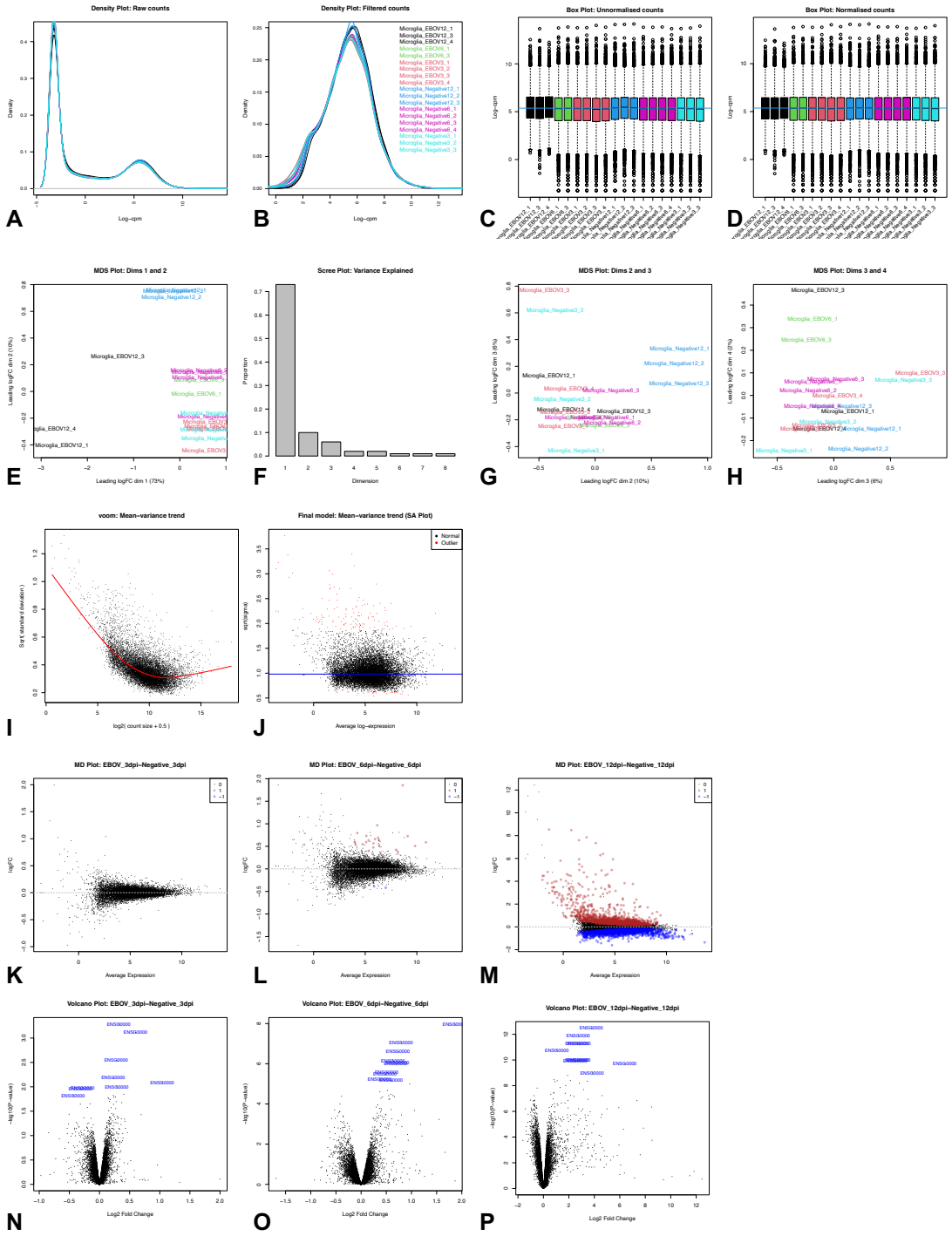


Figure 82: Transcriptome analysis microglia 3, 6, 12dpi: supplementary data limma-voom. **(A)** density plot of raw counts, **(B)** density plot of filtered counts ($\geq$5 counts per million reads in n=3 samples), **(C)** box plot of unnormalized counts, **(D)** boxplot of normalized counts, **(E)** MDS plot of dimension 1 and 2, **(F)** scree plot explaining variance, **(G)** MDS plot of dimension 2 and 3, **(H)** MDS plot of dimension 3 and 4, **(I)** mean-variance trend, **(J)** mean-variance trend of the final model (SA-plot), **(K)** MD plot of significantly up-/downregulated genes in microglia infected with EBOV 3dpi (Log2FC versus average expression), **(L)** MD plot of significantly up-/downregulated genes in microglia infected with EBOV 6dpi (Log2FC versus average expression), **(M)** MD plot of significantly up-/downregulated genes in microglia infected with EBOV 12dpi (Log2FC versus average expression), **(N)** volcano plot of significantly up-/downregulated genes in microglia infected with EBOV 3dpi (log10 p-adjusted versus Log2FC), **(O)** volcano plot of significantly up-/downregulated genes in microglia infected with EBOV 6dpi (log10 p-adjusted versus Log2FC), **(P)** volcano plot of significantly up-/downregulated genes in microglia infected with EBOV 12dpi (log10 p-adjusted versus Log2FC).

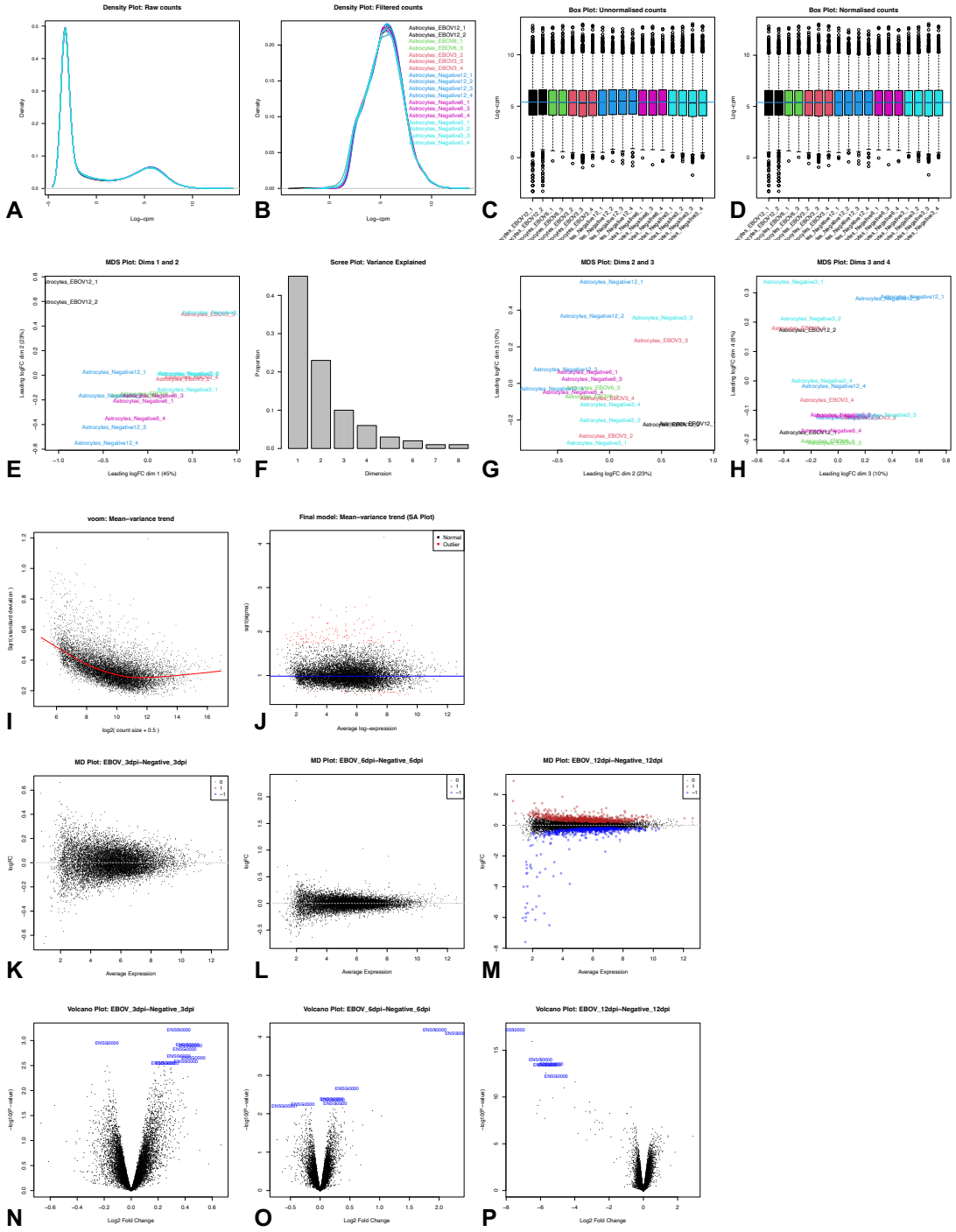


Figure 83: Transcriptome analysis astrocytes 3, 6, 12dpi: supplementary data limma-voom. (A) density plot of raw counts, **(B)** density plot of filtered counts ($\geq$5 counts per million reads in n=3 samples), **(C)** box plot of unnormalized counts, **(D)** boxplot of normalized counts, **(E)** MDS plot of dimension 1 and 2, **(F)** scree plot explaining variance, **(G)** MDS plot of dimension 2 and 3, **(H)** MDS plot of dimension 3 and 4, **(I)** mean-variance trend, **(J)** mean-variance trend of the final model (SA-plot), **(K)** MD plot of significantly up-/downregulated genes in astrocytes infected with EBOV 3dpi (Log2FC versus average expression), **(L)** MD plot of significantly up-/downregulated genes in astrocytes infected with EBOV 6dpi (Log2FC versus average expression), **(M)**MD plot of significantly up-/downregulated genes in astrocytes infected with EBOV 12dpi (Log2FC versus average expression), **(N)** volcano plot of significantly up-/downregulated genes in astrocytes infected with EBOV 3dpi (log10 p-adjusted versus Log2FC), **(O)** volcano plot of significantly up-/downregulated genes in astrocytes infected with EBOV 6dpi (log10 p-adjusted versus Log2FC), **(P)** volcano plot of significantly up-/downregulated genes in astrocytes infected with EBOV 12dpi (log10 p-adjusted versus Log2FC).

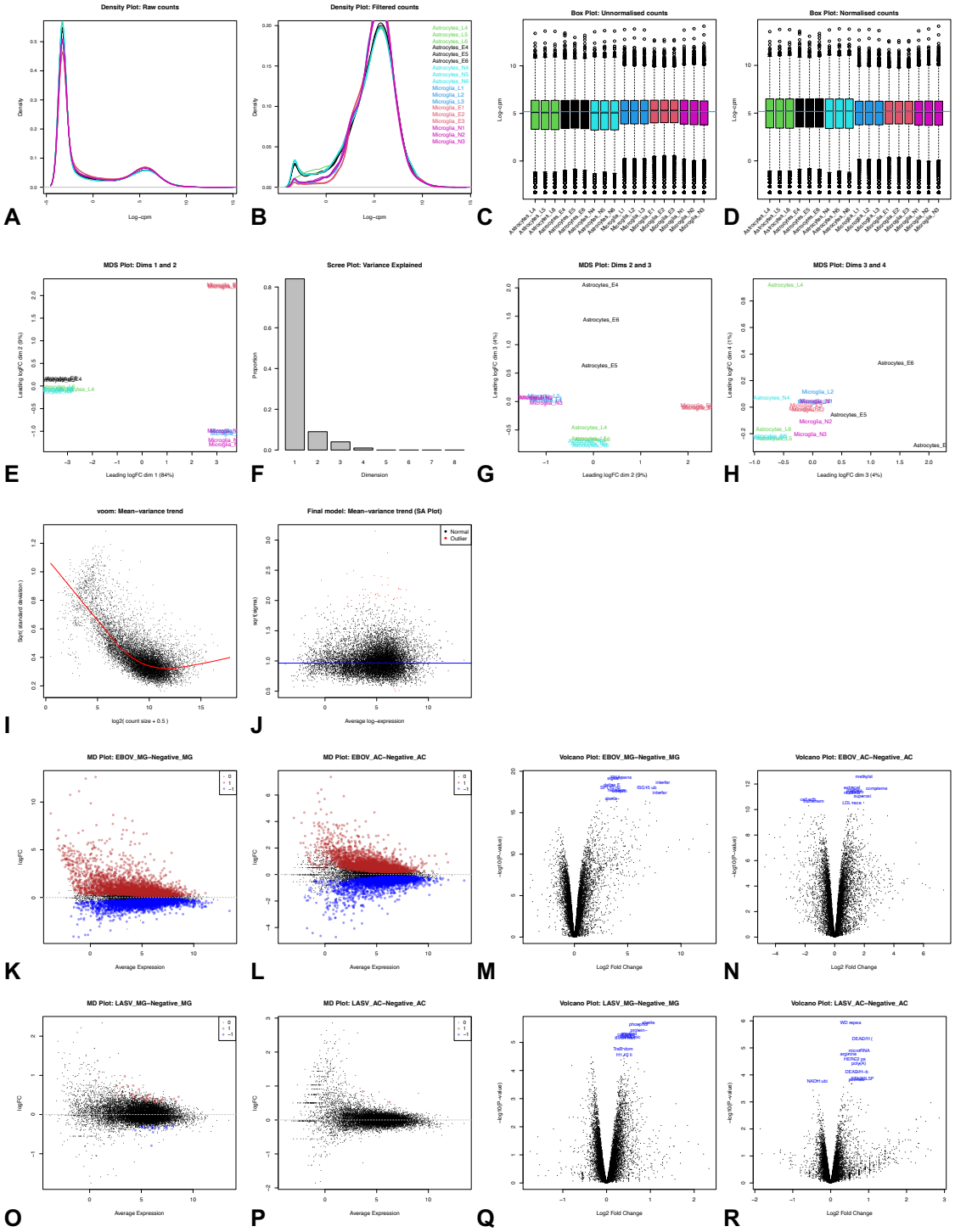


Figure 84: Transcriptome analysis 20dpi: supplementary data limma-voom. **(A)** density plot of raw counts, **(B)** density plot of filtered counts ($\geq$5 counts per million reads in n=3 samples), **(C)** box plot of unnormalized counts, **(D)** boxplot of normalized counts, **(E)** MDS plot of dimension 1 and 2, **(F)** scree plot explaining variance, **(G)** MDS plot of dimension 2 and 3, **(H)** MDS plot of dimension 3 and 4, **(I)** mean-variance trend, **(J)** mean-variance trend of the final model (SA-plot), **(K)** MD plot of significantly up-/downregulated genes in microglia infected with EBOV (Log2FC versus average expression), **(L)** MD plot of significantly up-/downregulated genes in astrocytes infected with EBOV (Log2FC versus average expression), **(M)** volcano plot of significantly up-/downregulated genes in microglia infected with EBOV (log10 p-adjusted versus Log2FC), **(N)** volcano plot of significantly up-/downregulated genes in astrocytes infected with LASV (log10 p-adjusted versus Log2FC), **(O)** MD plot of significantly up-/downregulated genes in microglia infected with LASV (Log2FC versus average expression), **(P)** MD plot of significantly up-/downregulated genes in astrocytes infected with EBOV (Log2FC versus average expression), **(Q)** volcano plot of significantly up-/downregulated genes in microglia infected with LASV (log10 p-adjusted versus Log2FC), **(R)** volcano plot of significantly up-/downregulated genes in astrocytes infected with LASV (log10 p-adjusted versus Log2FC).

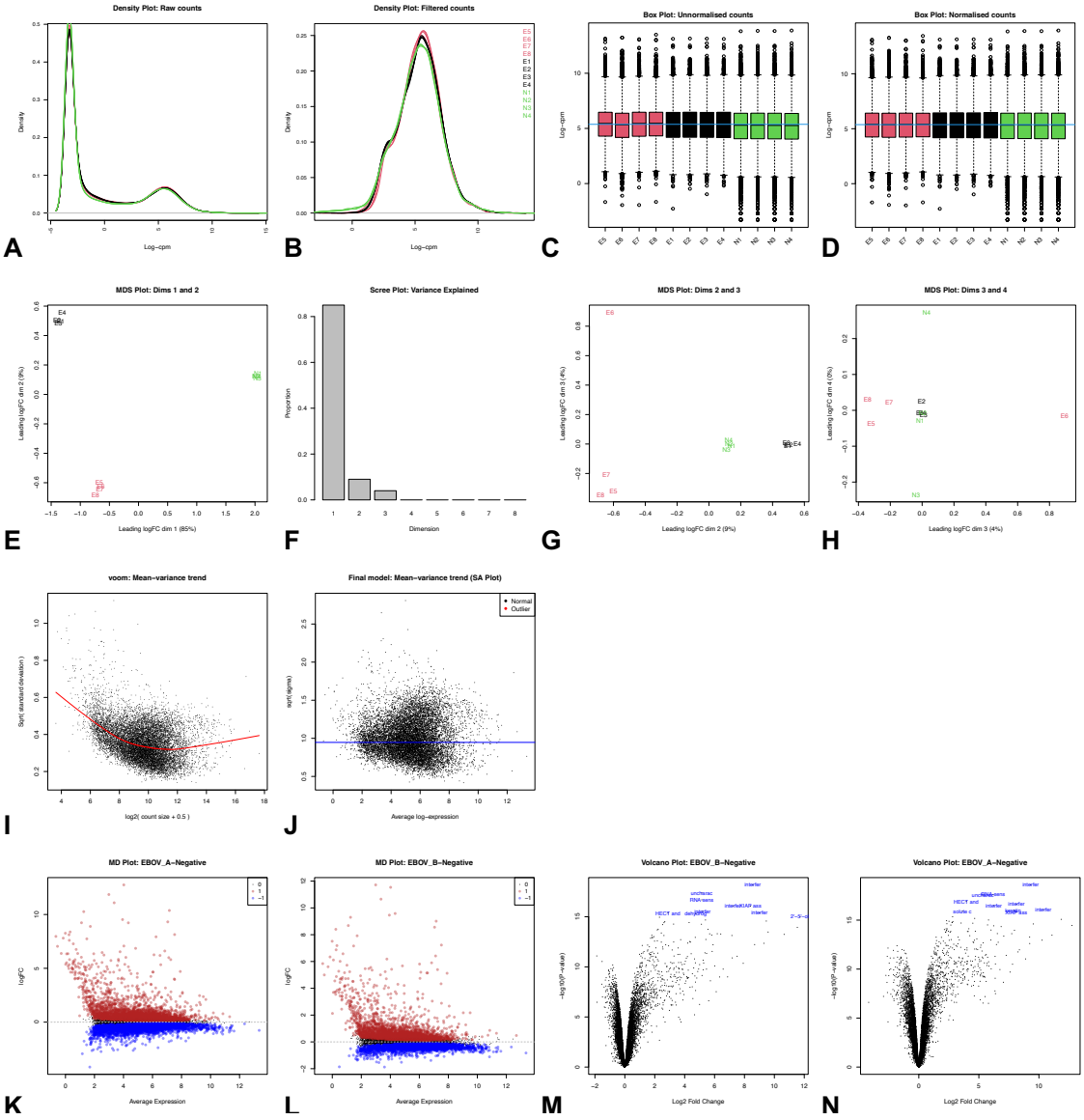


Figure 85: Transcriptome analysis after passaging: supplementary data limma-voom. (A) density plot of raw counts, **(B)** density plot of filtered counts (≥5 counts per million reads in n=3 samples), **(C)** box plot of unnormalized counts, **(D)** boxplot of normalized counts, **(E)** MDS plot of dimension 1 and 2, **(F)** scree plot explaining variance, **(G)** MDS plot of dimension 2 and 3, **(H)** MDS plot of dimension 3 and 4, **(I)** mean-variance trend, **(J)** mean-variance trend of the final model (SA-plot), **(K)** MD plot of significantly up-/downregulated genes in microglia passaged with EBOV flask A (Log2FC versus average expression), **(L)** MD plot of significantly up-/downregulated genes in microglia passaged with EBOV flask B (Log2FC versus average expression), **(M)** volcano plot of significantly up-/downregulated genes in microglia passaged with EBOV flask A(log10 p-adjusted versus Log2FC), **(N)** volcano plot of significantly up-/downregulated genes in microglia passaged with EBOV flask B(log10 p-adjusted versus Log2FC).

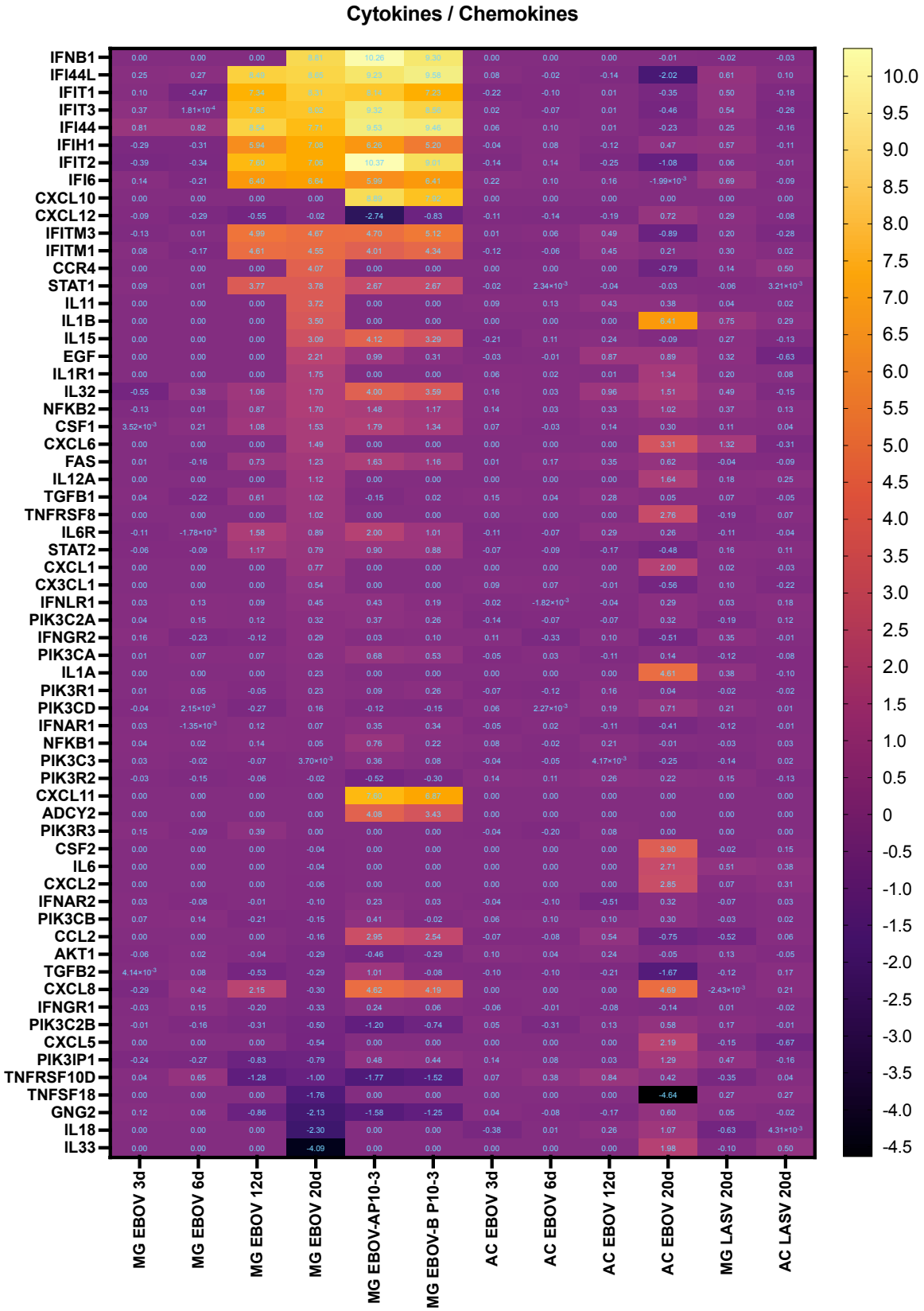


Figure 86: Heatmap of Log2FC in the expression of selected cytokine/chemokine signaling. Heatmap summarizing the Log2FC in the expression of all datasets in comparison to the respective negative control in selected Heatmap of Log2FC in the expression of selected GOIs involved in cytokine/chemokine signaling. MG = microglia, AC = astrocytes. 0 = not expressed in this cell type (≥5counts/million reads).

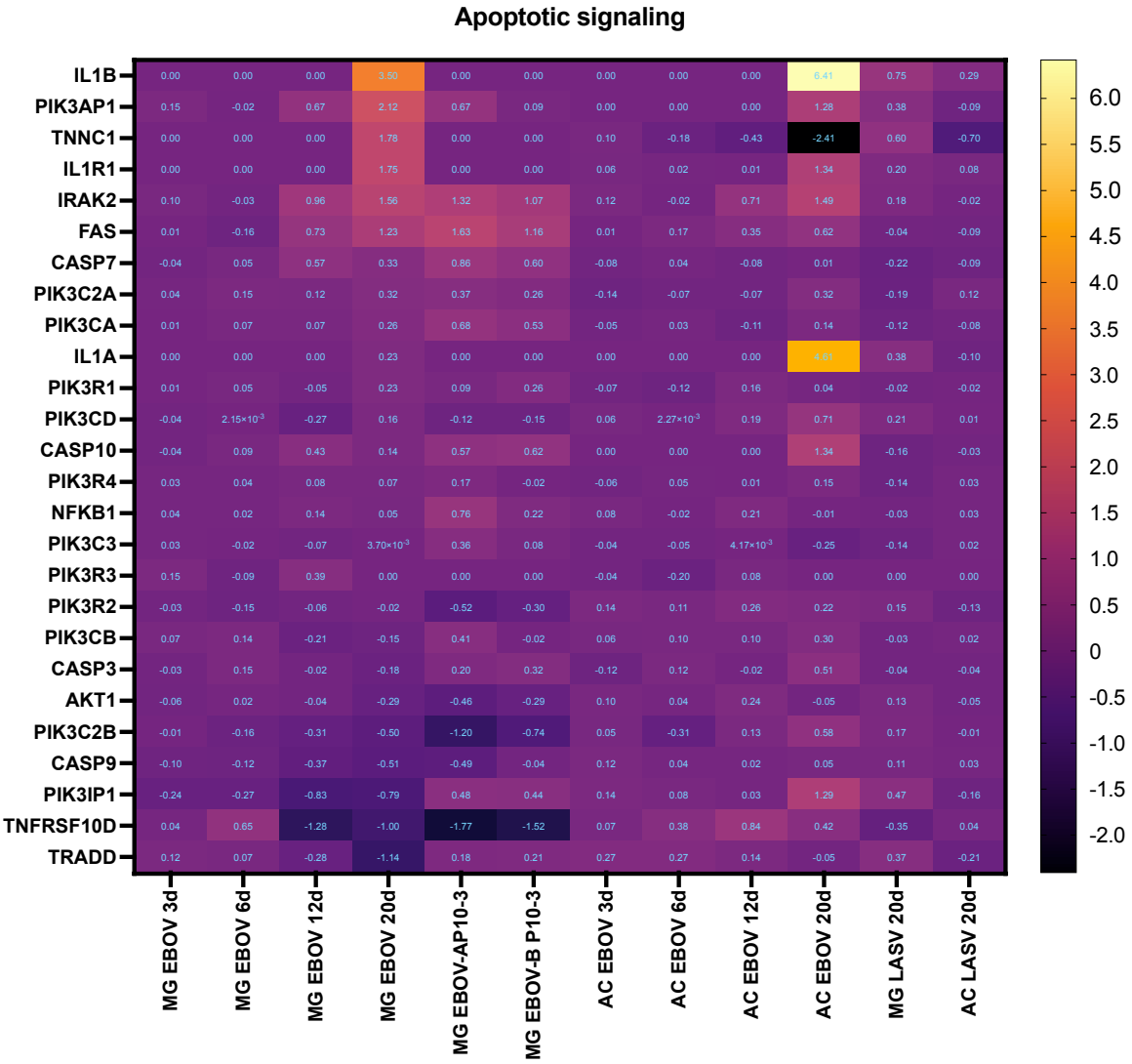


Figure 87: Heatmap of Log2FC in the expression of selected host factors in apoptotic signaling. Heatmap summarizing the Log2FC in the expression of all datasets compared to the respective negative control in selected Heatmap of Log2FC in the expression of selected GOIs involved in apoptotic signaling. MG = microglia, AC = astrocytes. 0 = not expressed in this cell type ($\geq$5counts/million reads).

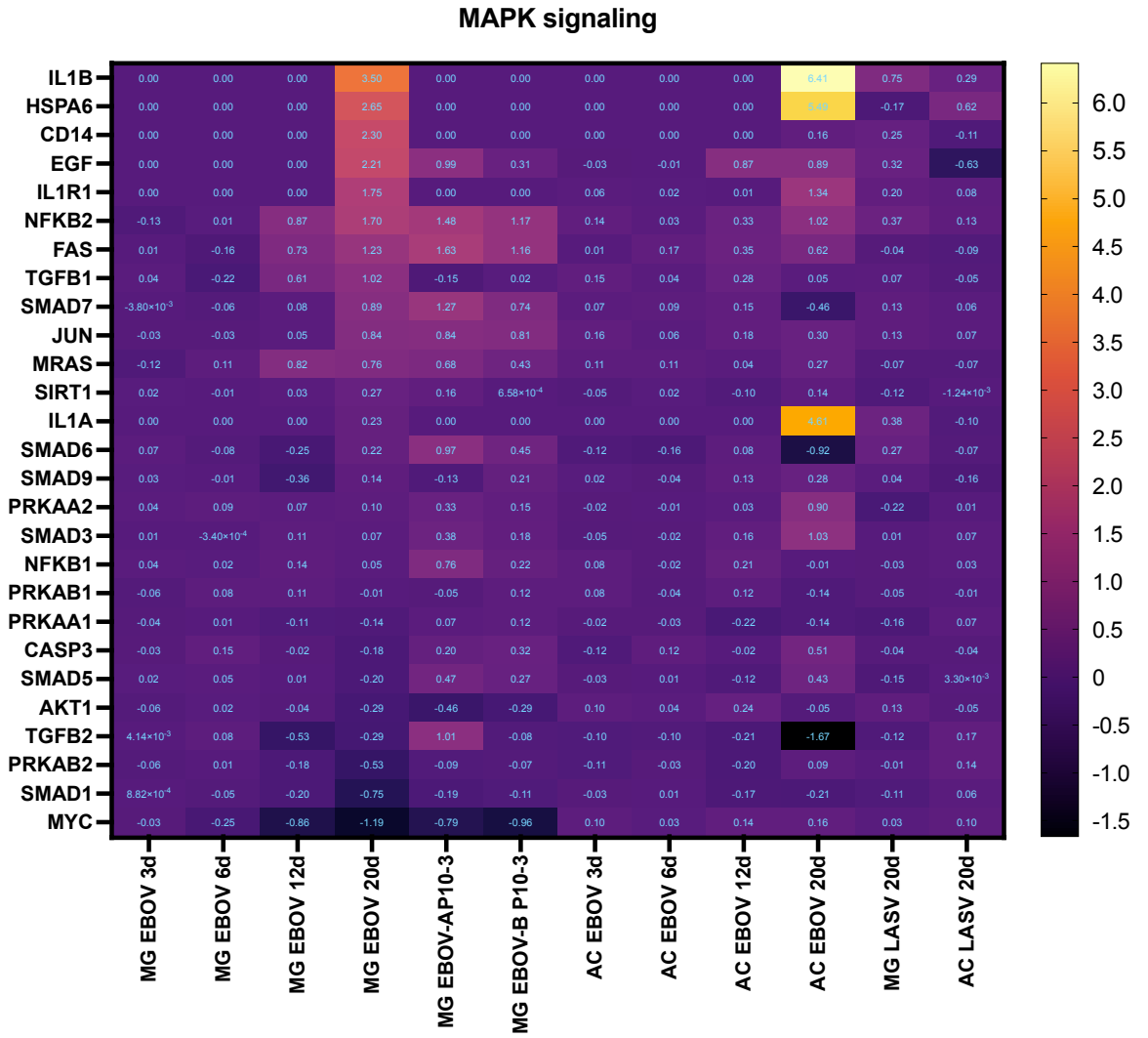


Figure 88: Heatmap of Log2FC in the expression of selected host factors in MAPK/PI3K/mTOR/AMPK signaling. Heatmap summarizing the Log2FC in the expression of all datasets compared to the respective negative control in selected Heatmap of Log2FC in the expression of selected GOIs involved in MAPK/PI3K/mTOR/AMPK signaling. MG = microglia, AC = astrocytes. 0 = not expressed in this cell type (≥5counts/million reads).

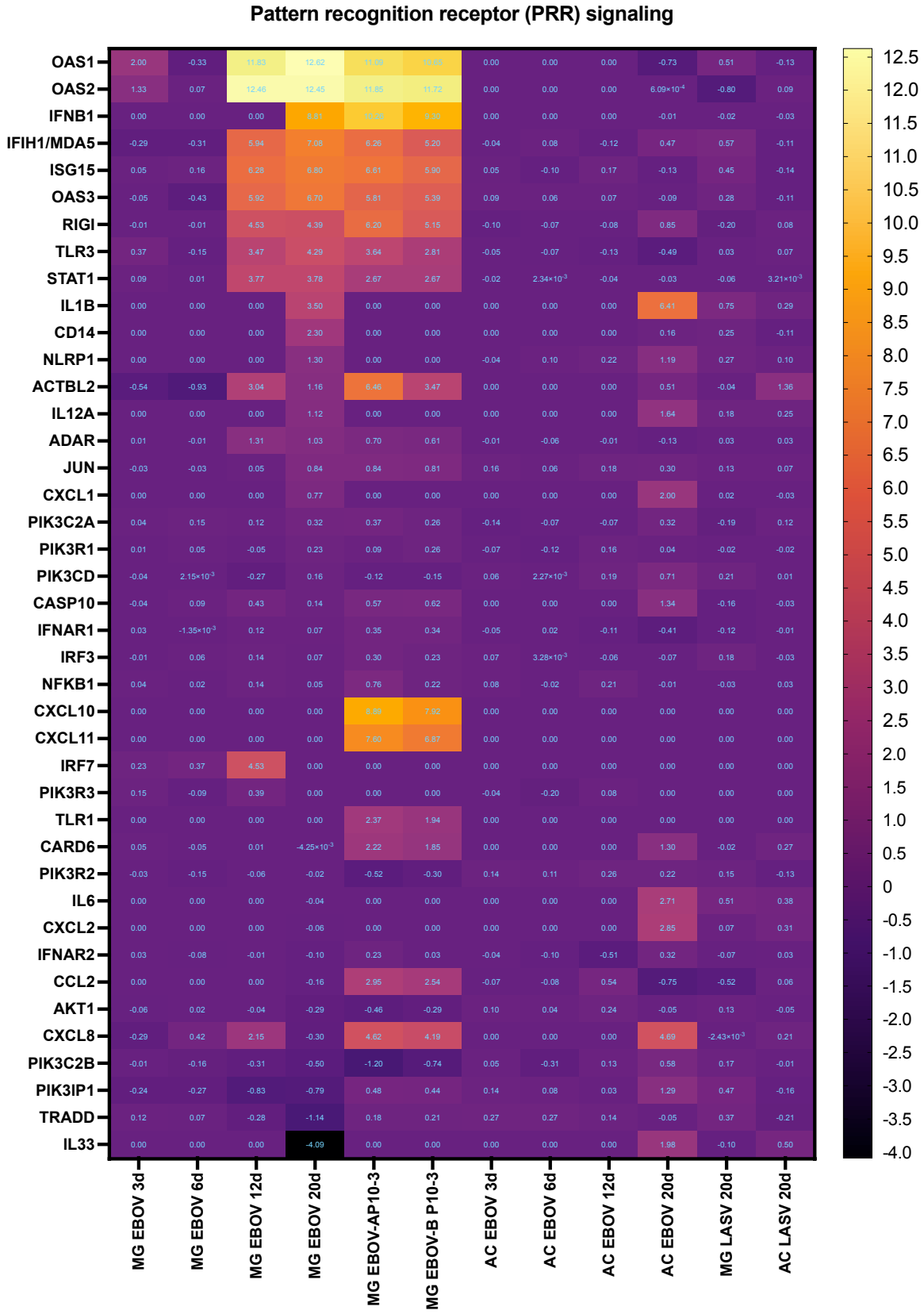


Figure 89: Heatmap of Log2FC in the expression of selected host factors in PRR signaling. Heatmap summarizing the Log2FC in the expression of all datasets compared to the respective negative control in selected Heatmap of Log2FC in the expression of selected GOIs involved in PRR signaling. MG = microglia, AC = astrocytes. 0 = not expressed in this cell type ($\geq$5counts/million reads).

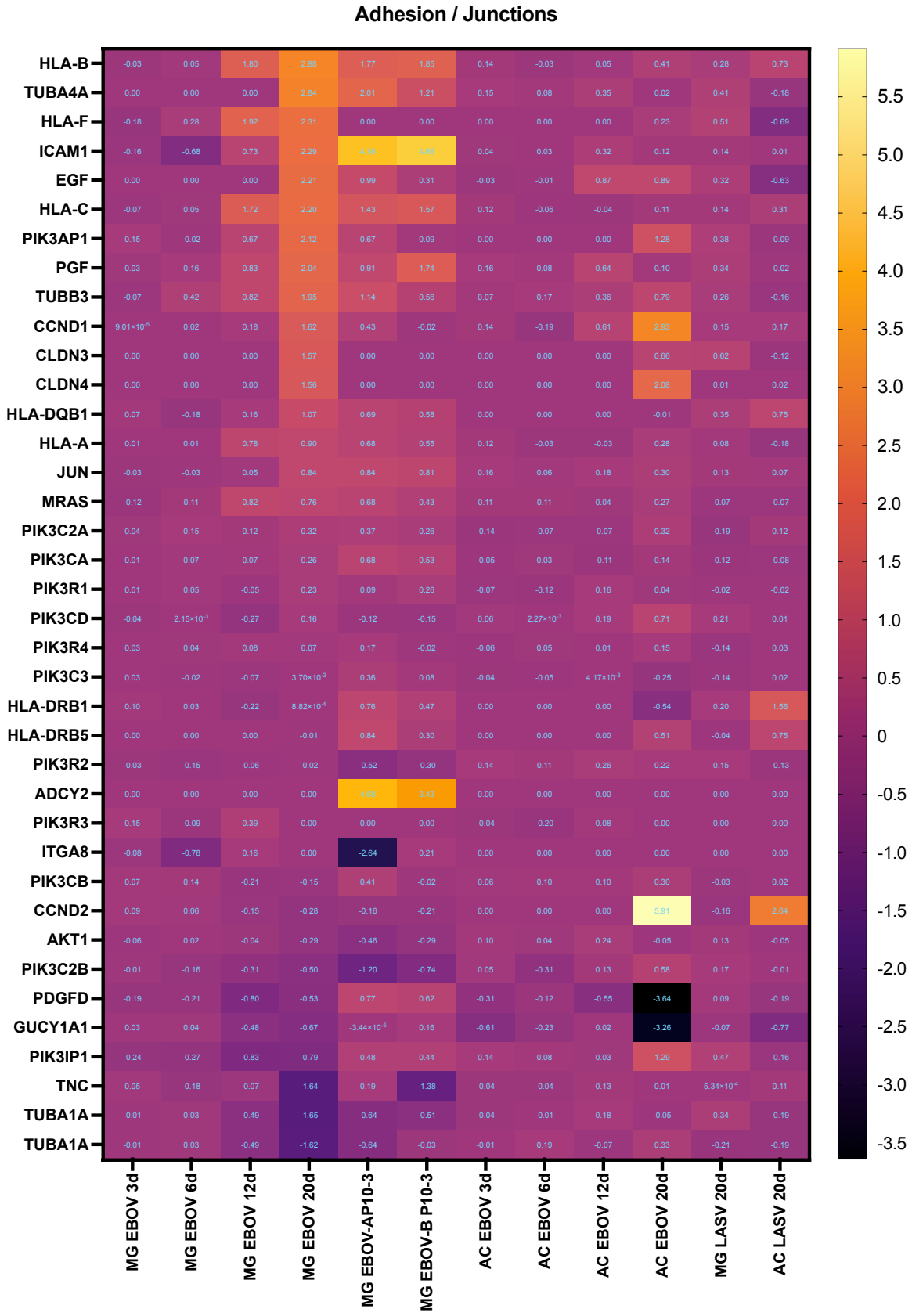


Figure 90: Heatmap of Log2FC in the expression of selected host factors in adhesion and motility signaling. Heatmap summarizing the Log2FC in the expression of all datasets compared to the respective negative control in selected Heatmap of Log2FC in the expression of selected GOIs involved in adhesion and motility signaling. MG = microglia, AC = astrocytes.

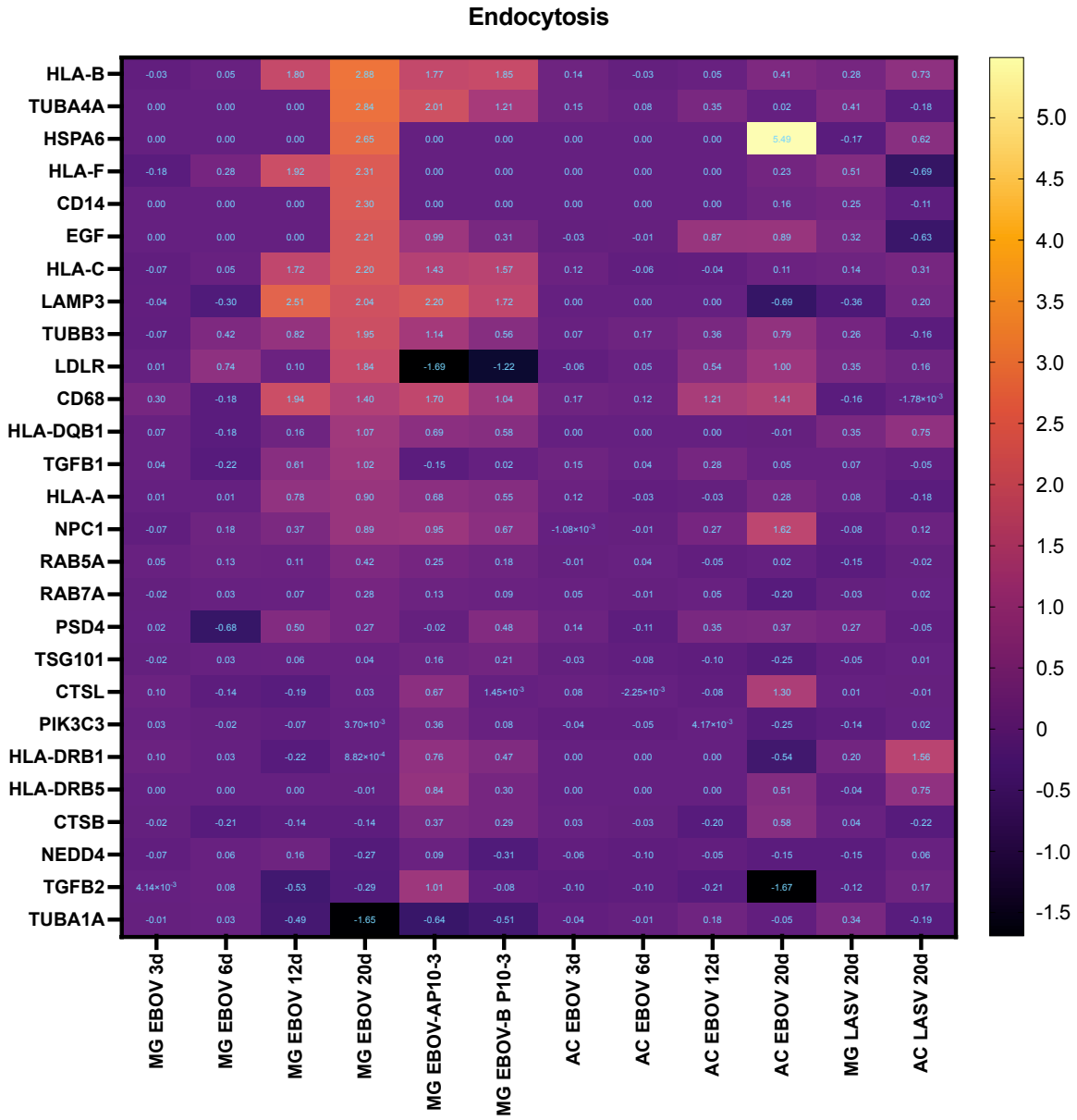


Figure 91: Heatmap of Log2FC in the expression of selected host factors in endocytosis pathway signaling. Heatmap summarizing the Log2FC in the expression of all datasets compared to to the respective negative control in selected Heatmap of Log2FC in the expression of selected GOIs involved in endocytosis pathway signaling. MG = microglia, AC = astrocytes. 0 = not expressed in this cell type ($\geq$5counts/million reads).

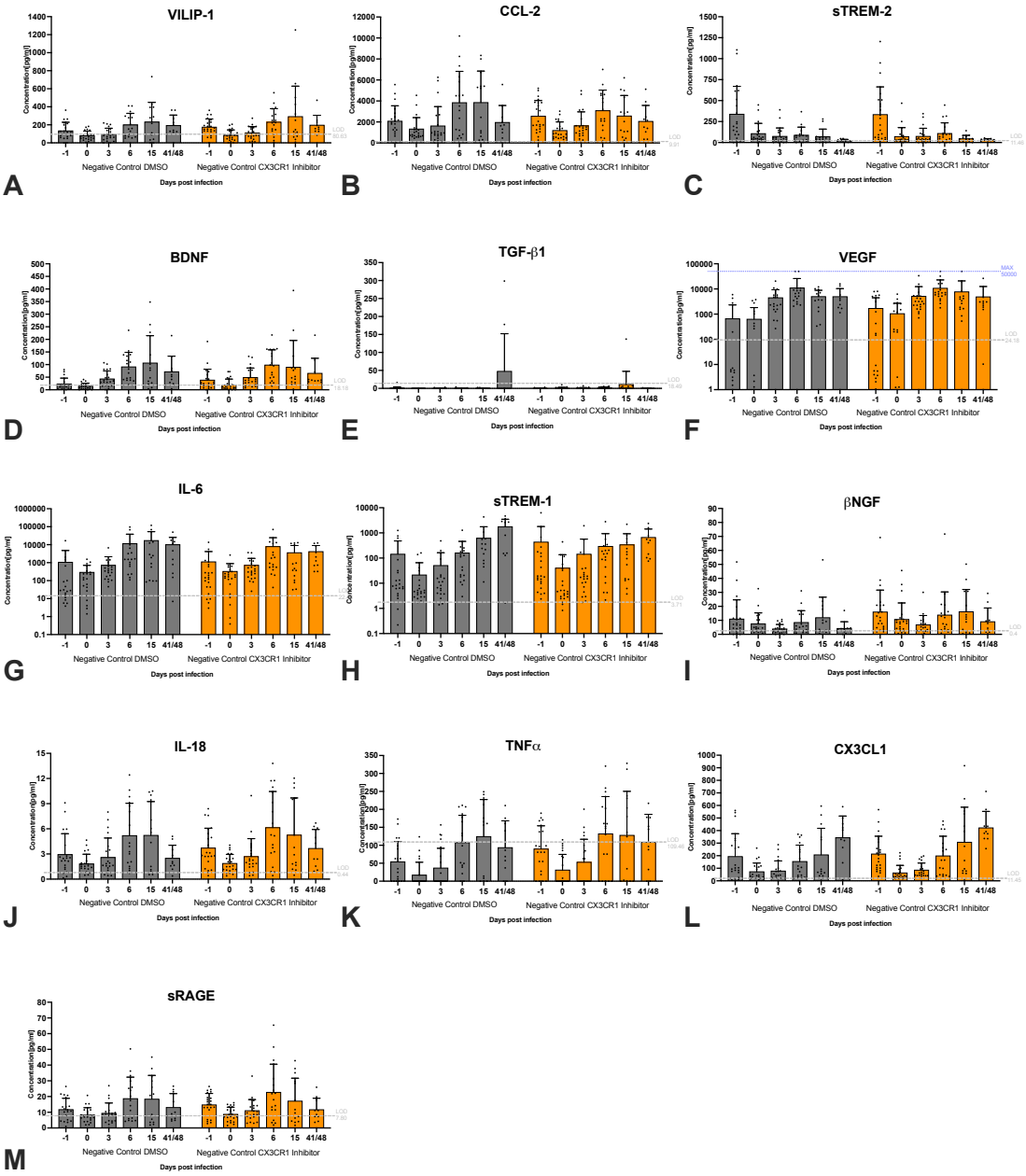


Figure 92: Cytokine/chemokine concentration in the supernatant of human choroid organoids treated with CX3CR1 Inhibitor. Mean (+SD) cytokine/chemokine levels [pg/ml] in the supernatant of untreated (grey), or CX3CR1 (AZD8797) treated (orange) human choroid plexus organoids before treatment (d-1), 24 h after treatment (d0) and at 3, 6, 15, 41/48 days. At least n=10 organoids originating from two independent organoid batches and experiments per time point per group. Mixed-effects model with Tukey's multiple comparisons with significant differences ($p \leq 0.05$) indicated by brackets. LOD is indicated as grey dotted line as marking the higher limit of either of the measurements. **(A)** visinin-like protein 1 (VILIP-1), **(B)** CC-Chemokin-Ligand-2 (CCL2), **(C)** soluble triggering receptor expressed on myeloid cells 2 (sTREM-2) **(D)** brain-derived neurotropic factor (BDNF), **(E)** tumor growth factor 1 β , **(F)** vascular endothelial growth factor (VEGF), **(G)** Interleukin 6 (IL-6), **(H)** soluble triggering receptor expressed on myeloid cells 1 (sTREM-1), **(I)** β nerve growth factor (β-NGF), **(J)** interleukin 18 (IL-18), **(K)** tumor necrosis factor α (TNF-α), **(L)** fractalkine, C-X3-C motif chemokine ligand 1 (CX3CL1), **(M)** soluble receptor of advanced glycosylation end-products (sRAGE).

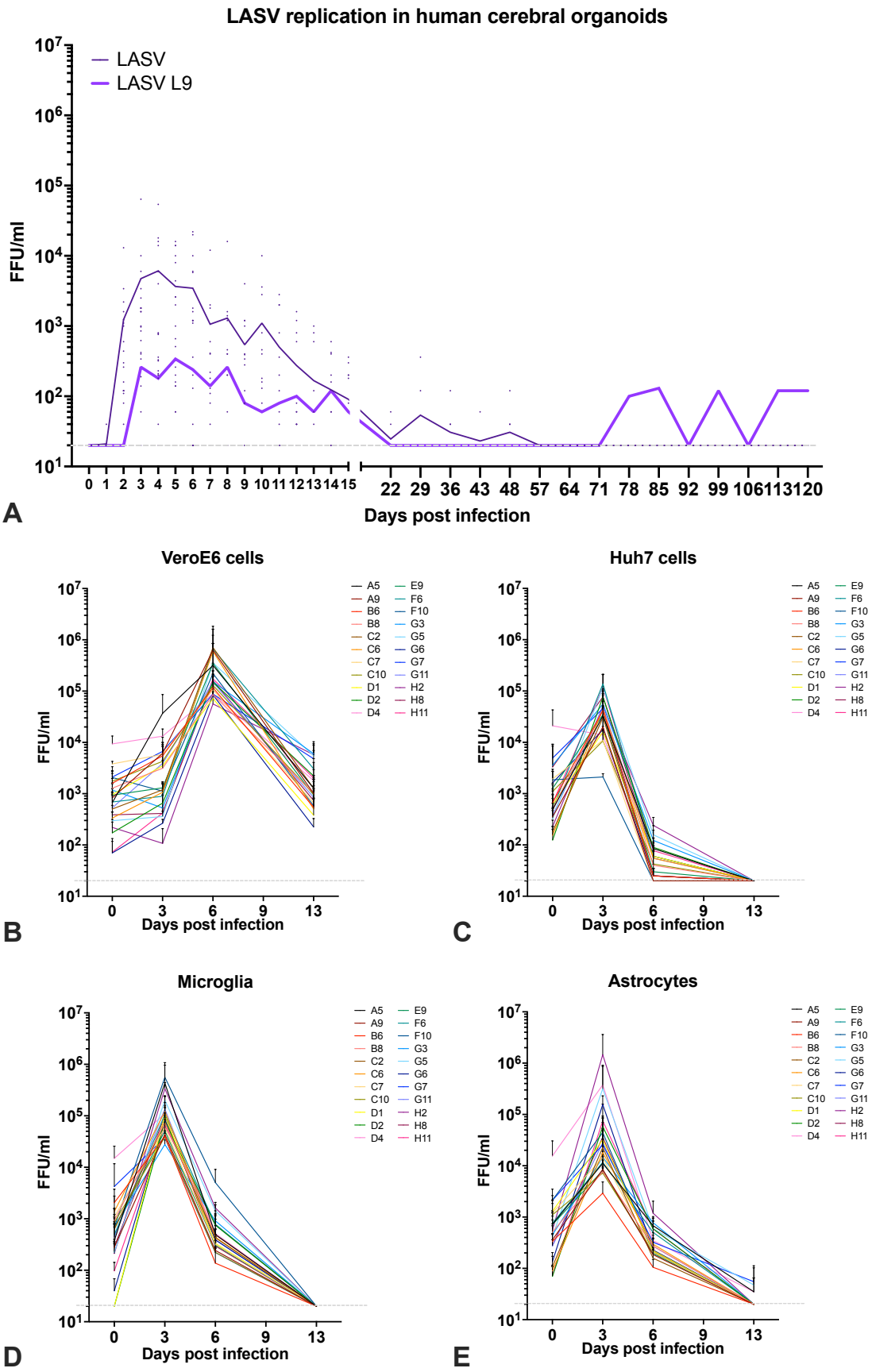


Figure 93: Replication of LASV$_{n120}$ in VeroE6 cells, Huh7 cells, microglia, and astrocytes. (A) Mean (+SD) titers [FFU/ml] of all LASV-infected cerebral organoids (purple, thin line) versus titers of organoid L9 with recurring infectious particles in the supernatant (purple, thick) (already depicted in Figure 26). Mean titers [FFU/ml] of LASV$_{n120}$ isolates in **(B)** VeroE6 cells, **(C)** Huh7 cells, **(D)** microglia and **(E)** astrocytes (n=4 replicates in one experiment, MOI=0.01). LOD=20FFU/ml marked as grey dotted line.

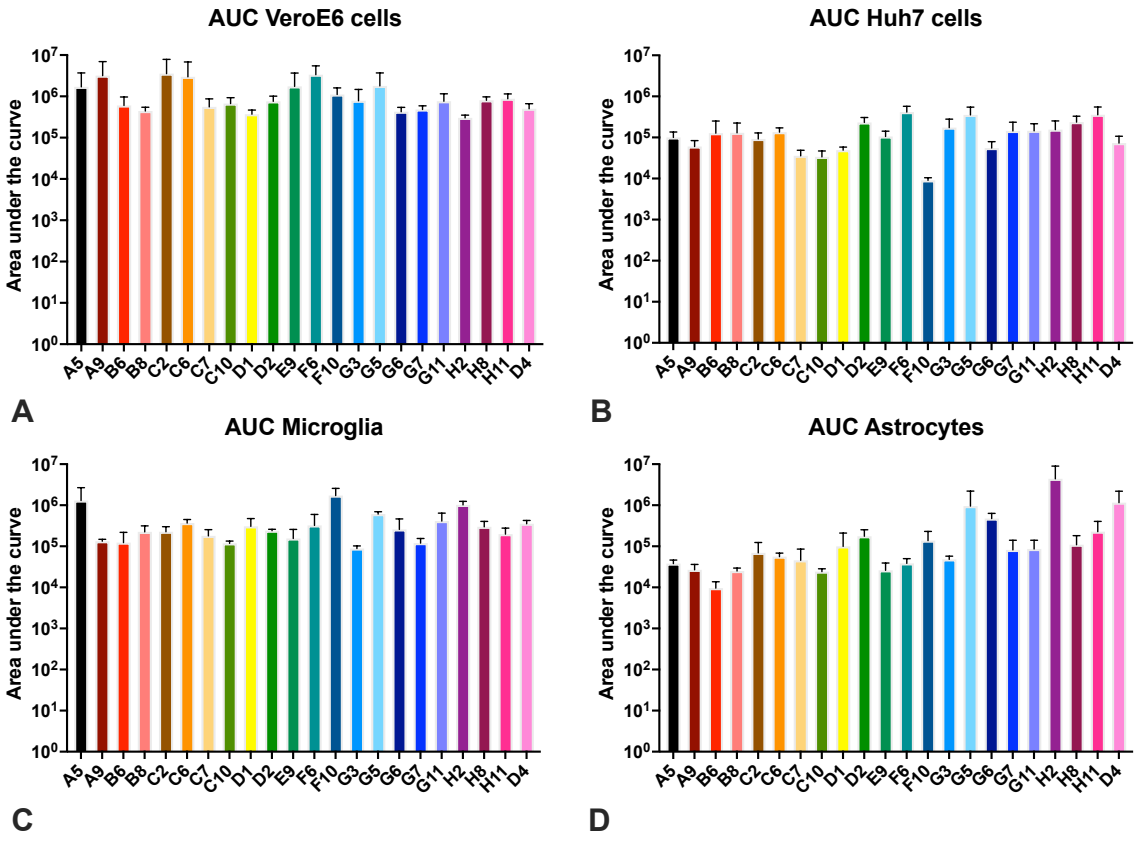


Figure 94: AUC of LASV$_{n120}$ in VeroE6 cells, Huh7 cells, microglia, and astrocytes. Area under the curve (AUC) calculated for the viral titers of LASV$_{n120}$ variants in **(A)** VeroE6 cells, **(B)** Huh7 cells, **(C)** microglia, **(D)** astrocytes (n=4 replicates in one experiment, MOI=0.01).

UKE - Institut für Transfusionsmedizin Dok. / [Vers.]: 9-56.220.5-0 / [003] gültig ab 05.07.2018 Seite 1/1

Anforderung von Blutprodukten zur wissenschaftlichen Verwendung

Angaben zur anfordernden Klinik bzw. Institut: Bitte füllen Sie die nachfolgend abgefragten Details lückenlos aus. Wir benötigen von Ihnen eine kurze Zusammenfassung was Sie benötigen. Hierbei bitten wir um gezielte Angaben zur Menge und Zeitraum. Welche Angaben wünschen Sie zu den Produkten zu bekommen? Wer ist Ihr Arbeitsgruppenleiter und somit Verantwortlicher für Rückfragen?

Angaben zur anfordernden Arbeitsgruppe / Institut / Klinik:	
Zentrum	BERNHARD-NOCHT INST. F. TROPENMED
Klinik	
Institut	S.O.
Arbeitsgruppe	MUÑOZ-FONTELA / VIRUS IMMUNOLOGIE
Leiter der Arbeitsgruppe bzw. Projektleiter	C. MUÑOZ-FONTELA
Sitz der Arbeitsgruppe (Gebäude)	LABOR 3 (E6) HAUPTGEBÄUDE
Kontaktperson der Arbeitsgruppe	LINA WIDERSPICK
Telefon- Nr. der Kontaktperson	+49 1525206 5112

Kurze Zusammenfassung des Projektes (kurze Erklärung, wofür das Blutprodukt benötigt wird):
Infektion primärer Zellkopul. (moDC / MD Microglia) mit Filoviren, Henipaviren.
Voraussichtliche Laufzeit des Projektes: 4 MONATE

Angaben zum gewünschten Produkt:		
Gewünschtes Produkt	☒ PBC	☐ Anderes:
Wie viele Produkte?	☐ Regelmäßige Bestellung Anzahl Produkte / Woche:	☒ Einmalig Anzahl Produkte: 3
Von Ihnen gewünschte Zusatzinformation zum Produkt	☐ CMV- Status des Spenders ☐ Geschlecht des Spenders	☐ Alter des Spenders ☐ Andere:

Bitte bestätigen Sie uns folgende Angaben		
Das von uns erhaltene Material wird vom Anfordernden **nicht** in Mensch- oder Tierversuchen eingesetzt.	☒ Ja	☐ Nein
Das von uns erhaltene Material wird vom Anfordernden **nicht** an Dritte weitergegeben.	☒ Ja	☐ Nein
Das infektiöse Restrisiko des von uns erhaltenen Materials ist dem Anfordernden bekannt und wird entsprechend beachtet.	☒ Ja	☐ Nein
Die ordnungsgemäße Entsorgung von Restmaterial obliegt der Verantwortung des Anfordernden.	☒ Ja	☐ Nein

Datum, Unterschrift Institutsleiter bzw. Projektleiter

CESAR MUÑOZ-FONTELA — 03/11/2021

Name in Blockschrift — Datum, Unterschrift

Bitten senden Sie das unterschriebene Formular entweder per Fax an 040 7410 54134 oder per email an anja.borger@uke.de und produ-transmed@uke.de. Wir werden Ihre Wünsche auf Durchführbarkeit prüfen und uns bei Ihnen melden.

Auszufüllen vom Institut für Transfusionsmedizin:	Datum / Kürzel:
☐ Blutprodukte können geliefert werden	
☐ Rücksprache mit dem Anfordernden gehalten.	
☐ „Einsendergruppe" in Swisslab angelegt.	

Figure 95: Ethics approval PBMC.